Modeling of Galaxy and Massive Black Hole Evolution Since Cosmic Dawn

Nianyi Chen

Department of Physics
Carnegie Mellon University

Thesis Committee:
Tiziana Di Matteo (Chair)
Hy Trac
Rupert Croft
Matt McQuinn

July 26, 2024

Submitted in partial fulfillment of the requirements
for the degree of Doctor of Philosophy.

Abstract

This thesis explores the evolution of galaxies and massive black holes (MBHs) since cosmic dawn, focusing on cosmic reionization and MBH binaries. I develop and employ novel numerical methods for more accurate modeling of cosmic reionization and MBH binaries to better understand these processes, and for putting astrophysical constraints with ongoing and future observations. Cosmic reionization starts with the formation of the first galaxies and influences all the baryon components in the Universe. I develop and apply semi-numerical algorithms to better understand the timing and duration of cosmic reionization, as well as its spatial progression, with current observational constraints from the cosmic wave background. Massive black hole binaries offer another promising channel for understanding the Universe since the first galaxies formed. I advance the modeling of the massive black hole binary population in cosmological simulations of galaxy formation. This leads to a more accurate characterization of the MBH binary population across all redshift and mass ranges. I investigated the binary evolution in realistic galaxy environments and made theoretical predictions for the ongoing and upcoming electromagnetic and gravitational wave observations of these binaries. These predictions can be useful in interpreting observations and constraining MBH seeds, growth and assembly histories. My study of cosmic reionization and MBH binaries constitutes theoretical progress in understanding several aspects of galaxy formation, especially in the high-redshift Universe.

Acknowledgments

This work is made possible by the contribution and support of many.

First and foremost, I want to express my gratitude to my thesis advisors, Tiziana and Hy, for being great mentors over the past six years both in science and in personal growth. Both of them truly care for their students' academic success and mental well-being. They have encouraged me to challenge myself and pursue questions that are interesting but difficult, and always cheer for the little achievements I made along the way. I will be forever inspired by their enthusiasm for science, kindness to others, and optimism when faced with difficulties. I would also like to thank my thesis committee members Rupert and Matt, and senior collaborators Simeon Bird, Michael Tremmel, Miguel Holgado, and Colin DeGraf. All of them have provided great help and advice on the projects included in this thesis and I always appreciate the fruitful science discussions with them. I thank Katie Breivik, Nora Shipp, Anna O'Grady, and other people in the McWilliams Center for providing unwavering guidance as I went through the job application process. I want to express my special thanks to Scott Dodelson, who first brought me into cosmology research and made the experience enjoyable enough for me to keep pursuing a PhD in the field.

I still remember the warmness of people in the senior classes in the Physics Department, who made me feel a sense of belonging from the beginning. These include but are not limited to Hung-Jin Hwang, Husni Almoubayyed, Kuan-Wei Hwang, and Aklant Bhowmick. In particular, I want to thank Matt Ho and Yueying Ni, who despite being only a year more senior than me, are so mature as a researcher and human being and have always been a role model for me in many aspects. I also want to thank the postdocs that I had the fortune to come across and interact closely with during my six years at the McWilliams Center. I thank Markus Michael Rau and Qirong Zhu for teaching me so much about statistics and simulations, and for organizing the journal clubs with me during the pandemic; Mohit Bhardwaj for his cheerfulness and enthusiasm about life, people, and science; Xiangchong Li for his sense of humor, life wisdom, and for taking care of my cat when I am traveling. All of them have shared valuable and honest career advice with me and gave me a sneak peek at the lives of postdocs and what it meant to be a good researcher.

I thank my dear officemates Andy Park, Kuldeep Sharma, Tianqing Zhang, Ann-Marsha Alexis, and Alan Zhou for providing a daily dose of motivation to come to work in the office. I really enjoyed the random chic-chatting when I needed to take a break from my computer screens. I also want to thank my group-mates Diptajyoti Mukherjee, Yihao Zhou, and Patrick LaChance: I have learned so much from them despite being more senior in the group. I thank I-Hsuan Kao, Andresa de Campos, Ryan Muzzio, Kuldeep Sharma and Tianqing Zhang from my cohort for their friendship and for going through this tough process with me. I also want to thank my old friends who kept in touch all these years, especially Camy Liu, Xinyue Xia, Yuxuan Zhang, who have always been there for me when I want to talk about anything.

I owe my greatest gratitude to my parents for giving me the best care they could provide since childhood and for all the education that I had the privilege to receive. They are my

first and best teachers and have always been my biggest supporters until today. Lastly, I want to express my deep appreciation to my partner Biwei Dai. I thank him for all the happiness as well as hardships we shared over the past few years, especially during and after the pandemic – this PhD journey would have been unimaginably harder without his love, understanding, and support (emotionally and intellectually). He is the most brilliant, kind, and humble person I know, and always inspires me to become a better person.

Contents

List of Tables

List of Figures

Chapter 1

Introduction

It is now an exciting era for studying the galaxy evolution in the high-redshift Universe, and relate it spatially to the evolution of instruction on larger scales, and temporally to the present-day galaxies. The state of the field rapidly changing change due to a suite of instruments and telescopes that are operating now or will become available in the next few years. For example, the James Webb Space Telescope (JWST) with its large mirror and infrared frequency coverage, continues to break the record of the highest redshift galaxies and AGN observations. These observations also challenge some of the existing theories of high-redshift galaxy and massive black hole formation. Additionally, our understanding of the epoch of reionization and the IGM will soon be replaced by a more complete picture of the neutral hydrogen distribution in the Universe by current and upcoming radio telescopes including the Low-Frequency Array (LOFAR), Square Kilometer Array (SKA) and Hydrogen Epoch of Reionization Array (HERA). The recent development in gravitational wave (GW) astronomy also enables the study of black holes through the GW emission from black hole mergers. Particularly relevant to the understanding of high-redshift massive black hole formation is the Laser Interferometer Space Antenna (LISA), to be launched in about a decade. All the instruments above will complement each other and revolutionize our understanding of the galaxy evolution theory since cosmic dawn.

In this thesis, I aim to use novel numerical methods to understand galaxy evolution since the first galaxies formed, and to make testable theoretical predictions for ongoing and future observations. In this chapter, I am going to describe a few topics that constitute the bedrock of this thesis. Section 1.1 describes the key components of modern cosmological galaxy formation simulations, which is the foundation for many works in this thesis. Section 1.2 introduces massive black holes, with a focus on their numerical modeling and massive black hole binaries. In Section 1.3 I describe the theoretical modeling of cosmic reionization, followed by the imprint of reionization on the cosmic wave background.

1.1 Cosmological Hydrodynamic Simulations

Cosmological simulations are computational models used to simulate the evolution of the Universe from an early time to the present day. They are usually performed in a periodic box representative of a fraction of the observable Universe. Cosmological simulations can be broadly categorized into two main types. N-body simulations model only gravitational interactions and track the motion of individual particles representing matter. These simulations can be performed at $> Gpc$ scales and with a wide range of cosmological parameters, and are often used to understand the statistical properties of large-scale structure formation and dark matter halos. These simulations, when combined with semi-analytical modeling of the baryon and galaxy distribution or other forms of post-processing, can also be useful in modeling statistics of galaxy properties and evolution.

Building upon N-body simulations of gravity, hydrodynamic simulations also include gas dynamics and other fluids. They involve complex non-linear interactions of gravity and hydrodynamics, the formation of stars and black holes. In this approach, the physics at these much smaller galaxy scales is self-consistently coupled to large cosmological scales. Here we introduce the basic building blocks of cosmological hydrodynamical simulations, which enables many works done in this thesis.

1.1.1 Initial Condition

As systems of coupled differential equations, cosmological simulations start from an initial condition, usually set by the positions (or densities) and velocities of the particles (cells) involved. The initial condition is often set at an early enough time such that the density fluctuation is mostly in the linear regime (i.e. the over-densities $\delta(\mathbf{x}) \ll 1$ and can be approximated by first-order terms). According to the theory of inflation which seeded the density fluctuations, the initial density field is a Gaussian random field, where the joint probability distribution of density fluctuations is a multidimensional Gaussian completely specified by its matter power spectrum defined from the over-densities as

$$\left\langle \widetilde{\delta}\left(k\right)\widetilde{\delta}\left(k'\right)\right\rangle = (2\pi)^3 P\left(k\right)\delta^D\left(k+k'\right) \tag{1.1}$$

where $\tilde{\delta}(\mathbf{k}) = \int d^3\mathbf{x} e^{-i\mathbf{k}\cdot\mathbf{x}}\delta(\mathbf{x})$ is the Fourier transform of the over-density field [see e.g. Dodelson, 2003, for details].

The initial power spectrum is specified by the transfer function $T(k)$, calculated by solving the sets of coupled Einstein-Boltzmann equations numerically (with solvers such as CAMB [Lewis and Challinor, 2011] and CLASS [Lesgourgues, 2011]). After the initial power spectrum is set, the density field can be realized with a random phase factor. We then displace particles involved in the simulation (typically dark matter or baryons) from a uniform-density background (Cartesian lattice or glass-like) towards the target density field using first/second-order perturbation theories, sometimes with adjustments on small scales [e.g. Bertschinger, 2001, Garrison et al., 2016, Hahn and Abel, 2011, Jenkins, 2010, Zel'dovich,

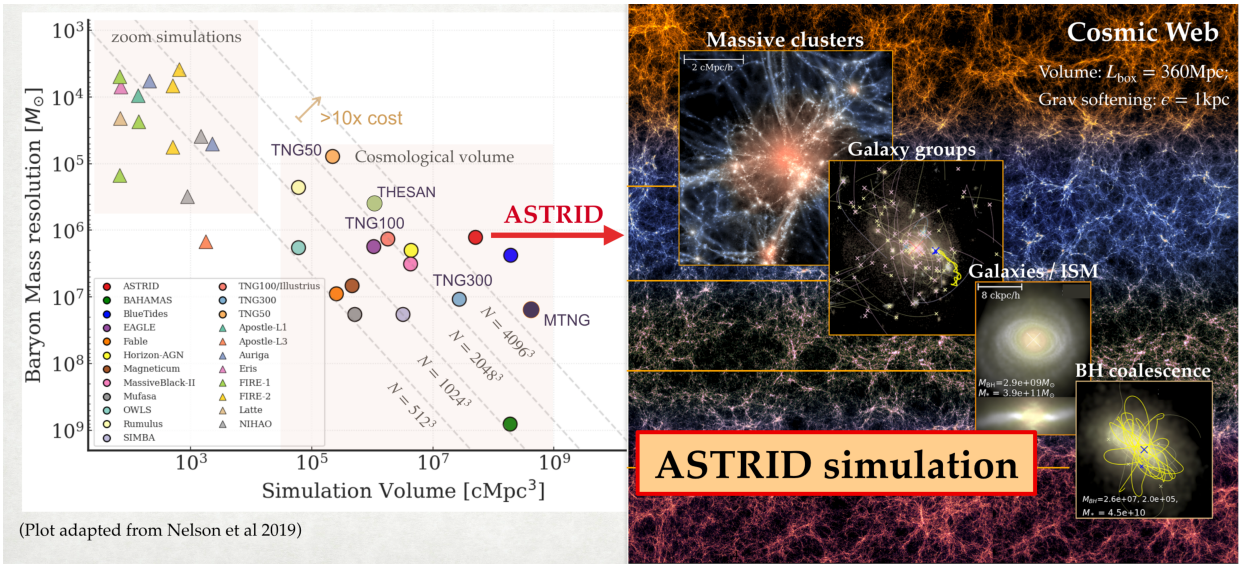

Figure 1.1: The resolution and box size of existing cosmological galaxy formation simulations (left), and an illustration of the various scales, physics, and components in the ASTRID simulation (right).

1970]. Baryon positions and velocities are set similarly, and the baryon temperature is initialized to the redshift-dependent microwave background temperature.

1.1.2 Gravity

After the initial conditions of particle positions are set, the time evolution of the particles is governed by the physics relevant to specific species. Gravity is a fundamental force influencing the evolution of all species modeled in simulations. Gravitationally interacting particles can be described by the collisionless Boltzmann equation coupled to the Poisson equation in an expanding universe. A commonly used method to solve gravity is the N-body method, which uses discrete particles as tracers for the matter distribution and gravitational potential. Cosmological N-body methods can be categorized into the particle-particle (PP) method, particle-mesh (PM) method, or a combination/approximation of them (e.g. Tree, Fast Multipole Method (FMM), TreePM, P^{3}M, refined mesh).

PP method directly calculates the particle-particle interactions and therefore has $O(\mathcal{N}^2)$ computation time. More specifically, it solves the discretized Poisson equation in its integral form via

$$\phi(\mathbf{x}_i) = -\sum_{j=1}^{N} \left\{ \frac{m_j}{|\mathbf{x}_j - \mathbf{x}_i| + \epsilon\left(|\mathbf{x}_j - \mathbf{x}_i|\right)} \right\}. \tag{1.2}$$

Here $\epsilon\left(|\mathbf{x}_j - \mathbf{x}_i|\right)$ is a softening kernel that prevents the singularity at close separations, and the size of the kernel is often empirically set to $\sim 1/30$ of the mean particle separation in cosmological simulations. We also note that in the cosmological context, since we impose

periodic boundary conditions, the distance is calculated from the nearest image of particle j [see e.g. Springel et al., 2021, for a detailed mathematical formulation].

The direct PP method, despite its accuracy and simplicity, can be too computationally expensive to be applied in the cosmological context, and thus its approximations are more widely used. One popular alternative is the oct-tree algorithm [Barnes and Hut, 1986], which groups source particles at further distances from the sink particle and only computes their gravitational contribution as a monopole. Another alternative is the fast-multiple method [FMM, Greengard and Rokhlin, 1987], which approximates distant interactions with multipole expansions. The FMM approach can be faster than a classic tree because the multipole expansion is not only carried out at the source side but also on the sink side where the target particles are located.

The Poisson equation can also be solved in its differential form

$$\nabla^2\phi(\mathbf{x}) = 4\pi G\rho(\mathbf{x}) \tag{1.3}$$

using a mesh-based method. Particle-mesh (PM) methods map particles to a density field on a grid and discretize Poisson's equation directly. The equation is most conveniently solved when transformed into the Fourier space as $k^2\widetilde{\Phi}(\mathbf{k}) = -4\pi G\widetilde{\rho}(\mathbf{k})$ through fast Fourier transform-based methods. This algorithm is also $O(\mathcal{N}\log(\mathcal{N}))$, but here N is the total grid count instead of the particle count. The advantage of the PM method is that it is computationally efficient and can be easily parallelized. The primary disadvantage is that the force accuracy is fixed at the grid size, which is often large in the cosmological context.

P^{3}M combines the direct PP method and the PM approach, by computing the short-range gravity from direct PP summation, and computing long-range gravity with PM. It scales better with the number of particles compared to the pure PP method, and has higher force resolution than the PM method, and therefore is widely used in current cosmological simulations.

1.1.3 Gas dynamics

Hydrodynamical simulations also model the baryon component, which consists mostly of hydrogen and helium gas. In addition to gravity, gas is also subject to pressure, cooling, and heating, and its dynamics follow the set of hydrodynamical equations:

$$\frac{\partial\rho}{\partial t} + \nabla\cdot(\rho\mathbf{v}) = 0, \tag{1.4}$$

$$\frac{\partial\mathbf{v}}{\partial t} + (\mathbf{v}\cdot\nabla)\mathbf{v} = -\left(\nabla\Phi + \frac{\nabla P}{\rho}\right), \tag{1.5}$$

$$\frac{\partial}{\partial t}\left[\rho\left(\frac{v^2}{2}+u\right)\right] + \nabla\cdot\left[\rho\left(\frac{v^2}{2}+\frac{P}{\rho}+u\right)\mathbf{v}\right] - \rho\mathbf{v}\cdot\nabla\Phi = \mathcal{H}-\mathcal{C}. \tag{1.6}$$

Here ρ is the gas density, P is the pressure, $\mathbf{v}$ is the velocity and u is the specific internal energy. The terms on the right-hand side of Equation 1.6 are the heating ($\mathcal{H}$) and cooling

($\mathcal{C}$) rates, which we will describe in more detail in the next subsection. The equations are closed by specifying the equation of state $P = (\gamma - 1)\rho u$, with $\gamma = 5/3$ for monotomic gas.

Current gas dynamics solvers in cosmological simulations can be classified into Lagrangian, Eulerian, and Arbitrary Lagrangian-Eulerian methods. Here we only focus on a description of the smoothed-particle hydrodynamics (SPH) based Lagrangian method, because it is employed in most of this thesis. For an introduction to the other two methods in the context of cosmological simulations, see e.g. Vogelsberger et al. [2020].

Lagrangian methods follow the individual fluid particles as they move through space and time. The most widely adopted Lagrangian method in astrophysics is the SPH method [e.g. Monaghan, 1992, Springel, 2010]. In SPH, the moving fluid particles are the carriers of thermodynamic quantities and their spatial distribution sets the resolution in the flow. The thermodynamic quantities of particles are obtained by a weighted average of neighboring particles with an SPH kernel specified by smoothing length h:

$$F_s(\mathbf{r}) \simeq \sum_j \frac{m_j}{\rho_j} F_j W\left(\mathbf{r} - \mathbf{r}_j, h\right), \tag{1.7}$$

where $F_s(\mathbf{r})$ is the field of interest and $W\left(\mathbf{r} - \mathbf{r}_j, h\right)$ is a spatial smoothing kernel. The advantages of the SPH formation include the adaptive spatial resolution which allows for detailed modeling of gas elements in dense environments. It is also easy to add to N-body simulations which are also particle-based. The main disadvantages of the SPH method lie in its limited capability to capture contact discontinuities, and shocks, and relatively poor accuracy for (high order) gradient estimates across density jumps. Some SPH implementations [Springel et al., 2005b] face challenges of spurious surface tension between high-density regions and low-density regions, prohibiting high-density particles from dissipating into low-density regions. This is solved by the pressure-entropy SPH formalism Hopkins [2013] that improves the handling of surface instabilities and model Kelvin- Helmholtz instability simulation properly.

1.1.4 Gas Cooling, Star Formation, and Stellar Feedback

As was already shown in Equation 1.6, gas can dissipate internal energy through radiative processes like collisional excitation, ionization, inverse Compton cooling, recombination, and free-free emission. In cosmological simulations, these processes are represented on a subgrid level, assuming the gas is optically thin and in ionization equilibrium with the background radiation field. Cooling processes are coupled to the energy equation using cooling functions that are either tabulated or extracted from chemical networks.

In this introduction I will only include the modeling of the gas, star-formation and feedback mechanisms most relevant to the works included. In SPH simulations, the atomic cooling process is implemented for individual gas particles. With radiative cooling rates tabulated for different species. For primordial gas that is mainly composed of hydrogen and helium, the primordial cooling rate is obtained by calculating the abundance of the different ionic species of gas after solving the ionization equilibrium between different species [Katz

et al., 1996]. In addition to primordial cooling, metal line cooling dominates the cooling process for temperatures $10^5 \sim 10^7 K$. Gas with $T < 10^4 K$ can only be cooled through the molecular cooling process.

The cooling process allows gas to collapse into dense clumps of molecular clouds and form stars. Many simulations transform a portion of the gas into collisionless star particles to model the star formation process under certain conditions. One widely adopted star-formation model was a sub-grid model developed by Springel and Hernquist [2003] that uses an effective equation of state to describe the interstellar medium (ISM). In this model, a gas particle is considered a mixture of cold, star-forming gas and hot ambient gas that exists in pressure equilibrium. A star-formation rate is assigned based on the density of gas in the cold phase and a characteristic timescale t_*. The feedback from supernova explosions of massive stars is associated with the star-formation rate of the gas particle, and the energy of this feedback can be deposited thermally or kinetically, depending on how the supernova explosion interacts with the gas environment. Stellar wind models are also developed to emulate the process of galactic-scale outflow launched by the supernova feedback. This momentum injection is modeled by decoupling star-forming gas from hydrodynamical interaction and ejecting it from the dense star-forming region. This is an important mechanism for regulating star formation. Stellar evolution and supernovae will also enrich the metals in the gas surrounding and in turn affect the cooling state of gas. To model this process, some cosmological simulations also track the stellar evolution and mass return of the stars to the gas environment based on metal yield models derived from stellar evolution theories. Recent developments in star formation models come up with ISM models that better resolve the multi-phase gas structure and even model the formation of individual stars.

1.2 Modeling the Evolution of Massive Black Holes

One main topics covered by this thesis are specifically related to the theoretical modeling of massive black holes. Therefore we spend a subsection to describe aspects of MBH modeling in cosmological simulations in more detail.

1.2.1 Numerical Modeling

Despite their small physical sizes relative to cosmological scales, MBHs play a large role in shaping the evolution of galaxies. This motivates modern hydrodynamic simulations to incorporate subgrid models for MBH-related physics. Examples of large volume simulations with black hole physics include Magneticum [Hirschmann et al., 2014, Steinborn et al., 2015] Horizon-AGN [Dubois et al., 2014, Volonteri et al., 2015], Eagle [Rosas-Guevara et al., 2015, Schaye et al., 2015] Illustris Genel et al. [2014], Sijacki et al. [2015], Vogelsberger et al. [2014], MassiveBlack-II [Khandai et al., 2015], BlueTides [Di Matteo et al., 2017, Feng et al., 2016], Romulus [Sharma et al., 2020, Tremmel et al., 2017], IllustrisTNG [Habouzit et al., 2021, Pillepich et al., 2018, Weinberger et al., 2017], SIMBA [Davé et al., 2019, Thomas et al.,

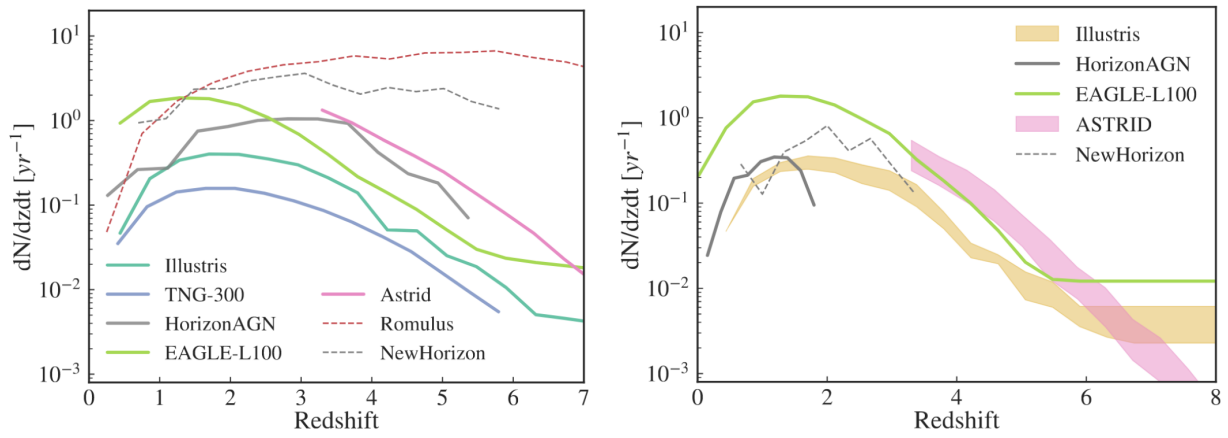

Figure 1.2: MBH merger rates across cosmic time predicted from various cosmological simulations. The modeling of accretion, seeding, and dynamics can affect the merger distribution and event count prediction.

2019], Astrid [Bird et al., 2022, Ni et al., 2022] (list of references follows from Di Matteo et al. [2023]).

Massive black holes in cosmological simulations are usually modeled as individual particle species, with their own set of properties. The physics related to MBHs can be roughly categorized into accretion, feedback, seeding, and dynamics. Here we briefly review the modeling of each, focusing on the dynamics that directly link to the next subsection on massive black hole binaries.

Accretion Massive black holes grow by swallowing the gas accumulated into the surrounding accretion disk. These disks are made of gas falling in from galaxy scales and typically have sizes smaller than a parsec. The detailed modeling of the MBH accretion mechanism and the dynamics in the accretion disk requires spatial and time resolutions beyond the reach of cosmological simulations and is typically done through GRMHD simulations [e.g. Guo et al., 2023]. Thus simplified effective models are adopted in cosmological simulations. The Bondi accretion model is the most widely used prescription for black hole growth in galaxy formation simulations since its first implementation in idealized galaxy merger simulations, which is calculated as

$$\dot{M}_{\rm Bondi} = \alpha \frac{4\pi G^2 M_{\rm BH}^2 \rho}{(c_{\rm s}^2 + v^2)^{3/2}}, \tag{1.8}$$

where c_s is the local gas sound speed, v is the velocity of the MBH, ρ is the local gas density, $M_{\rm BH}$ is the black holes mass, and G is the gravitational constant. We note the constant boost factor α in this formulation, which is added to compensate for the underestimation of the accretion rate due to the unresolved cold and hot phase of the subgrid interstellar medium nearby.

The Bondi accretion is limited by the Eddington rate, which is the maximum growth rate achieved through spherically symmetric accretion in the presence of radiation pressure:

$$\dot{M}_{\rm Edd} = \frac{4\pi G m_{\rm p} M_{\rm BH}}{\eta \sigma_{\rm T} c}, \tag{1.9}$$

where m_p is the proton mass, σ_T is the Thomson cross-section, c is the speed of light, and η is the radiation efficiency of the accretion flow.

The Bondi-Hoyle accretion model above can be oversimplified, and recent simulations showed that in gas-rich galaxies the gravitational torque of the stellar component plays a major role in transporting gas to the vicinity of the MBH [Anglés-Alcázar et al., 2017, 2021]. Simulations with torque-driven accretion models usually lead to more efficient growth of under-massive black holes, because the accretion rate is less sensitive to the black hole mass. However, this scenario may not be realized in early gas-rich galaxies or late-time elliptical galaxies, and a hybrid accretion model has also been developed to model the hot gas with Bondi accretion and cold, rotationally supported gas with the torque-driven model [e.g. Davé et al., 2019].

Feedback The rest-mass energy of the accreted material can be transformed into radiation through AGN accretion disks. Observations of AGN feedback in action include fast nuclear outflows, galaxy-scale winds, radio-emitting jets, and ionized QSO proximity zones. The bolometric luminosity is related to the accretion rate by:

$$L_{\rm bol} = \eta \dot{M}_{\rm BH} c^2, \tag{1.10}$$

where $\dot{M}_{\rm BH}$ is the black hole accretion rate as in Equation 1.9 and η is the radiating efficiency. The resulting radiation energy is deposited into the surrounding medium and can have a significant and long-term impact on the evolution of the AGN host galaxies, which we refer to as the "AGN feedback". The feedback mechanism is believed to play a major role in the self-regulation of MBH growth and the regulation of star-formation in galaxies [e.g. Di Matteo et al., 2005b].

In cosmological simulations, the feedback energy from MBHs can be coupled to the surrounding medium in multiple ways, depending on the accretion state of the MBH and the properties of the environments. One widely adopted model injects a fraction of the bolometric luminosity as thermal energy into the surrounding gas, increasing the gas temperature. To prevent the effective cooling which counteracts the heating effect of AGN, alternatives to this method have been applied. These include the temporary suspension of gas cooling of gas coupled to the AGN, depositing feedback energy in bulks, and injecting momentum instead of thermal energy into gas. Simulations also adopt a two-mode feedback model to model the high-accretion state ("quasar mode") and low-accretion state ("radio mode") separately. This allows for refined control of the MBH and galaxy evolution at different stages and reproduces the observed population of quenched galaxies and the color bi-modality [Weinberger et al., 2017].

Seeding The exact mechanism that seeded the MBHs in the early Universe at $z > 15$ remains to be revealed by ongoing and future observations. Several theoretical models have been proposed for the formation of the MBH "seeds" at high redshifts that can potentially lead to the SMBHs with masses already exceeding $\sim 10^9\,M_\odot$ at $z \sim 6$ and larger than $> 10^{10}\,M_\odot$ today. One plausible scenario is that the first black holes formed from the first massive stars (Population-III stars). These stars are quite massive due to the inability of molecular hydrogen gas to cool and can collapse into MBH seeds with $M_{\rm BH} \sim 100\,M_\odot$. A second channel of seed formation is through the direct collapse of gas clouds into a massive seed black hole without passing through all the phases of stellar evolution. These "direct collapse" models form seed black holes with $M_{\rm BH}$ between 10^4 and $10^6\,M_\odot$. A third channel involves a gravitational runaway event within a dense stellar cluster, where either massive stars or stellar-mass BHs go through runaway collision and mergers, which leads to MBH seeds with $M_{\rm BH} \sim 10^3\,M_\odot$.

The modeling of seed formation in cosmological simulations is usually much coarser than the proposed physical mechanisms, as the proposed seed masses are usually below the mass resolution of cosmological simulations. The simplest model of seeding MBHs puts an MBH seed at a fixed initial mass (usually ranging between $10^5 - 10^6\,M_\odot$) at the halo center when the halo first gets above a certain mass threshold (e.g. $\sim 10^{10}\,M_\odot$ in simulations such as Illustris, TNG, and EAGLE). The underlying assumption is that massive seeds through direct gas collapse form in abundance, or that the lighter seeds formed through other channels can grow efficiently. To probe the evolution of MBH seeds across a wider mass range, in ASTRID simulation the seed mass is stochastically drawn from a power-law distribution, in halos with $M_{\rm halo} = 10^{9.5} \sim 10^{10.5}\,M_\odot$. Some simulations such as Romulus and Horizon-AGN also consider the local gas environments in addition to the halo mass and only form MBH seeds in dense and pristine gas. Higher-resolution simulations with more detailed modeling of the gas and stellar population at high redshifts are used to explore the physical condition of MBH seed formation (e.g. the Renaissance and BRAHMA simulation suites), and derive refined seeding mechanisms for future large cosmological volumes. Finally, it is worth noting that the challenges of seeding smaller MBHs in cosmological simulations lie not only in the inability to resolve their forming environments, but also in the difficulty in modeling their subsequent evolution in dynamics and gas accretion when all other particle species are significantly heavier than the MBH particles.

Dynamics MBHs are subjected to gravitational interaction with all matter components and a drag force from the surrounding gas medium. In Section 1.1.2, we already introduced gravity modeling in cosmological simulations, but these methods are essentially a Monte Carlo sampling of the underlying gravitational field and are not accurate at the single-particle level. Thus the dynamics of black hole particles require additional treatment. Like the obstacles in the modeling of other aspects of MBHs, dynamics modeling is limited by the resolution in mass, space, and time. Observations found most SMBHs to sit at or close to the galactic center, while some smaller MBHs have been discovered away from the galaxy center ("wandering MBHs"). The main mechanism that keeps MBHs close to galaxy centers,

even after the dynamical disruption following galaxy mergers is the dynamical friction from dark matter, gas, and stars. When the black hole travels through a continuous medium or a medium consisting of particles with smaller masses than the black hole, it attracts the surrounding mass towards itself, leaving a tail of overdensity behind. Dynamical friction is the resulting gravitational force exerted onto the black hole by this tail of overdensity [e.g. Binney and Tremaine, 2008, Chandrasekhar, 1943]. Dynamical friction causes the orbits of SMBHs to decay towards the center of massive galaxies [e.g. Governato et al., 1994, Kazantzidis et al., 2005], and enables the black holes to stay at the high-density regions where they could go through efficient accretion and mergers.

In principle, dynamical friction is just a gravitational effect and should be already accounted for in N-body simulations assuming infinite spatial and time resolution. However, due to the gravitational softening term ϵ in Equation 1.2 (usually set to kpc scales in cosmological simulations for computational feasibility), gravity can not be well resolved in the vicinity of the MBHs, and thus the wake-induced-friction is not captured. As a result, MBHs have a hard time sinking to galaxy centers after dynamical disruptions (e.g. a galaxy merger). Another numerical difficulty lies in the mass contrast between other particle species and the black hole particles. If the MBHs are of comparable mass to the most massive particle species, the two-body scattering process can artificially inject energy into the MBHs and displace them from the potential minimum.

A simple fix to the spurious drift of MBHs from galaxy centers is to reposition them to the galaxy center at each timestep of the MBH evolution. This fix stops the gravitational interaction of the MBHs with other particles and simply assumes that they will always reside in the central region. Simulations with this model produce a reasonable central MBH population when calibrated on observations, but can become problematic when modeling MBH merger events or wandering MBHs.

Alternatively, we can add a sub-grid force onto the MBHs to account for the insufficient DF force. The derivation of the added force is motivated by the Chandrasekhar prescription of dynamical friction:

$$\mathbf{F}_{\rm DF} = -16\pi^2 G^2 M_{\rm BH}^2 m_a \log(\Lambda) \frac{\mathbf{v}_{\rm BH}}{v_{\rm BH}^3} \int_0^{v_{\rm BH}} dv_a v_a^2 f(v_a), \tag{1.11}$$

where $M_{\rm BH}$ is the black hole mass, $\mathbf{v}_{\rm BH}$ is the velocity of the black hole relative to its surrounding medium, m_a and v_a are the masses and velocities of the particles surrounding the black hole, and $\log(\Lambda) = \log(b_{\rm max}/b_{\rm min})$ is the Coulomb logarithm that accounts for the effective range of the friction between $b_{\rm min}$ and $b_{\rm max}$. $f(v_a)$ is the velocity distribution of the surrounding particles. This integral can be done analytically assuming that $f(v_a)$ follows a Maxwellian distribution. In Chapter 3 we will dive into the details of this model and its application in cosmological simulations. Variants of the Chandrasekhar-like models have also been derived and tested in simulations of MBH orbital decay. For example, Ma et al. [2021] derived a discrete formulation of the dynamical friction by taking into effect both the local and global interactions of MBHs. This method has the advantage of efficient implementation in particle-based simulations and explicit momentum conservation.

1.2.2 Massive Black Hole Binaries

Massive black holes not only grow in isolation via accretion but are subject to pairing with other MBHs following galaxy mergers, resulting in massive black hole binaries (MBHBs). MBHBs are unique multi-messenger sources where the host galaxies, binary AGN and the gravitational wave emission can potentially be observed simultaneously. Thus they can be used to constrain cosmology, black hole accretion as well as the MBH-galaxy relation. In this subsection, we introduce the evolution stages of MBHBs and their signatures in electromagnetic and gravitational wave observations.

Formation and Evolution of MBHBs MBH pairs' evolution towards coalescence is first summarized in Begelman et al. [1980], and the main picture is still adopted in the modeling of MBHBs today. During galaxy mergers, the central MBHs start at a large separation in the remnant galaxy (a few tens of kpc). These SMBH pairs slowly spiral toward the center of mass of the newly merged system and remain at a separation of $0.1 \sim 100\,\mathrm{kpc}$ for a few hundred Myrs [e.g. Begelman et al., 1980, Milosavljević and Merritt, 2001], during which dynamical friction is the major mechanism for driving the orbital decay, and enables the formation of a bound binary. When their separation is within the influence radius (the radius at which the enclosed stellar mass is equal to the sum of the MBH masses) an MBH binary begin to form, and other energy-loss channels begin to dominate, such as scattering with stars [e.g. Vasiliev et al., 2015], gas drag from the circumbinary disk [e.g. Haiman et al., 2009], and three-body scattering with a third black hole [e.g. Bonetti et al., 2018]. At even closer separation, GW emission becomes the dominant channel for binary energy loss. We usually use MBH binaries to refer to two MBHs gravitationally bound to each other, and use MBH pairs to refer to two MBHs at any evolution stage before the bound binary formation.

Not all MBH pairs can evolve to the stage of a bound binary, and could stall at various stages. At kpc separations, dynamical friction may not act efficiently, especially on small and naked MBHs. Thus wandering MBHs are theoretically predicted to reside in moderately-sized galaxies and also observational found. Even when the MBH pairs made it to the central $\sim$ pc region of the remnant galaxy center, the inefficient refilling of the loss cone can lead to binary stalling on PC scales (known as the "final parsec problem"). This is most relevant in "dry mergers" between late-time elliptical galaxies where the central region is gas-poor. Some binary MBH accretion disk simulations also found that in certain configurations the binary can widen instead of decay due to the interaction with surrounding gas. Several mechanisms have been proposed to alleviate the final-parsec stalling, such as the triaxial geometry of the remnant galaxy and interactions between more than two MBHs.

Modeling the full range of evolution from galaxy mergers to binary formation and gravitational wave emission involves a dynamical range over ~ 10 orders of magnitude and is almost impossible (in Chapter 6 we will focus on this problem). Therefore, people usually use analytical derivation or simulations to model the orbital decay rate at various stages and add them to estimate the timescale of the full evolution. An example of the evolution time through different stages and the dominating mechanism at different separations is shown in

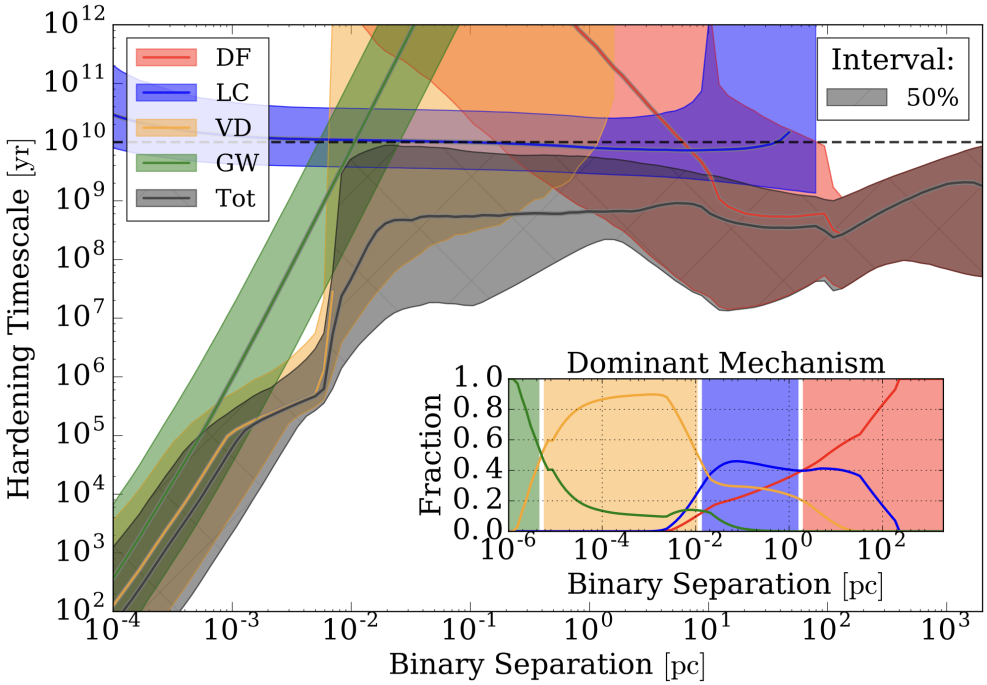

Figure 1.3: The timescale of MBH orbital decay through different mechanisms (dynamical friction (DF), loss-cone scattering (LC), viscous gas disk (VD) and gravitational wave emission (GW) at different binary separation for the binary population form the Illustris simulation. The inset panel shows the mechanism dominating the orbital decay at different scales. The Figure is adopted from Kelley et al. [2017b].

Figure 1.3.

Dual AGN MBHBs or their progenitors (MBH pairs before forming a bound binary) can be observed electromagnetically as dual AGN when both MBHs are actively accreting. Based on the binary evolution model in the previous paragraph, dual AGN should exist across a wide range of separations from before galaxy mergers to the bound binary stage. The number density across various phases can potentially inform us of the binary evolution models in each stage. It is also theoretically predicted that galaxy merger induces gas shocks and inflow which can boost AGN activity. This can also be tested with a detailed comparison between the single AGN population with dual AGN, and between the observed and simulated samples.

It is nonetheless difficult to collect a statistical sample of confirmed dual AGN in observations, especially toward small (sub-kpc scale) separation due to limitations in instrumentation, obscuration by AGN hosts, or confusion with other objects (e.g. lensed quasars). One method to find dual AGN uses spatial offset detection, which relies on having the angular resolution to discern a pair of AGN or an AGN displaced from the host galaxy center. Large

enough samples are beginning to be discovered to begin placing constraints on population statistics, for example, showing that dual-AGN occurrence rates are higher in more-major mergers and luminosities tend to increase at smaller separations Koss et al. [2012]—both consistent with predictions for merger-driven fueling of AGN. Radio observations are most promising in discovering bound dual AGN due to their superior spatial resolution. Currently, the closest-separation system is found at $\sim 7\,\mathrm{pc}$ projected separation by Rodriguez et al. (2006) in the radio galaxy 0402+379.

Another method uses the kinematic offsets in spectroscopy, identified either through two distinct lines components, or a redshifted line (velocity offset) relative to the host galaxy. Candidates identified through kinematic offsets are subjected to misclassification since double lines can also be produced by bipolar outflows or jets and even the two sides of an accretion disk. Therefore follow-up observations of the host galaxies or AGN are used to confirm the dual AGN nature. Other signatures of dual AGN include the periodic variability in the AGN brightness and features in the galaxy morphology or kinematics.

Current predictions on the dual AGN population in cosmological simulations are limited to duals at $>$ kpc scales, as this is the spatial resolution limit for the state-of-the-art large cosmological boxes ($> 100\,\mathrm{Mpc}$ boxes are needed to build a statistical sample of bright dual AGN sources). These simulations are useful in constructing a statistical sample of dual AGN from the underlying single AGN population, identifying distinctive signatures of the AGN in pairs, and building mock samples of dual AGN observations for the spatial offset methods. Idealized galaxy merger simulations and binary accretion disk simulations are useful in modeling the smaller-separation dual AGN and their accretion states. In Chapter 5, I will focus on the properties of the dual AGN sample and their host galaxies extracted from the ASTRID simulation.

Gravitational Waves from MBHBs Gravitational waves (GWs) from MBH mergers offer a promising way to observe the first MBH seeds and SMBH binaries [e.g. Barausse, 2012, Klein et al., 2016, Ricarte and Natarajan, 2018, Sesana et al., 2005], especially when combined with observations of the electromagnetic (EM) counterparts [DeGraf and Sijacki, 2020, Natarajan et al., 2017]. Compared to electromagnetic observations, GWs not only allow us to probe MBH seeds at higher redshift, but also provide MBH mass estimations independent of their instantaneous accretion state. GWs of MBH mergers with masses in the range $10^4 - 10^7\,M_\odot$ have a frequency around mHz, and they are primary targets for the Laser Interferometer Space Antenna (LISA), which can detect MBHs with such masses out to $z > 20$ [Amaro-Seoane et al., 2017]. At lower frequencies Pulsar Timing Arrays (PTAs) already detected GW background from MBHBs and the Square Kilometer Array (SKA) in the next decade will be a major leap forward in sensitivity. PTA observations are also likely to identify a number of continuous-wave sources representing the early inspiral phase of MBH binaries.

MBH binaries provide a variety of signals measurable by LISA since their chirp evolution in the frequency domain occurs near the low-frequency band edge of the LISA sensitivity curve. Binaries with $10^5 - 10^7 M_\odot$ total mass will provide a measurable inspiral, merger,

and ringdown leading to signals out to the cosmic horizon [Amaro-Seoane et al., 2017]. The binary inspiral is the initial stage of binary black hole coalescence when the two MBHs orbit one another at separations greater than the innermost stable circular orbit (ISCO; $R = 6GM_{\rm BH}/c^2$). At these separations, the orbit is usually treated with a post-Newtonian formalism. The merger stage follows the binary inspiral with a highly non-linear relativistic process. This process continues until the binary components form a single event horizon, leading to ringdown.

We use the characteristic strain, h_s, to model the binary signal which accounts for the time the binary spends in each frequency bin [Finn and Thorne, 2000]. The characteristic strain is given by [e.g. Moore et al., 2015]:

$$h_s(f) = 4f^2|\tilde{h}(f)|^2 \tag{1.12}$$

where $\tilde{h}(f)$ represents the Fourier transform of a time domain signal and can be computed through phenomenological models such as PhenomD. This $h_s - f$ relation assumes circular orbits for the binaries. The GW strain from an individual, eccentric source can be related to that of a circular source as [e.g. Amaro-Seoane et al., 2010, Kelley et al., 2017c]:

$$h_s^2(f_{\rm r}) = \left(\frac{2}{n}\right)^2 \sum_{n=1}^{\infty} h_{\rm r,circ}^2(f_{\rm h}) g(n,\epsilon)|_{f_{\rm h}=f_{\rm r}/n}, \tag{1.13}$$

where $h_{\rm r,circ}$ is the characteristic strain of a circular source given by Equation 1.12, $g(n,\epsilon)$ is the GW frequency distribution function given by Equation 20 in Peters and Mathews [1963] with $\sum_{n=1}^{\infty} g(n,\epsilon) = F(\epsilon)$, where $F(\epsilon)$ is defined by $F(\epsilon) = (1-\epsilon^2)^{-7/2}[1 + (73/24)\epsilon^2 + (37/96)\epsilon^4]$. During the GW-driven inspiral, the orbital eccentricity also evolves according to Peters [1964] Equation (5.7), such that it decays towards zero as the binary inspirals toward merger.

1.3 Modeling and Constraints of Cosmic Reionization

1.3.1 Theoretical Modeling

The Epoch of Reionization (EoR) is a period when the first stars, galaxies, and quasars emit UV photons and ionize the neutral hydrogen in the universe. These photons have a large impact on the state and temperature of the baryonic gas through photoionization and photoheating and hence also affect the structure formation in the late universe. This process is spatially inhomogeneous, as photons from galaxies penetrate through the sources and propagate into the more distant space, ionizing the neutral gas along the way. An accurate simulation of this process requires radiative transfer modeling on top of hydrodynamical simulations. These simulations directly trace the propagation of photons across different frequency bands and their interaction with the gas medium along multiple directions from the sources. As a result, they are much more costly than typical hydrodynamical simulations

described in Chapter 1.1, which means they can only be carried out in small boxes (usually $L < 100\,\mathrm{Mpc}$).

Here I will focus on introducing analytical and semi-numerical methods of cosmic reionization, which is most relevant for constraining the large-scale or global properties of the cosmic reionization when combined with CMB observations.

Analytical Models Analytical models are useful in modeling the global properties of reionization, and in constraining the key parameters such as the ionizing photon budget and gas clumpiness when combined with observations. We start with the local ionization balance equation of hydrogen:

$$\frac{dn_{\rm HII}}{dt} = \Gamma n_{\rm HI} + \gamma_{\rm coll} n_{\rm e} n_{\rm HI} - \alpha(T) n_{\rm e} n_{\rm HII} - 3H n_{\rm HII}, \tag{1.14}$$

where $n_{\rm HII}$ is the physical number density of ionized hydrogen, $n_{\rm e}$ is the physical number density of free electrons, $\gamma_{\rm coll}$ is the collisional ionization rate, Γ is the photoionization rate, α is the recombination coefficient and H is the Hubble parameter. The right-hand side contains four effects that govern the local ionization of hydrogen: the first two terms are photoionization and collisional ionization respectively, which increase ionized hydrogen number density, the third term is recombination which decreases the ionized hydrogen number density, while the last term accounts for the decrease in physical number density due to the universal expansion.

Taking volume-weighted average and dividing both sides by $\langle n_{\rm H}\rangle_{\rm V}$, we obtain the global equation for the mass-weighted ionization fraction:

$$\frac{d\langle x_{\rm HII}\rangle_{\rm M}}{dt} = \frac{\langle \Gamma n_{\rm HI}\rangle_{\rm V}}{\langle n_{\rm H}\rangle_{\rm V}} - \frac{\langle \alpha(T) n_{\rm e} n_{\rm HII}\rangle}{\langle n_{\rm H}\rangle_{\rm V}}. \tag{1.15}$$

$\langle \Gamma n_{\rm HI}\rangle_{\rm V}$ is effectively the global photon production rate and we can refactor the last term to express it in terms of the clumping factor C_R:

$$\frac{d\langle x_{\rm HII}\rangle_{\rm M}}{dt} = \frac{\langle \dot{n}_\gamma\rangle_{\rm V}}{\langle n_{\rm H}\rangle_{\rm V}} - C_{\rm R}\langle \alpha(T)\rangle_{\rm V}\langle n_{\rm H}\rangle_{\rm V}\left(1 + \frac{Y}{4X}\right)\langle x_{\rm HII}\rangle_{\rm M}^2, \tag{1.16}$$

Here $C_{\rm R}$ is the recombination clumping factor:

$$C_{\rm R} = \frac{\langle \alpha(T) n_{\rm HII} n_e\rangle_{\rm V}}{\langle \alpha(T)\rangle_{\rm V}\langle n_{\rm HII}\rangle_{\rm V}\langle n_e\rangle_{\rm V}}. \tag{1.17}$$

and is usually estimated through radiative transfer simulations. The differential equation in 1.16 summarizes the key components in the global evolution of reionization and will give a global reionization history with assumptions on $\dot{n}$ and C_R. This formalism can be applied, for example, to estimate the integrated Thomson depth τ_e

Semi-Numerical Models Semi-numerical simulation of reionization uses approximation methods for simulating the ionization state of the IGM. These simulations do not trace or resolve the detailed photon interaction with the gas, but approximate the structure of the IGM ionizing state, with much lower computation complexity compared to the radiative transfer simulations. Hence, these methods are widely used in modeling reionization in the cosmological context and in carrying out parameter space studies. The applications include 21cm cosmology and the fluctuations in the cosmic wave background (CMB).

One of the earliest and most popular semi-numerical codes for reionization is 21cmFast. It represents a class of semi-numerical methods using excursion-set formalism to track the ionization front through time. The key assumption is that the ionizing fronts propagate in an "inside-out" fashion from collapsed halos. More specifically, the size R of a spherically ionized region around the source halo is calculated by equating the total ionizing photon number produced within this region with the number of neutral hydrogen atoms. The ionizing photon number is assumed to be proportional to the fraction of matter collapsed into halos (related by parameters such as the star-formation efficiency f_* and the ionizing photons produced per baryon in stars) and $f_{\rm esc}$ of these photons can penetrate into the IGM. The baryon distribution is assumed to trace the underlying dark matter distribution, which is evolved through Lagrangian perturbation theory.

Another semi-numerical model class directly models the reionization redshift field, assuming that it is correlated with the underlying matter distribution or the radiation intensity field. AMBER, the model we use in Chapter 2 to study the patchy kSZ effect, is a recent development in this category. AMBER is motivated by the solution to the radiative transfer equation for the radiation angle-averaged intensity:

$$J_v(\mathbf{x}) = \frac{a}{4\pi}\int d^3x_1 \frac{S_v\left(\mathbf{x}_1\right)}{\left(\mathbf{x}-\mathbf{x}_1\right)^2} e^{-\tau_v(\mathbf{x},\mathbf{x}_1)}, \tag{1.18}$$

where $S_v\left(\mathbf{x}_1\right)$ is the source function. Under the assumption that $\tau_v\left(\mathbf{x},\mathbf{x}_1\right) \propto \frac{1}{\lambda_{\rm mfp}(v)}\left\|\mathbf{x}-\mathbf{x}_1\right\|$, the radiation intensity at $\mathbf{x}$ can be easily calculated as a radial convolution of the source field, significantly reducing the computation cost. The relative radiation intensity between cells then determines the order in which the cell gets ionized. This assumption is validated against radiative transfer simulations such as the SCORCH simulation suite [Trac, 2018].

1.3.2 Constrain Reionization with CMB Observations

In the ongoing CMB experiment, the most well-constrained EoR observable has been the Thomson-scattering optical depth τ_e. Constraints on τ_e informs us about the integrated electron number density n_e along the light-of-sight, as τ_e is related to n_e by:

$$\tau_{\rm e}(z) = \sigma_T \int_0^z dz' \frac{cdt}{dz'} \langle n_{\rm e}(z')\rangle_{\rm V}, \tag{1.19}$$

where σ_T is the Thomson cross section and $\langle n_{\rm e}(z')\rangle_{\rm V}$ is the volume-averaged free electron number density. Both the amplitude and shape of the CMB EE and TE power spectra on

large scales (low l) are very sensitive to the Thomson optical depth. In practice, the EE power spectrum alone is sufficient to discriminate different values of the optical depth from CMB polarisation measurements: its excess power around $l = 4 - 5$ is referred to as the reionization bump. This bump occurs on large scales because CMB photons stream freely after decoupling on the LSS until they are scattered off newly formed free electrons.

Because the mean baryon number density increases with redshift, an earlier reionization leads to higher values of τ_e, thus the EE spectrum could put constraints on the reionization redshift. However, it cannot discriminate between different reionization scenarios yielding the same value of τ_e, and it has been shown that τ_e is not sensitive to the detailed reionization histories beyond the redshift [e.g. Battaglia et al., 2013a].

The detailed reionization histories can be constrained by the patchy kinetic Sunyaev-Zel'dovich (kSZ) effect, which is the temperature fluctuation in the CMB due to the scattering of CMB photons off of free electrons in bulk motion during cosmic reionization. Small-scale temperature anisotropies are then generated by the coupling of large-scale velocity perturbations and the patchiness of the ionized field on small scales. The fractional temperature fluctuation induced by the patchy kSZ effect is calculated by integrating the electron momentum along the line of sight:

$$\frac{\Delta T_{ksz}}{T} = \sigma_T \int dz \frac{cdt}{dz} e^{-\tau_e(z,\hat{\mathbf{n}})} n_e(z, \hat{\mathbf{n}}) \hat{\mathbf{n}} \cdot \mathbf{v} \tag{1.20}$$

where $\mathbf{v}$ is the peculiar velocity of free electrons, τ_e is the Thomson optical depth calculated in Eq.1.19, and the integration limits are the beginning and end of reionization. Currently, most constraints on reionization from patchy kSZ come from the angular power spectrum [but see e.g. Smith and Ferraro, 2017, for the use of high-order statistics]. This is also the quantity of interest in the next chapter, and we will go into more detail about the calculation of the power spectrum and modeling of the patchy kSZ signal using simulations.

1.4 Thesis Outline

This thesis will focus on the modeling of and constraints on galaxy formation and massive black hole evolution since cosmic dawn using the numerical techniques and observation probes laid out in this Chapter. In Chapter 2, I use semi-numerical simulation AMBER to characterize the impact of reionization history and the morphology of the ionization field on the patchy kinetic Sunyaev-Zel'dovich signal, and evaluate the constraints on these parameters with current and future CMB observations. Chapter 3-6 focus on the dynamical modeling of massive black holes in cosmological simulations and the massive black hole binary population. In Chapter 3 I introduce the dynamical friction subgrid modeling of massive black holes accounting for surrounding dark matter, gas, and stars, and validate the model in the cosmological context. I also evaluate the impact of this more realistic modeling of MBH dynamics on the MBH merger rates compared with previous simulations. Chapter 4 uses the ASTRID cosmological simulation with the new dynamical friction model developed in Chapter 3 to study the MBH merger population and their host galaxy properties, with

a full binary evolution modeling as was described in Section 1.2.2. I also make predictions for the future LISA gravitational wave detector of high-redshift MBH mergers. In Chapter 5, I study the electromagnetic signatures of massive black hole pairs also using the ASTRID simulation by looking at the statistical properties such as separation distribution, and luminosity distribution. I also trace the gas environments and host galaxy properties of the dual AGN. In Chapter 6, I go beyond the current merger modeling in cosmological simulations and study the timescale of seed MBH mergers using high-resolution galaxy simulations, with initial conditions directly extracted from cosmological galaxy mergers.

The work in Chapters 2, 3, 4, 5, and 6 have been published in peer-reviewed journals Chen et al. [2023c], Chen et al. [2022c], Chen et al. [2022b], Chen et al. [2023a] and Chen et al. [2023b].

Chapter 2

Patchy Kinetic Sunyaev-Zel'dovich Effect with Controlled Reionization History and Morphology

Nianyi Chen[1], Hy Trac[12], Suvodip Mukherjee[3], Renyue Cen[4]

[1]McWilliams Center for Cosmology, Department of Physics, Carnegie Mellon University, 5000 Forbes Ave, Pittsburgh, PA 15213
[2] NSF AI Planning Institute for Physics of the Future, Carnegie Mellon University, Pittsburgh, PA 15213, USA
[3]Perimeter Institute for Theoretical Physics, 31 Caroline Street N., Waterloo, Ontario, N2L 2Y5, Canada
[4]Department of Astrophysical Sciences, Princeton University, Princeton, NJ 08544, USA

Abstract

Using the novel semi-numerical code for reionization AMBER, we model the patchy kinetic Sunyaev-Zel'dovich (kSZ) effect by directly specifying the reionization history with the redshift midpoint $z_{\rm mid}$, duration $\Delta_{\rm z}$, and asymmetry $A_{\rm z}$. We further control the ionizing sources and radiation through the minimum halo mass $M_{\rm h}$ and the radiation mean free path $\lambda_{\rm mfp}$. AMBER reproduces the free electron number density and the patchy kSZ power spectrum of radiation-hydrodynamic simulations at the target resolution ($1\,{\rm Mpc}/h$) with matched reionization parameters. With a suite of $(2\,{\rm Gpc}/h)^3$ simulations using AMBER, we first constrain the redshift midpoint $6.0 < z_{\rm mid} < 8.9$ using the Planck2018 Thomson optical depth result (95% CL). Then, assuming $z_{\rm mid} = 8$, we find that the amplitude of $D^{\rm pkSZ}_{\ell=3000}$ scales linearly with the duration of reionization Δ_z, and is consistent with the 1σ upper limit from the South Pole Telescope (SPT) results up to $\Delta_z < 5.1$ (Δ_z encloses 5% to 95% ionization). Moreover, a shorter $\lambda_{\rm mfp}$ can lead to a $\sim 10\%$ lower $D^{\rm pkSZ}_{\ell=3000}$ and a flatter slope in the $D^{\rm pkSZ}_{\ell=3000} - \Delta_z$ scaling relation, thereby affecting the constraints on Δ_z at $\ell = 3000$. Allowing $z_{\rm mid}$ and $\lambda_{\rm mfp}$ to vary simultaneously, we get spectra consistent with the

SPT result (95% CL) up to $\Delta_z = 12.8$ (but $A_z > 8$ is needed to ensure an end of reionization before $z = 5.5$). We show that constraints on the asymmetry require $\sim 0.1\,\mu k^2$ measurement accuracy at multipoles other than $\ell = 3000$. Finally, we find that the amplitude and shape of the kSZ spectrum are only weakly sensitive to M_h under a fixed reionization history and radiation mean-free path.

2.1 Introduction

The epoch of reionization (EoR) is the period in cosmic history when ionizing radiation emitted by the first galaxies and quasars ionized the baryons in the Universe, leading to a transition of the gas content from a neutral state to an ionized state. Because EoR happens at a relatively high redshift ($z = 5 \sim 15$), the limited observational evidence has hindered our full understanding of the whole physical process involved. Nevertheless, recent and future experiments using various probes are making the picture of the EoR more and more complete. For example, Planck Collaboration et al. [2018] recently inferred $\tau = 0.054 \pm 0.007$ from measurements of the Cosmic Wave Background (CMB) temperature and polarization angular power spectra, implying a late reionization midpoint at redshift $z \approx 7.7 \pm 0.6$ [e.g. Glazer et al., 2018]. Becker et al. [2015] find evidence of a dark Lyα trough extending down to $z \approx 5.5$ in the spectrum of a high-redshift quasar, suggesting that reionization could have ended at $z < 6$ [e.g. Keating et al., 2019], later than previously assumed. In addition, we also expect to gain tomographical information of the EoR through the 21cm observations such as Hydrogen Epoch of Reionization Array [DeBoer et al., 2017] and Square Kilometer Array [Koopmans et al., 2015], and a better understanding of the first ionizing sources through the space-based telescopes such as the James Webb Space Telescope [Windhorst et al., 2006] and Roman Space Telescope [Spergel et al., 2015].

Of particular interest to this paper is the use of CMB secondary at high multipoles to constrain the EoR. With the improvements in recent ground-based CMB experiments such as Atacama Cosmology Telescope (ACT[1]) and the South Pole Telescope (SPT[2]), we are already able to use anisotropies in the CMB temperature map to constrain reionization through Sunyaev-Zel'dovich (SZ) effect [Sunyaev and Zeldovich, 1980, Zeldovich and Sunyaev, 1969]. The SZ effect results from inverse-Compton scattering of CMB photons off high-energy electrons in the IGM, and it has the largest contribution among CMB secondary anisotropies on arc-minute scales. There are two types of SZ effect: thermal SZ effect (tSZ) comes from the electron pressure within the intra-cluster medium (ICM) and has a spectrum shifted from the CMB black body spectrum, while kinetic SZ (kSZ) effect is due to the bulk motion of electrons in the IGM with respect to the CMB rest frame and has the same spectrum as the CMB [e.g. Carlstrom et al., 2002]. kSZ signal can be further divided into two components and they have comparable amplitude [e.g. Shaw et al., 2012, Trac et al., 2011]: patchy kSZ originates from the inhomogeneous free-electron fraction in the universe during cosmic

[1] `https://act.princeton.edu`
[2] `http://pole.uchicago.edu`

reionization, and homogeneous kSZ results from the peculiar velocities of the galaxies after the universe is fully ionized [e.g. Ostriker and Vishniac, 1986].

Because patchy kSZ originates from inhomogeneous reionization, its amplitude and power spectrum are sensitive to the timing, duration, and detailed history of reionization. Thus, by probing patchy kSZ fluctuation we can put constraints on reionization history provided that we have a thorough understanding of their relation. In recent years, developments in numerical simulations enables us to understand connection between the patchy kSZ angular power spectrum and reionization [e.g. Alvarez, 2016, Battaglia et al., 2013a, Choudhury et al., 2021, Gorce et al., 2020, Iliev et al., 2007, McQuinn et al., 2005, Mesinger et al., 2011, Park et al., 2013, Paul et al., 2021, Tashiro et al., 2011, Zhang et al., 2004]. In particular, multiple works have demonstrated that semi-numerical simulations are powerful tools to study kSZ with various reionization scenarios in a relatively quick fashion. For example, Mesinger et al. [2012] and Choudhury et al. [2021] have used the semi-numerical simulations to study the dependence of reionization history and patchy kSZ power spectrum on the ionizing efficiency of high-redshift galaxies, the minimum virial temperature of haloes, and the ionizing photon mean free path. Battaglia et al. [2013a] combined N-body simulations with post-processed reionization-redshift field to study the effect of reionization history on the patchy kSZ power spectrum. Alvarez [2016] uses very large-scale simulations to study the different components to the kSZ signal, as well as the four-point statistics of patchy kSZ.

However, the majority of semi-numerical codes of reionization are based on the excursion set formalism method for reionization [e.g. Bond et al., 1991, Furlanetto et al., 2004], and it has been shown that [Zahn et al., 2011] these semi-numerical methods are in good agreement with radiative transfer simulations when compared at the same ionization fraction, but not at the same redshift without renormalization. Moreover, most of the semi-analytical models parametrize reionization on the power-spectrum level [e.g. Battaglia et al., 2013a, Gorce et al., 2020, Shaw et al., 2012], without directly controlling the reionization history [but see Paul et al., 2021, who controls the duration of reionization by varying the ionizing efficiency across redshift]. This motivates us to study the patchy kSZ signal using the novel semi-numerical simulation Abundance Matching Box for the Epoch of Reionization [AMBER; Trac et al., 2021], which takes reionization history as a direct input.

In this paper, we use the semi-numerical simulation AMBER to generate reionization CMB observables such as the Thomson optical depth and patchy kSZ for different sets of reionization history parameters and cosmological parameters. By doing so, we can disentangle the effect of individual parameters on the observed spectra. We present the dependence of kSZ power spectrum and Thomson optical depth on reionization parameters as well as cosmological parameters.

The paper is organized as follows: In Section 2.2, we introduce the theory and computation of the Thompson optical depth, patchy kSZ effect, and the patchy kSZ angular power spectra. In Section 6.2, we summarize the semi-analytical models used in AMBER, as well as the RadHydro simulations we use to calibrate the AMBER models. Section 2.4 shows comparisons between the AMBER outputs and the RadHydro simulations with matched reionization parameters and resolutions. In Section 2.5, we systematically study

the effect of reionization parameters and cosmological parameters on the patchy kSZ signal, including the maps and angular power spectra, and compare the results with observational constraints. Unless otherwise stated, we assume a flat ΛCDM cosmology with $[\Omega_m, \Omega_b, \sigma_8, n_s, h] = [0.3, 0.045, 0.8, 0.96, 0.7]$, and our fiducial values for reionization parameters are $[z_{\rm mid}, \Delta_z, A_z, M_h(M_\odot), \lambda_{\rm mfp}({\rm Mpc}/h)] = [8.0, 4.0, 3.0, 10^8, 3.0]$ (see later sections for a detailed description of these parameters).

2.2 Thomson Optical Depth and kSZ Effect

2.2.1 Thomson Optical Depth

In the ongoing CMB experiment, the most well-constrained EoR observable has been the Thomson-scattering optical depth τ_e. Constraints on τ_e informs us about the integrated electron number density n_e along the light-of-sight, as τ_e is related to n_e by:

$$\tau_e(z, \hat{\mathbf{n}}) = \sigma_T \int_0^z dz' \frac{cdt}{dz'} n_e(z', \hat{\mathbf{n}}), \tag{2.1}$$

where σ_T is the Thomson scattering cross section, $\hat{\mathbf{n}}$ is the direction of observation, and $n_e(z', \hat{\mathbf{n}})$ is the free electron number density at a specific redshift in the observed direction. The angular variation in τ_e is weak, so usually we drop the angular dependence in the computation, and use the global ionization fraction to compute $\tau_e(z)$ instead:

$$\tau_{\rm e}(z) = \sigma_T \int_0^z dz' \frac{cdt}{dz'} \langle n_{\rm e}(z') \rangle_{\rm V}, \tag{2.2}$$

where $\langle n_{\rm e}(z') \rangle_{\rm V}$ is the volume-averaged free electron number density.

Because the mean baryon number density increases with redshift, an earlier reionization leads to higher values of τ_e, and it has been shown that τ_e is not sensitive to the detailed reionization histories beyond the redshift [e.g. Battaglia et al., 2013a]. Moreover, current constraints on τ_e are primarily driven by the measurement of the low-ℓ EE polarization power spectrum (which is proportional to τ_e^2), and is independent of the small-scale anisotropies (in particular the patchy kSZ effect). Therefore, constraints on τ_e help break the degeneracy of reionization history parameters in the small-scale patchy kSZ measurements. Reversely, one can also use the patchy kSZ signal to break the degeneracy between τ_e and the primordial amplitude of scalar fluctuations A_s [e.g. Alvarez et al., 2021].

2.2.2 Patchy kSZ Effect

Next, we introduce the patchy kSZ effect and the computation of the kSZ power spectrum. The patchy kSZ effect is the temperature fluctuation in the CMB due to the scattering of CMB photons off of free electrons in bulk motion during cosmic reionization. Small-scale temperature anisotropies are then generated by the coupling of large-scale velocity perturbations and the patchiness of the ionized field on small scales. The fractional temperature

fluctuation induced by patchy kSZ effect is calculated by integrating the electron momentum along the line of sight:

$$\frac{\Delta T_{ksz}}{T} = \sigma_T \int dz \frac{cdt}{dz} e^{-\tau_e(z,\hat{\mathbf{n}})} n_e(z,\hat{\mathbf{n}}) \hat{\mathbf{n}} \cdot \mathbf{v} \tag{2.3}$$

where $\mathbf{v}$ is the peculiar velocity of free electrons, τ_e is the Thomson optical depth calculated in Eq.2.1, and the integration limits are the beginning and end of reionization.

Currently, most constraints on reionization from patchy kSZ come from the angular power spectrum [but see e.g. Smith and Ferraro, 2017, for the use of high-order statistics]. This is also the quantity of interest in this paper. To compute the kSZ angular power spectrum, we use the Limber approximation following Park et al. [2013]. First, we define the specific free electron momentum as:

$$\mathbf{q} = x_i \mathbf{v}(1+\delta), \tag{2.4}$$

where x_i is the mass-weighted ionization fraction, $\mathbf{v}$ is the peculiar gas velocity, and δ is the gas overdensity. Then, Equation 2.3 can be re-written as:

$$\frac{\Delta T_{ksz}}{T}(\hat{\mathbf{n}}) = \sigma_T n_{e,0} \int_{z_{beg}}^{z_{end}} \frac{ds}{a^2} e^{-\tau(z)} \hat{\mathbf{n}} \cdot \mathbf{q}, \tag{2.5}$$

where $n_{e,0}$ is the total number of electrons at the present epoch, a is the scale factor, and s is the comoving distance. The kSZ angular power spectrum is given by:

$$C_\ell = \left(\frac{\sigma_T n_{e,0}}{c}\right)^2 \int \frac{ds}{s^2 a^4} e^{-2\tau(z)} \frac{P_{q_\perp}(k=\ell/s, s)}{2}. \tag{2.6}$$

To compute $P_{q_\perp}(k)$, let $\tilde{\mathbf{q}}$ be the 3D Fourier transform of the momentum field. Then, the projection of $\tilde{\mathbf{q}}$ on the plane perpendicular to the mode vector is given by $\tilde{\mathbf{q}}_\perp(\mathbf{k}) = \tilde{\mathbf{q}}(\mathbf{k}) - \hat{k}(\tilde{\mathbf{q}}(\mathbf{k}) \cdot \hat{k})$. Finally, $P_{q_\perp}(k)$ is the power spectrum of $\tilde{\mathbf{q}}_\perp(\mathbf{k})$ given by:

$$(2\pi)^3 P_{q_\perp}(k) \delta(\mathbf{k} - \mathbf{k}') = \langle \tilde{\mathbf{q}}_\perp(\mathbf{k}) \cdot \tilde{\mathbf{q}}^*_\perp(\mathbf{k}) \rangle. \tag{2.7}$$

Note that we can also directly compute the kSZ power spectrum from full-sky patchy kSZ maps. However, since the scale of interest is small ($\ell > 1000$) and is well-approximated by the Limber approach, we choose to follow the Limber approximation for a less noisy spectrum and faster computation.

2.3 Simulations

The simulations in this work are run with the new semi-numerical code AMBER [Trac et al., 2021]. In this section, we will introduce the main models in the AMBER code relevant for calculating the kSZ signal. Moreover, we also briefly introduce the RadHydro simulation suite from the Simulations and Constructions of the Reionization of Cosmic Hydrogen (SCORCH) project [Chen et al., 2020, Doussot et al., 2019, Trac et al., 2015]. We will later use these RadHydro simulations to calibrate AMBER models and compare results from both simulations.

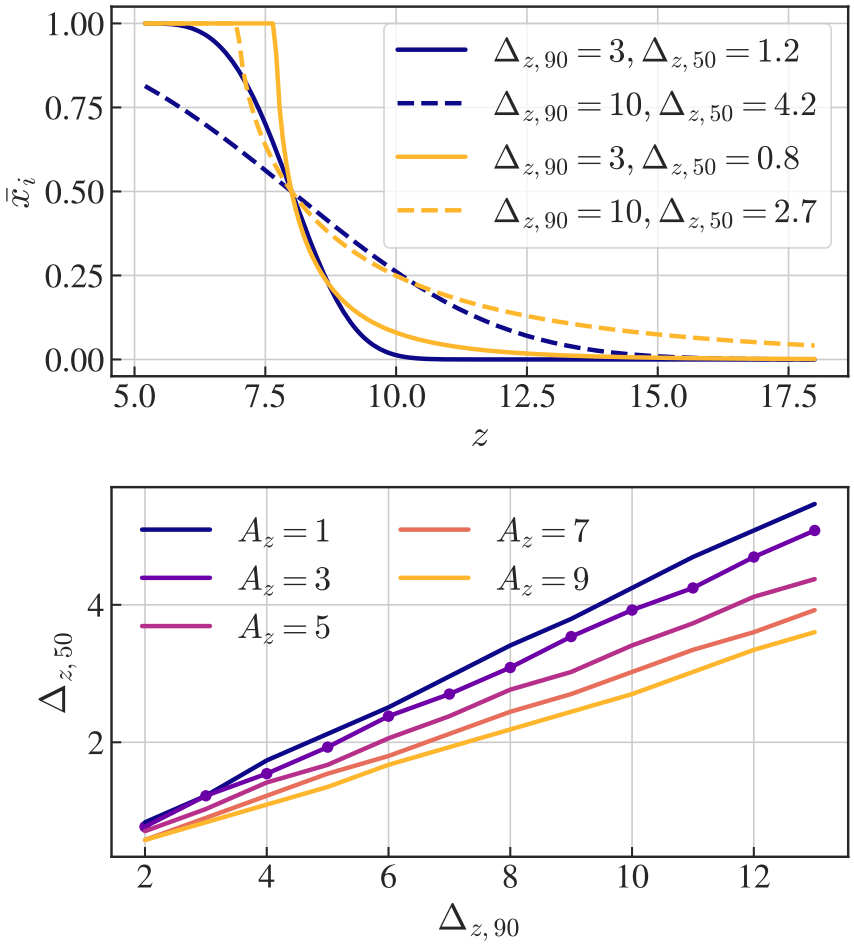

Figure 2.1: ***Top:*** example reionization histories with the same $\Delta_{z,90}$ but different A_z, leading to different $\Delta_{z,50}$. Note that $\Delta_{z,90}$ better captures the high-redshift tail of reionization. ***Bottom:*** Scaling relation between $\Delta_{z,90}$ and $\Delta_{z,50}$ for different levels of asymmetry.

2.3.1 AMBER

The reionization history $x_{\rm i}(z)$ is the fraction of hydrogen that are ionized at a certain redshift. It is of primary interest to our understanding of the EoR, because it reveals the possible astrophysical process during the EoR, and also directly affects many key EoR observables. For example, the integrated Thomson optical depth and the evolution of the global 21cm brightness temperature depend linearly on the ionized electron fraction $\bar{x}_{\rm i}(z)$ and neutral hydrogen fraction $\bar{x}_{\rm HI}(z)$, respectively. One of the major novelties of AMBER is that we directly control the reionization history in our reionization modeling.

Following the argument in Trac et al. [2008], AMBER parametrizes the reionization history with the midpoint, duration, and asymmetry parameters. In AMBER, we use the mass-weighted global ionization fraction $\bar{x}_{\rm i,M}$, and drop the subscript hereafter.

We define the midpoint redshift $z_{\rm mid}$ as the redshift at which 50% of the universe is ionized by mass. To characterize the duration of reionization Δ_z, let $z_{\rm ear} > z_{\rm mid}$ and $z_{\rm lat} < z_{\rm mid}$ correspond to the early and late stage of reionization, respectively. The duration is then defined as:

$$\Delta_{\rm z} \equiv z_{\rm ear} - z_{\rm lat}. \tag{2.8}$$

There are various definitions of Δ_z in previous works depending on how one defines $z_{\rm ear}$ and $z_{\rm lat}$. Throughout this work, we take $(z_{\rm ear}, z_{\rm lat})$ as the redshifts at which the universe is 5% and 95% ionized, respectively. Under this definition, $\Delta_{\rm z}$ more effectively quantifies the whole EoR. We refer to this definition as $\Delta_{z,90}$. We will drop the subscript "90" when we are not explicitly comparing with other definitions of Δ_z. Another popular definition takes $(z_{\rm ear}, z_{\rm lat})$ as the redshifts at which the universe is 25% and 75% ionized [e.g. Battaglia et al., 2013b, Gorce et al., 2020]. We will refer to the duration under this definition as $\Delta_{z,50}$, as it encloses 50% of the ionization process.

Finally, to characterize the likely asymmetric reionization scenarios, we define the asymmetry parameter as:

$$A_{\rm z} \equiv \frac{z_{\rm ear} - z_{\rm mid}}{z_{\rm mid} - z_{\rm lat}}. \tag{2.9}$$

Symmetric reionization histories would correspond to $A_{\rm z} = 1$, but reionization simulations typically find that the early stage of reionization takes longer than the later stage such that $A_{\rm z} > 1$. Note that with different levels of asymmetry, there is not a one-to-one correspondence between $\Delta_{z,90}$ and $\Delta_{z,50}$. In Figure 2.1, we show the relation between $\Delta_{z,90}$ and $\Delta_{z,50}$ for asymmetries ranging from 1 to 9. When the asymmetry level is lower, $\Delta_{z,90}$ corresponds to a higher value of $\Delta_{z,50}$. Hence, the scaling coefficient between observables and $\Delta_{z,50}$ is also affected by A_z. This is important for interpreting the comparisons between our results and previous works in later sections.

In AMBER, we interpolate the three ionization points at $(z_{\rm ear}, z_{\rm mid}, z_{\rm lat})$ with a modified Weibull function [Weibull, 1951],

$$\bar{x}_{\rm i}(z) = \exp\left[-\max\left(\frac{z - a_{\rm w}}{b_{\rm w}}, 0\right)^{c_{\rm w}}\right], \tag{2.10}$$

where the coefficients $a_{\rm w}$, $b_{\rm w}$, $c_{\rm w}$ are all positive values. The coefficients can be easily determined by first solving a nonlinear equation for $c_{\rm w}$ and then substituting its value into algebraic equations for the other two coefficients. We find that solutions exist for the asymmetry range $A_{\rm z} \lesssim 15$, which is more than sufficient for parameter space studies.

L [h^{-1}Mpc]	$N_{\rm dm}$	$N_{\rm gas}$	$N_{\rm RT}$	f_8	a_8	τ	$z_{\rm mid}$	$\Delta_{\rm z}$	$A_{\rm z}$	$M_{\rm h}$
50	2048^3	2048^3	512^3	0.13	1	0.060	7.91	5.45	2.69	$10^8\,M_\odot$

Table 2.1: Simulation parameters and measured reionization history parameters for the RadHydro Sim 1 in SCORCH II.

Reionization-Redshift Field

The key assumption in AMBER is that the order in which a cell gets ionized is determined by the relative radiation intensity in that cell. In this way, given a global reionization history $\bar{x}_{\rm i}(z)$, we can obtain a reionization redshift field by abundance matching against the unnormalized radiation intensity.

To begin with, the dark matter density and velocity fields are generated with second-order perturbation theory (2LPT) at the desired redshift. On moderately nonlinear scales, the dark matter and gas distributions are highly correlated and assumed to exactly trace each other. Thus we use the dark matter overdensity to approximate the gas overdensity in AMBER.

We then construct halo mass density fields with the Lagrangian version of the excursion set formalism (ESF-L) [see Trac et al., 2021, for more detailed descriptions]. We use the minimum halo mass parameter M_h to control the lowest halo mass for hosting ionizing sources. This step gives us the halo density field $\rho_{\rm halo}(\boldsymbol{x})$, which is a proxy of the ionizing sources in the simulation.

Then, assuming that radiation intensity of ionizing sources is proportional to the halo density, and that the photon flux attenuation follows $e^{-r/\lambda_{\rm mfp}}$, we obtain the (unnormalized) radiation intensity field $r(\boldsymbol{x}, z)$ by convolving $\rho_{\rm halo}(\boldsymbol{x})$ with a kernel function $\frac{1}{4\pi r^2}\exp\left(-\frac{r}{\lambda_{\rm mfp}}\right)$. $\lambda_{\rm mfp}$ would affect how much radiation is received by each cell in our simulation, and as a result how early each cell is ionized. Here we use an effective mean free path $\lambda_{\rm mfp}$ to account for the attenuation of the radiation field. In principle, the mean free path of photons is a local variable that could depend on the halo mass and redshift. However, given the semi-analytical nature of our model and the resolution at 1 Mpc/h, we set the photon mean free path as a global variable $\lambda_{\rm mfp}$. We plan to incorporate the temporal and spatial variations of $\lambda_{\rm mfp}$ in future developments.

Finally, the reionization-redshift field $z_{\rm re}(\boldsymbol{x})$ is assumed to be correlated with the radiation field $r(\boldsymbol{x}, z)$. A region with higher radiation intensity is considered to be photoionized earlier and has a higher reionization-redshift. The abundance matching technique assigns redshift values such that the reionization history follows a given mass-weighted ionization

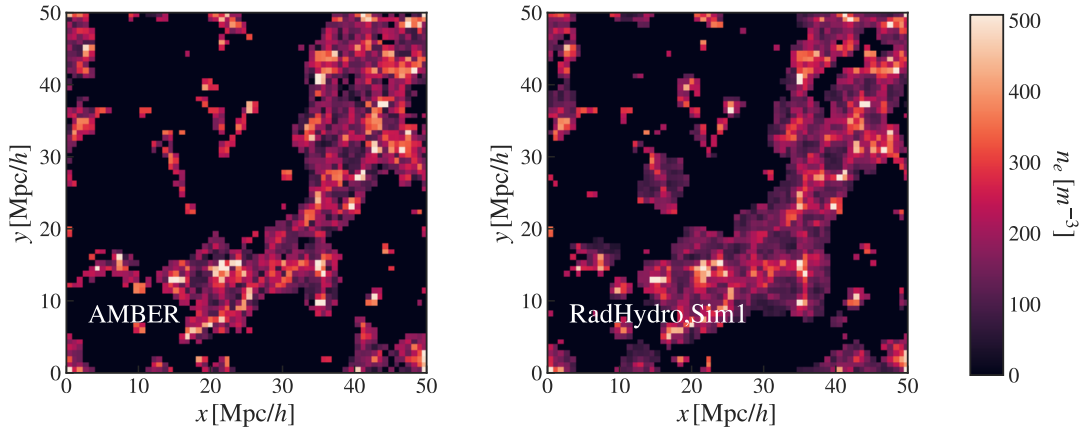

Figure 2.2: Visualization of a 50 Mpc/h × 50 Mpc/h × 1 Mpc/h (shown in 64^2 pixels) slice of the free electron number density at $z = 8$, from the RadHydro Sim 1 and AMBER with the matched reionization parameters. AMBER produce slightly more concentrated ionized regions compared to RadHydro.

fraction $\bar{x}_{\rm i}(z)$, specified with the redshift midpoint, duration, and asymmetry parameters and interpolated with a Weibull function (Equation 2.10).

We perform the abundance matching based on the radiation field at a single redshift $z_{\rm mid}$ for computational efficiency, but it can also be done tomographically using multiple redshift intervals. In Appendix 2.A, we discuss the effect of abundance matching at a single redshift $z_{\rm mid}$, and characterize the changes in the electron number density as well as the patchy kSZ signal when the abundance-matching redshift is chosen differently. The abundance matching at $z_{\rm mid}$ is performed as follows: at a given redshift bin z_n, we have a corresponding mass-weighted ionization fraction $\bar{x}_{\rm i}(z_n)$ from the specified reionization history. We then rank order the cells at this redshift in descending order by $r(\boldsymbol{x}, z_{\rm mid})$. Then we ionize the first k_n cells by this rank such that we reach an ionized mass fraction of $\bar{x}_{\rm i}(z_n)$. Here the ionized mass fraction is calculated from the linearly extrapolated overdensity with respect to the overdensity at the midpoint redshift. We note that the volume-weighted ionization fraction in this case is $k_n/N_{\rm cell}$ and it is typically lower than the mass-weighted $\bar{x}_{\rm i}(z_n)$.

2.3.2 RadHydro

The Simulations and Constructions of the Reionization of Cosmic Hydrogen (SCORCH) project [Chen et al., 2020, Doussot et al., 2019, Trac et al., 2015] is a set of N-body and radiation-hydrodynamic simulations that is designed to provide theoretical predictions and mock observations of reionization for more accurate comparisons with present and future observations. It is the motivation of AMBER, so we will briefly summarize the SCORCH simulations here. For details of the SCORCH project, please refer to Trac et al. [2015] and Doussot et al. [2019].

SCORCH II [Doussot et al., 2019] is a set of three radiation-hydrodynamic (RadHydro)

simulations with the same cosmic initial conditions, same galaxy luminosity functions, but with different radiation escape fraction $f_{\rm esc}(z)$ models. The simulations are designed to have the same Thomson optical depth $\tau \approx 0.06$, consistent with recent CMB observations [Planck Collaboration et al., 2018], and similar midpoints of reionization $7.5 \lesssim z \lesssim 8$, but with different evolution of the ionization fraction $\bar{x}_{\rm i}(z)$. They model high-redshift galaxies using an updated subgrid approach that allows systematic control of the galaxy distributions in the simulations while matching the observed luminosity functions from HST [e.g. Bouwens et al., 2015, Finkelstein et al., 2015].

Table 2.1 summarizes the parameters for RadHydro Sim 1, which we will later use to compare with the output of AMBER. Here a_8 and f_8 defines the redshift dependence of the photon escape fraction through $f_{\rm esc}(z) = f_8 \left(\frac{1+z}{9}\right)^{a_8}$ [see Doussot et al., 2019, for a more detailed description] We also show the measured midpoint, duration, and asymmetry parameters from the simulation output.

2.4 Comparison with RadHydro

In this section, we present the comparison of the free electron number density, the patchy kSZ 2D projected maps, and the patchy kSZ power spectra between AMBER and RadHydro Sim 1.

Since our target resolution when running AMBER is $1\,{\rm Mpc}/h$, we first bin down the RadHydro Sim 1 to 64^3 cells in the $50\,{\rm Mpc}/h$ box. More specifically, for the density and momentum fields we take the average over an 8^3 local region, and for the reionization redshift field, we smoothed it by calculating the redshift at which all the 8^3 local cells are ionized. Then we re-measure the reionization parameters in the binned Sim 1 and obtain $z_{\rm mid} = 7.85$, $\Delta_z = 4.73$, $A_z = 2.25$. Note that this is slightly different from the parameter measured in the original resolution shown in Table 2.1 because the we have averaged over a much larger region when determining the reionization redshift. In particular, some cells with early reionization may be postponed to a later time because the surroundings are not yet ionized. For the comparison, we run AMBER at the same resolution (64^3), with the same cosmological parameters and the same initial condition phase as RadHydro Sim 1, and we match the reionization parameters measured above. In RadHydro Sim 1, the minimum halo mass is $10^8\,M_\odot$, so we fix this parameter in AMBER. By varying $\lambda_{\rm mfp}$ in the range $[1\,{\rm Mpc}/h, 5\,{\rm Mpc}/h]$, we find that $\lambda_{\rm mfp} = 2.8\,{\rm Mpc}/h$ best matches the reionization redshift field of RadHydro Sim 1, so we present our comparison results at this value. Because we are using a small box here, we can calculate the maps under the flat sky approximation and do the 2D projection by summing the field along the z-axis at a fixed redshift.

2.4.1 Free Electron Number Density

We first examine the evolution of the free electron number density, as it is a crucial component for calculating both the Thomson optical depth and the patchy kSZ signal. The fluctuation in free-electron number density will dominate the patchy kSZ signal on small scales.

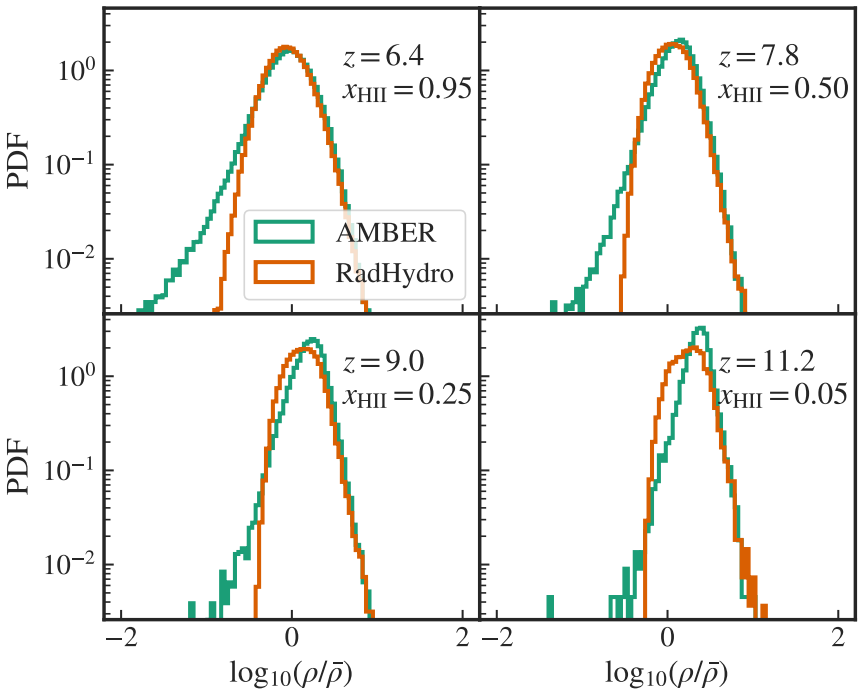

Figure 2.3: The distribution of gas densities in ionized regions. The ionized regions in AMBER have a peak at higher densities compared to RadHydro, especially during the early stage of reionization ($\bar{x}_i < 0.5$). The disagreement in under-dense regions is not concerning because it is due to the much smaller number of LPT particles and the different assignment and deconvolution process for AMBER. We would find the same effects for RadHydro if we use a lower resolution simulation and not done the simple binning.

After getting the reionization redshift field z_{re} following the procedures described in Section 2.3.1, we can use it to obtain the electron number density field at all redshifts by

$$n_e(\mathbf{x}, z) = x_i(\mathbf{x}, z) n_b(\mathbf{x}, z)(X + \frac{Y}{4}), \tag{2.11}$$

where n_b is the baryon number density, X is the mass fraction of hydrogen, Y is the mass fraction of helium. $x_i = n_{\rm e,free}/n_{\rm e,total}$ is the free electron fraction, and is set to be $x_i(\mathbf{x}, z) = 1$ if $z < z_{re}(\mathbf{x})$ and $x_i(\mathbf{x}, z) = 0$ if $z > z_{re}(\mathbf{x})$.

In Figure 2.2 we show the visualization of a $50 \times 50 \times 1\,{\rm Mpc}^3/h^3$ slice of the free electron number density at $z = 8$, from the RadHydro Sim 1 and AMBER with matched reionization parameters. At $z = 8$, about half of the mass in the universe is ionized, and we can see from both simulations that the ionized regions also correspond to the higher-density regions. The morphology of ionized regions from the AMBER code is very similar to RadHydro Sim 1. However, from the slice we notice that the RadHydro simulation has a larger ionized region in volume. Given the same mass-weighted ionization fraction, a larger volume-filling factor

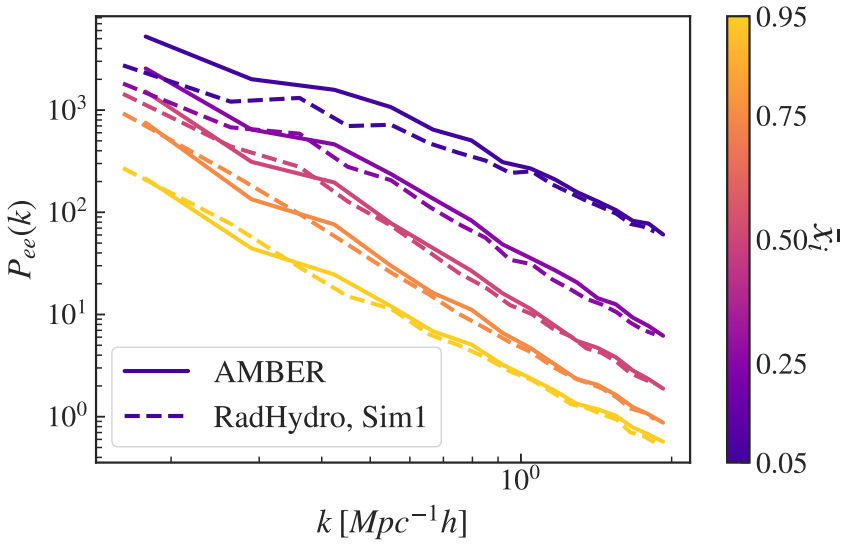

Figure 2.4: Comparison between the AMBER and RadHydro free electron number density power spectraum $P_{ee}(k, z)$ at different redshifts. In both simulations, the overall $P_{ee}(k, z)$ gets lower as reionization evolves, because as more mass in low-density regions get ionized, the ionized electron field becomes a less biased tracer of the matter density field. At very high redshift, AMBER has larger power on large scales, but from $z = 9$ onwards, the two simulation matches well with each other.

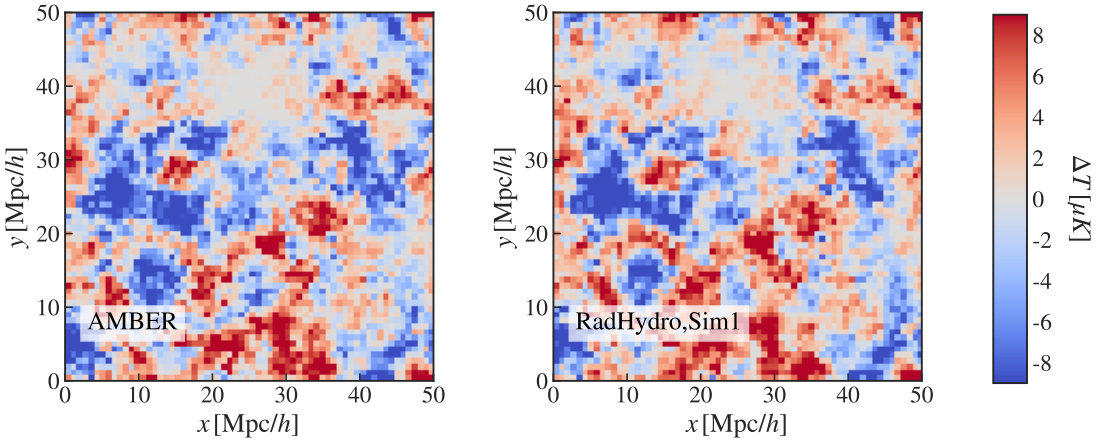

Figure 2.5: The 2D projected patchy kSZ temperature maps under flat sky approximation for RadHydro Sim 1 (*right*) and AMBER (*left*) in the same simulation as described in Figure 2.2. The projection is done at the redshift $z = 8.0$. Here we sum along z axis the electron momentum to get the fractional temperature difference in the CMB. The projected kSZ map of AMBER resembles that of RadHydro Sim 1 when the reionization parameters are matched.

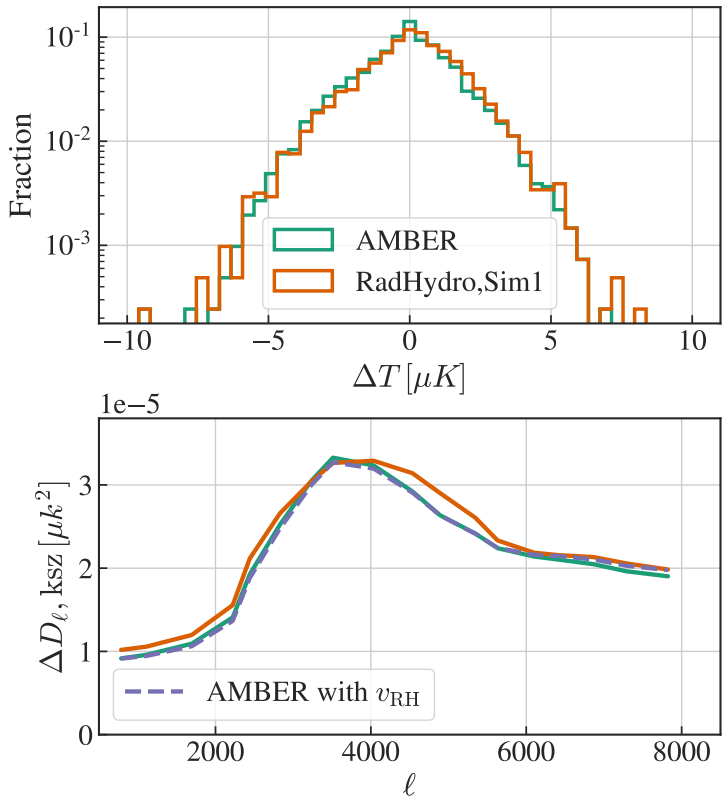

Figure 2.6: ***Top:*** The distribution of ΔT of the projected kSZ maps generated using AMBER (*green*) and RadHydro (*orange*) shown in Figure 2.5. ***Bottom:*** The 2D power spectra of the patchy kSZ maps from the two simulations. To disentangle the effect from the velocity difference, we also show the spectrum calculated using the AMBER n_e field with the velocity from RadHydro (*dashed purple*). We find good agreement at $\ell \sim 3000$. The difference at $\ell < 6000$ mainly results from the electron number density as opposed to the velocity.

in RadHydro means that the mean density of the ionized region is smaller, and that the ionizing front propagates further into the IGM.

This is confirmed by the distribution of the gas density in ionized regions shown in Figure 2.3. We can see from the distribution that the ionized regions in AMBER have a peak at higher densities compared to RadHydro, especially during the early stage of reionization ($\bar{x}_{\rm i} < 0.5$). This happens for two main reasons. First, the high-density regions have a high recombination rate and may remain neutral in RadHydro. However, this is currently not treated in AMBER, and thus AMBER tends to ionize more high-density regions. Second, the RadHydro simulations have episodic star formation and the highest-density collapsed regions do not necessarily produce the highest number of photons. These fluctuations show up more when there are small HII regions early on during reionization. The two processes combined lead to the more tilted PDF of ionized gas density in AMBER.

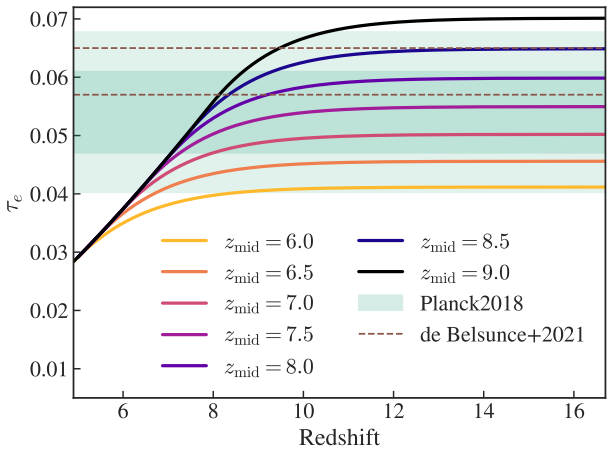

Figure 2.7: The evolution of τ_e with different values of $z_{\rm mid}$ ranging from $z_{\rm mid} = 6.0$ to $z_{\rm mid} = 9.0$. Out of the values shown, $z_{\rm mid} = 9.0$ are mildly inconsistent with the constraint from Planck Collaboration et al. [2018] at the 2σ level, while the other values are consistent. The dashed band shows the re-analysis of the Plank2018 data by de Belsunce et al. [2021], who found larger values of τ_e and favors higher $z_{\rm mid}$.

Then in Figure 2.4, we further compare between the AMBER and RadHydro free electron number density power spectra $P_{ee}(k, z)$ at different ionization levels. In both simulations, the overall $P_{ee}(k, z)$ gets lower as reionization evolves, because as more mass in low-density regions gets ionized, the ionized electron field becomes a less biased tracer of the matter density field. At the beginning of reionization, the ionized regions are concentrated in high-density regions around the source galaxies, and therefore n_e has a higher power on large scales compared to the underlying matter density field. From the comparison between the two simulations, we see that when reionization just begins ($z \sim 12$), AMBER has larger power on large scales. The disagreement in under-dense regions is not concerning because it is due to the much smaller number of LPT particles and the different assignment and deconvolution process for AMBER. We would find the same effects for RadHydro if we use a lower resolution simulation and not done the simple binning. As we have already seen in Figure 2.3, AMBER ionizes more high-density regions during the beginning of reionization. This leads to more bias on large scales at high redshifts.

From $z = 9$ onwards, the two simulation matches well with each other, because the bias in AMBER is less prominent as the ionizing fronts propagate further into the low-density regions. Finally, once reionization is almost over ($z \sim 6$) and all IGM atoms are ionized, the fluctuations in free electrons density follow those of dark matter on large scales.

2.4.2 Patchy kSZ

Next, we compare the 2D projected patchy kSZ temperature maps under flat sky approximation for RadHydro and AMBER. To get the flat-sky maps, we simply sum the free-electron

momentum along the z-axis to get the fractional temperature difference in the CMB introduced by the patchy kSZ effect, and then multiply by the CMB temperature $T_{\rm CMB} = 2.725$k to obtain the temperature fluctuation in the 2D plane. Here we assume a fixed $z = z_{\rm mid}$ ($x_{\rm HII} = 0.5$) since the box size is small enough for ignoring the redshift evolution.

From the projected maps in Figure 2.5, we can see that visually, the AMBER kSZ signal resembles that of RadHydro Sim 1. The blue and red regions correspond to the signal from the ionized regions along the line-of-sight, while the small white regions are neutral. Similar to what we have seen in Figure 2.2, because RadHydro has larger ionized regions, we see fewer white pixels in the kSZ map here.

Besides the visualization, in Figure 2.6 we further show the one-point and two-point statistics for the projected kSZ maps. The distributions of the temperature fluctuations shown in the top panel are very similar in the two simulations. From the PDF we do see a higher peak around $\Delta T = 0$ from AMBER, as we have discussed from the maps in the previous paragraph. Other than the difference in the peak, the overall shape and width of the distribution match well.

The bottom panel shows the dimensionless power spectrum of the flat-sky maps, related to the angular power spectrum C_ℓ by $D_\ell = \ell(\ell+1)C_\ell/2\pi$. We first notice that from both simulations, the power spectrum peaks at $\ell \sim 3500$. This scale corresponds to a size of the ionized bubbles of $\sim 11\,{\rm Mpc}/h$ at $z = 7.8$. Then, comparing the two curves, we see that the spectrum of RadHydro has $\sim 5\%$ higher power on small and large scales, while AMBER produces $\sim 10\%$ higher power at $\ell = 3500 - 4000$. There are two sources of the differences: first, RadHydro uses a P^3M N-body simulation to generate the velocity field, while AMBER uses 2LPT and produces less power on small scales compared to N-body [see e.g. Trac et al., 2021]; second, as was shown in the previous section, there are also differences in the free-electron number density field due to the slightly different morphology of ionized regions. To disentangle the two effects, we also show the spectrum calculated using the AMBER n_e field with the velocity from RadHydro (shown in dashed purple). We can see that when we correct for the difference from the velocity fields, the power on small scales ($\ell > 6000$) matches perfectly with RadHydro. This indicates that the small-scale difference is primarily due to the coupling of the n_e fields with the velocity fluctuations. For $\ell < 6000$ multipoles, however, using the RadHydro velocity does not change the kSZ spectrum in AMBER. This tells us that the $\ell < 6000$ arises from the difference in the free electron number density. Despite the minor differences we just discussed, we still find that overall the kSZ 2D spectrum from AMBER matches well with RadHydro.

2.5 Parameter Space Study

Having shown that AMBER agrees well with the RadHydro simulation for observations at the matched parameter values, now we vary the parameters around their fiducial values in order to study their effect on the patchy kSZ signal. We summarize the fiducial values for the parameters we study in Table **??**. Previous works [e.g. Battaglia et al., 2013a, Mesinger et al., 2012, Zahn et al., 2012, 2007] have shown that the kSZ signal from patchy reionization

depends on the midpoint redshift and duration of reionization. However, they did not directly parametrize the simulations with these parameters, so it is hard to control the reionization history and directly study its influence on the patchy kSZ signal. In this work, we will directly examine the effect of reionization history, parametrized by the midpoint, duration, and asymmetry, on the patchy kSZ effect of reionization. To generate the kSZ maps and power spectra shown in this section, we run $L_{\rm box} = 2\,{\rm Gpc}/h$ simulations on 2048^3 grids.

2.5.1 Redshift Midpoint

The midpoint redshift $z_{\rm mid}$ is the redshift at which half of the universe is ionized (by mass). When other parameters are kept fixed, a higher $z_{\rm mid}$ means that the whole reionization process is pushed to an earlier time when the universe has a higher energy density. We note that because we currently generate the reionization redshift field by abundance matching at $z_{\rm mid}$, a change in $z_{\rm mid}$ can also affect the relative order of ionization of the cells (i.e. we do not preserve the exact same ionization morphology by fixing all other parameters). However, we expect such an effect to be small, because the large halos at $z = 9$ should also correspond to large halos at $z = 7$. Therefore, we expect the main effect from varying $z_{\rm mid}$ to be the amplitude of the kSZ spectra: the overall amplitude should be larger with a higher $z_{\rm mid}$, because there would be a higher electron density when we integrate along the line of sight.

In the top two panels of Figure 2.8, we visualize the free electron number density n_e and the kSZ temperature change $\Delta T_{\rm kSZ}$ for a relatively early ($z_{\rm mid} = 9$) and late ($z_{\rm mid} = 7$) reionization. In this figure, the horizontal axis is the line-of-sight, and in the direction perpendicular to the page we plot a $1\,{\rm Mpc}/h$ slice from the 3D simulation box. From the n_e plots, we can see ionized bubbles form around the first galaxies at the beginning of reionization. These bubbles continue to grow in size and finally overlap and merge, leading to a fully ionized universe. In the left panel of Figure 2.10, we can see that increasing the midpoint redshift of reionization increases the amplitude of the kSZ spectra without changing the shape. Physically, the scenario that corresponds to an earlier $z_{\rm mid}$ could be a higher escape fraction, the ionization dominated by smaller sources, or a combination of multiple effects.

We note that there exist degeneracies between $z_{\rm mid}$ and other reionization parameters (most noticeably the duration of reionization), in terms of their effects on the patchy kSZ power spectrum (we will discuss more about it later). Such degeneracy is often broken by constraints from the Thompson optical depth τ_e from the low-ℓ EE polarization [e.g. Ferraro and Smith, 2018]. The value of τ_e is mainly affected by the redshift of reionization without being sensitive to other reionization parameters [e.g. Battaglia et al., 2013a]. In Figure 2.7, we show the evolution of τ_e with different values of $z_{\rm mid}$ ranging from $z_{\rm mid} = 6.0$ to $z_{\rm mid} = 9.0$. Out of the values shown, $z_{\rm mid} = 9.0$ is mildly inconsistent with the constraint from Planck Collaboration et al. [2018], while the other values are all within the 2σ range. However, we note that recent re-analysis of the Planck2018 data by Pagano et al. [2020] and de Belsunce et al. [2021] (shown as dashed lines) found larger values of τ_e and favors higher $z_{\rm mid}$. In either case, the constraint we get from τ_e on $z_{\rm mid}$ is tighter compared to the constraint from

purely patchy kSZ.

2.5.2 Duration

In the previous section, we have hinted at the degeneracy between $z_{\rm mid}$ and duration of reionization. Now we will turn to the effect of the duration on the patchy kSZ temperature fluctuations. Out of all the reionization parameters, Δ_z has the strongest effect on the amplitude of the spectra. For this reason, observations of the kSZ amplitude have been used to constrain the reionization duration for the past decade. The ACT and SPT-SZ surveys have published upper limits on the kSZ power [Addison et al., 2013, Dunkley et al., 2013, George et al., 2015], with a 95% CL upper limit on the patchy kSZ power being $D^{\rm pkSZ}_{\ell=3000} < 3.3\mu K^2$ from the 2500 degree^2 SPT-SZ survey. By combining SPT results with large-scale CMB polarization measurements, Zahn et al. [2012] constrains the amplitude of the patchy kSZ by setting an upper limit $D^{\rm pkSZ}_{\ell=3000} \leq 2.1\mu K^2$ (95% CL). The most recent observational constraints come from the SPTPol survey, where Reichardt et al. [2021] constrained the patchy kSZ amplitude to $D^{\rm pkSZ}_{\ell=3000} = 1.1^{+1.0}_{-0.7}\mu K^2$ using the models of homogeneous signal given in Shaw et al. [2012]. Using the fitting template provided in Battaglia et al. [2013a], they find the 95% CL upper limits on the duration of reionization to be $\Delta_{z,50} < 5.4$ (6.9/4.3 when considering a 25% uncertainty in the homogeneous spectrum), and a 68% confidence interval of $\Delta_{z,50} = 1.1^{+1.6}_{-0.7}$. Using a more recent semi-numerical model, Choudhury et al. [2021] placed a tighter constraint on the duration to be $\Delta_{z,50} < 2.9$ at 99% CL.

Before diving into the kSZ angular power spectra prediction with AMBER, we start by visualizing the patchy kSZ temperature fluctuations with different durations of reionization. In the middle panels of Figure 2.8, we show the light-cone projections of the free electron number density n_e and the kSZ temperature change $\Delta T_{\rm kSZ}$ assuming a quick reionization ($\Delta z = 2$, third row) and a slow reionization ($\Delta z = 6$, fourth row). From the comparison between the two durations, we see that under the $\Delta z = 6$ scenario, reionization starts earlier, and there are more ionized bubbles along the line-of-sight. The motion of these ionized bubbles relative to the background CMB would result in the observed kSZ fluctuation in the CMB we see from the bottom panels. In the bottom panels, we can clearly see the large-scale velocity fluctuations. These fluctuations dominate $\Delta T_{\rm kSZ}$ on large scales, while the n_e field fluctuation dominate on small scales.

In Figure 2.9, we show 4×4 degree^2 patches of the $\Delta T_{\rm kSZ}$ maps from the $2\,{\rm Gpc}/h$ simulations with different durations. These maps are made by ray-tracing through past light cones during reionization ($5 \leq z \leq 30$), and generated using `HEALPix` [Górski et al., 2005] with $N_{\rm side} = 4 \times N_{\rm mesh}$. The maps shown here are processed with a high-pass filter, where we only keep the spherical harmonics with $\ell > 1000$. This is because we are more interested in the small-scale features which is a direct result of patchy reionization. From the maps, we can see that a longer duration leads to larger fluctuations on small scales, because the small-scale kSZ is sourced by the electron number density fluctuation from patchy reionization. These fluctuations are incoherent and accumulate along the line of sight, leading to a larger small-scale inhomogeneity for a longer duration.

Finally, we show the change in the angular power spectra with respect to the duration in the second panel of Figure 2.10. Compared with the first panel on $z_{\rm mid}$, we see a strong degeneracy of the two parameters as expected, but the spectra are more sensitive to duration than the midpoint redshift. Here we also show the 1σ and 2σ confidence intervals derived in Reichardt et al. [2021], in order to show the extent of variation with the Δz parameter within the confidence intervals. For the colored lines, we keep all other parameters at their fiducial values, and we can see that durations of $\Delta_z < 5.1$ yield results consistent with the 1σ constraints from Reichardt et al. [2021]. This translates to $\Delta_{z,50} < 2.0$ under the definition of duration in Battaglia et al. [2013b], assuming a mildly asymmetric reionization history at $A_z = 3$ (see Figure 2.1 for the conversion). The limit agrees with the recent picture from a variety of observations arguing that reionization happened quickly.

Then we explore the maximum Δ_z that produces a $D^{\rm pkSZ}_{\ell=3000}$ consistent with the 2σ constraint from Reichardt et al. [2021]. In order to do this, we also vary the other two parameters, $z_{\rm mid}$ and $\lambda_{\rm mfp}$, that affect $D^{\rm pkSZ}_{\ell=3000}$ most. Since we know that lower values of $z_{\rm mid}$ and $\lambda_{\rm mfp}$ decreases $D^{\rm pkSZ}_{\ell=3000}$, we want $z_{\rm mid}$ and $\lambda_{\rm mfp}$ to be low in order to allow for a longer duration. We set $z_{\rm mid} = 6.5$, a value slightly below the 1σ interval from the τ_e prediction from Planck Collaboration et al. [2018]. We also set $\lambda_{\rm mfp} = 1\,{\rm Mpc}/h$, and $A_z = 8.0$ in order to ensure an end of reionization by $z = 5.5$. After minimizing $D^{\rm pkSZ}_{\ell=3000}$ with other parameters in consistency with other observation channels, we find that duration of $\Delta_z = 12.8$ reaches the top of the 2σ interval. This converts to $\Delta_{z,50} < 3.5$ under the assumption that $A_z = 8.0$.

We emphasize, however, that this should not be interpreted as a strict 2σ constraint of $\Delta_z < 12.8$ (or $\Delta_{z,50} < 3.5$), because here we do not systematically vary other reionization parameters. A full parameter space study is needed in order to derive a constraint on the duration from the simulation data and the observation data. We also note that our $D^{\rm pkSZ}_{\ell}$ are integrated from $z = 5$ to $z = 30$, while the confidence interval derived in Reichardt et al. [2021] is derived using an end of reionization redshift of $z = 5.5$. Converting to an end of reionization redshift of 5.0 may move the interval up by $\sim 5 - 10\%$. Finally, the uncertainty within the homogeneous kSZ spectra can cause $\sim 25\%$ fluctuations in the patchy kSZ estimation, according to Reichardt et al. [2021].

2.5.3 Asymmetry

The asymmetry parameter A_z characterizes the relative length of the beginning and end of reionization. Park et al. [2013] showed that the model adopted in Battaglia et al. [2013b] failed to account for an asymmetric reionization history, and cannot be used to provide universal modeling of the kSZ spectrum. In AMBER, the asymmetry parameter A_z allows us to have more control over the overall shape of the reionization history and reduce the modeling bias. When we set the asymmetry large, we are enforcing an earlier but slower beginning, and an earlier and abrupt end of reionization. When $A_z \sim 1$, we get a symmetric reionization history where the beginning and end have an equal length. In the bottom panels of Figure 2.8, we show the redshift evolution of n_e and $\Delta T_{\rm kSZ}$ with a symmetric reionization and a highly asymmetric reionization. We can see that even when the duration is kept fixed,

for the asymmetric reionization scenario, the ionizing bubbles begin to form at a much earlier redshift.

The right panel of Figure 2.10 shows the change in the kSZ spectrum when we only change the asymmetry of the reionization history. Compared with the other two reionization history parameters, the dependence of the kSZ spectra on A_z is weak. We notice that at the $\ell = 3000$ scale where the observation data lies, there is almost complete degeneracy between the different asymmetric reionization cases (but note that the cross-over scale may be different for other fiducial parameters.). Yet there is a noticeable change in the slope of the kSZ spectrum: large asymmetry would decrease the power on large scales and introduce slightly more power on small scales. This indicates that to further constrain the early and end phase of reionization in addition to the overall length, we will need more data at multipoles other than $\ell = 3000$.

2.5.4 Minimum Halo Mass

The minimum halo mass parameter, M_h, is a lower mass limit of halos that host ionizing sources in the simulation. Usually in simulations where we do not keep the reionization history and the photon mean-free path fixed, a smaller $M_{\rm h}$ can lead to earlier reionization because the ionizing sources are more abundant at high redshifts. However, this effect can be counter-balanced if the ionizing photon budget is small (e.g. the escape fraction is low). By directly controlling the reionization history, however, we do not have to explicitly account for the degeneracy between the sources and sinks.

In the left two columns of Figure 2.11, we show the evolution of the ionization fraction field assuming two extreme values in our parameter study, $M_h = 10^7 M_\odot$ and $M_h = 10^{10} M_\odot$, while fixing all other parameters at their fiducial values. Because the reionization history is fixed, at each redshift the global ionization fractions are the same. We can see that the change in M_h affects the morphology of ionized regions, but not very significantly. Before the Universe gets half ionized, larger M_h leads to more large-scale clustering of ionized regions around heavier sources, and there are fewer small ionized regions. In AMBER, when we change M_h from $10^{10} M_\odot$ to $10^7 M_\odot$, the smaller halos at $z = z_{\rm mid}$ will no longer be treated as sources. However, such effect is small if we only care about the rank-ordering of the radiation field: even when the smaller sources are turned on, they will have less radiation compared to large sources, and therefore have a lower priority in reionization compared to larger sources. On the other hand, compared with the non-source regions, the small sources are likely nearer to the large sources than under-dense regions are because of the clustering in structure. Hence, even when smaller sources are not turned on, they are still likely ionized earlier than the under-dense regions. We note that one limitation to the above argument is that we currently only use the halo density field at $z_{\rm mid}$ to seed the ionized bubbles. If we instead use a redshift-dependent source field for abundance matching, we may find fewer $M > 10^{10}\, M_\odot$ sources at high redshifts, and so the ionizing bubbles could be more concentrated around larger peaks at the beginning of reionization. In Appendix 2.A, we discuss the effect of abundance matching at various redshifts, and show that at the spectrum

level the changes due to different abundance-matching redshifts is within 5%.

A more quantitative characterization of the difference in clustering is shown in the left and middle panels of Figure 2.12, where we plot the power spectrum of the halo density field and ionization fraction field at $\bar{x}_i = 25\%, 50\%$ and 75% for the two M_h values. From the halo density spectra shown on the left, we see that there is a constant rise in halo bias by a factor of ~ 3 on large scales, while on scales above $k = 1\,\mathrm{Mpc}^{-1}h$ the bias increases to > 10. The bias contrast in the ionization fraction field, however, is not as significant. On large scales ($k < 0.2\,\mathrm{Mpc}^{-1}h$), there is a constant increase of power in the $M_h = 10^{10}M_\odot$ field, but only by $< 5\%$. On smaller scales, the power of the $M_h = 10^{10}M_\odot$ ionization fraction field falls compared with the $M_h = 10^7 M_\odot$ field by $\sim 30\%$ near the end of reionization.

Now that we understand the effect of M_h on the ionization morphology, in the **left** panel of Figure 2.13, we show the dependency of D_ℓ^{pkSZ} on M_h, while keeping the reionization history fixed. We can see that out of all the parameters, M_h has the least effect on the patchy kSZ signal, as should be expected from the small changes in the ionization fraction power spectrum. Only when we limit the sources to be above $10^9\,M_\odot$ can we see a slight increase in the angular power at $\ell \sim 2000$ and suppression of the smaller scale power. This means that a very large M_h can still affect the morphology of ionized regions, even if we fix the reionization history. While for smaller M_h values, we do not see an effect on the kSZ spectra when we change M_h. Note that this is not generally true if we do not fix the reionization history, because M_h can affect the timing of reionization and thus the kSZ power.

Figure 2.13 includes a wide range of M_h from $10^7 M_\odot$ to $10^{10} M_\odot$. However, the change in D_ℓ^{pkSZ} is at most $0.15\mu K^2$ at the higher multipoles. This is in contrast to the result shown in Paul et al. [2021], who predicts a $30 \sim 60\%$ increase in $D_{\ell=3000}^{\mathrm{pkSZ}}$ with a fixed reionization history. This is likely due to the different assumptions we made in order to keep the reionization history fully controlled (in our case the abundance-matching scheme, and in their case, a manually-set ionizing efficiency at each time step). In the context of our model, we cannot gain many constraints from D_ℓ^{pkSZ} directly on the ionizing halos. We will need to infer such constraints with extra assumptions on astrophysical parameters that link the reionization history and M_h.

2.5.5 Radiation Mean Free Path

Finally, we study the mean free path parameter λ_{mfp} that controls on average how far ionizing photons travel in the IGM before being absorbed. Many previous works have empirically related the angular scale at which the patchy kSZ power spectrum reaches its maximum ℓ_{max} to the typical size of ionized regions during reionization [e.g. Gorce et al., 2020, Iliev et al., 2007, McQuinn et al., 2005, Mesinger et al., 2012]. Under the scenario described in Section 2.5.2, larger bubbles result in a larger mean free path, as photons travel through the ionized region without being absorbed. Therefore, the photon mean free path is strongly correlated with the average bubble size during reionization. The ionized bubble size determines the peak of the patchy kSZ spectrum, as we would expect the kSZ spectrum to attain the most power on the scale of the size of these bubbles.

In AMBER, *the mean free path parameter $\lambda_{\rm mfp}$ is not equivalent to the physical mean free path of photons measured in the IGM.* Firstly, our $\lambda_{\rm mfp}$ is defined at the midpoint of reionization, as opposed to the usual definition at the end of reionization. Secondly, $\lambda_{\rm mfp}$ does not directly control the size of the ionized regions at a fixed redshift. The sizes of ionized regions depend on the relative radiation intensity as well as the ionization fraction at a specific redshift. Hence, we can imagine that even with $\lambda_{\rm mfp} = 3\,{\rm Mpc}/h$, the sizes of ionized regions will be much smaller than that at $x_{\rm HII} = 0.05$. Finally, even though the $\lambda_{\rm mfp}$ is a global parameter, it does not mean that the ionized regions all have fixed sizes. Large halos will still have larger ionized regions around them, because the photon budget of a cell is affected by the density in addition to the mean free path parameter.

Similar to the previous section, we begin by visualizing the evolution of ionized regions throughout the EoR with various $\lambda_{\rm mfp}$. On the right two columns of Figure 2.11, we show the ionization fraction fields with $\lambda_{\rm mfp} = 1\,{\rm Mpc}/h$ and $\lambda_{\rm mfp} = 5\,{\rm Mpc}/h$. Compared to M_h, we see a larger contrast in the ionization morphology when varying $\lambda_{\rm mfp}$: there are more numerous and smaller ionized bubbles in the $\lambda_{\rm mfp} = 1\,{\rm Mpc}/h$ run than the $\lambda_{\rm mfp} = 5\,{\rm Mpc}/h$ run throughout the entire EoR.

On the right panel of Figure 2.12, we plot the power spectrum of the ionization fraction field at $\lambda_{\rm mfp} = 1\,{\rm Mpc}/h$ and $\lambda_{\rm mfp} = 5\,{\rm Mpc}/h$. As was expected from the 2D visualizations, the $\lambda_{\rm mfp} = 5\,{\rm Mpc}/h$ field has ~ 3 times more power on $k < 0.5\,{\rm Mpc}^{-1}h$ scales, and half of the power on small scales. The increase in $\lambda_{\rm mfp}$ induces an almost constant large-scale bias at all ionization levels. Compared to M_h, we see that increasing $\lambda_{\rm mfp}$ has a much stronger effect on the ionization morphology. Moreover, there is a shift in the peaking scale of $\Delta^2_{\rm ion}$ with $\lambda_{\rm mfp}$. To correlate the $\lambda_{\rm mfp}$ parameter with the typical sizes of ionized bubbles, we measure the $k_{\rm peak}$ value at which $\Delta^2_{\rm ion}$ peaks, and use $r_{\rm peak} = 2\pi/k_{\rm peak}$ to approximate the characteristic size of ionized bubbles. The vertical lines in Figure 2.12 mark the peaking bubble scales for the ionization fraction 50%. For $\lambda_{\rm mfp} = 1\,{\rm Mpc}/h$, the characteristic bubble size is $r_{\rm peak} = 8.3\,{\rm Mpc}/h$. $\lambda_{\rm mfp} = 5\,{\rm Mpc}/h$ corresponds to $r_{\rm peak} = 21.6\,{\rm Mpc}/h$. For more detailed correspondence between $\lambda_{\rm mfp}$ and $r_{\rm peak}$, please refer to the axes of Figure 2.15.

From the **right** panel of Figure 2.13, we see that when we increase the global mean free path of photons, the peak of the spectra is shifted towards the higher end of ℓ, corresponding to a larger angular scale subtended by the ionized bubbles. At our fiducial $\lambda_{\rm mfp} = 3.0\,{\rm Mpc}/h$, the spectra peaks at $\ell = 2300$. Our finding is consistent with previous works [e.g. Gorce et al., 2020], although our $\lambda_{\rm mfp}$ parameter is different from their characterization of the bubble sizes. We note that our current model has no spatial and temporal variation of $\lambda_{\rm mfp}$. In future works the halo mass and redshift dependence of $\lambda_{\rm mfp}$ will be studied. The details of where these spectra peak and how they shift with the mean free path will be studied later in Section 2.5.6.

2.5.6 Scaling of $D^{\rm pkSZ}_{\ell=3000}$ with Reionization Parameters

As was discussed in the previous sections, the amplitude of the kSZ spectrum is most sensitive to $z_{\rm mid}$ and Δ_z, the slope of the spectra is affected by A_z, and the peak of the kSZ spectrum

is most sensitive to $\lambda_{\rm mfp}$. Now we want to study more quantitatively the dependence of the amplitude and shape of the kSZ spectrum on reionization parameters. Note that for the scaling relation study, we always only change one parameter at a time, and keep the other parameters fixed at their fiducial values.

In Figure 2.14, we show the amplitude of kSZ at $\ell = 3000$ with different $z_{\rm mid}$ and Δ_z values, respectively. From both panels, $D^{\rm pkSZ}_{\ell=3000}$ scales almost linearly with the parameter values. For comparison, we also plotted the scaling relation fitted in Battaglia et al. [2013a] (Equation (10) in their paper). Note that in Battaglia et al. [2013a], the duration is defined to be $\Delta_{z,50}$, and the asymmetry parameter is not measured. For comparison with our Δ_z, we assume an asymmetry of $A_z = 3$ and use the Weibull function (Equation 2.10) to specify the reionization history at $\Delta_z = [2, 3, 4, 5, 6]$. Then, for each of these reionization histories, we measure the value of $\Delta_{z,50}$. Finally, we input these measured $\Delta_{z,50}$ values into the Battaglia et al. [2013a] fits together with a specified $z_{\rm mid}$ value to obtain the green lines.

Comparing with Battaglia et al. [2013a]'s power law index of 0.47 on the duration, our measured $D^{\rm pkSZ}_{\ell=3000}$ has a steeper dependence on Δ_z. This is consistent with the findings in Gorce et al. [2020], although we did not directly show their results as we have different $z_{\rm mid}$ values. One possible difference in the scaling is the asymmetrical nature of our reionization histories. As was shown in Figure 2.1, if the asymmetry of the reionization history is not fixed, the relation between $\Delta_{z,50}$ and $\Delta_{z,90}$ may not be linear. Thus Battaglia et al. [2013a]'s 0.47 power-law index could result from an increase in asymmetry with the duration under their model. Another possible explanation is that Battaglia et al. [2013a] does not independently control the mean-free path parameter, which degenerates with Δ_z at $\ell = 3000$. To demonstrate the effect of $\lambda_{\rm mfp}$ on the Δ_z dependency, on the right panel we show the $D^{\rm pkSZ}_{\ell=3000} - \Delta_z$ relation with $\lambda_{\rm mfp} = 1\,{\rm Mpc}/h$ and $\lambda_{\rm mfp} = 5\,{\rm Mpc}/h$. We see that $D^{\rm pkSZ}_{\ell=3000}$ actually peaks around $\lambda_{\rm mfp} = 3\,{\rm Mpc}/h$, and the values at $\lambda_{\rm mfp} = 1\,{\rm Mpc}/h$ and $\lambda_{\rm mfp} = 5\,{\rm Mpc}/h$ are both lower. In the Battaglia et al. [2013a] model, because there is a decrease in $\lambda_{\rm mfp}$ with increased duration [see e.g. Figure 9 of Battaglia et al., 2013b] since the large-scale bias parameter of the reionization redshift field is fixed [e.g. Trac et al., 2021], the $D^{\rm pkSZ}_{\ell=3000} - \Delta_z$ relation deviates from a linear relationship.

Next, we look at how the asymmetry of reionization and $\lambda_{\rm mfp}$ affect different aspects of the kSZ spectrum. In the top panel of Figure 2.15, we plot the difference between the amplitudes at two sets of multipoles as a function of A_z. We show $D_{\ell=2000} - D_{\ell=4000}$ which is close to the current measurement at $\ell = 3000$, and $D_{\ell=3000} - D_{\ell=8000}$ which requires an extra measurement at a relatively high $\ell = 8000$. As we have discussed in Section 2.5.3, the spectra get flatter as asymmetry rises, and so $\Delta D^{\rm pkSZ}_\ell$ falls with larger A_z. The difference between $D_{\ell=3000}$ and $D_{\ell=8000}$ is larger at all A_z values, but the constraining power on A_z is simular between the two sets of ΔD_ℓs. To distinguish between two asymmetry values such as $A_z = 1$ and $A_z = 8$, we need to be able to measure either $D_{\ell=2000} - D_{\ell=4000}$ or $D_{\ell=3000} - D_{\ell=8000}$ at $\sim 0.3\,\mu k^2$ accuracy. Previously, Gorce et al. [2020] argued that focusing on $D_{\ell=3000}$ is not sufficient to characterize the kSZ signal, especially with various reionization scenarios that lead to asymmetric reionization histories. Our result further supports this argument by showing a quantitative scaling between the slope of the kSZ power and the asymmetry of

reionization.

In the bottom panel of Figure 2.15 we plot the location of the kSZ power spectrum peaks as a function of $\lambda_{\rm mfp}$. From the plot we see that $\ell_{\rm max}$ scales as $1/\lambda_{\rm mfp}$. This is expected as $\lambda_{\rm mfp}$ is correlated with the size of ionized regions, and is in general agreement with Figure 9 in Gorce et al. [2020]. To establish a correspondence between our effective mean-free path parameter and the typical ionized bubble sizes at $z_{\rm mid}$, on the top axis we label the peaking scale of the ionizing fraction power spectrum (i.e. the right panel of Figure 2.12). At our fiducial $\lambda_{\rm mfp} = 3\,{\rm Mpc}/h$, the typical bubble size is $14.4\,{\rm Mpc}/h$ (comoving) at $z = 8$.

We note that for all the scaling relations shown in this section, we have always fixed all the other reionization parameters and varied one at a time. This means that all the relations are conditioned, and so one should take caution when using such scaling relations directly to perform parameter constraints.

2.5.7 Cosmological Parameters

The process of reionization involves a complicated interplay between cosmology and astrophysical parameters, a large fraction of which remains highly uncertain. For instance, a larger σ_8 could lead to earlier onset of reionization, provided that the nature of the ionizing sources and the photon escape fraction is fixed. However, there is a lack of comprehensive study on how different cosmologies affect the astrophysics of reionization. In AMBER, the reionization history and cosmology are modeled independently. This circumvents the complicated treatment and unknown relation between the two, and allows us to separately analyze the effect of cosmology on the patchy kSZ signal. In this section, we study the change in the kSZ power spectra when we change two cosmological parameters $\Omega_{\rm m}$ and σ_8.

In Figure 2.16, we show the change in the patchy kSZ spectra when we vary Ω_m and σ_8. From the left panel, we can see that $D_\ell^{\rm pkSZ}$ is only weakly sensitive to the change in Ω_m, especially at $\ell = 3000$. Larger Ω_m leads to slightly higher amplitude on $\ell < 2000$ scales. On the right panel, σ_8 has more direct effects on the amplitude of the kSZ spectrum: the kSZ power doubles when we change σ_8 from 0.74 to 0.86. Such effect comes from two different sources. Firstly, in linear theory, both the density and velocity fluctuations scale as σ_8^2. Since the kSZ effect measures the momentum fluctuations, we should expect $\sim \sigma_8^4$ contribution from the change in the matter density and velocity fields [also see e.g. Shaw et al., 2012, Trac et al., 2011]. Secondly, the change in density contrast and clustering can also influence the reionization redshift field through the radiation intensity. Hence, a change in σ_8 will also affect the morphology of ionized regions at different redshifts. By comparing with the effects of reionization parameters in Figure 2.10 and 2.13, we see that there are degeneracies between σ_8, Δ_z, $z_{\rm mid}$ and $\lambda_{\rm mfp}$ in terms of $D_{\ell=3000}^{\rm pkSZ}$.

Compared with reionization parameters such as $z_{\rm mid}$ and Δz which only affect the patchy kSZ and τ_e through the reionization redshifts, cosmological parameters change the signals through both the density/velocity fields and the reionization redshift field (which is also correlated with the change in the density). For example, when we change σ_8 from 0.8 to 0.7, the decrease in the matter power spectrum will in itself decrease $P_{ee}(k)$, even when the

reionization redshift and morphology is fixed. On the other hand, decreasing the amplitude of the matter power spectrum also results in a different reionization redshift field, as the number of large ionizing sources decreases at the midpoint of reionization. In order to disentangle the change due to matter density from the change due to the reionization redshift field when varying σ_8, we show in Figure 2.17 the change in $P_{ee}(k,z)$ purely from $z_{\rm re}$, compared with the total change, at different ionization levels. Here we compare the ratio between $P_{ee}(k,z)$ at $\sigma_8 = 0.74$ with $P_{ee}(k,z)$ at the fiducial $\sigma_8 = 0.8$. For the dashed curve, we simply change the value of σ_8 in the code, so that both the gas density and the reionization redshift fields are affected. For the solid curve, we use $\sigma_8 = 0.74$ to generate the reionization redshift field, while the matter overdensity is kept at $\sigma_8 = 0.8$. By comparing the dashed curves at different ionization levels, we see that as the ionization level $\bar{x}_i$ raises, the ratio between the two P_{ee}'s drops on all scales. Noticeably, only near the end of reionization at $\bar{x}_i = 0.95$ does the $P_{\rm ee}$ ratio approach the expected matter power spectrum ratio of 0.85 on large scales. At higher ionization levels, the effect of the matter density field is subdominant, especially on large scales, where $> 95\%$ of power is retained. On small scales ($k > 1\,{\rm Mpc}/h$), however, the power drops significantly. By comparing with the solid curves where only $z_{\rm re}$ varies, we can see that the suppression on small scales still comes from the change in δ_m instead of $z_{\rm re}$, as the suppression in the solid curves are not as significant. Therefore, we conclude that changing σ_8 mostly affects P_{ee} near the end of reionization. Before the end of reionization, the change in $z_{\rm re}$ has a dominant effect over δ_m on large scales and only mildly affects P_{ee}. On small scales, P_{ee} is mainly affected by the matter density and varies more significantly with σ_8.

2.6 Conclusion

In this work, we use the new semi-numerical code for reionization AMBER to study the patchy kSZ effect under different reionization scenarios. We calibrate and test the AMBER predictions against the radiative-transfer RadHydro simulation suite [Doussot et al., 2019]. We find that at our target resolution of $1\,{\rm Mpc}/h$, AMBER produces electron number density field and kSZ angular power spectra that resemble those from RadHydro at all redshifts.

AMBER explicitly parametrizes the reionization history by the midpoint redshift, duration, and asymmetry parameters. By varying the midpoint redshift of reionization, we find that the range $z_{\rm mid} = [6.0, 8.9]$ has Thomson optical depth values consistent with the Planck Collaboration et al. [2018] measurements at the 2σ level. We also find that the peaking scale of the kSZ angular power spectrum is not sensitive to the midpoint redshift.

Then, assuming a value of $z_{\rm mid} = 8.0$ consistent with the Planck measurement, and fixing the other parameters at their fiducial values, we find that the amplitude of $D_\ell^{\rm pkSZ}$ at $\ell = 3000$ scales linearly with the duration of reionization Δ_z. The resulting $D_{\ell=3000}^{\rm pkSZ}$ values are consistent with the 1σ measurement from Reichardt et al. [2021] up to $\Delta_z < 5.1$ (Δ_z here encloses redshifts from 5% to 95% reionization). This translates to $\Delta_{z,50} < 2.0$ under the definition of duration in Battaglia et al. [2013b], assuming a mildly asymmetric reionization

history at $A_z = 3$. Then, allowing for other reionization parameters to vary simultaneously, we find that $\Delta_z < 12.8$ is the maximum duration consistent with the Reichardt et al. [2021] estimation at the 2σ level ($\Delta_{z,50} < 3.5$ assuming $A_z = 8$). Note that this extreme scenario requires a high asymmetry of the reionization hitory of $A_z > 8$, in order for reionization to end before $z = 5.5$. This is in broad agreement with the constraint from Reichardt et al. [2021] of $\Delta_{z,50} < 5.4$ (95% CL) using the Battaglia et al. [2013a] model, and the constraint by Choudhury et al. [2021] at $\Delta_{z,50} < 2.9$ (99% CL) using a different semi-numerical model.

Then, by considering reionization histories with different degrees of asymmetry, we find that the kSZ amplitude at $\ell = 3000$ is not sensitive to the detailed shape of reionization history beyond redshift and duration. However, the slope of the kSZ angular power spectrum does depend on the asymmetry. This is in line with the results shown in [e.g. Gorce et al., 2020, Park et al., 2013], and makes constraints on the beginning and end of reionization through patchy kSZ possible if measurements are made at different multipoles. Nevertheless, we find that constraints on the asymmetry require $\sim 0.1\,\mu k^2$ measurement accuracy of the patchy kSZ power spectrum at various multipoles other than $\ell = 3000$.

We also independently control the size of sources through the minimum halo mass (M_h), and the relative radiation intensity through the effective mean free path ($\lambda_{\rm mfp}$). With a fixed reionization history, the minimum halo mass has little effect on the ionization morphology at a fixed redshift. Therefore, the amplitude and shape of the kSZ spectrum are only mildly affected by the minimum halo mass M_h. This is in contrast to the results shown in Paul et al. [2021], and thus a more detailed investigation of which assumptions in our models lead to the differences is needed. The effective photon mean-free path affects the peaking location of the kSZ power spectrum, and at our fiducial $\lambda_{\rm mfp} = 3\,{\rm Mpc}/h$ (fitted to the RadHydro simulations), the spectrum peaks at $\ell \approx 2100$. Moreover, we explicitly showed that there is a degeneracy between the mean free path $\lambda_{\rm mfp}$ and the duration of reionization in terms of $D_\ell^{\rm pkSZ}$ at $\ell = 3000$. A shorter $\lambda_{\rm mfp}$ can lead to a $\sim 10\%$ lower $D_{\ell=3000}^{\rm pkSZ}$ and a flatter slope in the $D_{\ell=3000}^{\rm pkSZ} - \Delta_z$ scaling relation. This partly explains the steeper power-law scaling relationship we get compared with Battaglia et al. [2013a], as the ionized bubble sizes in their model decrease with a longer duration.

Finally, we study the effect of cosmological parameters Ω_m and σ_8 on the patchy kSZ power spectrum under fixed reionization parameters. We find that with a fixed reionization history, the kSZ power spectrum does not have noticeable change with Ω_m, especially near $\ell = 3000$. However, σ_8 affects the overall amplitude of the kSZ power spectrum, which results in a degeneracy between σ_8 and Δ_z. On large scales ($k < 1\,{\rm Mpc}^{-1}h$), σ_8 affects the electron number density mainly through the $z_{\rm re}$ field, while on small scales ($k < 1\,{\rm Mpc}^{-1}h$), the effect comes from the matter density field.

Even though we have given a rough estimate of the duration of reionization consistent with current observations from ground-based telescopes, such constraints are only a first-order estimation because we only search a 1D parameter space at a time. To carry out the analysis properly, we need to take into account the correlation between different parameters by marginalizing over other model parameters. In order to achieve that, we will need a tool to estimate the kSZ spectra faster than what we can achieve with our simulations.

Moreover, in order to separate out the patchy component from the spectrum, one would need a good description of the homogeneous spectrum. Currently, the homogeneous spectrum quoted in Reichardt et al. [2021] comes from Shaw et al. [2012], but we can use results updated with more recent simulations [e.g. He et al., 2021] to get a better estimation of how accurately one can recover the patchy signal.

2.A Effect of Abundance Matching at the Midpoint Redshift

In Section 2.3.1, we mentioned that currently in AMBER, the reionization redshift field is abundance-matched against the radiation intensity at a single redshift $z_{\rm mid}$ for computation efficiency. However, we do note that due to the non-linear growth of structure and especially the non-linearity in the halo density field, this choice can cause uncertainties in the EoR observables. To make the model more physical, we will work towards a tomographic abundance-matching scheme, where the reionization redshift is determined by the source field at several redshifts spanning the EoR. Since this work is based on the single-redshift abundance matching, here we characterize the level of uncertainties induced by the choice the abundance-matching redshift $z_{\rm match}$.

We keep all parameters at their fiducial values unless otherwise stated (in particular we always fix $z_{\rm mid} = 8$), and we change the redshift at which we generate the source field for matching $z_{\rm re}(\mathbf{x})$. Here we have chosen two relatively extreme values: at $z = 10$, $x_{\rm HII} \approx 0.1$ and reionization has just started; at $z = 6.5$, $x_{\rm HII} \approx 0.95$ and we are approaching the end of EoR. We note that for single-redshift abundance matching, $z_{\rm match} = z_{\rm mid}$ is still a better choice than the others. At higher redshifts, the sources are scarce and so the resulting $z_{\rm re}(\mathbf{x})$ can be noisier. The sources at lower redshifts are more abundant, but they are not the main driver of reionization since the EoR has almost finished by then. Hence, the $z_{\rm mid}$ halos are a better representation of the sources that are responsible for driving the ionization process. Here by showing the $z_{\rm match}$ at extreme values, we aim to bracket the range of uncertainty caused by the single-redshift abundance matching.

In Figure 2.A.1, we show the (dimensionless) free-electron number density power spectra Δ^2_{ee} with $z_{\rm re}(\mathbf{x})$ matched against the radiation field at $z_{\rm match} = 6.5$, $z_{\rm match} = 8$ (which is the $z_{\rm mid}$) and $z_{\rm match} = 10$. Compared with the original choice of $z_{\rm match} = 8$, using the source field at $z_{\rm match} = 10$ increases the power on most scales by a constant factor of $< 5\%$ except at the beginning of reionization, and there is a larger difference on small scales compared to large scales. Using the reionization redshift matched at a later time ($z_{\rm match} = 6.5$) decrease Δ^2_{ee} by $< 5\%$.

Figure 2.A.2 shows the effect of changing $z_{\rm match}$ on the patchy kSZ power spectra. At our fiducial set of reionization parameters (see Table **??**), using $z_{\rm match} = 10$ increases the kSZ power at $\ell > 1000$ by an almost-constant factor of 5%, while using $z_{\rm match} = 6.5$ decreases the power by a similar fraction (shown by the solid curves on both the top and bottom plots). To further investigate the potentially larger influence of $z_{\rm match}$ on highly asymmetric

reionization scenarios, we also show on the top panel the difference between three $z_{\rm match}$ at $A_z = 8$ (without changing the midpoint or the duration). We see that for a larger A_z, the change in D_ℓ is indeed larger, but the overall fluctuation is still kept within $\sim 7\%$ on all scales of interest. On the bottom panel of Figure 2.A.2, we show the effect of various $z_{\rm match}$ with larger sources at $M_h = 10^{10}\,M_\odot$. A higher source threshold is expected to enlarge the effect of varying $z_{\rm match}$, as the halo mass function increases more with redshift at the high-mass end. Indeed, we can see that with $M_h = 10^{10}\,M_\odot$, the deviation of $z_{\rm match} = 10$ and $z_{\rm match} = 6.5$ from $z_{\rm match} = 8$ reaches a maximum of $\sim 15\%$ at $\ell = 500 - 1000$. Nonetheless, on the scale of interest for the patchy kSZ measurement ($\ell \gtrapprox 2000$), effect of $z_{\rm match}$ is still kept within 5%. Hence, we conclude with our investigations that changing the redshift at which we match the reionization redshift field does have an impact at the observable level, but on the scale of interest this impact is within $\sim 5\%$.

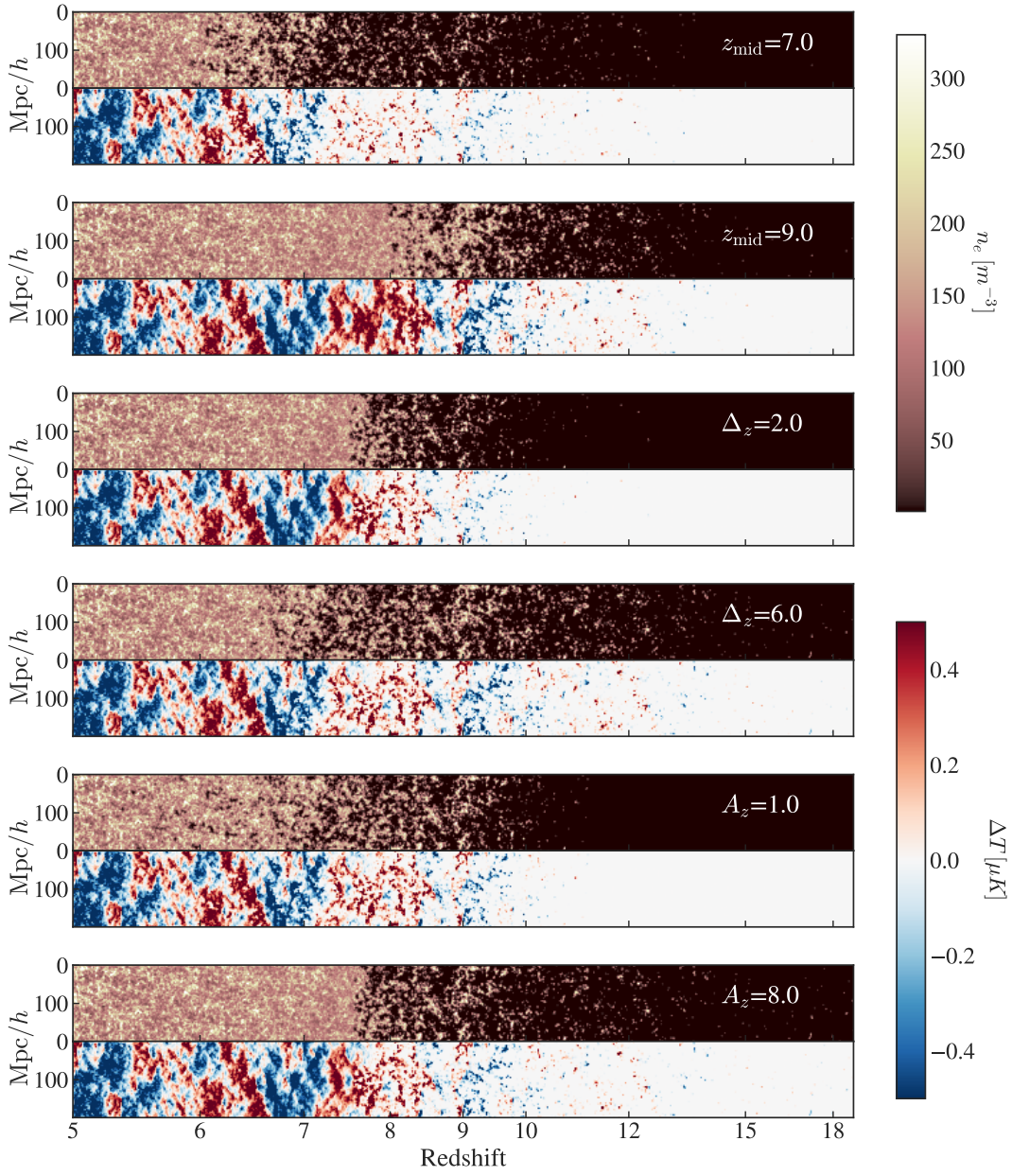

Figure 2.8: Visualization of the redshift evolution of n_e (*dark background*) and $\Delta T_{\rm kSZ}$ (*white background*). ***Row 1/2:*** we vary the midpoint of reionzation from $z_{\rm mid} = 7.0$ to $z_{\rm mid} = 9.0$, while keeping other parameters at their fiducial values. ***Row 3/4:*** we vary the duration of reionzation from $\Delta_z = 2.0$ to $\Delta_z = 6.0$. We can see the large-scale velocity coherence across redshifts. With a longer duration, there is more ionizing bubbles stacked along the line-of-sight. ***Row 5/6:*** we vary the asymmetry of reionzation history from $A_z = 1.0$ to $A_z = 8.0$. With a larger A_z, ionizing bubbles begin to form as early as $z = 18$, although $z_{\rm mid}$ and Δ_z is kept fixed.

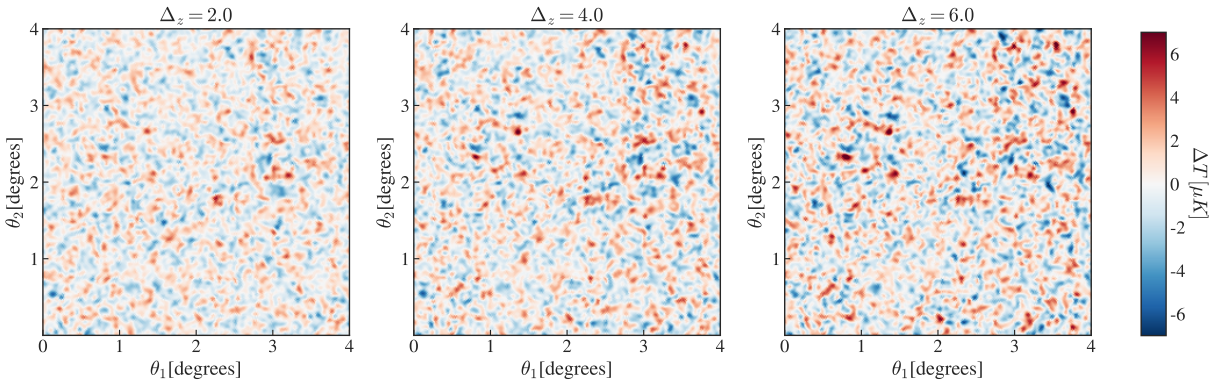

Figure 2.9: 4×4 degree^2 maps of the kSZ temperature fluctuation for different durations of reionization. This is a filtered map with only the small-scale ($\ell > 1000$) modes to show the effect of patchy reionization rather than the large-scale velocity fluctuation. A longer duration ($\Delta_z = 6$, *right*) leads to larger fluctuations on small scales, while the map with a shorter duration appears smoother. This is because the small-scale kSZ is sourced by the electron number density fluctuation from patchy reionization. These fluctuations are incoherent and accumulate along the line of sight, leading to a larger small-scale inhomogeneity for a longer duration.

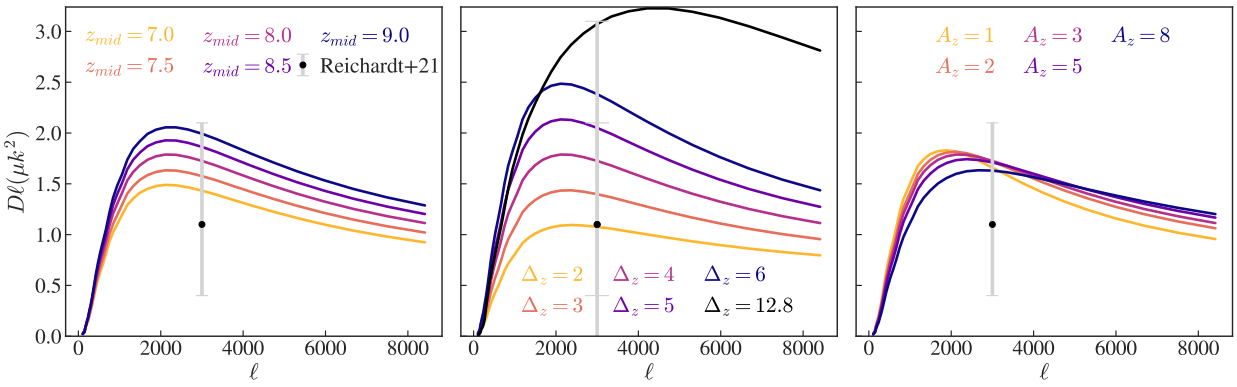

Figure 2.10: Patchy kSZ angular power spectrum for different reionization history parameters. The fiducial parameters are $[z_{\rm mid}, \Delta_z, A_z] = [8.0, 4.0, 3.0]$. The smaller error bars show the 1σ confidence interval of $D^{\rm kSZ}_{\ell=3000}$ from Reichardt et al. [2021], and the larger error bar in the middle panel shows the 2σ confidence interval. ***Left:*** The overall amplitude of the kSZ spectrum increases as we shift the midpoint redshift of reionization earlier, but all variations are consistent with the 1σ interval. ***Middle:*** Increasing the duration of reionization also increases the overall power of the kSZ spectrum, and it affects the kSZ amplitude most significantly. The black line shows the maximum Δ_z that produces $D^{\rm kSZ}_{\ell=3000}$ within the 2σ interval, where we let $z_{\rm mid} = 6.5$, $A_z = 8$ (to ensure reionization ended before $z = 5.5$), and $\lambda_{\rm mfp} = 1.0\,{\rm Mpc}/h$. ***Right:*** The asymmetry parameter A_z does not have a big impact on the kSZ spectrum comparing with the midpoint and duration, but we can see that increasing the asymmetry (meaning that the beginning of reionization is longer) results in flatter slope of the kSZ spectrum.

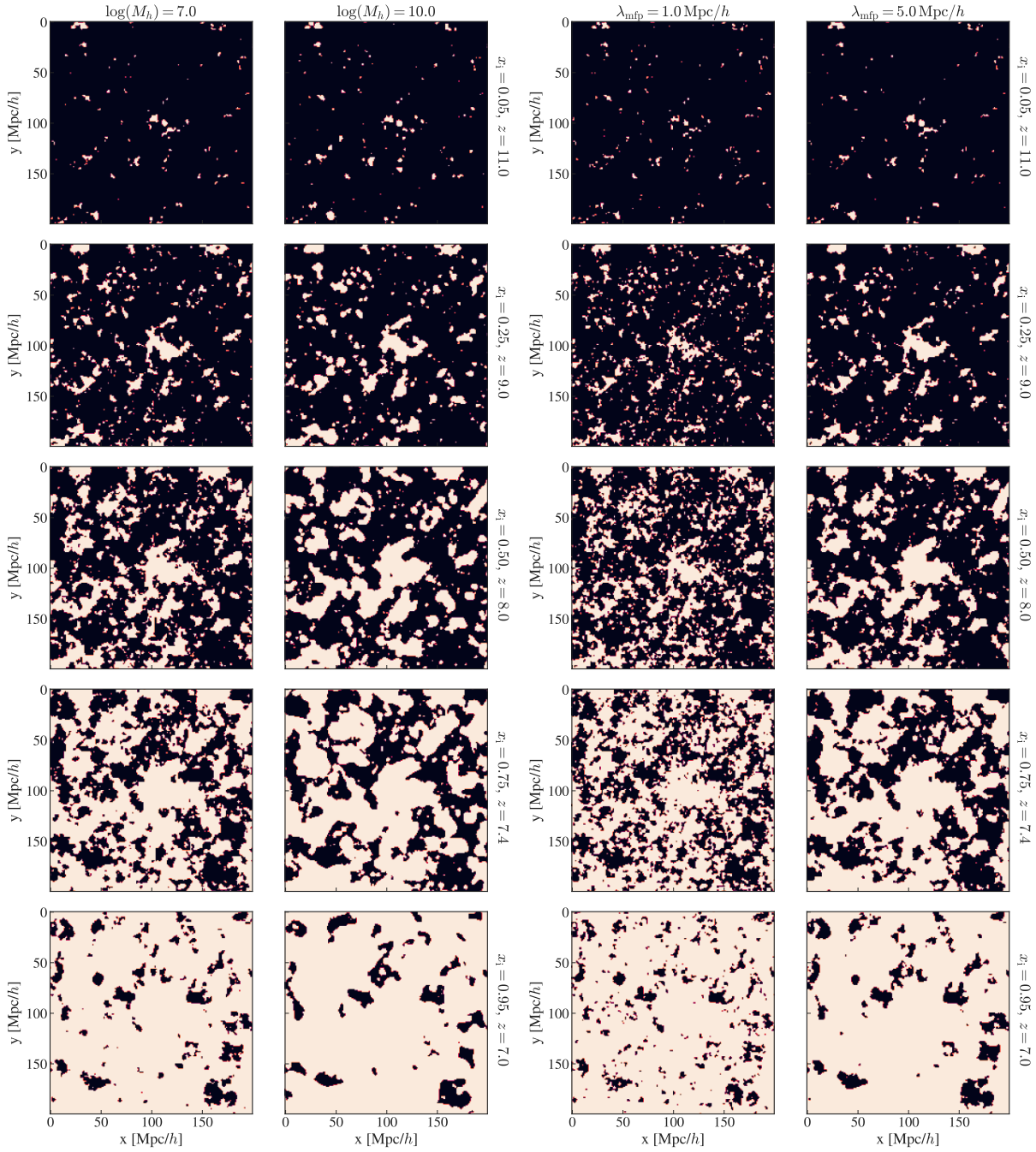

Figure 2.11: Ionization fraction field across different (mass-weighted) ionization levels, with white regions marking the ionized bubbles. From top to bottom with show a $(200\,\mathrm{Mpc}/h)^2 \times 1\,\mathrm{Mpc}/h$ slice at $\bar{x}_i = 5\%$, 25%, 50%, 75%, and 95% , respectively. ***Left:*** ionized regions with a minimum halo mass of $10^7\,M_\odot$ (*first column*) and $10^{10}\,M_\odot$ (*second column*). With very large minimum halo mass for ionizing galaxies, the ionized bubbles are smoother and more clustered on large scales. However, the overall morphology are not drastically different from when $M_\mathrm{h} = 10^7 M_\odot$. ***Right:*** ionized regions with $\lambda_\mathrm{mfp} = 1.0\,\mathrm{Mpc}/h$ (*third column*) and $\lambda_\mathrm{mfp} = 5.0\,\mathrm{Mpc}/h$ (*fourth column*). We see that in AMBER, with a fixed reionization history, λ_mfp has a stronger effect on the ionization morphology than the minimum halo mass M_h. With a smaller λ_mfp, the typical sizes of ionized regions are significantly smaller than with a larger λ_mfp.

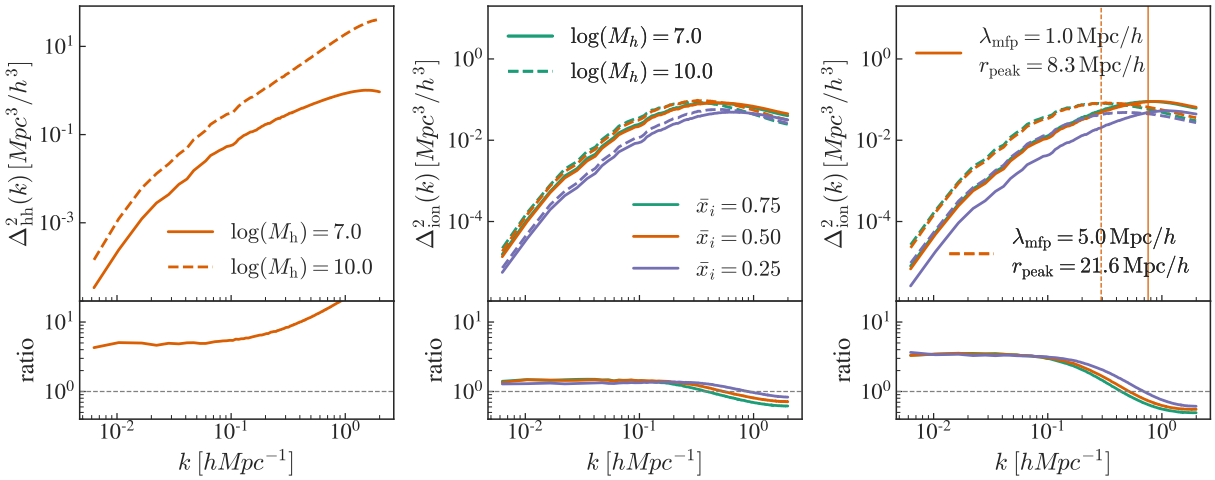

Figure 2.12: Dimensionless power spectra of the AMBER halo density fields (*left*) and ionization fraction fields (*middle and right*) with different minimum halo mass and photon mean free path. For the ionization fraction power spectra we show the spectra at three global ionization levels ($\bar{x}_i = 0.25, 0.50, 0.75$, corresponding to the *purple, orange* and *green* lines, respectively). ***Left:*** dimensionless halo density power spectra for $M_h = 10^7\,M_\odot$ (*solid*) and $M_h = 10^{10}\,M_\odot$ (*dashed*). ***Middle:*** $\Delta^2_{\rm ion}(k)$ for $M_h = 10^7\,M_\odot$ (*solid*) and $M_h = 10^{10}\,M_\odot$ (*dashed*). ***Right:*** $\Delta^2_{\rm ion}(k)$ for $\lambda_{\rm mfp} = 1.0\,{\rm Mpc}/h$ (*solid*) and $\lambda_{\rm mfp} = 5.0\,{\rm Mpc}/h$ (*dashed*). The bottom panels show the ratio of the power spectra, with the ratio being $P_{\rm ion,log(M)=10.0}/P_{\rm ion,log(M)=7.0}$ in the left/middle panels and $P_{\rm ion,\lambda=5}/P_{\rm ion,\lambda=1}$ on the right.

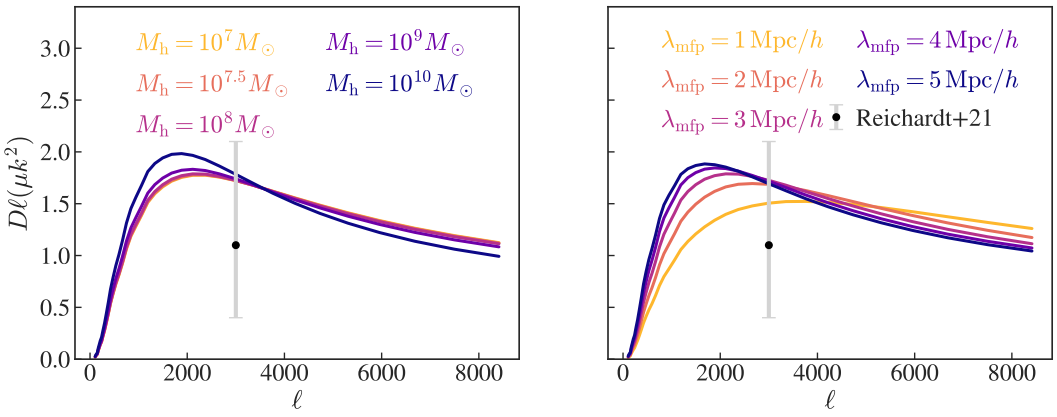

Figure 2.13: ***Left:*** Out of all the parameters, M_h has the least effect on the patchy kSZ signal. Only when we limit the sources to be above $10^9\,M_\odot$ can we see some suppression on the small scale power. ***Right:*** $\lambda_{\rm mfp}$ is correlated with the average bubble size of ionized bubbles. Increasing the mean free path shifts the peak towards higher multipoles in the kSZ spectrum.

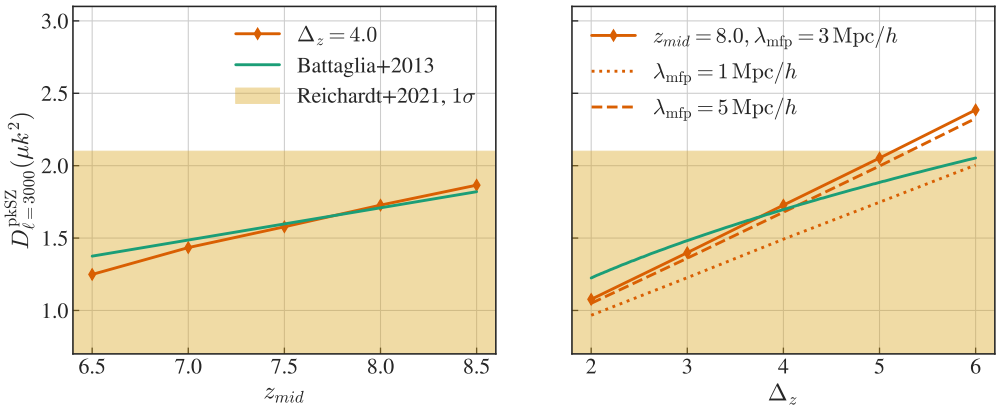

Figure 2.14: Relationship between the amplitude of the kSZ angular power spectra $D_\ell^{\rm pkSZ}$ at $\ell = 3000$ and the redshift and duration of reionization. The yellow regions are the 1σ constraint from Reichardt et al. [2021]. ***Left:*** with a fixed duration $\Delta_z = 4.0$, AMBER produces $D_{\ell=3000}^{\rm pkSZ}$ that scales almost linearly with the midpoint redshift of reioziation (*orange*). Compared with the scaling relation fitted in Battaglia et al. [2013a] (*green*), we have a slightly steeper slope. ***Right:*** when we fix $z_{\rm mid} = 8.0$, $D_{\ell=3000}^{\rm pkSZ}$ also scales linearly with the duration of reionization. Compared with Battaglia et al. [2013a] who found a power-law dependence of ~ 0.47, we find a steeper dependence of $D_{\ell=3000}^{\rm pkSZ}$ on Δ_z. We also show the relation at $\lambda_{\rm mfp} = 1\,{\rm Mpc}/h$ (*dotted orange*) and $\lambda_{\rm mfp} = 5\,{\rm Mpc}/h$ (*dashed orange*), in order to demonstrate the dependence of the scaling relation on $\lambda_{\rm mfp}$.

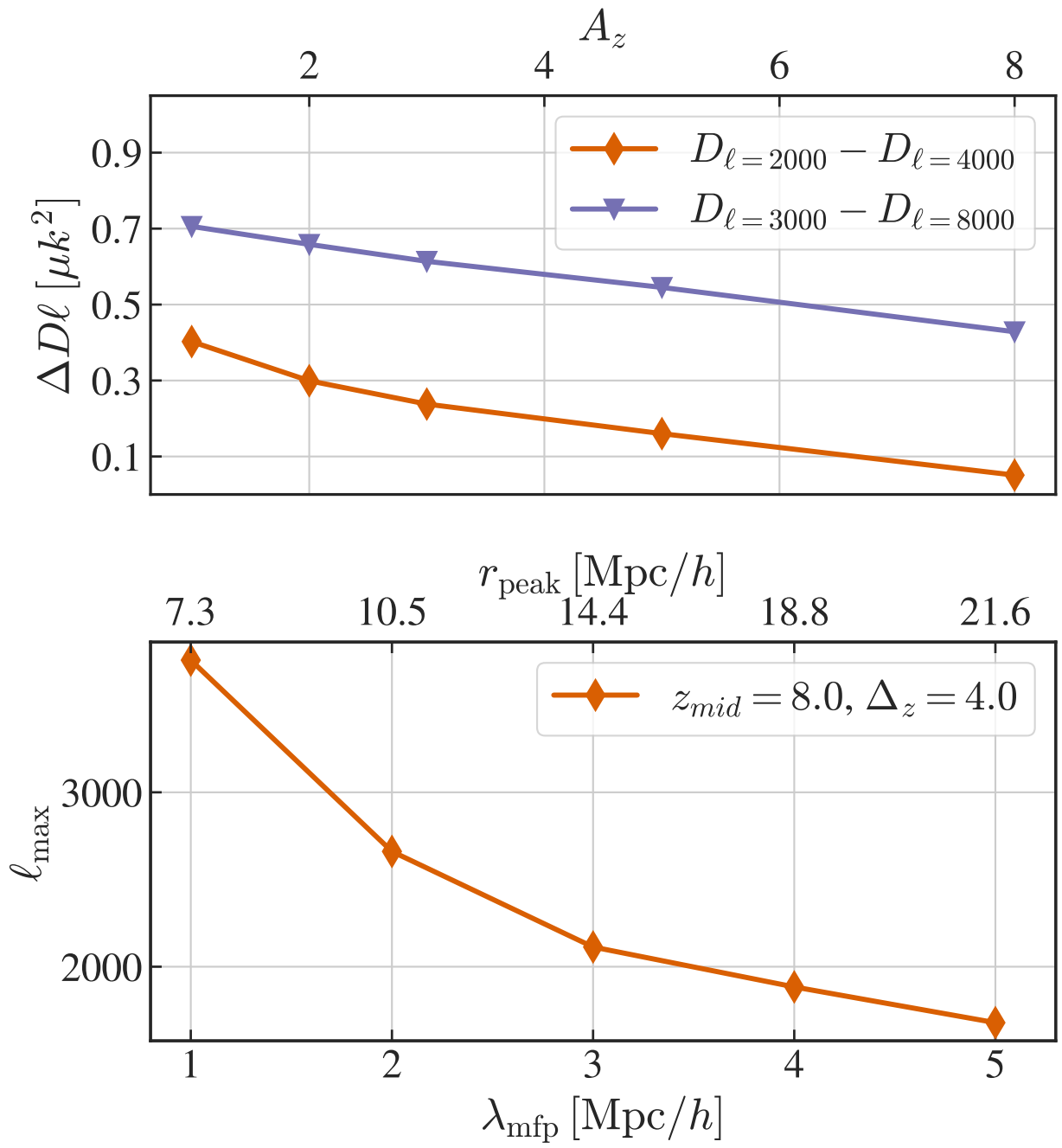

Figure 2.15: ***Top:*** Change in the slope of the kSZ power spectrum with the asymmetry of reionization history A_z. **Here we show the difference between two sets of ℓ values: $D_{\ell=2000} - D_{\ell=4000}$ (*orange*) which is close to the current measurement at $\ell = 3000$, and $D_{\ell=3000} - D_{\ell=8000}$ (*purple*) which requires an extra measurement at a relatively high ℓ.** ***Bottom:*** Shift in the peak of kSZ spectrum with the mean free path parameter $\lambda_{\rm mfp}$ (*bottom axis*) and the mean bubble sizes (*top axis*).

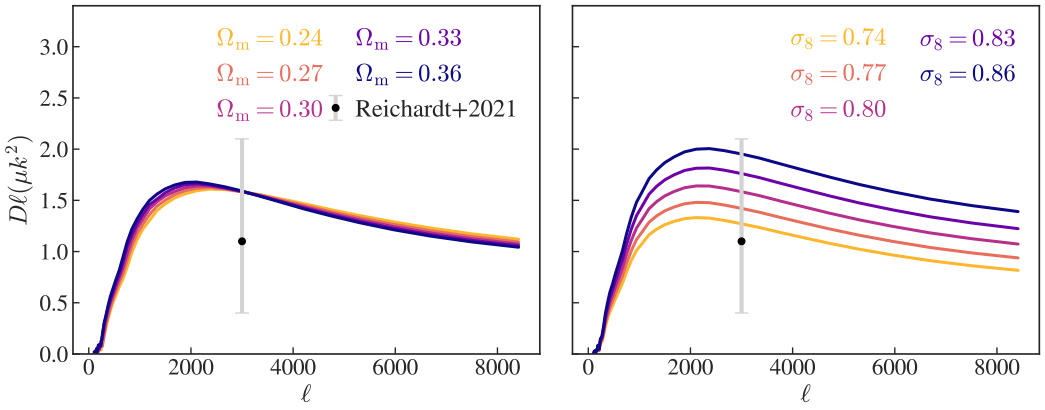

Figure 2.16: Patchy kSZ angular power spectrum with the same reionization history but different cosmological parameters (Ω_m and σ_8). While there is complete degeneracy between different Ω_m values at $\ell = 3000$, σ_8 affects the kSZ amplitude on all scales.

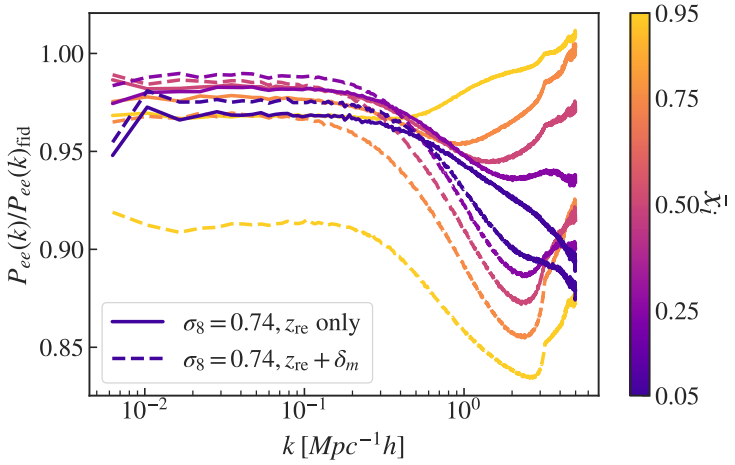

Figure 2.17: The ratio between the electron number density power spectra $P_{ee}(k)$ at $\sigma_8 = 0.74$ and $\sigma_8 = 0.8$ (the fiducial value). The the solid curves are generated by changing only the reionization redshift field $z_{\rm re}$ to $\sigma_8 = 0.74$, while the dashed curves are generated by changing both $z_{\rm re}$ and the matter density field δ_m. The different colors represent the spectra at different ionization levels.

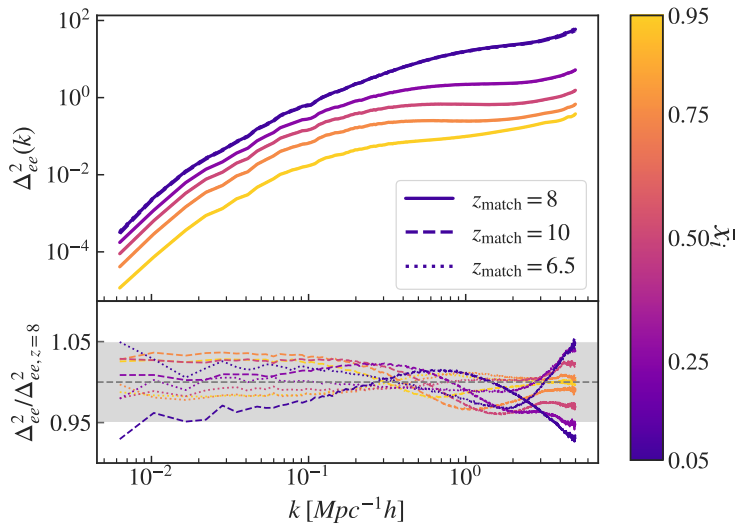

Figure 2.A.1: The free-electron number density power spectra at different stages of reionization, calculate with reionization redshift fields matched at $z_{\rm match} = 8$ (*solid*), $z_{\rm match} = 10$ (*dashed*), and $z_{\rm match} = 6.5$ (*dotted*). The bottom panel shows the ratio between the $\Delta^2_{\rm ee}$ at $z_{\rm match} = 10$ ($z_{\rm match} = 6.5$) and that at the fiducial $z_{\rm match} = z_{\rm mid} = 8$.

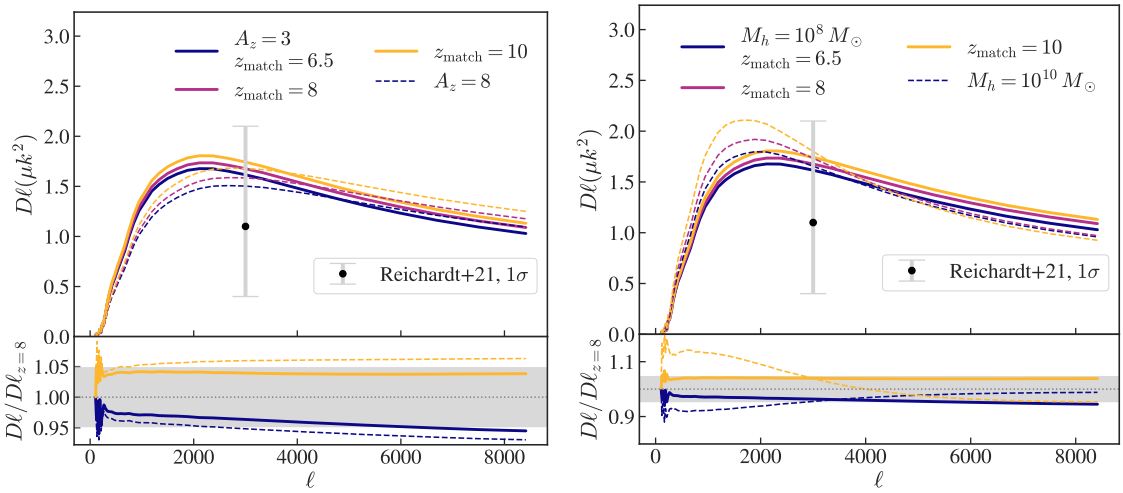

Figure 2.A.2: The patchy kSZ power spectra calculated with the reionization redshift field abundance-matched at different points across the reionization history. Here we have always assumed the fiducial $z_{\rm mid} = 8$ and $\Delta_z = 4$, but the z_{re} fields are abundance-matched against the radiation field at $z_{\rm match} = 6.5$ (*dark blue*), $z_{\rm match} = 8$ (*purple*), and $z_{\rm match} = 10$ (*yellow*). ***Top:*** The effect of $z_{\rm match}$ at the fiducial $A_z = 3$ as well as a larger asymmetry of $A_z = 8$. ***Bottom:*** The effect of $z_{\rm match}$ at the fiducial $M_h = 10^8\,M_\odot$ and a larger source threshold of $M_h = 10^{10}\,M_\odot$.

Chapter 3

Dynamical Friction Modeling of Massive Black Holes in Cosmological Simulations and Effects on Merger Rate Predictions

Nianyi Chen,[1] Yueying Ni,[1] Michael Tremmel,[2] Tiziana Di Matteo,[1,3,4] Simeon Bird, [5] Colin DeGraf,[1] Yu Feng [6]

[1]McWilliams Center for Cosmology, Department of Physics, Carnegie Mellon University, Pittsburgh, PA 15213, USA
[2]Astronomy Department, Yale University, P.O. Box 208120, New Haven, CT 06520, USA
[3]NSF AI Planning Institute for Physics of the Future, Carnegie Mellon University, Pittsburgh, PA 15213, USA
[4] OzGrav-Melbourne, Australian Research Council Centre of Excellence for Gravitational Wave Discovery
[5] Department of Physics and Astronomy, University of California Riverside, Riverside, CA 90217, USA
[6]Berkeley Center for Cosmological Physics and Department of Physics, University of California, Berkeley, CA 94720, USA

Abstract

In this work we establish and test methods for implementing dynamical friction for massive black hole pairs that form in large volume cosmological hydrodynamical simulations which include galaxy formation and black hole growth. We verify our models and parameters both for individual black hole dynamics and for the black hole population in cosmological volumes. Using our model of dynamical friction (DF) from collisionless particles, black holes can effectively sink close to the galaxy center, provided that the black hole's dynamical mass is at least twice that of the lowest mass resolution particles in the simulation. Gas drag also plays a role in assisting the black holes' orbital decay, but it is typically less effective than that from collisionless particles, especially after the first billion years of the black hole's

evolution. DF from gas becomes less than 1% of DF from collisionless particles for BH masses $> 10^7$ $M_\odot$. Using our best DF model, we calculate the merger rate down to $z = 1.1$ using an $L_{\rm box} = 35$ Mpc/h simulation box. We predict ~ 2 mergers per year for $z > 1.1$ peaking at $z \sim 2$. These merger rates are within the range obtained in previous work using similar-resolution hydro-dynamical simulations. We show that the rate is enhanced by factor of ~ 2 when DF is taken into account in the simulations compared to the no-DF run. This is due to $> 40\%$ more black holes reaching the center of their host halo when DF is added.

3.1 Introduction

Super Massive Black Holes (SMBHs) are known to exist at the center of the majority of massive galaxies [e.g. Kormendy and Ho, 2013, Kormendy and Richstone, 1995, Magorrian et al., 1998, Soltan, 1982]. As these galaxies merge [e.g. Lacey and Cole, 1993, Lotz et al., 2011, Rodriguez-Gomez et al., 2015], the SMBHs that they host also go through mergers, resulting in the mass growth of the SMBH population [e.g. Begelman et al., 1980]. SMBH mergers following their host galaxy mergers become an increasingly important aspect of SMBH growth for more massive black holes (BHs) in dense environments [e.g. Kulier et al., 2015]. As a by-product of BH mergers, gravitational waves are emitted, and their detection opens up a new channel for probing the formation and evolution of early BHs in the universe [e.g. Barausse, 2012, Sesana et al., 2007b].

The gravitational wave detection by LIGO [Abbott et al., 2016] proves the experimental feasibility of using gravitational waves for studying BH binaries. While LIGO cannot detect gravitational waves from binaries more massive than $\sim 100 M_\odot$ [Mangiagli et al., 2019], long-baseline experiments are being planned for detections of more massive BH binaries. Specifically, the upcoming Laser Interferometer Space Antenna (LISA) [Amaro-Seoane et al., 2017] mission will be sensitive to low-frequency ($10^{-4} - 10^{-1}$Hz) gravitational waves from the coalescence of massive black holes (MBHs) with masses $10^4 - 10^7 M_\odot$ up to $z \sim 20$. At even lower frequencies Pulsar Timing Arrays (PTAs) are already collecting data and the Square Kilometer Array (SKA) in the next decade will be a major leap forward in sensitivity. PTA observations are likely to identify a number of continuous-wave sources representing the early inspiral phase of MBH binaries. PTAs experiments [e.g. Jenet et al., 2004, 2005] may also detect the inspiral of tight MBH binaries with mass $> 10^8 M_\odot$. While massive BH binaries are the primary sources for PTAs and LISA, these two experiments probe different stages of massive BH evolution. PTAs are most sensitive to the early inspiral (orbital periods of years or longer) of nearby ($z < 1$) (massive) sources [Mingarelli et al., 2017]. In contrast, LISA is sensitive to the inspiral, merger, and ringdown of MBH binaries at a wide range of redshifts [Amaro-Seoane et al., 2012]. The two populations of MBH binaries probed by PTAs and LISA are linked via the growth and evolution of SMBH across cosmic time.

LISA will provide a unique way of probing the high-redshift universe and understanding the early formation of the SMBHs, especially when combined with the soon-to-come observations of the electromagnetic (EM) counterparts [DeGraf and Sijacki, 2020, Natarajan et al., 2017]. For instance, they will potentially allow us to distinguish between different BH

seeding mechanisms at high-redshift [Ricarte and Natarajan, 2018], to obtain information on the dynamical evolution of massive black holes [Bonetti et al., 2019], and to gain information about the gas properties within the accretion disc [Derdzinski et al., 2019].

To properly analyze the upcoming results from the gravitational wave as well as the EM observations, we need to gain a thorough understanding of the physics of these MBH mergers with theoretical tools and be able to make statistical predictions on the binary population. In particular, it is important that the BH dynamics is modeled accurately, so that we can minimize the degeneracy with other physical properties of the merger, and gain accurate information about when and where BH coalescence is expected.

Hydrodynamical cosmological simulations provide a natural ground for studying the evolution and mergers of MBHs. In particular, large-volume cosmological simulations [e.g. Davé et al., 2019, Feng et al., 2016, Hirschmann et al., 2014, Pillepich et al., 2018, Schaye et al., 2015, Vogelsberger et al., 2014, Volonteri et al., 2016] have the statistical power to make merger rate predictions for the upcoming observations.

In order to accurately predict when black hole mergers occur in these simulations, one must account for the long journey of the central black holes after the merger of their host galaxies: during galaxy mergers, the central SMBHs are usually separated by as much as a few tens of kpc. These SMBHs then gradually lose their orbital energy and sink to the center of the new galaxy due to the dynamical friction exerted by the gas, stars and dark matter around them [e.g. Chandrasekhar, 1943, Ostriker, 1999]. When their separation reaches the sub-parsec scale, they form a binary and other energy-loss channels begin to dominate, such as scattering with stars [e.g. Quinlan, 1996, Sesana et al., 2007a, Vasiliev et al., 2015], gas drag from the circumbinary disk [e.g. Haiman et al., 2009], or three-body scattering with a third black hole [e.g. Bonetti et al., 2018].

However, due to limited mass and spatial resolution, large-scale cosmological simulations cannot feasibly include detailed treatment of the black hole binary dynamics. Without any additional correction to the BH dynamics, the smoothed-away small-scale gravity prevents effective orbital decay of the black hole after the orbit approaches the gravitational softening length. Once the binary reaches the innermost region of the remnant galaxy, the gravitational potential (close to the resolution limit) can be noisy. Such a noisy potential can scatter the black hole around within the host galaxy, or in some cases even kick the BH to the outskirts of the galaxy if the black hole mass is small. To avoid unexpected scattering of the BHs around the center of the galaxy, large-volume cosmological simulations usually resort to pinning the black holes at the halo minimum potential (a.k.a. repositioning). This repositioning algorithm has the undesirable effect of making the black holes merge rather efficiently once they reach the center of the galaxy. Post-processing techniques have been used [e.g. Katz et al., 2020, Kelley et al., 2017a, Salcido et al., 2016, Volonteri et al., 2020] to account for the additional dynamical friction effects on scales close to the gravitational smoothing scales of the black holes. This allows for an approximate estimation of the expected delay in the BH mergers. The post-processing calculations are mostly based on idealized analytical models, and therefore do not account for the variety of individual black hole environments.

Due to the increased merger efficiency induced by BH repositioning and the limits of

post-processing in dynamical friction calculations, emerging works have been adding sub-grid modeling of dynamical friction self-consistently in cosmological simulations and removing the artificial repositioning approximation. Chapon et al. [2013], Dubois et al. [2014] are the first large simulations to include the dynamical friction from gas, while Hirschmann et al. [2014] and Tremmel et al. [2017] account for dynamical friction from collisionless particles, and both have shown success in stabilizing the black holes at the halo centers. The dynamical friction modeling and its effect on the BH merger time scale have been well-tested in Tremmel et al. [2015] and Pfister et al. [2019] in the context of their relatively high-resolution simulations in a controlled single-halo environment, but they have also pointed out the failure of their model when the dark matter particle mass exceeds the black hole mass, and so their models might not be directly applicable to lower-resolution cosmological simulations. In the context of low-resolution cosmological simulations, the dynamical friction modeling is less well-tested, and its effects on the BH evolution and merger rate are not fully explored.

In this work, we carefully develop and test the sub-grid modeling of dynamical friction from both gas and collisionless particles in the context of cosmological simulations with resolution similar to the aforementioned large-volume, low-resolution hydrodynamical simulations (i.e. with a spatial resolution of $\sim$1kpc and mass resolution of $M_{\rm DM} \sim 10^7 M_\odot$). We evaluate the models both by looking at individual black hole dynamics, growth and mergers, and by statistically comparing the behavior of different models in terms of the mass growth and merger statistics. In particular, we focus on how various models affect the BH merger rate in the cosmological simulations, which is essential for making merger rate predictions for the LISA mission.

This paper proceeds as follows: in Section 3.2 we describe the numerical code and the gaussian-constrained technique we use to study large SMBHs within a small volume. In Section 3.3, we talk about the different dynamical models for black hole mergers that we study and test in this work. Section 3.4 is dedicated to investigating the effect of the different models on the evolution of individual black holes, while Section 3.5 studies the differences statistically. Finally, in Section 3.6, we show merger rate predictions with a model chosen based on the results of the previous sections, and compare with previous simulations at similar resolutions.

3.2 The Simulations

3.2.1 The Numerical Code

We use the massively parallel cosmological smoothed particle hydrodynamic (SPH) simulation software, MP-Gadget [Feng et al., 2016], to run all the simulations in this paper. The hydrodynamics solver of MP-Gadget adopts the new pressure-entropy formulation of SPH [Hopkins, 2013]. We apply a variety of sub-grid models to model the galaxy and black hole formation and associated feedback processes already validated against a number of observables [e.g. Bhowmick et al., 2018, Di Matteo et al., 2017, Feng et al., 2016, Huang et al., 2018, Marshall et al., 2020, 2021, Ni et al., 2018, 2020, Tenneti et al., 2018, Waters et al.,

2016, Wilkins et al., 2017]. Here we review briefly the main aspects of these. In the simulations, gas is allowed to cool through radiative processes [Katz et al., 1999], including metal cooling. For metal cooling, we follow the method in Vogelsberger et al. [2014], and scale a solar metallicity template according to the metallicity of gas particles. Our star formation (SF) is based on a multi-phase SF model [Springel and Hernquist, 2003] with modifications following Vogelsberger et al. [2013]. We model the formation of molecular hydrogen and its effects on SF at low metallicity according to the prescription of Krumholz and Gnedin [2011]. We self-consistently estimate the fraction of molecular hydrogen gas from the baryon column density, which in turn couples the density gradient to the SF rate. We include Type II supernova wind feedback [the model used in BlueTides Feng et al., 2016, Okamoto et al., 2010] in our simulations, assuming that the wind speed is proportional to the local one dimensional dark matter velocity dispersion.

BHs are seeded with an initial seed mass of $M_{\rm seed} = 5 \times 10^5 M_\odot/h$ in halos with mass more than $10^{10} M_\odot/h$ if the halo does not already contain a BH. We model BH growth and AGN feedback in the same way as in the *MassiveBlack I&II* simulations, using the BH subgrid model developed in Di Matteo et al. [2005a], Springel et al. [2005a] with modifications consistent with BlueTides. The gas accretion rate onto the BHs is given by Bondi accretion rate,

$$\dot{M}_B = \alpha \frac{4\pi G^2 M_{\rm BH}^2 \rho}{(c_s^2 + v_{\rm rel}^2)^{3/2}}, \tag{3.1}$$

where c_s and ρ are the local sound speed and density of the cold gas, $v_{\rm rel}$ is the relative velocity of the BH to the nearby gas, and $\alpha = 100$ is a numerical correction factor introduced by [Springel et al., 2005b]. This can also be eliminated (without affecting the values of the accretion rate significantly) in favor of a more detailed modeling of the contributions in the cold and hot phase accretion [Pelupessy et al., 2006].

We allow for super-Eddington accretion in the simulation [e.g. Volonteri and Rees, 2005, Volonteri et al., 2015], but limit the accretion rate to 2 times the Eddington accretion rate:

$$\dot{M}_{\rm Edd} = \frac{4\pi G M_{\rm BH} m_p}{\eta \sigma_T c}, \tag{3.2}$$

where m_p is the proton mass, σ_T the Thompson cross section, c is the speed of light, and $\eta = 0.1$ is the radiative efficiency of the accretion flow onto the BH. Therefore, the BH accretion rate is determined by:

$$\dot{M}_{\rm BH} = {\rm Min}(\dot{M}_B, 2\dot{M}_{\rm Edd}). \tag{3.3}$$

The SMBH is assumed to radiate with a bolometric luminosity $L_{\rm Bol}$ proportional to the accretion rate $\dot{M}_{\rm BH}$:

$$L_{\rm Bol} = \eta \dot{M}_{\rm BH} c^2 \tag{3.4}$$

with $\eta = 0.1$ being the mass-to-light conversion efficiency in an accretion disk according to Shakura and Sunyaev [1973]. 5% of the radiated energy is thermally coupled to the

surrounding gas that resides within twice the radius of the SPH smoothing kernel of the BH particle. This scale is typically about $\sim 1-3\%$ of the virial radius of the halo.

The cosmological parameters used are from the nine-year Wilkinson Microwave Anisotropy Probe (WMAP) [Hinshaw et al., 2013] ($\Omega_0 = 0.2814$, $\Omega_\Lambda = 0.7186$, $\Omega_b = 0.0464$, $\sigma_8 = 0.82$, $h = 0.697$, $n_s = 0.971$). For our fiducial resolution simulations, the mass resolution is $M_{\rm DM} = 1.2 \times 10^7 M_\odot/h$ and $M_{\rm gas} = 2.4 \times 10^6 M_\odot/h$ in the initial conditions. The mass of a star particle is $M_* = 1/4 M_{\rm gas} = 6 \times 10^5 M_\odot/h$. The gravitational softening length is $\epsilon_g = 1.5$ ckpc$/h$ in the fiducial resolution for both DM and gas particles. The detailed simulation and model parameters are listed in Tables 3.2.1 and 3.2.2.

3.2.2 Gaussian Constrained Realization

MBHs at high redshift typically reside in rare density peaks, which are absent in the small uniform box (~ 10 Mpc$/h$) simulations. In order to test the dynamics for more massive BHs (with $M_{\rm BH} > 10^8 M_\odot$) in our small volume simulation, we apply the Constrained Realization (CR) technique [1] to impose a relatively high density peak in the initial condition (IC), with peak height $\nu = 4\sigma_0$ on scale of $R_G = 1$ Mpc$/h$.

The prescription for the CR technique was first introduced by Hoffman and Ribak [1991] as an optimal way to construct samples of constrained Gaussian random fields. This formalism was further elaborated and extended by van de Weygaert and Bertschinger [1996] as a more general type of convolution format constraints. The CR technique imposes constraints on different characteristics of the linear density field. It can specify density peaks in the Gaussian random field with any desired height and shape, providing an efficient way to study rare massive objects with a relatively small box and thus lower computational costs [e.g. Ni et al., 2020]. In this study, we specify a $4\sigma_0$ density peak in the IC of our 10 Mpc$/h$ box, boosting the early formation of halos and BHs to study the dynamics of massive BHs. Before applying the peak height constraint, the highest density peak has $\nu = 2.4\sigma_0$ and the largest BH has mass $< 6 \times 10^7 M_\odot$ at $z = 3$ in our fiducial model (`DF_4DM_G` in Table 3.2.1). After applying the $4\sigma_0$ constraint, the largest BH has mass $3 \times 10^8 M_\odot$ at $z = 3$ in the same box.

3.3 BH Dynamics

3.3.1 BH Dynamical Mass

In our simulations, the seed mass of the black holes is $5 \times 10^5 M_\odot/h$, which is 20 times smaller than the fiducial dark matter particle mass at $1.2 \times 10^7 M_\odot/h$. Such a small mass of the BH relative to the dark matter particles will result in very noisy gravitational acceleration on the black holes, and causes instability in the black hole's motion as well as drift from the halo center. Moreover, as shown in previous works [e.g. Pfister et al., 2019, Tremmel et al., 2015],

[1] `https://github.com/yueyingn/gaussianCR`

Table 3.2.1: Constrained Simulations

Name	Lbox $[h^{-1}\mathrm{Mpc}]$	$\mathrm{N_{part}}$	$\mathrm{M_{DM}}$ $[h^{-1}\mathrm{M_\odot}]$	$\mathrm{M_{Dyn,seed}}$ $[\mathrm{M_{DM}}]$	ϵ_g $[h^{-1}\mathrm{kpc}]$	BH Dynamics	Merging Criterion
NoDF_4DM	10	176^3	1.2×10^7	4	1.5	gravity	distance
NoDF_4DM_G	10	176^3	1.2×10^7	4	1.5	gravity	distance & grav.bound
DF_4DM	10	176^3	1.2×10^7	4	1.5	gravity+DF	distance
Drag_4DM_G	10	176^3	1.2×10^7	4	1.5	gravity+Drag	distance & grav.bound
DF+Drag_4DM_G	10	176^3	1.2×10^7	4	1.5	gravity+DF+Drag	distance & grav.bound
DF_4DM_G	10	176^3	1.2×10^7	4	1.5	gravity+DF	distance & grav.bound
DF_2DM_G	10	176^3	1.2×10^7	2	1.5	gravity+DF	distance & grav.bound
DF_1DM_G	10	176^3	1.2×10^7	1	1.5	gravity+DF	distance & grav.bound
DF(T15)_4DM_G	10	176^3	1.2×10^7	4	1.5	gravity+DF(T15)	distance & grav.bound
DF_HR_4DM_G	10	256^3	4×10^6	4	1.0	gravity+DF	distance & grav.bound
DF_HR_12DM_G	10	256^3	4×10^6	12	1.0	gravity+DF	distance & grav.bound

Table 3.2.2: Unconstrained Simulations

Name	Lbox $[h^{-1}\mathrm{Mpc}]$	N_{part}	M_{DM} $[h^{-1}M_{\odot}]$	$M_{\mathrm{Dyn,seed}}$ $[M_{\mathrm{DM}}]$	ϵ_{g} $[h^{-1}\mathrm{kpc}]$	BH Dynamics	Merging Criterion
L15_Repos_4DM	15	256^3	1.2×10^7	4	1.5	reposition	distance
L15_NoDF_4DM	15	256^3	1.2×10^7	4	1.5	gravity	distance
L15_NoDF_4DM_G	15	256^3	1.2×10^7	4	1.5	gravity	distance & grav.bound
L15_DF_4DM	15	256^3	1.2×10^7	4	1.5	gravity+DF	distance
L15_DF_4DM_G	15	256^3	1.2×10^7	4	1.5	gravity+DF	distance & grav.bound
L15_DF(T15)_4DM_G	15	256^3	1.2×10^7	4	1.5	gravity+DF(T15)	distance & grav.bound
L15_DF+drag_4DM_G	15	256^3	1.2×10^7	4	1.5	gravity+DF+Drag	distance & grav.bound
L35_NoDF_4DM_G	35	600^3	1.2×10^7	4	1.5	gravity+DF	distance & grav.bound
L35_DF+drag_4DM_G	35	600^3	1.2×10^7	4	1.5	gravity+DF+drag	distance & grav.bound

under the low $M_{\rm BH}/M_{\rm DM}$ regime, it is challenging to effectively model dynamical friction in a sub-grid fashion.

To alleviate dynamical heating by the noisy potential due to the low $M_{\rm BH}/M_{\rm DM}$ ratio, we introduce a second mass tracer, the dynamical mass $M_{\rm dyn}$, which is set to be comparable to $M_{\rm DM}$ when the black hole is seeded. This mass is used in force calculation for the black holes, including the gravitational force and dynamical friction, while the intrinsic black hole mass $M_{\rm BH}$ is used in the accretion and feedback process. $M_{\rm dyn}$ is kept at its seeding value $M_{\rm dyn,seed}$ until $M_{\rm BH} > M_{\rm dyn,seed}$. After that $M_{\rm dyn}$ grows following the black hole's mass accretion. With the boost in the seed dynamical mass, the sinking time scale will be shortened by a factor of $\sim M_{\rm BH}/M_{\rm dyn}$ compared to the no-boost case. Because of the boost in mass, we note that while our model can be safely applied to the more massive black holes, there is limitation in the seed black hole dynamics. On the other hand, we also note that the bare black hole sinking time scale estimated in the no-boost case could over-estimate the true sinking time, as the high-density stellar bulges sinking together with the black hole are not fully resolved [e.g. Antonini and Merritt, 2012, Biernacki et al., 2017, Dosopoulou and Antonini, 2017].

The boost we need to prevent dynamical heating depends on the dark matter particle mass $M_{\rm DM}$ (if we have high enough resolution the boost is no longer necessary), so we parametrize the dynamical mass in terms of the dark matter particle mass, $M_{\rm dyn,seed} = k_{\rm dyn} M_{\rm DM}$, instead of setting an absolute seeding dynamical mass for all simulations. We expect that as we go to higher resolutions where $M_{\rm DM}$ is comparable to $M_{\rm BH,seed}$, the dynamical seed mass should converge to the black hole seed mass, if we keep $k_{\rm dyn}$ constant. We study the effect of setting different $k_{\rm dyn}$ by running three simulations with the same resolution and dynamical friction models, but various $k_{\rm dyn}$ ratios. They are listed in Table 3.2.1 as `DF_4DM_G`, `DF_2DM_G`, and `DF_1DM_G`, with $k_{\rm dyn} = 4, 2, 1$, respectively.

To explore the effects of the BH seed dynamical mass on the motion and mergers of the black hole, we test a variety of $M_{\rm dyn,seed}$ values in our simulations. The comparison between different $M_{\rm dyn,seed}$ can be found in Appendix 3.A.

3.3.2 Modeling of Black Hole Dynamics

Reposition of the Black Hole

Before introducing our dynamical friction implementations, we first describe a baseline model utilized by many large-volume cosmological simulations: the reposition model. As the name suggests, the reposition model of black hole dynamics places the black hole at the location of a local gas particle with minimum gravitational potential at each time step, in order to avoid the unrealistic motion of the black holes due to limited mass and force resolution. This is particularly preferred for large-volume, low-resolution cosmological simulations [e.g. Booth and Schaye, 2009, Pillepich et al., 2018, Schaye et al., 2015, Sijacki et al., 2007, Springel et al., 2005b], where the black hole mass is smaller than a star or gas particle mass and the BH can be inappropriately scattered around by two-body forces as well as the noisy local potential.

This simple fix of repositioning, however, comes with many disadvantages. For example,

it may lead to higher accretion and feedback of the black holes, as they sink to the high-density regions too quickly. As was shown in Wurster and Thacker [2013] and Tremmel et al. [2017], repositioning also leads to burstier feedback of the BHs, which is more likely to quench star-formation in the host galaxies. Moreover, repositioning leads to ill-defined velocity and non-smooth trajectories of the black hole particles. Because of the ill-defined velocity and extremely short orbital decay time, such methods cannot be reliably used for merger rate predictions without careful post-processing calculations to account for the orbital decays.

In our study, we use the reposition model as a reference for the black hole statistics, as it is still widely adopted in many existing simulations. We want to compare the dynamical friction models with the reposition model and quantify the effect of repositioning on BH mass growth and merger rate compared with the dynamical friction models.

Dynamical Friction from Collisionless Particles

When the black hole travels through a continuous medium or a medium consisting of particles with smaller masses than the black hole, it attracts the surrounding mass towards itself, leaving a tail of overdensity behind. Dynamical friction is the resulting gravitational force exerted onto the black hole by this tail of overdensity [e.g. Binney and Tremaine, 2008, Chandrasekhar, 1943]. Dynamical friction causes the orbits of SMBHs to decay towards the center of massive galaxies [e.g. Governato et al., 1994, Kazantzidis et al., 2005], and enables the black holes to stay at the high-density regions where they could go through efficient accretion and mergers.

We follow Equation (8.3) in Binney and Tremaine [2008] for the acceleration of the black hole due to dynamical friction:

$$\mathbf{F}_{\rm DF} = -16\pi^2 G^2 M_{\rm BH}^2 m_a \log(\Lambda) \frac{\mathbf{v}_{\rm BH}}{v_{\rm BH}^3} \int_0^{v_{\rm BH}} dv_a v_a^2 f(v_a), \tag{3.5}$$

where $M_{\rm BH}$ is the black hole mass, $\mathbf{v}_{\rm BH}$ is the velocity of the black hole relative to its surrounding medium, m_a and v_a are the masses and velocities of the particles surrounding the black hole, and $\log(\Lambda) = \log(b_{\rm max}/b_{\rm min})$ is the Coulomb logarithm that accounts for the effective range of the friction between $b_{\rm min}$ and $b_{\rm max}$(we will specify how we set these parameters later). $f(v_a)$ is the velocity distribution of the surrounding particles (unless we explicitly state otherwise, all variables involving the black hole's surrounding particles are calculated using stars and dark matter particles). Here we have assumed an isotropic velocity distribution of the particles surrounding the black hole, so that we are left with an 1D integration.

We test two different numerical implementations of the dynamical friction (DF) in our simulations: one with a more aggressive approach which likely overestimates the effective range of DF, but could be more suitable for large-volume simulations (we refer to it as DF(fid) in places where we carry out explicit comparisons between the two DF models, and drop the 'fid' in all other places); the other with a more conservative method which aims to only account for the DF below the gravitational softening length, and is well-tested for smaller volume, high-resolution simulations [Tremmel et al., 2015] (we refer to it as DF(T15)).

We begin by introducing the DF(fid) model. In this model, we further follow the derivation in Binney and Tremaine [2008], and approximate $f(v_a)$ by the Maxwellian distribution, so that Equation 4.2 reduces to:

$$\mathbf{F}_{\rm DF,fid} = -4\pi\rho_{\rm sph}\left(\frac{GM_{\rm dyn}}{v_{\rm BH}}\right)^2 \log(\Lambda_{\rm fid})\mathcal{F}\left(\frac{v_{\rm BH}}{\sigma_v}\right)\frac{\mathbf{v}_{\rm BH}}{v_{\rm BH}}. \tag{3.6}$$

Here $\rho_{\rm sph}$ is the density of dark matter and star particles within the SPH kernel (we will sometimes refer to these particles as "surrounding particles") of the black hole. All other definitions follow those of Equation 4.2, except that we have substituted $M_{\rm BH}$ with $M_{\rm dyn}$ following the discussion in 3.3.1. We caution the reader that throughout our paper, this boost in mass could lead to an overestimation of the dynamical friction, and therefore an underestimation of the dynamical friction decay timescale, especially for seed black holes. The function $\mathcal{F}$ defined as:

$$\mathcal{F}(x) = \mathrm{erf}(x) - \frac{2x}{\sqrt{\pi}}e^{-x^2},\ x = \frac{v_{\rm BH}}{\sigma_v} \tag{3.7}$$

is the result of analytically integrating the Maxwellian distribution, where σ_v is the velocity dispersion of the surrounding particles.

The subscript "fid" in $\log(\Lambda)$ means that this definition of Λ is specific to the DF(fid) model, with

$$\Lambda_{\rm fid} = \frac{b_{\rm max,fid}}{(GM_{\rm dyn})/v_{\rm BH}^2},\ b_{\rm max,fid} = 10\ \mathrm{ckpc}/h. \tag{3.8}$$

Note that here we have defined $b_{\rm max}$ as a constant roughly equal to 6 times the gravitational softening. As there is no general agreement on the distance above which dynamical friction is fully resolved, we tested several values ranging from ϵ_g to $20\epsilon_g$. We found that values above $2\epsilon_g$ are effective in sinking the black hole, although a smaller $b_{\rm max}$ tends to result in more drifting black holes at higher redshift. By using this definition, we are likely overestimating the effective range of dynamical friction. However, we find this over-estimation necessary in the early stage of black hole growth to stabilize the black hole motion.

We also implement a more localized version of dynamical friction following Tremmel et al. [2015] which we call DF(T15). Under the DF(T15) model, the dynamical friction is expressed as:

$$\mathbf{F}_{\rm DF,T15} = -4\pi\rho(v < v_{\rm BH})\left(\frac{GM_{\rm dyn}}{v_{\rm BH}}\right)^2 \log(\Lambda_{\rm T15})\frac{\mathbf{v}_{\rm BH}}{v_{\rm BH}}. \tag{3.9}$$

$\mathbf{v}_{\rm BH}$ is the velocity of the black hole relative to its surrounding medium. Note that different from Equation 4.2, the surrounding density here only accounts for the particles moving slower than the BH with respect to the environment. More formally,

$$\rho(v < v_{\rm BH}) = \frac{M(< v_{\rm BH})}{M_{\rm total}}\rho_{\rm T15}, \tag{3.10}$$

where $M_{\rm total}$ is the total mass of the nearest 100 DM and stars, $M(< v_{\rm BH})$ is the fractional mass counting only DM and star particles with velocities smaller than the BH, and ρ_{T15} is the density calculated from the nearest 100 DM/Star particles (note that in comparison, the SPH kernel contains 113 gas particles but far more collisionless particles (see Figure 3.4.4)). By using $\rho(v < v_{\rm BH})$ in place of $\rho_{\rm sph}\mathcal{F}$, we are approximating the velocity distribution of surrounding particles by the distribution of the nearest 100 collisionless particles. Another major difference from the DFsph model is the Coulomb logarithm, where in this model we define:

$$\Lambda_{\rm T15} = \frac{b_{\rm max,T15}}{(GM_{\rm dyn})/v_{\rm BH}^2},\ b_{\rm max,T15} = \epsilon_g. \tag{3.11}$$

The choice of a lower $b_{\rm max}$ is consistent with the localized density and velocity calculations, and by doing so we have assumed that dynamical friction is fully resolved above the gravitational softening.

Gas Drag

In addition to the dynamical friction from dark matter and stars, the black hole can also lose its orbital energy due to the dynamical friction from gas (to distinguish from dynamical friction from dark matter and stars, we will refer to the gas dynamical friction as "gas drag" hereafter). Ostriker [1999] first came up with the analytical expression for the gas drag term from linear perturbation theory, and showed that in the transonic regime the gas drag can be more effective than the dynamical friction from collisionless particles. Although later studies show that Ostriker [1999] likely overestimates the gas drag for gas with Mach numbers slightly above unity [e.g. Chapon et al., 2013, Escala et al., 2004], simulations with gas drag implemented still demonstrate that this is an effective channel for black hole energy loss during orbital decays [e.g. Chapon et al., 2013, Dubois et al., 2013, Pfister et al., 2019].

In order to investigate the relative effectiveness of DF and gas drag, we also include gas drag onto black holes in our simulations following the analytical approximation from Ostriker [1999]:

$$\mathbf{F}_{\rm drag} = -4\pi\rho\left(\frac{GM_{\rm dyn}}{c_s^2}\right)^2 \times \mathcal{I}(\mathcal{M})\frac{\mathbf{v}_{\rm BH}}{v_{\rm BH}}, \tag{3.12}$$

where c_s is the sound speed, $\mathcal{M} = \frac{|\mathbf{v}_{\rm BH}-\mathbf{v}_{\rm gas}|}{c_s}$ is the Mach number, and $\mathcal{I}(\mathcal{M})$ is given by:

$$\mathcal{I}_{\rm subsonic} = \mathcal{M}^{-2}\left[\frac{1}{2}\log\left(\frac{1+\mathcal{M}}{1-\mathcal{M}}\right) - \mathcal{M}\right] \tag{3.13}$$

$$\mathcal{I}_{\rm supersonic} = \mathcal{M}^{-2}\left[\frac{1}{2}\log\left(\frac{\mathcal{M}+1}{\mathcal{M}-1}\right) - \log\Lambda_{\rm fid}\right], \tag{3.14}$$

where $\log\Lambda_{\rm fid}$ is the Coulomb logarithm defined similarly to the collisionless dynamical friction.

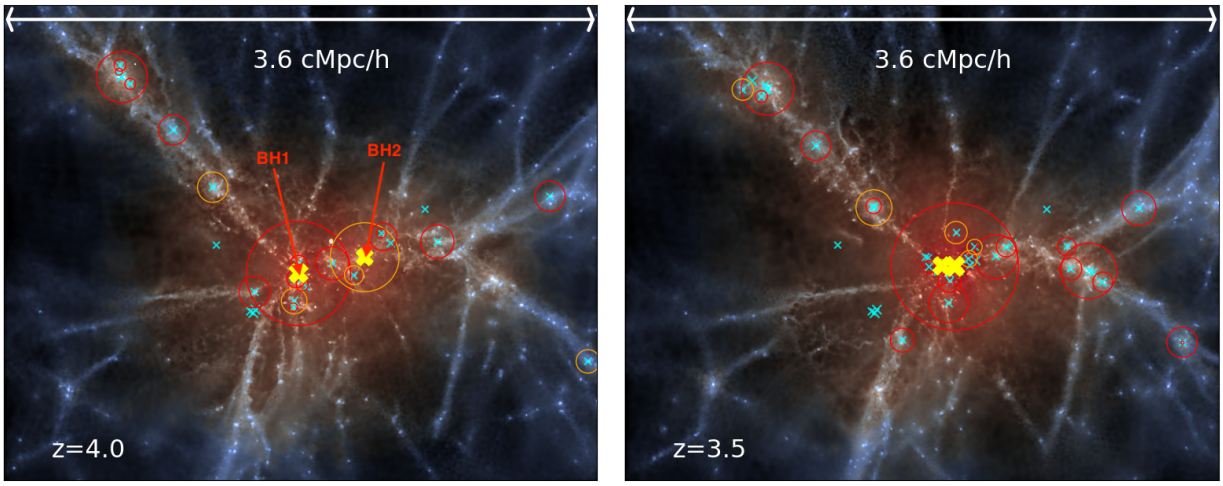

Figure 3.3.1: Visualization of $4\sigma_0$ density peak of the `DF_4_DM_G` simulation at $z = 4.0$ and $z = 3.5$. The brightness corresponds to the gas density, and the warmness of the tone indicates the mass-weighted temperature of the gas. We plot the black holes (**cross**) with mass $> 10^6 M_\odot$, as well as the halos (subhalos) hosting them (**red circles** correspond to central halos, **orange circles** correspond to subhalos. The circle radius shows the virial radius of the halo; halos are identified by Amiga's Halo Finder(AHF)). This density peak hosts the two largest black holes in our simulations (**yellow cross**), and they are going through a merger along with the merger of their host halos between $z = 4$ and $z = 3$. For the black hole and merger case studies, we will use examples from the circled halos/black holes shown in this figure.

3.3.3 Merging Criterion

In all of our simulations, we set the merging distance to be $2\epsilon_{\rm g}$, because the BH dynamics below this distance is not well-resolved due to our limited spatial resolution. We conserve the total momentum of the binary during the merger.

Under the baseline repositioning treatment of the BH dynamics, the velocity of the black hole is not a well-defined quantity. Therefore, in cosmological simulations with repositioning, the distance between the two black holes is often the only criterion imposed during the time of mergers (for example BlueTides [Feng et al., 2016], Illustris [Vogelsberger et al., 2013] and IllustrisTNG [Pillepich et al., 2018]). One problem with using only the distance as a merging criterion is that it can spuriously merge two passing-by black holes with high velocities, when in reality they are not gravitationally bound and should not merge just yet (or may never merge). Although some similar-resolution simulations such as EAGLE [Crain et al., 2015, Schaye et al., 2015] also check whether two black hole particles are gravitationally bound, the black holes still do not have a well-defined orbit and sinking time due to the discrete positioning.

When we turn off the repositioning of the BHs to the nearby minimum potential, the BHs will have well-defined velocities at each time step (this is true whether or not we add the dynamical friction). This allows us to apply further merging criteria based on the velocities and accelerations of the black hole pair, and thus avoid earlier mergers of the gravitationally unbound pairs. Also, as the BH pairs now have well-defined orbits all the way down to the numerical merger time, we will be able to directly measure binary separation and eccentricity from the numerical merger, and use the measurements as the initial condition for post-processing methods without having to assume a constant initial value [e.g. Kelley et al., 2017a].

We follow Bellovary et al. [2011] and Tremmel et al. [2017], and use the criterion

$$\frac{1}{2}|\mathbf{\Delta v}|^{\mathbf{2}} < \mathbf{\Delta a}\mathbf{\Delta r} \tag{3.15}$$

to check whether two black holes are gravitationally bound. Here $\mathbf{\Delta a}$,$\mathbf{\Delta v}$ and $\mathbf{\Delta r}$ denote the relative acceleration, velocity and position of the black hole pair, respectively. Note that this expression is not strictly the total energy of the black hole pair, but an approximation of the kinetic energy and the work needed to get the black holes to merge. Because in the simulations the black hole is constantly interacting with surrounding particles, on the right-hand side we use the overall gravitational acceleration instead of the acceleration purely from the two-body interaction.

3.4 Case Studies of BH Models

Given the variety of models we have described so far, we first study the effect of different BH dynamics models by looking at the individual black hole evolution and black hole pairs using the constrained simulations. The details of these simulations and specific dynamical

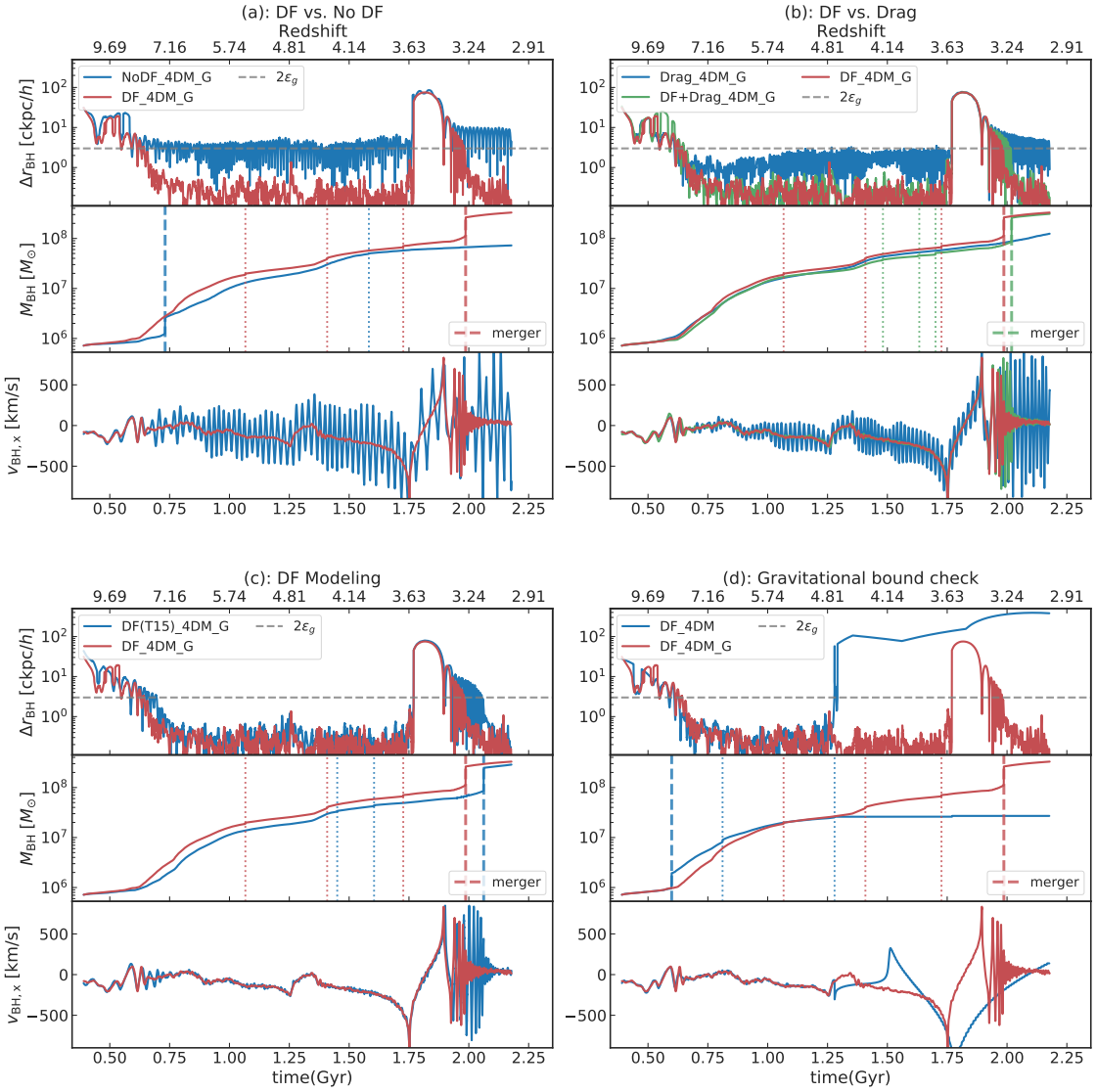

Figure 3.4.1: The evolution of BH2 in Figure 3.3.1 under different BH dynamics prescriptions. We show the distance to halo center (**top**), black hole mass (**middle**) and the x-component of the black hole velocity (**bottom**). Mergers are shown in vertical lines (thick dashed lines are major mergers ($q > 0.3$), and thin dotted lines are minor mergers) **(a):** comparison between no-DF and DF models. DF clearly helps the black hole sink to the halo center and stay there. **(b):** Effects of DF from stars and dark matter compared with gas drag. DF has a stronger effect throughout, except that in the very early stage the drag-only model is comparable to the DF-only model. **(c)**: Comparison between the DF(fid) and DF(T15) model. In general, the DF(fid) model results in a more stable black hole motion and faster sinking, but the difference is small. **(d)**: Black hole dynamics with and without the gravitational bound check during mergers. Without the gravitational bound check, the black holes can merge while still moving with large momenta, and thereby get kicked out of the halo by the injected momentum.

models are shown in Table 3.2.1. For all the constrained simulations, we use the same initial conditions, which enables us to do a case-by-case comparison between different BH dynamical models.

For the case studies, we choose to study the growth and merger histories of the two largest black holes and a few surrounding black holes within the density peak of our simulations. The halos and black holes at the $4\sigma_0$ density peak in `DF_4DM_G` are shown in Figure 3.3.1. The halos and subhalos shown in circles are identified with Amiga's Halo Finder [AHF, Knollmann and Knebe, 2009]. The halos are centered at the minimum-potential gas particle within the halo, and the sizes of the circles correspond to the virial radius of the halo. Throughout the paper, we will always define the halo centers by the position of the minimum-potential gas particle, and we note that the offset between the minimum-potential gas and the halo center given by AHF (found via density peaks) is always less than 1.5 ckpc/h. The cyan crosses are black holes with mass larger than $10^6 M_\odot/h$, and the yellow crosses are the two largest black holes in the simulation. From the plot, we can see that in the `DF_4DM_G` simulation, most of the black holes already reside in the center of their hosting halos at $z = 4$, although we also see some cases of wandering BHs outside of the halos.

3.4.1 Black Hole Dynamics Modeling

To compare different dynamical models, we look at the distance between the black hole and the halo center $\Delta r_{\rm BH}$ (we will sometimes refer to this distance as "drift" hereafter), the black hole mass, and the velocity along the x direction through the entire history of BH2 from Figure 3.3.1.

We evaluate the black hole drift with two approaches: at each time-step, we find the minimum potential gas particle within 10 ckpc/h of the black hole and calculate the distance between this gas particle and the black hole. This is a quick evaluation of the drift that allows us to trace the black hole motion at each time step, but it fails to account for orbits larger than 10 ckpc/h, and the minimum-potential gas particle may not reside in the same halo as the black hole. Therefore, for each snapshot we saved, we define the drift more carefully by running the halo finder and calculate the distance between the black hole and the center of its host halo. Whenever the black hole is further than 9 ckpc/h from the minimum potential gas particle, we take the distance from the two nearest snapshots and linearly interpolate in time between them. Otherwise we use the distance to the local minimum potential gas particle calculated at each time step.

DF and No Correction

Before calibrating our dynamical friction modeling, we first demonstrate the effectiveness of our fiducial DF model, `DF_4DM_G`, by comparing it with the no-DF run `NoDF_4DM_G` (note that throughout the paper, no-DF means no correction to the BH dynamics of any form besides the resolved gravity). We keep all parameters fixed except for the black hole dynamics modeling. The details of these simulations can be found in Table 3.2.1.

In Figure 3.4.1(a), we show the evolution of BH2 in Figure 3.3.1 under the no-DF and the fiducial DF models. Without any correction to the black hole dynamics, even the largest black hole in the simulation does not exhibit efficient orbital decay throughout its evolution: the distance from the halo center is always fluctuating above $2\epsilon_g$. This is because the black hole does not experience enough gravity on scales below the softening length, and cannot lose its angular momentum efficiently. Now when we add the additional dynamical friction to compensate for the missing small-scale gravity, the black hole is able to sink to within 1 ckpc/h of the halo centers in <200 Myr and remain there.

The 90 ckpc/h peak in the drift of the black hole marks the merger between BH1 and BH2 in Figure 3.3.1, when the host halo of BH2 merges into the host of BH1, and the halo center is redefined near the merger. After the halo merger, dynamical friction is able to sink the black hole to the new halo center and allows it to merge with the black hole in the other halo, whereas in the no-DF case we do not see the clear orbital decay of the black holes after the merger of their host halo until the end of the simulation.

Besides the drift, we also show the x-component of the black hole's velocity relative to its surrounding collisionless particles (lower panel). Here we show one component instead of the magnitude to better visualize the velocity oscillation. With dynamical friction turned on, the velocity of the black hole is more stable, as the black hole's orbit has already become small and is effectively moving together with the host halo. Without dynamical friction, the black hole tends to oscillate with large velocities around the halo center without losing its angular momentum.

The different dynamics of the black hole can also affect accretion due to differences in density and velocities, so we also look at the black holes' mass growth in the two scenarios (middle panel). The mass growths of the two black holes are similar under the two models, although when subjected to dynamical friction, the black holes have more and earlier mergers. Even though the black hole mass is less sensitive to the dynamics modeling, the merger rate predictions can be affected significantly as we will discuss later.

Note that for our no-DF model, we have also boosted the dynamical mass to $4 \times M_{\rm DM}$ at the early stage to prevent scattering by the dark matter and star particles. However, even after the boost, the black holes cannot lose enough angular momentum to be able to stay at the halo center. This means that even though dynamical heating is alleviated through the large dynamical mass, the sub-resolution gravity is still essential in sinking the black hole to the host halo center.

Dynamical Friction and Gas Drag

In the previous subsection, we've only included collisionless particles (DM+Star) when modeling the dynamical friction, now we will look into the effects of dynamical friction of gas (gas drag) in comparison with the collisionless particles in the context of our simulations.

From Equation 4.3 and 3.12, the relative magnitudes of DF and drag mainly depend on two components: the relative density of DM+stars versus gas, and the values of $\mathcal{F}(x)$ and $\mathcal{I}(\mathcal{M})$. Ostriker [1999] has shown that when a black hole's velocity relative to the medium

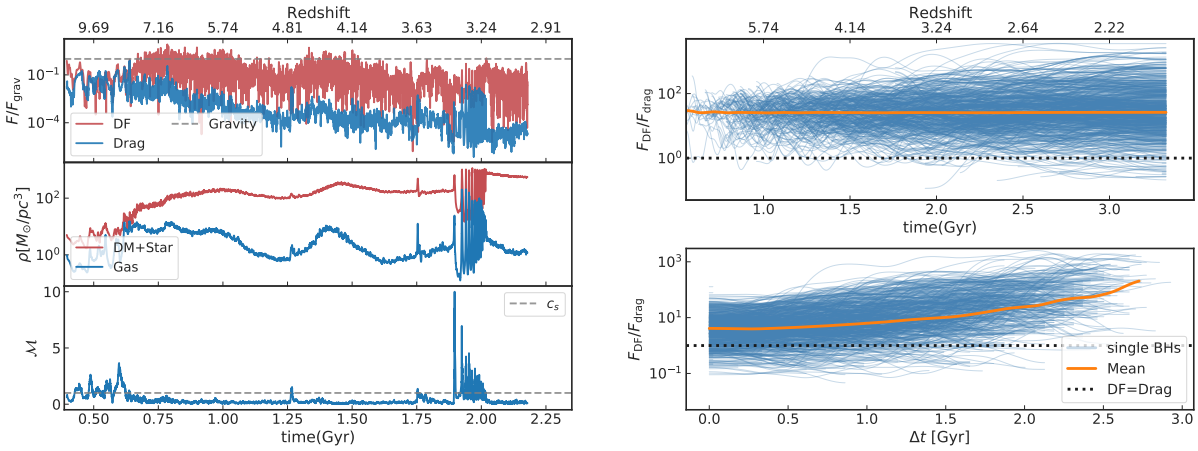

Figure 3.4.2: Comparisons between DF and hydro drag. **Left:** comparison for a single black hole. In the top panel we show the magnitude of the DF (**red**) and gas drag (**blue**) relative to gravity for the same black hole, in the `DF+Drag_4DM_G` run. During the early stage of the black hole evolution, DF and gas drag have comparable effect, while after $z = 7.5$ the gas drag becomes less and less important, as the gas density decreases relative to the stellar density (**middle**), and the black hole velocity goes into the subsonic regime (**lower**). **Right:** Ratio between DF and gas drag for all black holes. We plot the ratio both as a function of redshift (**top**) and as a function of time after a black hole is seeded (**bottom**). The orange lines represent the logarithmic mean of the scatter. The $F_{\rm DF}/F_{\rm drag}$ ratio depends strongly on the evolution time of the black hole: the longer the black hole evolves, the less important the drag force is. However, there is not a strong correlation between redshift and the $F_{\rm DF}/F_{\rm drag}$ ratio.

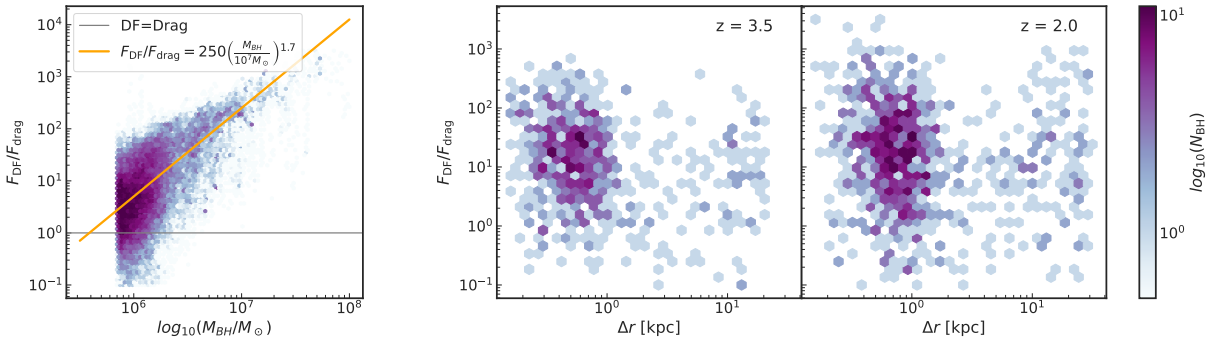

Figure 3.4.3: **Left:** Scattering relation between the $F_{\rm DF}/F_{\rm drag}$ ratio and the black hole mass. For each black hole, we sample its mass at uniformly-distributed time bins throughout its evolution, and we show the scattered density of all samples. DF has significantly larger effects over gas drag on larger BHs. We fit the scatter to a power-law shown in the orange line. **Right:** Scattering relation between the $F_{\rm DF}/F_{\rm drag}$ ratio and the BHs' distance to the halo center. Comparing with the BH mass, we do not see a clear dependence of the $F_{\rm DF}/F_{\rm drag}$ ratio on the distance to halo center. For BHs at all locations within the halo, DF is in general larger than the gas drag.

falls in the transonic regime (i.e. near the local sound speed), $\mathcal{I}$ is a few times higher than $\mathcal{F}$, while in the subsonic and highly supersonic regimes $\mathcal{I}$ is smaller or equal to $\mathcal{F}$. Therefore, we would expect the gas drag to be larger when the black hole is in the early sinking stage with a relatively high velocity and a high gas fraction.

In Figure 3.4.2, the left panel shows the comparison between the magnitude of DF and gas drag through different stages of the black hole evolution, as well as the factors that can alter the effectiveness of the gas drag. In the very early stages ($z > 7.5$) of black hole evolution, DF and gas drag have comparable effects, while after $z = 7.5$ the gas drag becomes significantly less important and almost negligible compared with DF. The reason follows what we have discussed earlier: the gas density decreases relative to the stellar density (shown in the middle panel), and the black hole's velocity relative to the surrounding medium goes into the subsonic regime as a result of the orbital decay (shown in the lower panel). Around $z = 3.5$, there is a boost in the black hole's velocity due to disruption during a major merger with a larger galaxy and black hole. The effect of gas is again raised for a short period of time (although still subdominant compared to the DF).

In Figure 3.4.1(b) we plot the black hole evolution for the DF-only (`DF_4DM_G`), drag-only (`Drag_4DM_G`), and DF+drag (`DF+Drag_4DM_G`) simulations. Both the drag-only and DF-only models are effective in sinking the black hole at early times ($z > 7$). However, at lower redshifts, the gas drag is not able to sink the black hole by itself, whereas DF is far more effective in stabilizing the black hole at the halo center. For this reason, in low-resolution cosmological simulations, dynamical friction from collisionless particles is necessary to prevent the drift of the black holes out of the halo center.

To further illustrate the relative importance between DF and gas drag for the entire BH population, we examine the dependencies of the $F_{\rm DF}/F_{\rm drag}$ on variables related to the BH evolution for all BHs in the `DF+Drag_4DM_G` simulation. First, in the right panel of Figure 3.4.2 we show the time evolution of $F_{\rm DF}/F_{\rm drag}$. The top panel shows the ratio as a function of cosmic time, while the bottom panel shows the ratio as a function of each BH's seeding time. The DF/Drag ratio has a wide range for different BHs, but overall DF is becoming larger relative to the gas drag as the black hole evolves. From the mean value of the DF/drag ratio, we see that when the black holes are first seeded, DF is only a few times larger than the gas drag. After a few Gyrs of evolution, DF becomes 2-3 orders of magnitude larger than the gas drag. However, there is not a strong correlation between redshift and the $F_{\rm DF}/F_{\rm drag}$ ratio. Given the resolution of our simulations, we do not resolve some high-density gas clumps nor the stellar clusters in our simulations, and therefore the comparison between DF and drag is only limited to simulations of a comparable resolution. The result from very high-resolution simulations may be different from ours.

In the left panel of Figure 3.4.3, we show the scattering relation between the $F_{\rm DF}/F_{\rm drag}$ ratio and the black hole mass $M_{\rm BH}$. We see a strong correlation between the $F_{\rm DF}/F_{\rm drag}$ ratio and the black hole mass: DF has significantly larger effects over gas drag on larger BHs, although the range of the ratio is large ar the low mass end. We fit a power-law to the

median of the scatter:

$$\frac{F_{\rm DF}}{F_{\rm drag}} = 250 \left(\frac{M_{\rm BH}}{10^7 M_\odot} \right)^{1.7}, \tag{3.16}$$

which roughly characterize the effect of the two forces on BHs of different masses. From this relation we see that for BHs with masses $> 10^7 M_\odot$, gas drag is in general less than 1% of DF. Finally, the right panels show the relation between the $F_{\rm DF}/F_{\rm drag}$ ratio and the BH's distance to the halo center: there is not a strong dependency on the BH's position within the halo.

Comparisons with the T15 Model

For the collisionless particles, we test and study two different implementations for the dynamical friction: DF(fid) and DF(T15) (see Section 3.3 for detailed descriptions). In Section 3.3 we pointed out three main differences between them: different kernel sizes (SPH kernel vs. nearest 100 DM+star), different definitions of $b_{\rm max}$ (10 ckpc vs. 1.5 ckpc/h), and different approximation of the surrounding velocity distribution (Maxwellian vs. nearest 100-sample distribution). Essentially, these differences mean that DF(fid) is a less-localized implementation than DF(T15). Now we would like to evaluate the effectiveness of these two implementations and show how different factors affect the final dynamical friction calculation.

Figure 3.4.4 shows the relevant quantities in the DF computation for the two methods. The two kernels both contain ~ 100 dark matter and star particles at high redshift ($z > 8$), but after that the SPH kernel (defined to include the nearest 113 gas particles) begins to include more and more stars and dark matter. The mass fraction of stars in the SPH kernel dominates over that of dark matter by ~ 10 times for a BH at the center of the galaxy. The larger kernel of DF(fid) has two effects: first, the DF density will be smoother over time; second, during halo mergers, the DF(fid) kernel can "see" the high-density region of the larger halo, which results in a higher DF near mergers compared to DF(T15). This is confirmed by the second panel, where we show the density for dynamical friction calculation from the two kernels. The densities calculated from the two kernels are similar in magnitude throughout the evolution, although the DF(T15) kernel yields slightly larger density due to its smaller size. Around the BH merger, the density in DF(fid) is larger due to its inclusion of the host halo's central region.

The third panel shows the Coulomb logarithm in the two models. Recall that $\Lambda = \frac{b_{\rm max}}{(GM_{\rm BH})/v_{\rm BH}^2}$, and so the Coulomb logarithm depends on the black hole's mass, its velocity relative to the surrounding particles, and the value of $b_{\rm max}$. From Figure 3.4.1(c), the mass of the DF(T15) black hole is slightly smaller, but the mass difference is small compared with the 6 times difference in $b_{\rm max}$. Given $b_{\rm max}$=10 ckpc/h in DF(fid) and $b_{\rm max}$=1.5 ckpc/h in DF(T15), we would expect the Coulomb logarithm to be larger for the former. However, there is yet another tweak: the $v_{\rm BH}^2$ term turns out to be significantly larger in the DF(T15) model(fourth panel). Note that in the DF(T15) model $v_{\rm BH}^2$ is calculated using only 100 surrounding particles, and for the high-density region we are considering here, the velocity

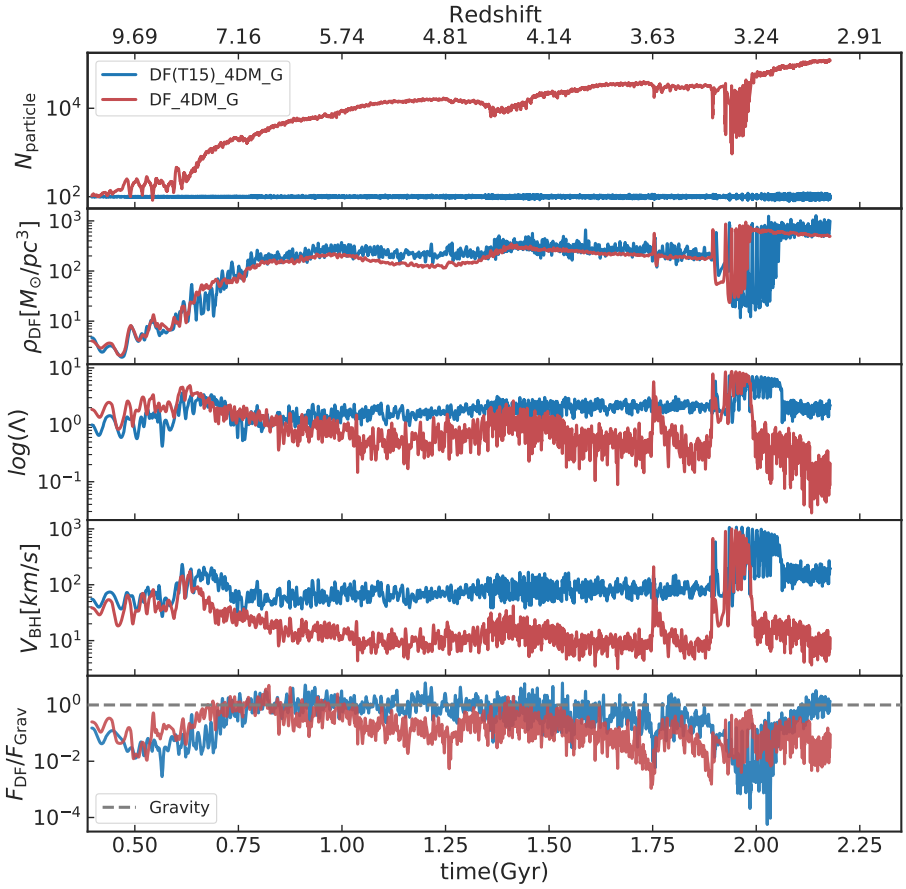

Figure 3.4.4: Comparison between different components in the two dynamical friction models, DF(fid) (**red**) and DF(T15) (**blue**) (see Section 3.3 for descriptions). We show the number of stars and dark matter particles included in the DF density and velocity calculation (**top panel**), the density used for DF calculation (**second panel**), the Coulomb logarithm used in the two methods (**third panel**), the velocity of the BH relative to the surrounding particles (**fourth panel**, note that the "surrouding particles" are defined differently for the two models), and the magnitude of DF relative to gravity (**bottom panel**). The higher DF in the DF(fid) model at $z > 8$ is due to the larger Coulomb logarithm. After $z \sim 7$, the higher density of DF(T15) due to more localized density calculation counterbalances its lower $\log(\Lambda)$, resulting in similar DF between $z = 8$ and $z = 3.5$. During the halo merger at $z = 3.5$, the DF(fid) model included particles from the target halo into the density calculation, and therefore yields larger DF during the merger.

of the nearest 100 particles is very noisy in time. As we will show in Appendix 3.B, for smaller black holes the difference in $v_{\rm BH}^2$ is not as large, and usually DF(fid) has a larger logΛ due to its larger $b_{\rm max}$.

In Figure 3.4.1(c), we show the evolution of the black hole under these two models. At high redshift ($z > 8$), due to the large log(Λ), the black hole in the DF(fid) simulation sinks slightly faster to the halo center. Between $z = 8$ and $z = 3.5$, both models have similar dynamical friction (as discussed in the previous paragraph) and the motion and mass accretion are also similar. Then at $z = 3.5$, within the host halo of the black hole major merger, dynamical friction in DF(fid) is again larger because the density kernel includes more particles from the high-density region in the target halo, and this leads to an earlier merger time.

Overall, the performance of the two models is similar. However, as we have seen in the velocity calculation of the black holes relative to the surrounding particles, DF(T15) could be too localized for simulations of our resolution ($\epsilon_g \sim 1$kpc/h) and is sometimes subject to numerical noise. Therefore, in our subsequent statistical runs we pick DF(fid) as our fiducial model, and will drop the 'fid' in its name hereafter.

Gravitationally Bound Merging Criterion

The merging criterion can affect not only the merging time, but also the dynamics and evolution of the black holes. Naively, we might expect the distance-only merging to produce more massive black holes, because black holes are merged more easily. However, in many cases this is not true, and we will illustrate here through one example.

Figure 3.4.1(d) shows the evolution of the same black hole with the same dynamical friction prescription, but different merging criteria. We note a drastic difference in the black hole's trajectories: while the BH in the gravitationally bound merger case is staying at the center of its host halo, the BH in the distance-only merger flies out of its host after a merger. This is because with the distance-only model, it is possible for one black hole to have a very large velocity at the time of the merger, since we do not limit the black hole's velocity. By momentum conservation, the black hole with a larger velocity can transfer the momentum to the other black hole (and the merger remnant) which might have already sunk to the halo center. The sunk black hole then drifts out of the halo center after a merger due to the large momentum injection. This is especially common in simulations where the black hole's dynamical mass is boosted, because the injected momentum is also boosted with mass and a smaller black hole in a satellite galaxy can easily kick a larger black hole out. If we add on the gravitational bound check, there will be more time for the black holes to lose their angular momentum, and so the injected momentum is far less, and in most cases does not kick each other out of the central region.

3.4.2 Black Hole Mergers

Having seen the effect of different dynamical models on the evolution of individual black holes, next we will discuss how the dynamics, together with different BH merging criteria, affect

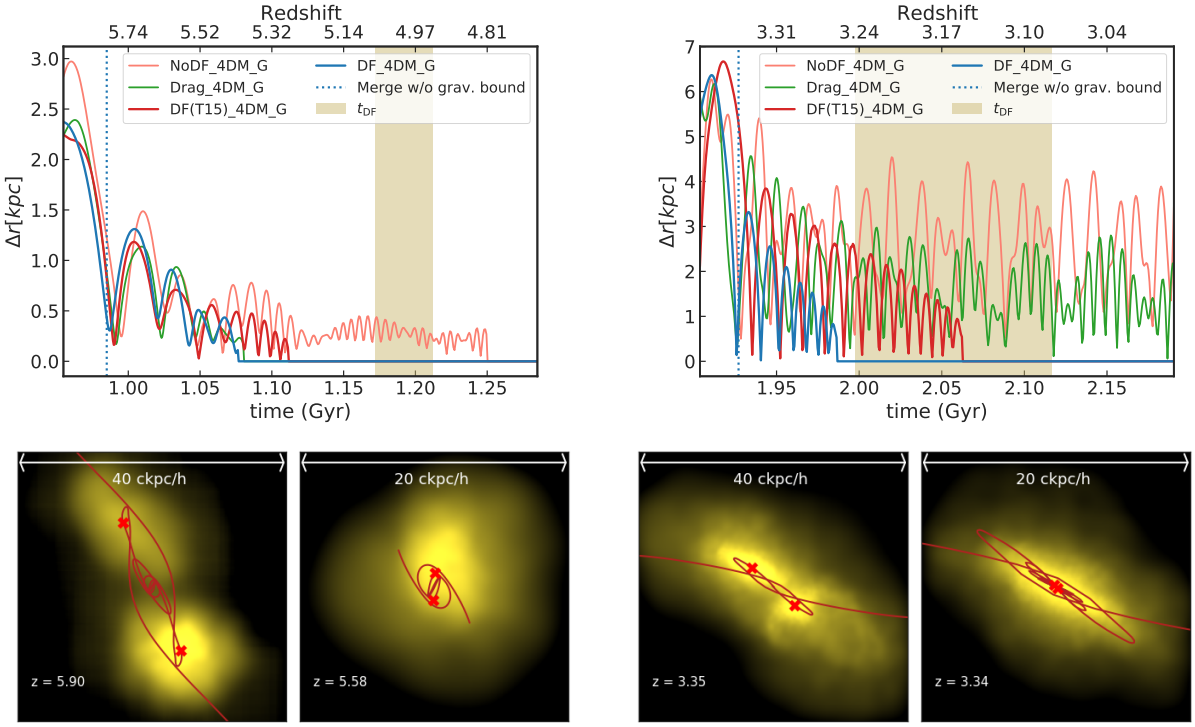

Figure 3.4.5: The comparison between the distance of two merging black holes in the no-correction, DF(fid), DF(T15) and gas drag models in the early stage (**left**) and later stage (**right**) of the black hole evolution. For early mergers, the effect of the frictional forces (DF and drag) is not very prominent but still noticeable. The DF and gas drag both allow the black holes to merge faster compare to the no-DF case. For the later merger happening in a denser environment, the effect of dynamical friction is clear. However, the gas drag does not have a big effect on the black hole at this late stage compared with the no-DF case. The lower panels show the merging black holes within their host galaxies as well as their trajectories towards the merger in the `DF_4DM_G` run. The left images show the early phase of the orbital decay, and the right images show the later phase when the orbits get smaller.

the evolution and mergers of the black holes. In particular, we want to study their merging time and trajectories before and after the mergers. Similar to the previous subsection, we will draw our examples from the two halos shown in Figure 3.3.1.

Effect of Dynamical Friction Modeling

We first look at how different dynamical models affect the time scale of black hole orbital decay and mergers. We pick two cases of mergers: one is an early merger at $z > 5$ when the black holes have not outgrown their dynamical masses; the other is a later merger at $z \sim 3.3$ when both BHs are larger than their seed dynamical masses (the major merger between BH1 and BH2 in Figure 3.3.1). Following Tremmel et al. [2015], we also compute the dynamical friction time for the two mergers using Equation (12) - Equation (15) from Taffoni et al. [2003]:

$$t_{\rm DF} = 0.6 \times 1.67{\rm Gyr} \times \frac{r_c^2 V_h}{G M_s} \log^{-1}\left(1 + \frac{M_{\rm vir}}{M_s}\right)\left(\frac{J}{J_c}\right)^{\alpha}, \tag{3.17}$$

where M_s is the mass of the smaller black hole (which we treat as the satellite), $M_{\rm vir}$ is the virial mass of the host halo of the larger black hole (found by AHF), V_h is the circular velocity at the virial radius of the host, and r_c is the radius of a circular orbit with the same energy as the satellite black hole's initial orbit. The last term $\left(\frac{J}{J_c}\right)^{\alpha}$ is the correction for orbital eccentricity, where J is the angular momentum of the satellite, J_c is the angular momentum of the circular orbit with the same energy as the satellite, and α is given by:

$$\alpha\left(\frac{r_c}{R_{\rm vir}}, \frac{M_s}{M_{\rm vir}}\right) = 0.475\left[1 - \tanh\left(10.3\left(\frac{M_s}{M_{\rm vir}}\right)^{0.33} - 7.5\left(\frac{r_c}{R_{\rm vir}}\right)\right)\right]. \tag{3.18}$$

In our calculation, the virial radius, velocity, and mass are obtained from the AHF outputs, and the circular radius, orbit energy, and angular momentum are calculated by fitting the halo density profile to the NFW profile.

Figure 3.4.5 shows distances between two merging black holes in the no-DF, DF(fid), DF(T15), and gas drag models in the early and later stages of their evolution. For the early merger, the effect of the frictional forces (DF and drag) is not very big but still noticeable. The DF and gas drag have similar effects on the orbital decay at higher redshifts, consistent with our discussion in Section 3.4.1. The DF(T15) model sinks the black hole a little slower than the DF(fid) model, but the difference is within 50 Myrs. All three friction models allow the black holes to merge faster compared to the no-DF case by ~ 150 Myrs.

For the later merger, which takes place in a denser environment, the effect of dynamical friction is clearer: the dynamical friction allows the black holes to sink within the gravitational softening of the particles in < 200 Myrs. Without dynamical friction the black hole's orbit does not have a clear decay below 2 kpc and does not merge at the end of our simulation. Furthermore, the gas drag does not have a big effect on the black hole at this late stage compared with the no-correction case. This follows from our discussion in section 3.4.1 that gas drag is much less effective at lower redshift compared to dynamical friction.

In both plots, the yellow shaded region is the dynamical friction time from the analytical calculation in Equation 4.7. Here we draw a band instead of a single line, because the black hole's orbit is not a strict ellipse, and the black hole is continuously losing energy. We calculate $t_{\rm DF}$ at multiple points between the first and second peak in the black hole's orbit (e.g. between $z = 5.9$ and $z = 5.7$ in the earlier case), and plot the range of those $t_{\rm DF}$. For both mergers, the analytical prediction is less than 150 Myrs later than the merger of the (fid) model. We note that the Taffoni et al. [2003] analytical $t_{\rm DF}$ is a fit to the NFW profiles, and the previous numerical and analytical comparisons on the black hole dynamical friction[e.g. Pfister et al., 2019, Tremmel et al., 2015] are performed in idealized NFW halos with a fixed initial black hole orbit. In our case, the halo profiles and black hole orbits are not directly controlled, and therefore deviation from the analytical prediction is expected. We will study such deviations statistically later in Section 3.5.3.

Effect of Gravitational Bound Check

In Section 3.3.3 we introduced two criteria which we use to perform black hole mergers in our simulations: we can merge two BHs when they are close in distance, and we can also require that the two BHs are gravitationally bounded in addition to the distance check.

In Figure 3.4.5 we show the difference in black holes' merging time with and without the gravitational bound criterion. The vertical dashed line marks the time that the two black holes in the `DF_4DM_G` simulation would merge if there was not the gravitational bound check. Without the gravitational bound check, the orbit of the black holes is still larger than 1 kpc when they merge, whereas with the gravitational bound check, the orbit size generally decays to less than 300 pc when the black holes merge. The merger without gravitational bound check generally makes the merger happen earlier by a few hundred Myrs (we will study the orbital decay time statistically in the next section). Therefore, for more accurate merger rate predictions as well as the correct accretion and feedback, it is necessary to apply the gravitational bound check during black hole mergers whenever the black hole has a well-defined velocity.

3.5 Black Hole Statistics

After looking at individual cases of black hole evolution, we now turn to the whole SMBH population in the simulations with different modeling of black hole dynamics. For statistics comparison, instead of using the $L_{\rm box} = 10$ Mpc/h constrained realizations **where we added 4σ density peaks to our small volumes (see Section 3.2.2)**, we now use $L_{\rm box} = 15$ Mpc/h unconstrained simulations. The details of our $L_{\rm box} = 15$ Mpc/h simulations are shown in Table 3.2.2.

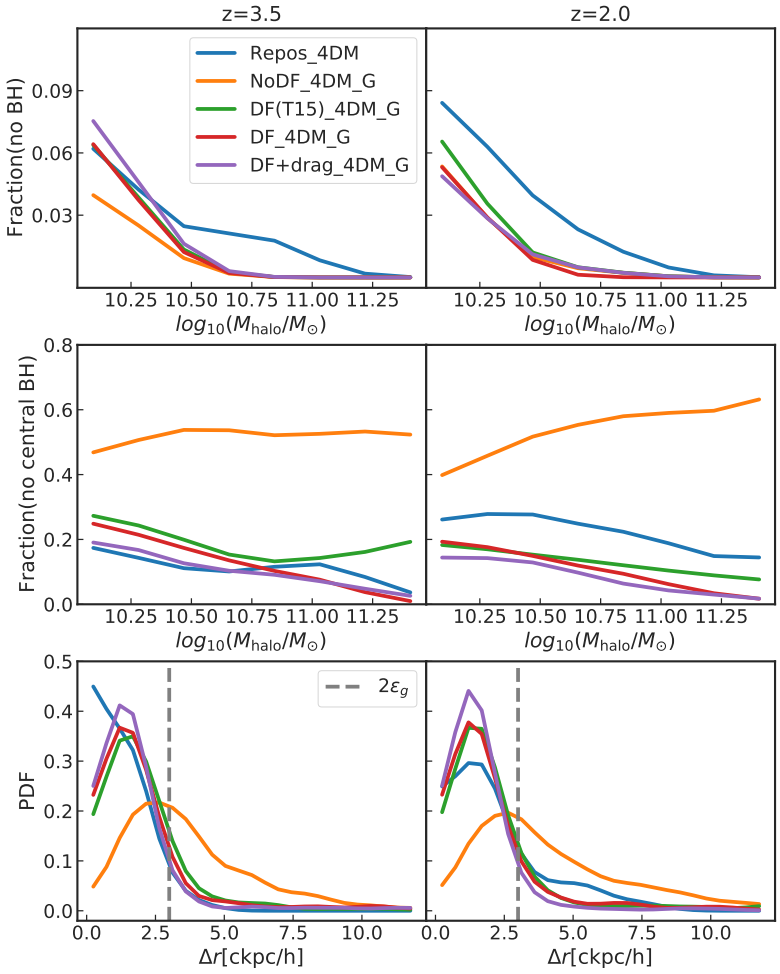

Figure 3.5.1: The effect of different BH dynamics modeling on BH position relative to its host. We include the reposition model (blue), no-DF model (orange),DF(T15) model (green), DF(fid) model (red) and the DF+drag model (purple). **Top:** The fraction of halos(subhalos) without a black hole for halos with masses above the black hole seeding mass at $M_{\rm halo} = 10^{10} M_\odot/h$. **Middle:** The fraction of halos without a central black hole ("central" means within $2\epsilon_g$ from the halo center identified by the halo finder), out of all halos with black holes. **Bottom:** Distribution of black holes' distance to its host halo center.

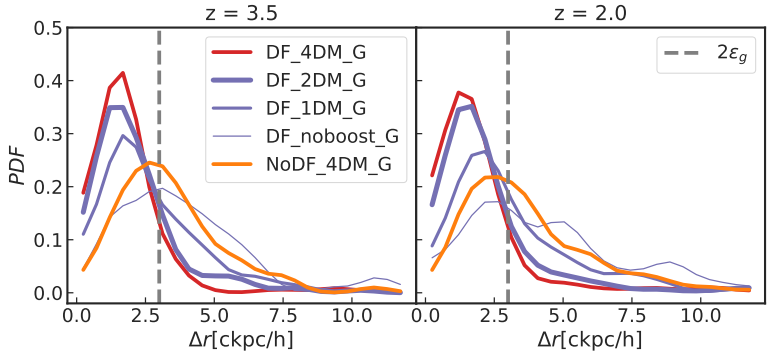

Figure 3.5.2: The effect of different choice of dynamical mass on the black holes' sinking status. We compare our fiducial DF model (`L15_DF_4DM`, red) with $M_{\rm dyn} = 4M_{\rm dm}$ to models with $M_{\rm dyn} = 2M_{\rm dm}$ (thick purple), $M_{\rm dyn} = M_{\rm dm}$ (purple), and $M_{\rm dyn} = M_{\rm BH}$ (thin purple). For $M_{\rm dyn} > M_{\rm dm}$, the majority of the BHs stay within $2\epsilon_g$ of the halo center, while for $M_{\rm dyn} < M_{\rm dm}$, many BHs still stalls at a relatively large radius. Noticeably, if we do not boost the dynamical mass of the BHs, the sinking is even worse than if we boost the dynamical mass but do not apply additional dynamical friction.

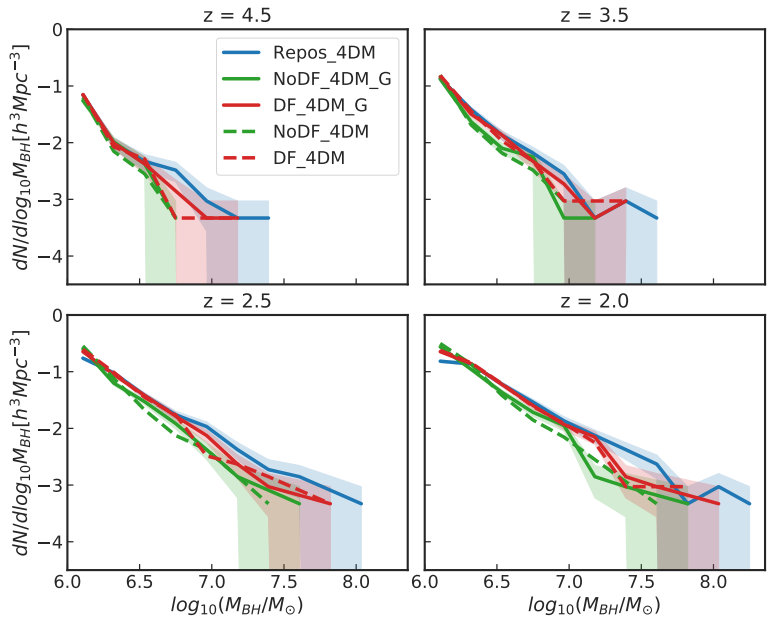

Figure 3.5.3: Mass functions for reposition, DF and no-DF simulations. With reposition (**blue**), we have the highest mass function and earlier formation of $10^8 M_\odot$ black holes. The no-DF simulations (**green**) have lower mass functions, which is expected due to low-accretion and merger rates from the black hole drifting. The dynamical friction model (**red**) yields a mass function in between.

3.5.1 Sinking of the Black Holes

With the added dynamical friction, we hope to assist the orbital decay of the black holes and prevent the stalling due to the smoothed gravity. Hence, we start by looking at the black holes' position relative to the host halos. Due to the resolution limit of our simulations, we would not expect the black holes to be able to sink to the exact minimum potential. Instead we consider a $< 2\epsilon_g = 3$ ckpc/h distance to be "good sinking".

In Figure 3.5.1, we show the statistics related to black holes' sinking status. We included the comparison between the reposition model (`L15_Repos_4DM`), the no-DF model (`L15_NoDF_4DM`), the two dynamical friction models (`L15_DF_4DM` and `L15_DF(T15)_4DM`) and the DF+drag model(`L15_DF+drag_4DM`). To start with, we simply count the fraction of halos without a black hole when its mass is already above the black hole seeding criterion (i.e. $10^{10} M_\odot/h$). The top panel shows the fraction of large halos without a BH for different models at $z = 3.5$ and $z = 2$. Surprisingly, the no-DF model ends up with the least halos without a black hole. This is because even though the black holes without dynamical corrections cannot sink effectively, the high dynamical mass still prevents sudden momentum injections from surrounding particles, and therefore most BHs still stays within their host galaxies. The dynamical friction models perform equally well, with $< 10\%$ no-BH halos at the low-mass end. The reposition model, however, ends up with the most no-BH halos, even though repositioning is meant to pin the black holes to the halo center. This happens because under the repositioning model, the central black holes tend to spuriously merge into a larger halo during fly-by encounters, leaving the smaller sub-halo BH-less.

Next we look at where the black holes are located within their host galaxies. For all the halos with at least one black hole, we examine whether the black hole is located at the center (i.e.$< 2\epsilon_g = 3$ckpc/h from the halo center). The middle panel of Figure 3.5.1 shows the fraction of halos without a central BH. The no-DF model has significantly more halos without a central BH compared to the other models, with over half of the halos hosting off-center BHs. Among the three runs with dynamical friction, the DF(T15) and DF(fid) models have a similar fraction of halos ($\sim 20\%$) without a central BH, and we can see this fraction dropping from $z = 3.5$ to $z = 2$, meaning that many BHs are still in the process of sinking towards the halo center. When we further add the gas drag, 10% more halos host at least one central BH, and the difference between the drag and no-drag central BHs is more prominent at high redshifts.

Our definition of a "central" BH depends on the resolution of our simulation, but we note that our conclusions above do not change if we shift this criterion by a factor of ~ 2. Moreover, even though we consider the smaller fraction of off-centered BHs as an evidence that the dynamical friction is taking effect, we note that there are both theoretical and observational evidences that off-center BHs do exit and merge with each other [e.g. Bellovary et al., 2010, Kulier et al., 2015, Volonteri and Rees, 2005]. In the case of dual/offset AGN observations, we should also expect to see BHs further than 5 kpc apart [e.g. Barrows et al., 2018, Reines et al., 2020]. Therefore, the amount of off-center BHs should not be treated as an absolute standard for evaluating BH dynamical models.

Interestingly, the repositioning algorithm is not as efficient at sinking the BHs at $z = 2$ as

the DF. This is because our repositioning algorithm places the BHs at the minimum potential position within the accretion kernel, instead of within the entire halo. The majority of the offset between the BH positions and the halo center comes from the offset between the minimum-potential position accessible to the BH (i.e. minimum-potential in the accretion kernel) and the minimum-potential position in the halo. Such offset can be especially severe at lower redshift, when the size of the accretion kernel gets smaller and mergers happen more frequently, making it easier for the black holes to get stuck at a local minimum.

In the bottom panels we show the distributions of the black holes' distance to the halo centers under different models. For the no-DF run, again we see that the black holes fail to move towards the halo center at lower redshift, resulting in a much flatter distribution compared to all the other models. In comparison, when we add dynamical friction to the black holes, for both the DF(fid) and the DF(T15) models the distributions are pushed much closer to the halo center, with a peak around the gravitational softening length. When we then add the gas drag in addition to DF, the peak at ϵ_g becomes slightly higher than those in the DF-only runs. The combination of DF and gas drag, as we would expect from the case studies, is the most effective in sinking the black holes to the halo centers and stabilizing them. Finally, we plot the repositioning model for reference. It does well in putting the black hole close to the minimum potential, and often the black holes can be located at the exact minimum-potential position (the distributions peak at 0 for $z = 3.5$). However, as discussed in the previous paragraph, there are cases where the local minimum potential found by the repositioning algorithm does not coincide with the global minimum potential of the halo, and that is why we also see non-zero probability density for $\Delta r > 3$ ckpc/h at $z = 2$.

In Figure 3.5.2, we show the effect of different choice of dynamical mass on the black holes' sinking status. We compare our fiducial DF model (`L15_DF_4DM`) with $M_{\rm dyn} = 4M_{\rm dm}$ to models with $M_{\rm dyn} = 2M_{\rm dm}$, $M_{\rm dyn} = M_{\rm dm}$, and $M_{\rm dyn} = M_{\rm BH}$. We can see that for $M_{\rm dyn} > M_{\rm dm}$, the majority of the BHs stay within $2\epsilon_g$ of the halo center, while for $M_{\rm dyn} < M_{\rm dm}$, many BHs still stalls at a relatively large radius. Noticeably, if we do not boost the dynamical mass of the BHs, the sinking is even worse than if we boost the dynamical mass but do not apply additional dynamical friction.

The statistics we have seen for the models above are consistent with the results from the case studies. This shows that even though for the case studies we have focused mainly on large black holes in one of the biggest halo, a similar trend still applies to other black holes in the cosmological simulations, which are embedded in smaller halos or subhalos. Moreover, the fact that we still have off-center BHs even after adding the dynamical friction is in line with predictions from previous simulations [e.g. Bellovary et al., 2011, Governato et al., 1994, Tremmel et al., 2018a, Volonteri and Rees, 2005], and is not due to the inefficient sinking within our simulation.

3.5.2 Black Hole Mass Function

Next we look at how different dynamics affect the black hole mass function (BHMF). One problem with the repositioning method is that it places the black holes at the galaxy center

too quickly, which could result in excess accretion and thus a higher mass function. On the other hand, if we do not add any correction to the black hole motion, many BHs will not go though efficient accretion and mergers, and we will see a lower mass function. We would expect the BHMF in the dynamical friction run to fall between the repositioning case and the no-DF case.

Figure 3.5.3 shows the BHMF from the reposition(`L15_Repos_4DM`), dynamical friction (without gravitational bound check:`L15_DF_4DM`; with gravitational bound check:`L15_DF_4DM_G`), and no-DF (without gravitational bound check: `L15_NoDF_4DM`; with gravitational bound check: `L15_NoDF_4DM_G`) runs. The reposition model yields the highest mass function, and is the only simulation with more than one $10^8 M/h$ black holes at $z = 2$. This is expected from the over-efficient BH mergers and the high-density surroundings in the reposition model. Moreover, it creates increasingly more massive BHs over time, as the increased merger rate produces a stronger effect over time. The no-DF runs produces the lowest mass function due to the off-centering, while the DF mass function falls between the reposition and no-DF case as we expected.

Naively, we would expect the models without gravitational bound checks to produce a higher mass function, because it allows for easier mass-accretion via mergers. However, as discussed in Section 3.4.1, this is not the case if we compare the dashed lines and solid lines with the same colors. For example, under the DF model, the `L15_DF_4DM_G` simulation forms more massive black holes than the `L15_DF_4DM` simulation, especially at lower redshift. The reason can be traced back to what we have seen in Figure 3.4.1(d): when there is no gravitational bound check, the large momentum injection during a merger kicks the black hole out of the halo center, thus preventing the efficient growth of large black holes.

Considering the relatively large uncertainties due to the limited volume, the difference in the mass function is not very significant. We would expect other factors such as the black hole seeding, accretion and feedback to have a larger effect on the mass function compared to the dynamical models we show here [e.g. Booth and Schaye, 2009].

3.5.3 Dynamical Friction Time and Mergers

Because the reposition method is used in most large-volume cosmological simulations, a post-processing analytical dynamical friction time is calculated in order to make more accurate merger rate predictions. Now that we have accounted for the dynamical friction on-the-fly, we want to study how our numerical mergers with dynamical friction compare against the analytical predictions, and how different dynamical models impact the black hole merger rate.

In Section 3.4.2, we compared the numerical merging time to the analytical predictions for two merger cases. Now we use the same method to calculate an analytical dynamical friction time for all black hole mergers in our `L15_DF_4DM_G` simulation. For each pair, we begin the calculation at the time $t_{\rm beg}$ when the black hole pair first comes within 3 ckpc$/h$ of each other, as this mimics the merging time without the gravitational bound check, and is also close to the merging criterion under the reposition model. The numerical dynamical friction

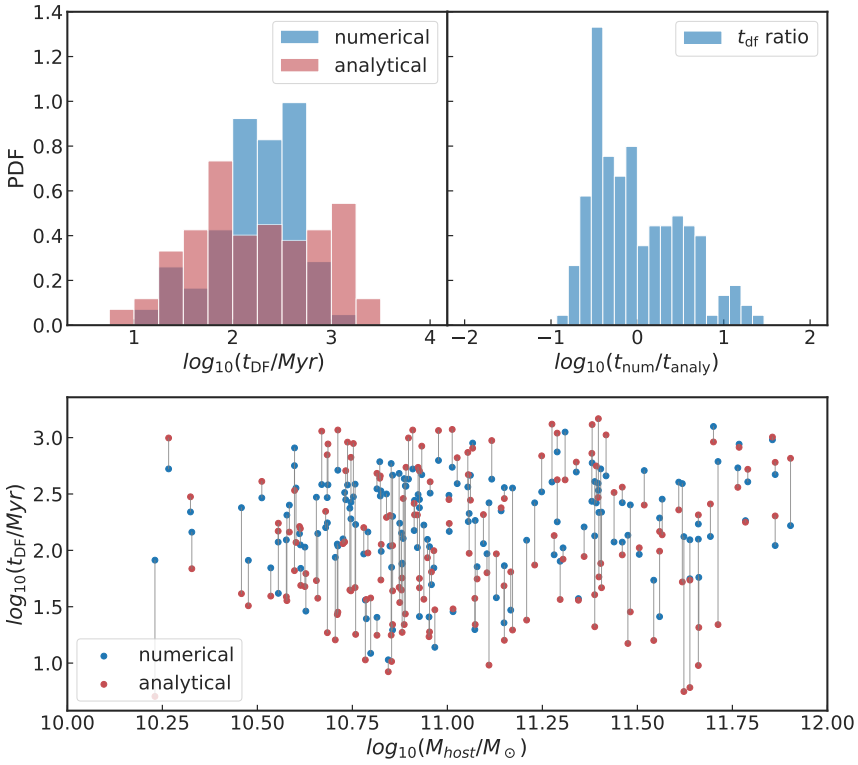

Figure 3.5.4: The delay of mergers due to the dynamical friction time. Here we compare the numerical dynamical friction time,$t_{\rm num}$, to the analytically calculated time (following Equation 4.7) $t_{\rm analy}$. **Top left:** distribution of the dynamical friction time from numerical merger (blue) and analytical predictions (red). **Top right:** ratio between the numerical and analytical $t_{\rm df}$. Their difference is less than one order of magnitude in all merger cases. **Bottom:** dynamical friction time as a function of the virial mass of the host halo for the numerical (blue) merger and analytical predictions (red). The same merger event is linked by a grey line.

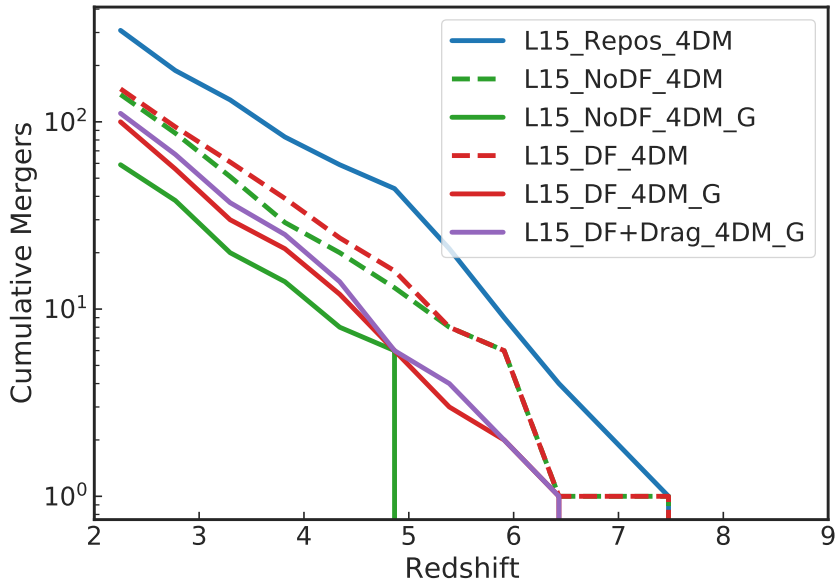

Figure 3.5.5: The cumulative mergers for different BH dynamics and merging models. The reposition model (**blue solid**) predicts more than two times the total mergers compared with the other models. Without the gravitational bound check, the DF (**red dashed**) and the no-DF model (**green dashed**) predicts similar numbers of mergers, indicating that the first encounters of the black hole pairs are similar under the two models. However, if we add the gravitational bound check, the dynamical friction model (**red solid**) yields $\sim 50\%$ more mergers compared to the no-correction model. Adding the gas drag in addition to dynamical friction (**purple solid**) raises the mergers by a few.

time $t_{\rm num}$ is the time between the numerical merger and $t_{\rm beg}$. The analytical dynamical friction time $t_{\rm analy}$ is calculated using the host halo information in the snapshot just before $t_{\rm beg}$ and the black hole information at the exact time-step of $t_{\rm beg}$.

Figure 3.5.4 shows the comparison between the numerical and analytical dynamical friction times. In the top panel we show the distribution of the two times as well as the distribution of their ratio. We note that for all the mergers happening numerically, $t_{\rm analy}$ does not exceed 2 Gyrs, and most have $t_{\rm analy}$ less than 1 Gyr. This means that we do not have many fake mergers that shouldn't merge until much later (or never). Also, the ratio plot shows that the numerical and analytical times are always within an order of magnitude of each other, with most of the numerical mergers earlier than the analytical mergers. The numerical merger time is peaked between 100 Myrs and 1 Gyrs, whereas the analytical calculation yields a flatter distribution. We would expect $t_{\rm analy}$ to be longer than $t_{\rm num}$, both because we have a selection bias on $t_{\rm DF}$ by ending the similation at $z = 2$, and because we numerically merge the black holes when their orbit is still larger than 3 ckpc/h. However, this does not explain why $t_{\rm analy}$ has a higher probability between 10 Myrs and 100 Myrs.

To see the individual merger cases in the distribution more clearly, in the lower panel of Figure 3.5.4 we plot all the numerical and analytical dynamical friction times as a function of the host halo's virial mass. From this figure we do not see a clear dependence of either dynamical friction times on the host halo's virial mass. There is also no strong correlation between the $t_{\rm num}/t_{\rm analy}$ ratio and the halo mass. We do not further investigate the discrepancies between the numerical and analytical results, as these results can vary significantly from system to system.

We note that although the numerical model has free parameters (such as $b_{\rm max}$, $M_{\rm dyn,seed}$) that can impact the merging time (but see Appendix 3.C), it can account for the immediate environment around black hole and adjust the dynamical friction on-the-fly. More importantly, it also accounts for the interaction between the satellite BH and its own host galaxy, which could reduce the sinking time significantly [e.g. Dosopoulou and Antonini, 2017]. The analytical model, though verified by N-body simulations, does not react to the environment of the merging galaxies by always assuming an NFW profile. Moreover, it only models the sinking of a single BH without embedding it in its host galaxy. Therefore, we expect the numerical result to be a more realistic modeling of the binary sinking process.

After comparing the DF model against the analytical prediction, next we compare different numerical models in terms of the black hole merger rate. Figure 3.5.5 shows the cumulative mergers from $z = 8$ to $z = 2$. We have included comparisons between the reposition, dynamical friction and no-DF models, both with and without the gravitational bound check. The reposition model predicts more than twice the total number of mergers compared to the other models. Without the gravitational bound check, the DF and the no-DF models predict similar numbers of mergers, indicating that the first encounters of the black hole pairs are similar under the two models. However, if we add the gravitational bound check, the DF model yields $\sim 50\%$ more mergers compared to the no-DF model, because the addition of DF assists energy loss of the binaries and leads to earlier bound pairs. Finally, the merger rate is not very sensitive to adding the gas drag: the merger rate in the DF-only model is

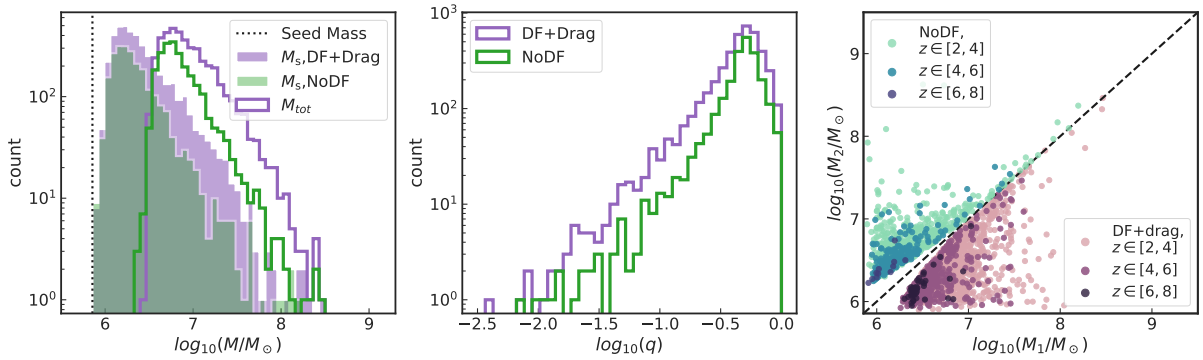

Figure 3.6.1: **Left:** Distribution of the mass of the smaller black hole (M_s), and distribution of the total mass of the binary ($M_{\rm tot}$). For both simulations, the mergers in which at least one of the black holes is slightly above the seed mass dominate. The most massive binary has a total mass of $3 \times 10^8 M_\odot$. **Middle:** The mass ratio q between the two black holes in the binary. We see a peak at $\log(q) = -0.5$, corresponding to pairs in which one BH is about three times larger than the other. **Right:** Scatter of the two black hole masses in the binaries, binned by redshift. To separate the scatter in the two simulations, for the DF+drag run we take M_1 to be the mass of the larger BH, while for the NoDF run M_2 is the larger BH.

similar to that of the DF+drag model. This can be foreseen in the comparison shown in Figure 3.4.2, where the gas drag is subdominant in magnitude.

3.6 Merger Rates in the 35Mpc/h Simulations

Based on all the previous test of BH dynamics modeling, we have reached the conclusion that the DF+drag model with $M_{\rm dyn} = 4M_{\rm DM}$ is most capable of sinking the black hole to the halo center. Hence, we choose to use this model to run our larger-volume simulation `L35_DF+drag_4DM_G` for the prediction of the BH coalescence rate. Besides this model, we also perform a same-size run without the dynamical friction, `L35_NoDF_4DM_G`, as a lower limit for the predicted rate. Our `L35` simulations are run down to $z = 1.1$. The black hole seed mass is $5 \times 10^5 M_\odot/h$ and the minimum halo mass for seeding is $10^{10} M_\odot/h$. The details of these two simulations are shown in Table 3.2.2.

3.6.1 The Binary Population

Because this work mainly focuses on model verification and is not intended for accurate merger-rate predictions, we do not account for the various post-numerical-merger time delays. These delays can be caused by physical processes such as sub-ckpc scale dynamical friction, scattering with stars, gravitational wave driven inspiral and triple MBH systems [e.g. Bonetti et al., 2018, Dosopoulou and Antonini, 2017, Quinlan, 1996, Sesana et al.,

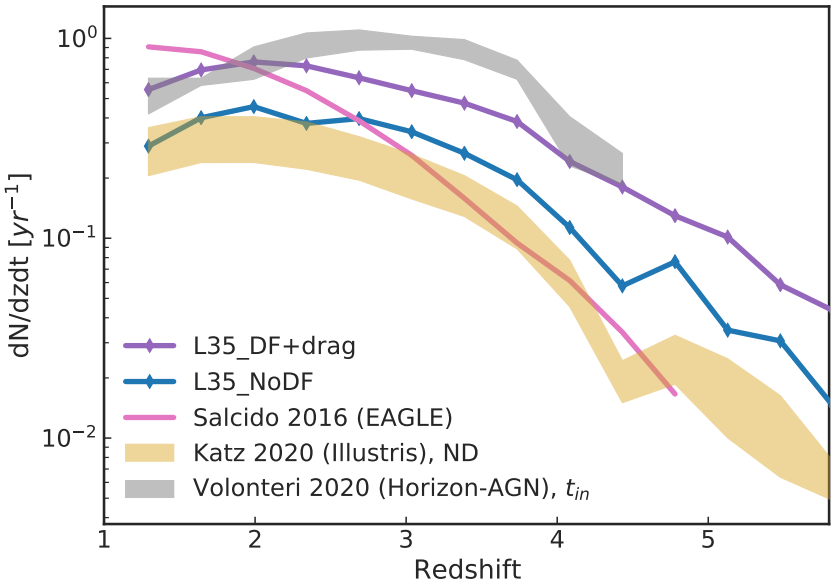

Figure 3.6.2: Merger rate per year of observation per unit redshift predicted from our `L35_DF+drag_4DM_G` (**purple**) and `L35_NoDF_4DM_G` (**blue**) simulations. For comparison, we also show the the prediction from recent hydro-dynamical simulations. We include three simulations of similar mass-resolution: Volonteri et al. [2020] from the Horizon-AGN simulation (**gray**), Katz et al. [2020] (**yellow**) from the Illustris simulation and Salcido et al. [2016] from the EAGLE simulations (**pink**). We note that the merger rate is sensitive to the BH seeding criterion which can be different among the simulations shown. Since we do not apply any post-processing delays after the numerical mergers, we only compare to results without delays.

2007a, Vasiliev et al., 2015]. We consider all the numerical mergers as true black hole merger events. Without any post-process selection, there are 25224 black holes and 4237 mergers in the `L35_DF+drag_4DM_G` run, and 27693 black holes and 2349 mergers in the `L35_NoDF_4DM_G` run down to $z = 1.1$.

Figure 3.6.1 shows the distribution of the binary parameters for the mergers in our simulations. For both simulations, there is at least one black hole around the seed mass for most mergers, but the peak does not lie at the exact seed mass. The most massive binary has a total mass of $3 \times 10^8 M_\odot$. For the mass ratio q between the two black holes in the binary, we see a peak at $\log(q) = -0.3$, corresponding to pairs in which one BH is about two times larger than the other. Finally, we show the scatter of the two progenitor masses. The low mass end of the population deviates more from $q = 1$, while the majority of same-mass mergers come from the $5 \times 10^6 M_\odot \sim 5 \times 10^7 M_\odot$ mass range.

Comparing with previous simulations such as Katz et al. [2020], Salcido et al. [2016], we do not see as many cases of seed-seed mergers, but our distribution in q is similar to that shown in Weinberger et al. [2017] where the larger progenitor is a few times larger than the small progenitor. This is due to our larger black hole seed mass of $5 \times 10^5 M_\odot$ ($10^6 M_\odot$ in Weinberger et al. [2017]): the mass accretion in the early stage is proportional to $M_{\rm BH}^2$, and so during the time before the black hole mergers, our black holes accrete more mass compared to the simulations with smaller seeds. This explains why both of our black holes in the binaries are not peaked at the exact seed mass.

3.6.2 Merger Rate Predictions

We use the binary population shown in the previous section to predict the merger rate observed per year per unit redshift. The merger rate per unit redshift per year is calculated as:

$$\frac{dN}{dz\, dt} = \frac{N(z)}{\Delta z V_{c,sim}} \frac{dz}{dt} \frac{dV_c(z)}{dz} \frac{1}{1+z}, \tag{3.19}$$

where $N(z)$ is the total number of mergers in the redshift bin z, Δz is the width of the redshift bin, $V_{c,sim}$ is the comoving volume of our simulation box and $dV_c(z)$ is the comoving volume of the spherical shell corresponding to the z bin.

We compare our results against recent predictions from hydro-dynamical simulations of similar resolution, Salcido et al. [2016], Katz et al. [2020] and Volonteri et al. [2020]. Here we briefly summarize relevant information about their merger catalogs. The Ref-L100N1504 simulation in the EAGLE suite used in Salcido et al. [2016] has an 2^3 times larger simulation box and slightly higher resolution than our simulations. They seed $1.4 \times 10^5 M_\odot$ black holes in $1.4 \times 10^{10} M_\odot$ halos. They adopt the reposition algorithm for black hole dynamics, but set a distance and relative speed upper limit on the repositioning to prevent black holes from jumping to satellites during fly-by encounters. We compare with their no-delay rate during the inspiral phase. The *Illustris* simulation used in Katz et al. [2020] has a similar box size, resolution and BH dynamics to the Ref-L100N1504 simulation in EAGLE, except that their halo mass threshold for seeding BHs is $7 \times 10^{10} M_\odot$. We compare against their ND model,

in which mergers are also taken to occur at the numerical merger time without any delay processes. The Horizon-AGN simulation in Volonteri et al. [2020] is 4^3 times larger than our simulation box, with ~ 5 times coarser mass resolution and a black hole seed mass of $10^5 M_\odot$. Instead of seeding BHs in halos above certain mass threshold, the seeding in Volonteri et al. [2020] is based on the local gas density and velocity dispersion, and seeding is stopped at $z = 1.5$. For black hole dynamics, they apply dynamical friction from gas, but not from collisionless particles.

Figure 4.5.1 shows our merger rate prediction in the `L35_DF+drag_4DM_G` and `L35_NoDF_4DM_G` simulations. The `L35_DF+drag_4DM_G` run predicts ~ 2 mergers per year of observation down to $z = 1.1$, while the `L35_NoDF_4DM_G` run predicts ~ 1. The merger rates from both simulations peak at $z \sim 2$. This factor-of-two difference between the two simulations is consistent with what we predicted in the $L_{\rm box} = 15$ Mpc/h runs in Figure 3.5.5. Although we did not run a $L_{\rm box} = 35$ Mpc/h simulation with the repositioning model, we expect such a run to predict $5 \sim 6$ mergers per year down to $z = 1.1$ according to 3.5.5.

Generally speaking, our simulations yield similar merger rates as the raw predictions from the previous works of comparable resolution. However, we still note some differences both in the overall rates and in the peak of the rates. We will now elaborate on the reasons for those discrepancies.

First, both of our simulations predict more mergers compared with the Katz et al. [2020] ND model prediction. This is surprising given that in the 15 Mpc/h runs we saw $2 \sim 3$ times more mergers when we used the reposition method like Katz et al. [2020] and Salcido et al. [2016] did, comparing to our DF+Drag model. Although Katz et al. [2020] cut out $\sim 25\%$ secondary seed mergers and binaries with extreme density profiles, their rate is still lower after adding the cut-out population. One major reason for the higher rate from our simulation compared to Katz et al. [2020] is the different seeding parameters we use: our minimum halo mass for seeding a black hole is $10^{10} M_\odot/h$, which is 5 times smaller compared with Katz et al. [2020]. Moreover, our seeds are a factor of 5 larger. Hence, we have a denser population of black holes in less-massive galaxies, which is likely to result in a higher merger rate even compared to the reposition model used in *Illustris*.

Second, although the rates from EAGLE, Horozon-AGN and our `L35_DF+drag_4DM_G` simulation cross over at $z \sim 2$, the slope of our merger rate is very different. Volonteri et al. [2020] predicts most mergers at $z \sim 3$, whereas the Salcido et al. [2016] rate peaks at $z \sim 1$. This difference can also be traced to the different seeding rate in the three simulations: in Salcido et al. [2016], the seeding rate keeps increasing until $z \sim 0.1$, while we observe a drop in seeding rate at $z = 3$ in our simulations. In Volonteri et al. [2020], due to the different seeding mechanism, BH seeds form significantly earlier, leading to a peak in merger rate at a higher redshift. Hence the peak in the BH merger rate is strongly correlated with the peak in the BH seeding rate.

Finally, besides the effect due to different BH seed models on the merger rate, higher resolution can significantly increase the BH merger rates in the simulations. As was shown in previous work [e.g. Barausse et al., 2020, Volonteri et al., 2020], dwarf galaxies in low-mass halos can have large numbers of (small mass) BH mergers, and so resolving such halos and

galaxies can increase the BH merger rate significantly. The merger rate differences between high and low resolution and the associate choice for the seed models can lead to large differences in the predictions of merger rates than taking account DF in the BH dynamics.

3.7 Conclusions

In this work we have tested methods for implementing dynamical friction from collisionless particles (i.e. stars and dark matter) and gas in low-resolution cosmological simulations (with mass resolution $M_{\rm DM} \sim 10^7 M_\odot$ and spatial resolution of $\epsilon_g \sim$1kpc/h), both for single black hole evolution/mergers using constrained simulations, and for the black hole population using unconstrained simulations.

We showed that dynamical friction from collisionless particles can effectively assist the black hole orbit to decay to within $2\epsilon_g$ of the galaxy center, representing a marked improvement over models that do not include any dynamical correction. Importantly, we find that for our prescription to work well, the dynamical mass of the black holes must be at least twice the mass of the dark matter particles. This is in agreement with results from Tremmel et al. [2015]. The dynamical friction implementation from Tremmel et al. [2015] (DF(T15)) and our implementation adapted to lower-resolution simulations (DF(fid)) result in dynamical friction of a similar magnitude, and have comparable effects on the black holes' dynamics. However, we find that our fiducial model is marginally more suitable for low-resolution simulations, as the nature of the calculation results in less noisy force corrections.

After applying the dynamical friction and performing the gravitational bound check on the black hole pairs, the dynamical friction time of the black holes is consistent with analytical predictions, although the variances can be large for individual black holes due to their varied environments. We note that checking whether the two black holes are gravitationally bound at the time of the merger is necessary both for preventing sudden momentum injection onto the black holes, and for allowing a more realistic orbital decay time.

By direct comparison of the force magnitudes throughout the simulation, we find that dynamical friction from collisionless particles dominate in the majority of cases. The influence of gas drag is highest at the high redshifts, but even then it is typically similar to or less than the contribution from stars and dark matter. This is in broad agreement with the results from Pfister et al. [2019], though we stress that our simulations cannot resolve the structure of gas on the smallest scales. It is possible that interactions with gas is still important, such as migration within circumbinary disks [e.g. Haiman et al., 2009].

Using our fiducial DF+drag model, we calculate the cumulative merger rate down to $z = 1.1$ using a $L_{\rm box} = 35$ Mpc$/h$ simulation. Without considering any post-merger delays, we predict ~ 2 mergers per year for $z > 1.1$, and we lower bound our prediction by a no-dynamical-friction run which predicts ~ 1 merger per year. Compared with existing predictions from hydro-dynamical simulations [Katz et al., 2020, Salcido et al., 2016, Volonteri et al., 2020], our rates are consistent with the raw merger rates (rates before post-processing delays are added) from previous works of similar resolution. While the dynamics modeling has significant effects (factor of a few according to our experiments) on the BH merger rate,

we also found that the different BH seeding criteria and mechanisms account also play a big role in the merger rate predictions.

Our work has demonstrated the feasibility of recovering sub-kpc-scale BH dynamics in low-resolution cosmological simulations by adding the unresolved dynamical friction. This is the first step in improving upon the widely-adopted reposition model and in tracking the BH dynamics directly down to the resolution limit. Beyond the resolution limit, we still need to account for several smaller-scale binary processes before we can make realistic merger rate predictions [e.g. Bonetti et al., 2018, Dosopoulou and Antonini, 2017, Haiman et al., 2009, Katz et al., 2020, Kelley et al., 2017a, Quinlan, 1996, Sesana et al., 2007a, Vasiliev et al., 2015]. Nevertheless, having access to the full dynamical information of the binary at the time of the numerical merger also helps us to better model these small-scale processes. We will leave the analysis of post-merger delays for future works.

There are still several aspects of the DF model that remain somewhat uncertain. Most importantly, the parameters (e.g. $b_{\rm max}$,$M_{\rm dyn,seed}$) in the current dynamical friction model can induce uncertainties in the sinking timescale and the merger rate predictions. For example, reducing $M_{\rm dyn,seed}$ to a value similar to or below the dark matter particle mass will reduce the merger rate by a factor of two or more. Our current choice is well tested in our simulations, but it is still subject to the limitations of our spatial and mass resolution. The limit in the $M_{\rm BH}/M_{\rm DM}$ ratio also hinders comprehensive studies of BH seeding scenarios in the cosmological context. We would need insights from high-resolution simulations [e.g. Dosopoulou and Antonini, 2017, Pfister et al., 2019] to better model the dynamics of low-mass BHs within cosmological simulations.

3.A Dynamical Mass and Resolution Effect

3.A.1 Varying Dynamical Mass

One major difference between our model and previous modeling of the dynamical friction is that we boost the mass term during the early stage of black hole growth by a factor of $k_{\rm dyn} = M_{\rm dyn,seed}/M_{\rm BH}$. This is to prevent the drifting of the black holes due to dynamical heating when the black hole mass is below the dark matter particle mass in the context of large and low-resolution cosmological simulations.

Here we show the effect of setting different $k_{\rm dyn}$ by running three simulations with the same resolution and dynamical friction models, but various $k_{\rm dyn}$ ratios. They are listed in Table 3.2.1 as `DF_4DM_G`, `DF_2DM_G`, and `DF_1DM_G`, with $k_{\rm dyn} = 4, 2, 1$, respectively.

Figure 3.A.1(a) shows the evolution of the same black hole for different $k_{\rm dyn}$. By comparing the three cases, we can see that the black hole's behavior is very similar for all the physical quantities we have plotted. However, we also note that the similar behavior of different $M_{\rm dyn}$ is case-dependent. The case we present here is a black hole within a large density peak where the black hole is subject to a deep potential and can sink more easily, but the sinking of BHs in shallower potentials can be more sensitive to the seed dynamical mass. Nevertheless, $k_{\rm df} = 2$ is generally sufficient to assist the sinking of most black holes

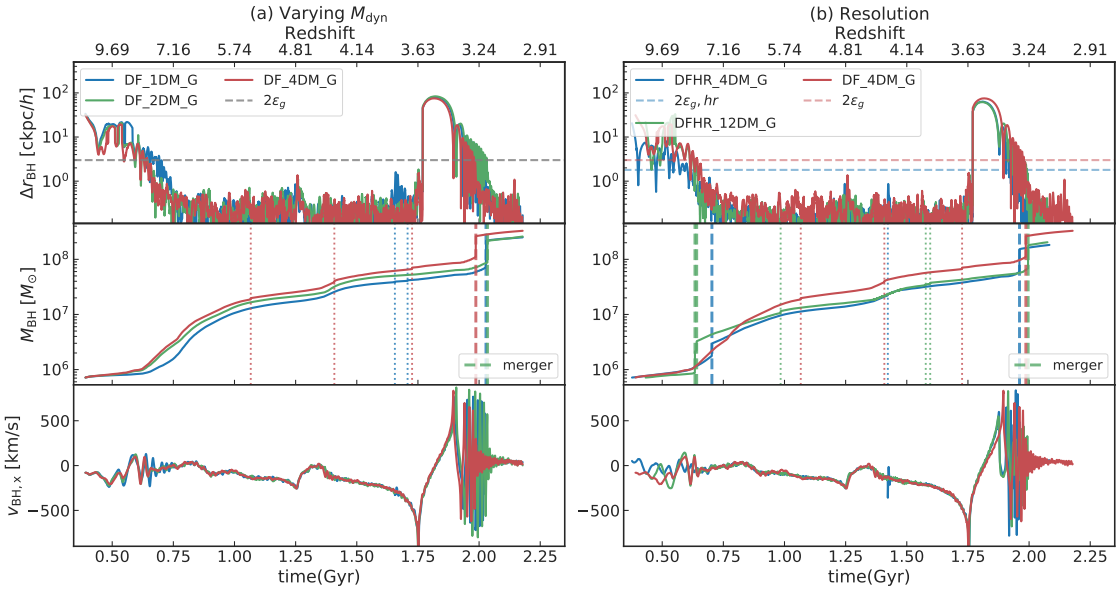

Figure 3.A.1: **(a)**: Comparisons of different black hole seed dynamical mass. The effect of varying $M_{\rm dyn,seed}$ is small in this case. But this is partially due to the large BH we pick. **(b):** Comparison with higher-resolution run with the same $M_{\rm dyn}/M_{\rm DM}$ ratio.

and produces similar merger rates to $k_{\rm df} = 4$ (see Appendix 3.C). The convergence at $k_{\rm df} = 2$ is consistent with the $M_{\rm BH}/M_{\rm DM} = 3$ ratio used in Tremmel et al. [2018a], and relaxes the ratio used in previous works [e.g. Pfister et al., 2019, Tremmel et al., 2015] of $M_{\rm BH} \sim 10 M_{\rm DM}$.

3.A.2 Resolution Effect

Here we show how our model performs under different resolutions. For this experiment we use our fiducial resolution run `DF_4DM_G`, a higher resolution run `DF_HR_4DM_G` with the same $k_{\rm df}$, but a factor of three difference in the mass resolution, and a high resolution run `DF_HR_12DM_G` with the same $M_{\rm dyn,seed}$ as the fiducial resolution run. We would want the black holes to behave similarly independent of resolution if the $M_{\rm dyn,seed}/M_{\rm DM}$ is kept constant.

Figure 3.A.1(b) shows the same black hole in the simulations with different resolution. In the high-resolution run `DF_HR_4DM_G`, even though the seeding dynamical mass is 3 times smaller than the low-resolution run, the sinking time remains the same. Furthermore, if we keep the absolute seeding dynamical mass the same in the low-resolution and high-resolution runs (by comparing `DF_HR_12DM_G` with `DF_4DM_G`), the black holes still shows similar evolution. This indicates that a constant $k_{\rm df} = M_{\rm dyn,seed}/M_{\rm DM}$ is robust under different resolutions, and our model of dynamical mass does converges to the true black hole mass if we go to higher resolutions.

3.B DF(fid) vs. DF(T15): cases of smaller black holes evolution

In Section 3.4.1, we compared the two DF models by showing the example of an early forming black hole located at the center of the largest halo in the simulation. However, that black hole might not be representative of the entire BH population due to its early seeding and large mass. Now we pick more cases of smaller black holes to demonstrate the differences/similarities between the models. In particular, we will look at how the smaller BHs are affected by the DF(fid)/DF(T15) implementation.

Figure 3.B.1 shows the evolution of three small BHs in the `DF_4DM_G` and the `DF(T15)_4DM_G` simulations. We plot three $M_{\rm BH} < 5 \times 10^6 M_\odot$ black holes. In these cases, the number of particles within the SPH kernel is still at least an order of magnitude more than 100 at lower redshift, and so the density calculated in DF(T15) still tends to be larger but more noisy. The value of the Coulomb logarithm is now mainly affected by $b_{\rm max}$, because we do not see as much noise in the velocity of the surrounding particles as in the case of a very large BH. The density and the Coulomb logarithm counteract each other, and the magnitude of the dynamical friction is similar in the two models.

These cases again verifies that the two models are consistent with each other, with DF(T15) a more localized implementation than DF(fid). The choice of DF(fid) as our fiducial model is mainly due to our resolution limit.

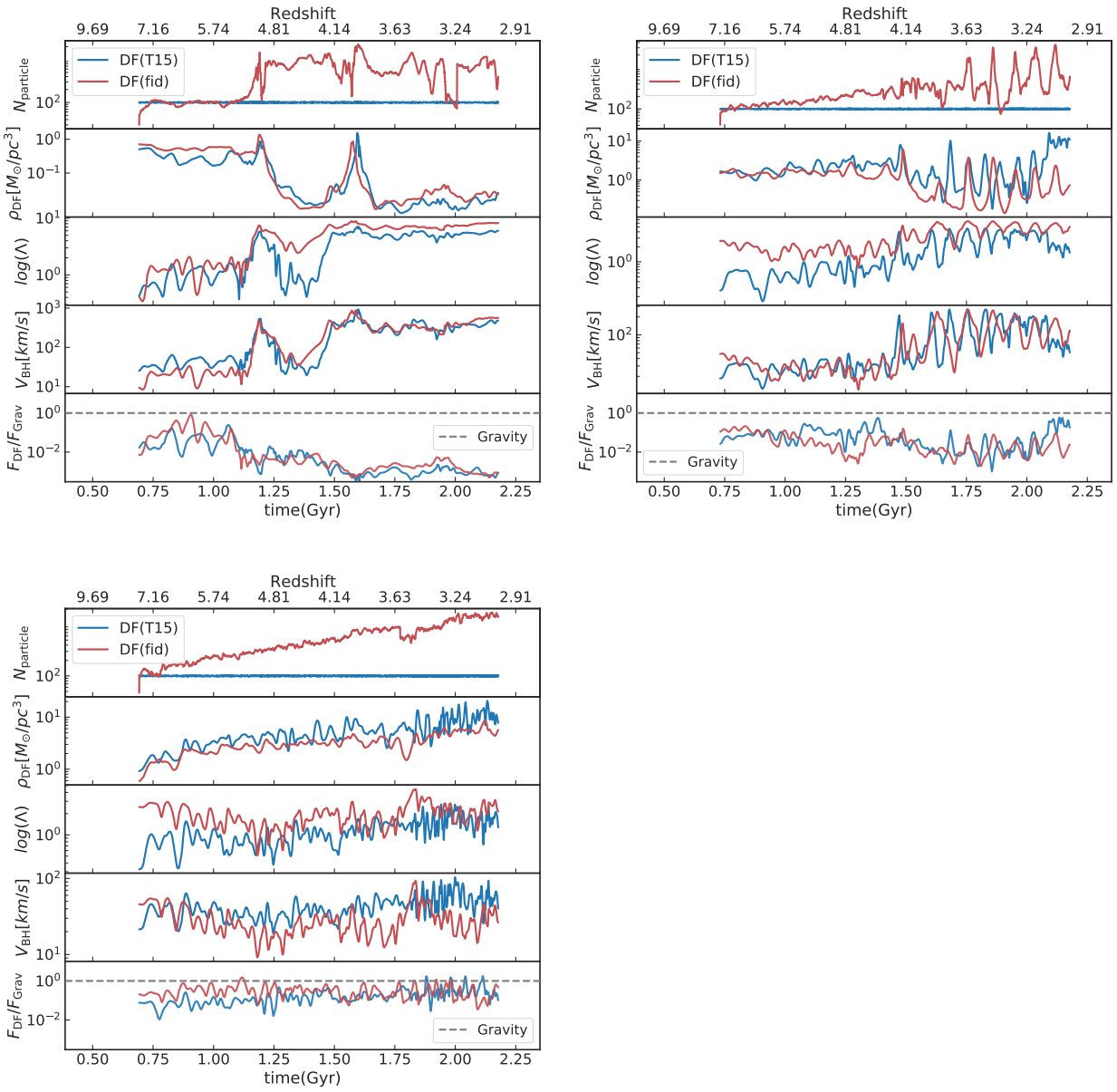

Figure 3.B.1: Components of the dynamical friction in the `DF(fid)_4DM_G` (**red**) and the `DF(T15)_4DM_G` (**blue**) simulations, for three $M < 5 \times 10^6 M_\odot$ black holes. In these cases, the number of particles within the SPH kernel is still at least an order of magnitude more than 100 at lower redshift. The value of the Coulomb logarithm is now mainly affected by $b_{\max}$, because we do not see as much noise in the velocity of the surrounding particles as in the case of a very large BH. In all three cases shown, the magnitude of the dynamical friction is similar in the two models.

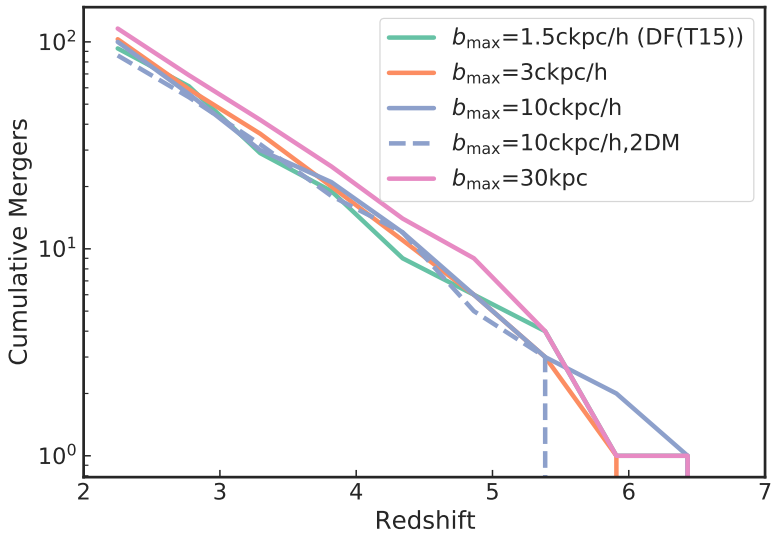

Figure 3.C.1: The cumulative merger rates for different values of $b_{\rm max}$, in the $L_{\rm box}$=15 Mpc/h simulations. We tested $b_{\rm max}$ values of 3 ckpc/h,10 ckpc/h and 30 kpc, and the difference in the cumulative merger rate is less than 10%. The difference between the DF(fid) models and the DF(T15) model with $b_{\rm max}$=1.5 ckpc is also very small. Hence, although different choices of $b_{\rm max}$ changes the magnitude of the dynamical friction, it does not affect the merger rate predictions significantly.

3.C Effect of Model Parameters on the Merger Rate

For the merger rate predictions in 3.6, we use the DF+Drag model with $b_{\rm max}$=10 ckpc/h and $M_{\rm dyn,seed} = 4M_{\rm DM}$. In this section, we will show that the merger rate prediction is not sensitive to the choice of these two parameters, and hence our prediction is relatively robust against parameter variations within a reasonable range.

Figure 3.C.1 shows the cumulative merger rates for different values of $b_{\rm max}$ in the $L_{\rm box}$=15 Mpc/h simulations. We tested $b_{\rm max}$ values of 3 ckpc/h,10 ckpc/h and 30 kpc, and the difference in the cumulative merger rate is less than 10%. The difference between the DF(T15) models and the DF(fid) model with $b_{\rm max}$=1.5 ckpc is also very small. Hence, although different choices of $b_{\rm max}$ changes the magnitude of the dynamical friction, it does not affect the merger rate predictions significantly.

We also test a lower value of $M_{\rm dyn,seed} = 2M_{\rm DM}$ using the $L_{\rm box}$=15 Mpc/h simulation. The resulting cumulative merger rate prediction is also shown in Figure 3.C.1. Compared with the similar run with $M_{\rm dyn,seed} = 4M_{\rm DM}$, the earliest merger is slightly postponed, but the cumulative rate at $z \sim 2$ has very little difference. Therefore, even though for the predictions in Section 3.6 we have chosen a particular set of parameter values, changing those parameters would not affect the result significantly given the larger effects of other factors such as the resolution and seeding.

Chapter 4

Massive Black Hole Mergers with Orbital Information: Predictions from the ASTRID Simulation

Nianyi Chen,[1] Yueying Ni,[1,2] A. Miguel Holgado,[1] Tiziana Di Matteo,[1,2] Michael Tremmel,[3] Colin DeGraf,[4] Simeon Bird,[5] Rupert Croft,[1,2] Yu Feng[6]
[1] McWilliams Center for Cosmology, Department of Physics, Carnegie Mellon University, Pittsburgh, PA 15213
[2] NSF AI Planning Institute for Physics of the Future, Carnegie Mellon University, Pittsburgh, PA 15213, USA
[3] Astronomy Department, Yale University, P.O. Box 208120, New Haven, CT 06520, USA
[4] Department of Physics, Truman State University, Kirksville, MO 63501, USA
[5] Department of Physics & Astronomy, University of California, Riverside, 900 University Ave., Riverside, CA 92521, USA
[6] Berkeley Center for Cosmological Physics and Department of Physics, University of California, Berkeley, CA 94720, USA

Abstract

We examine massive black hole (MBH) mergers and their associated gravitational wave signals from the large-volume cosmological simulation `Astrid` . `Astrid` includes galaxy formation and black hole models recently updated with an MBH seed population between $3 \times 10^4 h^{-1} M_\odot$ and $3 \times 10^5 h^{-1} M_\odot$ and a sub-grid dynamical friction (DF) model to follow the MBH dynamics down to 1.5 ckpc/h. We calculate the initial eccentricities of MBH orbits directly from the simulation at kpc-scales, and find orbital eccentricities above 0.7 for most MBH pairs before the numerical merger. After approximating unresolved evolution on scales below $\sim 200\,\mathrm{pc}$, we find that the in-simulation DF on large scales accounts for more than half of the total orbital decay time ($\sim 500\,\mathrm{Myrs}$) due to DF. The binary hardening time is an order of magnitude longer than the DF time, especially for the seed-mass binaries ($M_{\rm BH} < 2M_{\rm seed}$). As a result, only $\lesssim 20\%$ of seed MBH pairs merge at $z > 3$ after considering

both unresolved DF evolution and binary hardening. These $z > 3$ seed-mass mergers are hosted in a biased population of galaxies with the highest stellar masses of $> 10^9\,M_\odot$. With the higher initial eccentricity prediction from `Astrid` , we estimate an expected merger rate of $0.3-0.7$ per year from the $z > 3$ MBH population. This is a factor of ~ 7 higher than the prediction using the circular orbit assumption. The LISA events are expected at a similar rate, and comprise $\gtrsim 60\%$ seed-seed mergers, $\sim 30\%$ involving only one seed-mass MBH, and $\sim 10\%$ mergers of non-seed MBHs.

4.1 Introduction

Massive Black Holes (MBHs) are known to exist at the center of galaxies [e.g. Kormendy and Ho, 2013, Kormendy and Richstone, 1995, Magorrian et al., 1998, Soltan, 1982]. As these galaxies merge [e.g. Lacey and Cole, 1993, Lotz et al., 2011, Rodriguez-Gomez et al., 2015], the MBHs that they host will also merge, resulting in the mass growth of the MBH population [e.g. Begelman et al., 1980]. MBH mergers following their host galaxy mergers are an important aspect of the growth of MBHs in dense environments [e.g. Kulier et al., 2015]. Even more importantly, as a by-product of MBH mergers, gravitational waves are emitted, and their detection opens up a new channel for probing the formation and evolution of early MBHs in the universe [e.g. Barausse, 2012, Sesana et al., 2007b].

The gravitational wave (GW) detection by LIGO [Abbott et al., 2016] proves the experimental feasibility of using gravitational waves for studying black hole (BH) binaries. While LIGO cannot detect GWs from binaries more massive than $\sim 100M_\odot$ [Mangiagli et al., 2019], long-baseline experiments are being planned for the detections of more massive BH binaries. Specifically, the upcoming Laser Interferometer Space Antenna (LISA) [Amaro-Seoane et al., 2017] mission will be sensitive to low-frequency ($10^{-4}-10^{-1}$Hz) gravitational waves from the coalescence of MBHs with masses $10^4 - 10^7 M_\odot$ up to $z \sim 20$. At lower frequencies, Pulsar Timing Arrays (PTAs) are already collecting data and the Square Kilometer Array (SKA) in the next decade will be a major leap forward in sensitivity. While MBH binaries are the primary sources for PTAs and LISA, these two experiments probe different stages of MBH evolution. PTAs are most sensitive to the early inspiral (orbital periods of years or longer) of nearby ($z < 1$) massive ($M_{\rm BH} \gtrsim 10^8\,M_\odot$) sources [Mingarelli et al., 2017]. In contrast, LISA is sensitive to the inspiral, merger, and ringdown of MBH binaries at a wide range of redshifts [Amaro-Seoane et al., 2012] and from smaller sources ($M_{\rm BH} \in [10^4 M_\odot, 10^7 M_\odot]$).

GWs from MBH mergers will provide a unique way of probing the high-redshift universe and understanding the early formation of the MBH seeds, especially when combined with observations of the electromagnetic (EM) counterparts [DeGraf and Sijacki, 2020, Natarajan et al., 2017]. For instance, an MBH merger multi-messenger detections should allow us to distinguish between different MBH seeding mechanisms at high-redshift [Ricarte and Natarajan, 2018], to obtain information on the dynamical evolution of massive black holes [Bonetti et al., 2019], and to gain information about the gas properties within the accretion disc [Derdzinski et al., 2019].

To properly access the potential of the upcoming GW signals as well as the EM observations of MBH binaries, we need to gain a thorough understanding of the physics of these events with theoretical tools and be able to make statistical predictions for the binary population. Early studies have provided merger rate predictions for MBH binaries using analytic models [e.g. Haehnelt, 1994, Jaffe and Backer, 2003, Wyithe and Loeb, 2003]. Some more recent predictions made use of semi-analytic models [e.g. Barausse, 2012, Ricarte and Natarajan, 2018, Sesana et al., 2004, Tanaka and Haiman, 2009] to enhance the model complexity and physical realism. Recent developments in large-volume cosmological simulations [e.g. Davé et al., 2019, Feng et al., 2016, Hirschmann et al., 2014, Pillepich et al., 2018, Schaye et al., 2015, Vogelsberger et al., 2014, Volonteri et al., 2016] have enabled the study of MBH mergers within the context of cosmological galaxy formation [e.g. Katz et al., 2020, Kelley et al., 2017b, Salcido et al., 2016, Volonteri et al., 2020]. These simulations directly associate MBH binaries with their host galaxies, and they are carried out in large enough cosmological volumes to provide the statistical power to make merger rate predictions across cosmic time which are crucial for the upcoming observations.

In order to accurately predict when MBH mergers occur in these simulations, one must account for the orbital decay and binary hardening timescales in a wide dynamical range. During galaxy mergers, the central MBHs start at large separation in the remnant galaxy (as much as a few tens of kpc). These MBHs then gradually lose their orbital energy and sink to the center of the remnant galaxy due to the dynamical friction exerted by the gas, stars, and dark matter around them [e.g. Chandrasekhar, 1943, Ostriker, 1999]. When their separation is $\lesssim 1$ parsec, a MBH binary forms and other energy-loss channels begin to dominate, such as scattering with stars [e.g. Berczik et al., 2006, Berentzen et al., 2009, Khan et al., 2011, 2013, Quinlan, 1996, Sesana et al., 2007a, Vasiliev et al., 2015], gas drag from the circumbinary disk [e.g. Haiman et al., 2009], or, if relevant, three-body scattering with a third black hole [e.g. Bonetti et al., 2018].

Among these processes, only the dynamical friction decay affects the dynamics at orbital separation above the resolution of large-volume cosmological simulations. However, so far there is limited attempt to directly model dynamical friction (at small scales, close to the resolution) in the large-volume cosmological simulations mentioned above. In most cosmological simulations, once MBHs are within a given halo, they are simply repositioned to the minimum potential position of the host galaxy at each time step. For these simulations, (although sometimes the effects of subgrid dynamical friction are treated in post-processing), many spurious mergers occur during fly-by encounters. Among simulations that do include subgrid modeling of DF on-the-fly, Dubois et al. [2014] only includes the friction from gas but not stars, while Tremmel et al. [2017] and Hirschmann et al. [2014] model the dynamical friction from stars and dark matter particles. Most recently, Mannerkoski et al. [2021] uses a hybrid model to track the MBH dynamics during galaxy mergers on small scales, while including on-the-fly dynamical friction and stellar scattering computations.

Here we study MBH mergers using the large volume cosmological simulation `Astrid` which uses a novel power-law seeding with a range of MBH seed masses and so includes relatively low mass MBHs. More importantly, it directly incorporates additional dynamical friction

modeling, following the recent model by [Chen et al., 2021] for the MBH dynamics down to the resolution limit [see also similar implementations by Hirschmann et al., 2014, Tremmel et al., 2015]. With more physical modeling of the MBH dynamics, we can follow the in-simulation mergers for a more extended period of time over hundreds of Myrs, and almost completely prevent mergers during fly-by encounters. Moreover, for the first time we can aim to measure the orbital evolution and eccentricities of MBH pairs on sub-kpc scales. Such information should be important both for estimating the binary hardening timescales and for predicting the GW signals from the MBH mergers.

This paper is organized as follows: in Section 6.2 we introduce the `Astrid` simulation, in particular the MBH modeling, and describe how we obtain the merger catalog from the simulation; in Section 4.3, we describe our methods for measuring the MBH orbital eccentricity from the simulation, and present results of our measurements. Section 4.4 focuses on the modeling of post-processing delay times including the dynamical friction time and binary hardening time after the numerical merger. Then in Section 4.5, we present our prediction for MBH merger rate at $z > 3$, and investigate the properties of high-redshift MBH merger systems. Finally, in Section 4.6 we show the GW strain and signal-to-noise ratios for the binary population that merges at $z > 3$.

4.2 Simulation

4.2.1 The `Astrid` Simulation

The `Astrid` simulation is a large-scale cosmological hydrodynamic simulation in a $250\,\mathrm{Mpc}/h$ box with 2×5500^3 particles. `Astrid` contains a statistical sample of halos which can be compared to future survey data from JWST, while resolving galactic halos down to $10^9\,M_\odot$ (corresponding to 200 dark matter particles). The initial conditions are set at $z = 99$ and the current final redshift is $z = 3$. The cosmological parameters used are from [Planck Collaboration et al., 2020], with $\Omega_0 = 0.3089$, $\Omega_\Lambda = 0.6911$, $\Omega_\mathrm{b} = 0.0486$, $\sigma_8 = 0.82$, $h = 0.6774$, $A_s = 2.142 \times 10^{-9}$, $n_s = 0.9667$. The mass resolution of `Astrid` is $M_\mathrm{DM} = 6.74 \times 10^6 h^{-1} M_\odot$ and $M_\mathrm{gas} = 1.27 \times 10^6 h^{-1} M_\odot$ in the initial conditions. The gravitational softening length is $\epsilon_\mathrm{g} = 1.5 h^{-1}\,\mathrm{kpc}$ for both DM and gas particles.

`Astrid` contains models for inhomogeneous hydrogen and helium reionization, baryon relative velocities and massive neutrinos, as well as 'full-physics' star formation model, BH accretion and associated supernova and AGN feedback respectively. The star formation model is unchanged from Feng et al. [2016], which followed the implementation of Springel and Hernquist [2003]. The BH model includes mergers driven by dynamic friction rather than repositioning. Our treatment of MBHs largely follows the `BlueTides` simulation in terms of the BH accretion and feedback, which is based on the earlier work by Di Matteo et al. [2005b], Springel et al. [2005b]. The gas accretion rate onto the BH is estimated via the Bondi-Hoyle-Lyttleton-like prescription applied to the smoothed properties of the 112 gas particles within the SPH kernel of the BH. We allow for short periods of super-Eddington accretion in the simulation, but limit the accretion rate to 2 times the Eddington accretion

rate. The MBH produces thermal feedback on the surrounding gas, and radiates with a bolometric luminosity $L_{\rm Bol}$ proportional to the accretion rate $\dot{M}_{\rm BH}$, with a mass-to-light conversion efficiency $\eta = 0.1$ in an accretion disk according to Shakura and Sunyaev [1973]. 5% of the radiated energy is thermally coupled to the surrounding gas, residing within twice the radius of the SPH smoothing kernel of the BH particle.

Compared with `BlueTides` , we slightly changed the seeding scheme of MBHs by drawing the seed mass from a power-law distribution instead of using a universal seed mass. Furthermore, we use a dynamical friction model [tested and validated in Chen et al., 2021] to evolve the binary black holes and include the sinking and merger of MBHs in the simulation in a more physical way. Here we briefly summarize the black hole seeding and dynamics treatment in `Astrid`, and refer to Bird et al. [2021] and Ni et al. [2021] for detailed presentations of physical models for star formation and black holes.

MBH Seeding

To seed MBHs in the simulation, we periodically run a FOF group finder on the fly with a linking length of 0.2 times the mean particle separation, to identify halos with a total mass and stellar mass satisfying the seeding criteria $\{ M_{\rm halo,FOF} > M_{\rm halo,thr}; M_{*,\rm FOF} > M_{*,\rm thr}\}$. We apply a mass threshold value of $M_{\rm halo,thr} = 5 \times 10^9 h^{-1} M_\odot$ and $M_{*,\rm thr} = 2 \times 10^6 h^{-1} M_\odot$.

Considering the complex astrophysical process involved in BH seed formation in realistic cases, halos with the same mass can form different mass MBH seeds. Therefore, in `Astrid`, instead of applying a uniform seed mass for all MBHs, we probe a mass range of the MBH seed mass $M_{\rm seed}$ drawn probabilistically from a power-law distribution:

$$P(M_{\rm seed}) = \begin{cases} 0 & M_{\rm seed} < M_{\rm seed,min} \\ \mathcal{N}(M_{\rm seed})^{-n} & M_{\rm seed,min} \leq M_{\rm seed} \leq M_{\rm seed,max} \\ 0 & M_{\rm seed} > M_{\rm seed,max} \end{cases} \tag{4.1}$$

where $\mathcal{N}$ is the normalization factor. The minimum seed mass is $M_{\rm seed,min} = 3 \times 10^4 h^{-1} M_\odot$ and the maximum seed mass is $M_{\rm seed,max} = 3 \times 10^5 h^{-1} M_\odot$, with a power-law index $n = -1$. For each halo that satisfies the seeding criteria but does not already contain at least one BH particle, we convert the densest gas particle into a BH particle. The new-born BH particle inherits the position and velocity of its parent gas particle.

MBH Dynamics and Mergers

Instead of constantly repositioning the black hole towards the potential minimum, as in earlier simulations, in Chen et al. [2021] we implemented and tested a model for sub-grid dynamical friction [similar to Tremmel et al., 2015, 2017]. Dynamical friction is an artificial force for modeling unresolved small-scale interactions between the MBH and nearby stars and dark matter. These interactions transfer momentum from the MBH to individual stars in the surrounding star clusters, gradually reducing the momentum of the MBH particle relative to the surrounding collisionless objects in the bulge [e.g. Governato et al., 1994,

Kazantzidis et al., 2005]. The additional dynamical friction also stabilizes the MBH motion at the center of the galaxy.

We estimate dynamical friction on MBHs using Eq. 8.3 of Binney and Tremaine [2008]:

$$\mathbf{F}_{\rm DF} = -16\pi^2 G^2 M_{\rm BH}^2 m_a \log(\Lambda) \frac{\mathbf{v}_{\rm BH}}{v_{\rm BH}^3} \int_0^{v_{\rm BH}} dv_a v_a^2 f(v_a), \tag{4.2}$$

where $M_{\rm BH}$ is the BH mass, $\mathbf{v}_{\rm BH}$ is the BH velocity relative to its surrounding medium, m_a and v_a are the masses and velocities of the particles surrounding the BH, and $\log(\Lambda) = \log(b_{\rm max}/b_{\rm min})$ is the Coulomb logarithm that accounts for the effective range of the friction between the specified $b_{\rm min}$ and $b_{\rm max}$. $f(v_a)$ in Eq. 4.2 is the velocity distribution of the surrounding collisionless particles including both stars and dark matter. Here we have assumed an isotropic velocity distribution of the particles surrounding the BH so that we are left with a 1D integration.

In `Astrid`, the BH seed mass extends down to $3 \times 10^4 M_\odot/h$, which is one order of magnitude smaller than the stellar particle mass. In this regime, the dynamical friction of BH is likely unrealistic due to its small mass compared to the masses of other particles, and so the dynamics of the seed BH would be unstable due to dynamical heating (when $M_{\rm BH}$ is below the mass resolution). Therefore, we boost the dynamical friction in this regime with $M_{\rm dyn} = 2 \times M_{\rm DM}$ when $M_{\rm BH} < M_{\rm dyn} < 1$. This temporarily boosts the BH dynamical mass for BHs near the seed mass and helps stabilize their motion during the early post-seeding evolution.

We approximate the distribution function $f(v_a)$ by the Maxwellian distribution [as, e.g. Binney and Tremaine, 2008], and account for the neighbouring collisionless particles up to the range of the SPH kernel of the BH particle [see, Chen et al., 2021, for more details]. Eq. 4.2 becomes

$$\mathbf{F}_{\rm DF} = -4\pi\rho_{\rm sph} \left(\frac{GM_{\rm dyn}}{v_{\rm BH}}\right)^2 \log(\Lambda) \mathcal{F}\left(\frac{v_{\rm BH}}{\sigma_v}\right) \frac{\mathbf{v}_{\rm BH}}{v_{\rm BH}}. \tag{4.3}$$

Here $\rho_{\rm sph}$ is the density of dark matter and star particles within the SPH kernel, $\mathcal{F}$ is the integral in Equation 4.2 assuming a Maxwellian distribution of stellar velocities. σ_v is the velocity dispersion of the dark matter and star particles within the SPH kernel.

The boost of the initial $M_{\rm dyn}$ may overestimate the dynamical friction for small BHs and the resultant sinking timescale will be shortened by a factor of $\sim M_{\rm BH}/M_{\rm dyn}$ compared to the no-boost case. On the other hand, it is also possible that the BH sinking time scale estimated in our simulation in the no-boost case could overestimate the true sinking time, as the high-density stellar bulges are not fully resolved [e.g. Antonini and Merritt, 2012, Biernacki et al., 2017, Dosopoulou and Antonini, 2017]. Therefore, boosting the initial $M_{\rm dyn}$ seems a reasonable compromise to model the dynamics of small mass BHs while also alleviating the noisy perturbation of dynamic heating brought by the limit of resolution. Note that even if our dynamic friction implementation overestimates the force, it still provides a substantially more conservative estimation of BH sinking than the common model where BHs are repositioned to the potential minimum.

In our simulations, we set the merging distance to be $2\epsilon_{\rm g} = 3\,{\rm ckpc}/h$, because the MBH dynamics below this distance is not well resolved. We conserve the total momentum of the binary during the merger. Moreover, when we turn off the repositioning of the MBHs to the nearby potential minimum, the MBHs will have well-defined velocities at each time step (this is true whether or not we add the dynamical friction). This allows us to apply further merging criteria based on the velocities and accelerations of the black hole pair, and thus avoid early mergers of gravitationally unbound pairs.

We follow Bellovary et al. [2011] and Tremmel et al. [2017], and use the criterion

$$\frac{1}{2}|\mathbf{\Delta v}|^{\mathbf{2}} < \mathbf{\Delta a \Delta r} \tag{4.4}$$

to check whether two black holes are gravitationally bound. Here $\mathbf{\Delta a}$,$\mathbf{\Delta v}$ and $\mathbf{\Delta r}$ denote the relative acceleration, velocity and position of the black hole pair, respectively. Note that this expression is not strictly the total energy of the black hole pair, but an approximation of the kinetic energy and the work needed to get the black holes to merge. Because in the simulations the black hole is constantly interacting with surrounding particles, on the right-hand side we use the overall gravitational acceleration instead of the acceleration purely from the two-body interaction.

4.2.2 The Merger Catalog

There are a total of 445635 BH mergers in the simulation for $z > 3$. We note that since our merging criterion has a distance threshold at $2\epsilon_g = 3\,{\rm ckpc}/h$ ($0.75\,{\rm pkpc}/h$ at z=3) below which the gravitational force cannot be reliably computed, most of the MBH pairs retain an orbital size of a few hundred parsecs when "merged" in the simulation. Moreover, we may have missed some $z > 3$ mergers due to an underestimation of the dynamical friction from the flattened density profiles near our resolution limit.

The subsequent MBH dynamics and merging time will have to be calculated in post-processing, and the result depends on the subgrid models used for those calculations (to be described later in more detail). For each merger event, we extract the relevant environmental variables (the density profiles of gas, dark matter and stars, and the stellar velocity dispersion) from the nearest snapshot before and after the merger. The snapshots used are separated by ~ 20 Myrs. In a small fraction of cases, the mergers take place within 20 Myrs after one of the MBHs is born, and so we cannot find the corresponding MBH in the previous snapshot. We remove these mergers from the catalog, after which 440999 mergers remain.

From the snapshots immediately before and after the merger, we identify the host halos and subhalos containing the binaries using FOF and SubFind, respectively. Out of the mergers that remain in the catalog, we further remove those not associated with any halo/subhalo, and those whose host galaxy has less than 200 star particles. The hosts for these binaries are not well resolved in our simulation, so we cannot reliably compute the binary hardening time in post-processing. This leaves us with a final catalog of 430938 black hole merger candidates. For each host halo identified, we define the halo center as the position of the

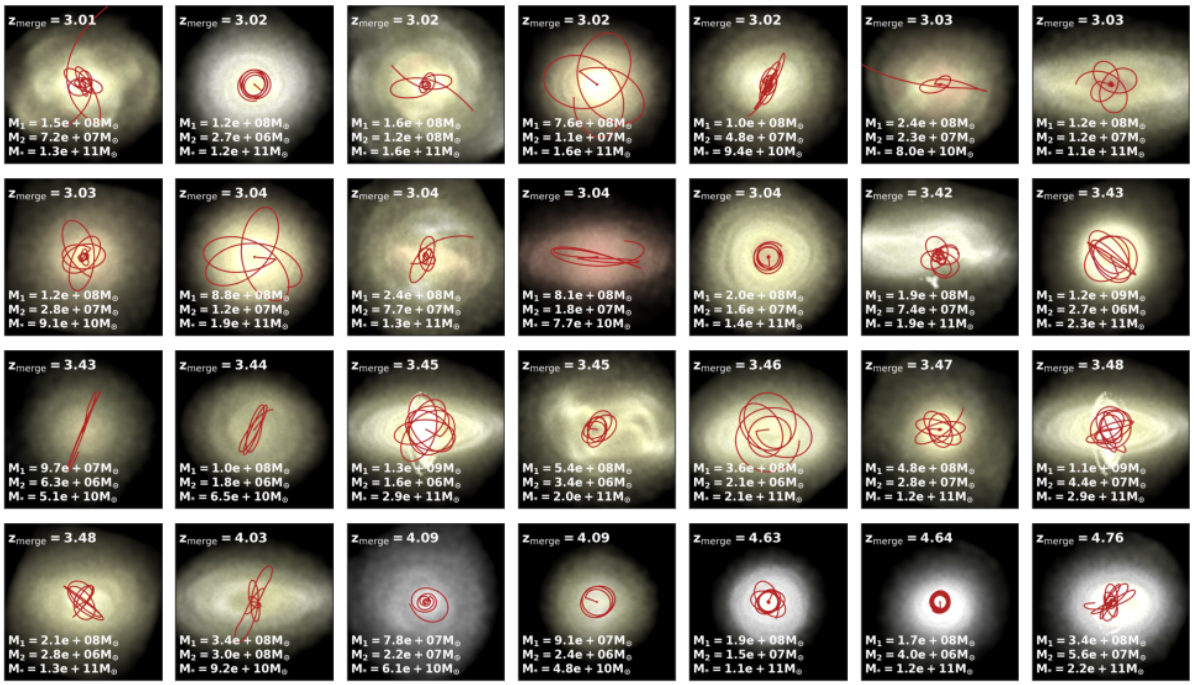

Figure 4.3.1: The last few orbits (starting from $\sim 80\,\mathrm{Myrs}$ before the merger) of selected binaries in the `Astrid` simulation plotted on their host galaxies. The distance from left to right of each image is $10\,\mathrm{ckpc}/h$. The brightness corresponds to the stellar density, and the colors show the stellar age with older stars being redder. The red curves are the BH pairs' position relative to their center of mass. In most cases we see a Rosetta orbit, as the local potential is a spherical potential dominated by stars and dark matter. We find that some orbits circularize over time (e.g. third row, fifth column), although the majority of the orbits still remain eccentric when merging (see e.g. Figure 4.3.2).

particle with the minimum potential, and calculate galaxy properties such as the density profiles and half-mass radius with respect to this point.

In Figure 4.3.1, we show the last few orbits of a few selected BH pairs in our merger catalog plotted on their host galaxies' stellar distributions. The distance from left to right of each image is $8\,\mathrm{ckpc}/h$. The brightness corresponds to the stellar density, and the colors show the stellar age with older stars being redder and younger stars being whiter. The red curves are the BH pairs' positions relative to their center of mass.

4.3 Orbital Eccentricity

As was described in Section 4.2.1, our simulation has a build-in sub-grid dynamical friction model, which allows us to follow the black holes' orbits before their numerical mergers down to the resolution limit. Figure 4.3.1 shows several examples of the last few orbits of BH pairs

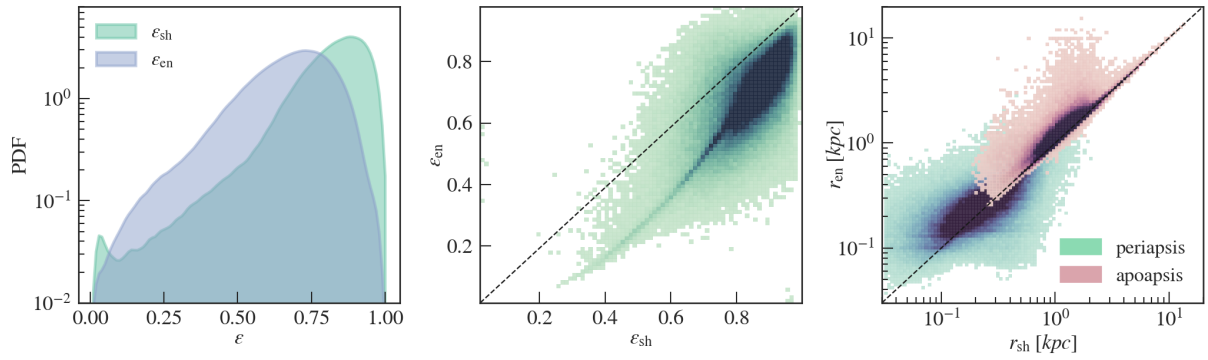

Figure 4.3.2: Comparison between eccentricity measurements from the shape method and the energy method. **Left:** the distribution of the (generalized) orbital eccentricity from the two measurements. In both cases, the distribution is dominated by highly-eccentric binaries, as we can also see from the images in Figure 4.3.1. The shape method has a more skewed distribution compared to the energy method. **Middle:** A scattered plot of the eccentricity from the two measurements. We can see that the two measurements yield similar results by comparing the distribution to the diagonal line. In most cases, the energy measurement is $\sim 10\%$ lower than the shape measurement. **Right:** In addition to the eccentricity, we show the apoapses and periapases of the two measurements. The orange dots are the apoapses and the green dots are the periapases. The scatter relation also follows the diagonal line quite closely. When the two black holes merge in the simulation, the apoapsis is usually a few kpc and the periapsis is usually less than 1kpc.

just before they merge in the simulation. The black hole orbits are plotted in the center-of-mass frame of the BH pairs, with a face-on projection on the 2D plane perpendicular to the mean angular momentum of the last orbit. Since we record the BH information at each time step when the BH is active, the orbits are much better resolved in time compared with the galaxies. Most orbits start off at a semi-major axis of > 1 kpc, and gradually go through orbital decay until the merger.

From the images, we see that the majority of the orbits are very non-circular during the initial encounter of the BHs. While some of them circularize with time, most orbits still retain a high eccentricity at the time of the merger in the simulation. This motivates us to characterize the orbital eccentricity before merging, as it is an important piece of information not only for estimating the binary hardening time with analytical models, but also for calculating the GW signals from the merger events. In this section, we will describe two ways of characterizing the orbital eccentricities of the BH pairs in our simulation.[1]

4.3.1 Shape Measurement

Given the images in Figure 4.3.1, a natural way of measuring the orbital eccentricity is to use the shape of the orbits just before the numerical merger, and this is the first approach we take.

On $\sim$ kpc scales, since most orbits are not Keplerian except those of the most massive BHs and the orbits are constantly shrinking, the BH orbits do not fit an ellipse. Instead, they exhibit the feature of a Rosetta orbit (the feature is most prominent in e.g. second row, second column of Figure 4.3.1, although standard Rosetta orbits do not shrink over time). For orbits resulting from the spherically symmetric potential, we can characterize the eccentricity by the size of the inner radius and the size of the outer radius. More specifically, for each orbit, we define Δr_2 to be the position of the secondary BH with respect to the center of mass, and we take the local minimum of Δr_2 as the (generalized) periapsis of the orbit, and the local maximum of Δr_2 as the apoapsis. Then, we represent the orbital eccentricity of the binary by the generalized eccentricity, defined for a spherical potential as: [Binney and Tremaine, 2008]:

$$\epsilon = \frac{r_{\rm apo} - r_{\rm peri}}{r_{\rm apo} + r_{\rm peri}}, \tag{4.5}$$

where $r_{\rm apo}$ and $r_{\rm per}$ are the apoapsis and the periapsis of the orbit, respectively. To distinguish between the measurement of the two methods, we will use the subscript "sh" to refer to the measurements from this shape-based method. We average the eccentricity measurements over the last three orbits. We note, however, that the distribution in eccentricity does not change significantly when we take the average of the last one, two, or three orbits.

[1] We also tried applying the method of osculating elements [e.g., Efroimsky and Goldreich, 2004, and references therein] to the orbital trajectories; however, we found that the stellar environment dominated the binary's evolution, such that it could not be adequately described as a post-Keplerian orbit.

4.3.2 Solving the Orbital Equation

In addition to the shape-based measurement in §3.1, we also calculate the generalized orbital eccentricity by simply solving the orbital equation. Using these two independent methods we will then be able to compare the robustness of the BH orbit eccentricity distribution measurement from the simulations.

When the BH merger occurs in the simulation, the separation between the black hole pair is ~ 3 ckpc/h. At this distance, the gravitational potential is dominated by the surrounding stars and dark matter particles instead of the BHs themselves. Under such circumstances, the orbit of the satellite BH is non-Keplerian, as we have shown in Section 4.3.1. In the case of a spherical potential, the (generalized) apoapsis and periapsis can be obtained by solving the generalized orbital equation [Binney and Tremaine, 2008]:

$$\frac{1}{r^2} + \frac{2[\phi(r) - E]}{J^2} = 0, \tag{4.6}$$

where $\phi(r)$ is the gravitational potential computed from the density profile of surrounding particles, E is the total energy per unit mass and J is the angular momentum per unit mass of the secondary black hole with respect to the host galaxy center. The larger root of the equation corresponds to $r_{\rm apo}$ and the smaller root is $r_{\rm peri}$.

When solving Equation 4.6, we take E and J to be the average energy and angular momentum over the last half-orbit (i.e. from the last local maximum to the last local minimum of the BH separation) of the BH. We did not take the average over a more extended period of time because the black hole pair is constantly losing energy. After getting the two apses, we again use Equation 4.5 to calculate the orbital eccentricity. We refer to this method as the energy method, and use the subscript "en" when showing results.

Figure 4.3.2 shows a comparison between the (generalized) eccentricity measurements from the shape method and the energy method. The left panel shows the distribution of eccentricities for all the mergers in the simulation. The measurements from both methods show that the BH binary population is dominated by highly eccentric orbits, with a peak at $\epsilon \sim 0.85$ for the shape-based method and ~ 0.75 for the energy-based method. Comparing the two distributions, we see that the shape measurement generally produces a distribution with higher eccentricities than the energy method. In the middle panel, we show a scatter plot of the eccentricities from the two measurements. There is a positive correlation between the two eccentricities, with the majority of the measurements close to the diagonal line. This means that the two measurements are not only close in distribution, but also yield correlated results for each individual orbit. Similar to what is shown by the 1D distributions, the shape method predicts higher values of eccentricity for most pairs than the energy method (typically $\sim 10\%$ lower).

In addition to the eccentricity, in the right panel of Figure 4.3.2 we further compare the apoapses and periapases from the two measurements. Overall, we can see that the apoapsis peaks around $1 \sim 3$ kpc, while the periapsis peaks around $0.1 \sim 0.7$ kpc. Again there is a good alignment between the two measurements, with the peaks distributed close to the diagonal line. In the majority of cases, the shape measurement gives a larger apoapsis value.

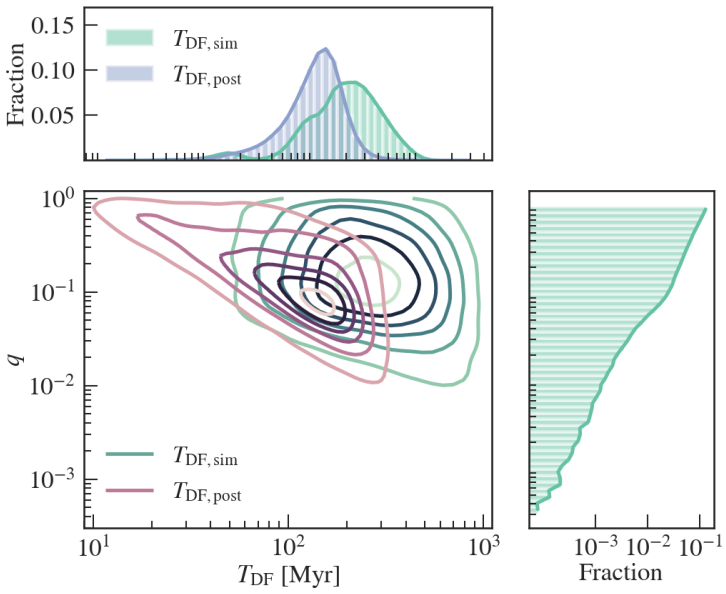

Figure 4.4.1: Comparison between the pre-merger dynamical friction time and the post-merger dynamical friction time. **Top:** Distributions of the pre- and post- merger DF times for all MBH pairs in `Astrid`. The two distributions are similar and both peak around 200 Myrs, indicating that by adding dynamical friction to the simulation, we have resolved more than half of the total dynamical friction delay. **Bottom left:** Relation between the DF times and the mass ratio between the two MBHs (q). We observe the expected negative correlation between DF times and q. **Bottom right:** 1D distribution of the mass ratio q.

To estimate the binary hardening time, we will use the measured binary eccentricities as an input to the model. By doing so, we do not consider any time-evolution of the binary eccentricity due to dynamical friction beyond the point of numerical merger [Colpi et al., 1999, Hashimoto et al., 2003]. In particular, we will only show results using the values from the energy-based method ($\epsilon_{\rm en}$) in later sections, and we have tested that the effect of using the shape-based values is minor compared with the uncertainties from other sources (e.g. density in the central region of the galaxy).

4.4 Post-processing Delays

4.4.1 Dynamical Friction

In `Astrid`, we have already accounted for the dynamical friction timescale above the resolution limit, leading to significant delays of in-simulation mergers compared to the traditional MBH repositioning methods. However, dynamical friction will continue to dominate over other delay processes on scales of $10 \sim 100$ pc [e.g. Kelley et al., 2017b], which is beyond

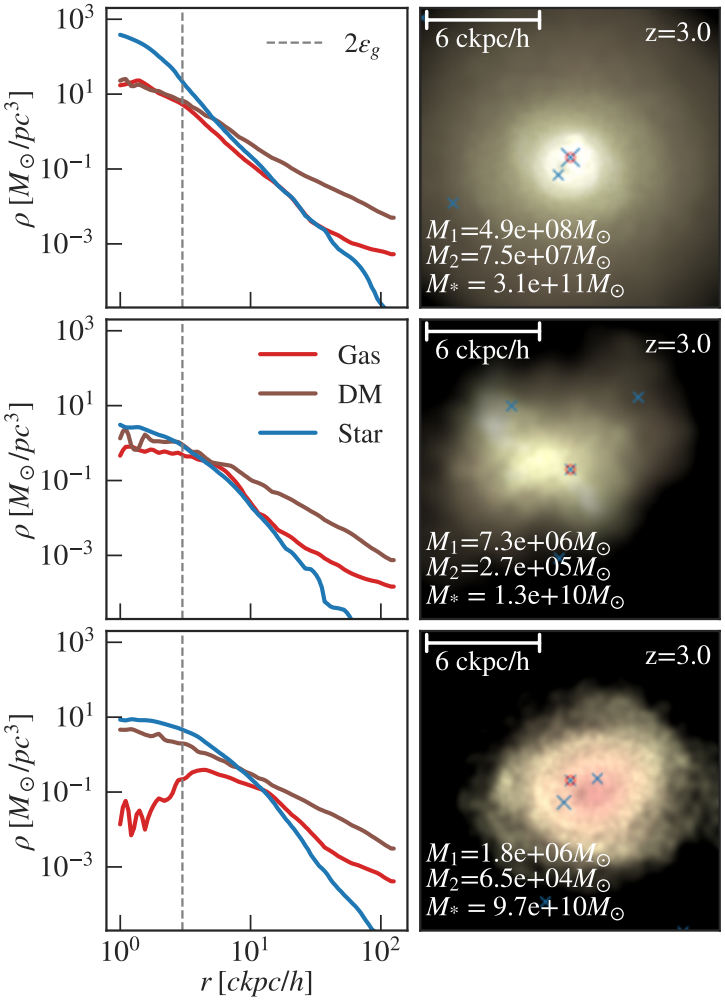

Figure 4.4.2: Density profiles (left) and images (right) of the host galaxies of three MBH mergers in the simulation. The blue crosses mark all MBHs in the host galaxy, scaled by the BH mass. The red circles mark the merging binary. **Top:** Host of a very massive binary with $M_{\rm tot} = 5.6 \times 10^8 M_\odot$ at $z = 3$. The stellar density is the dominant component on scales below ~ 10 ckpc$/h$. **Middle:** Host of a binary with $M_{\rm tot} = 7.6 \times 10^6 M_\odot$ at $z = 3$. For this less massive binary, the density of the three components is comparable at $r < 10$ ckpc$/h$, and the density profile flattens at a larger radius. **Bottom:** Host of a binary with two seed-mass MBHs. The mass of the host galaxy is high relative to the binary mass. The binary is not the most massive MBHs in this galaxy, but the merger still occurs in a relatively central region.

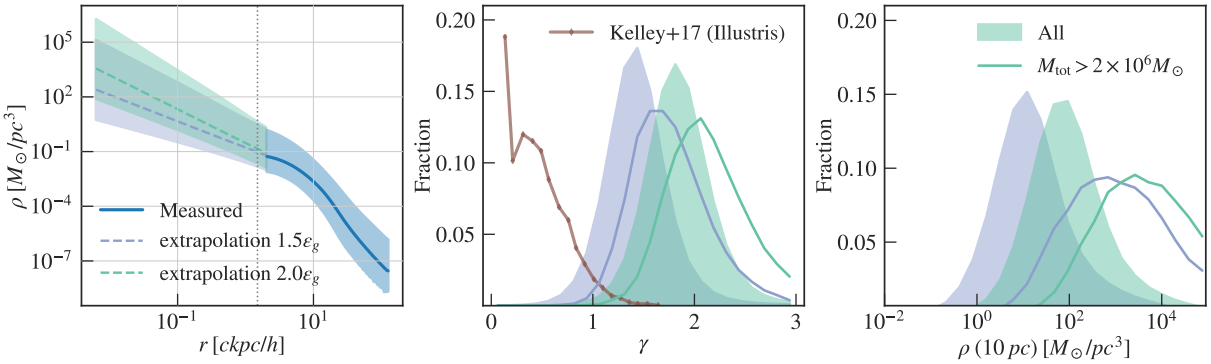

Figure 4.4.3: **Left:** The density profiles of `Astrid` galaxies that host a recent numerical merger. The blue solid line shows the median density of all binary hosts measured from the simulation and the shaded region encloses 95% of the population. The power law extrapolation is shown by dashed lines. Here we show the results for extrapolation scales $r_{\rm ext} = 1.5\epsilon_g$ (purple) and $r_{\rm ext} = 2\epsilon_g$ (green). A larger $r_{\rm ext}$ results in a steeper power-law slope. **Middle:** Distribution of the power-law index of the density profile γ, measured at $r_{\rm ext} = 1.5\epsilon_g$ (purple) and $r_{\rm ext} = 2\epsilon_g$ (green). For $r_{\rm ext} = 1.5\epsilon_g$, the distribution peaks at $\gamma = 1.4$, while for $r_{\rm ext} = 2.0\epsilon_g$, the distribution peaks at $\gamma = 1.9$. We plot the power-index estimate in Kelley et al. [2017c] for comparison. **Right:** Distribution of density extrapolated to 10 pc. We compare the two $r_{\rm ext}$ values. The extrapolated density is sensitive to the change in $r_{\rm ext}$: $r_{\rm ext} = 1.5\epsilon_g$ gives a distribution centered at $10\,M_\odot/{\rm pc}^3$, while $r_{\rm ext} = 2.0\epsilon_g$ gives a distribution centered at $100\,M_\odot/{\rm pc}^3$.

our current resolution. In this section, we will compute the unresolved DF timescales for the MBH mergers, and compare them with the in-simulation DF timescale.

For the in-simulation DF time, we measure it in the following way: for each black hole pair that merges within the simulation at $z_{\rm merge}$, we track their trajectories before the merger event, and find the redshift $z_{\rm encounter}$ at which they are first within $2\epsilon_g$ of each other. $z_{\rm encounter}$ is the approximate time at which the BHs would merge if we did not account for the dynamical friction time at all (note that under the reposition model, BHs usually merge even before $z_{\rm encounter}$). We consider the time difference between $z_{\rm encounter}$ and $z_{\rm merge}$ as the in-simulation DF time, $T_{\rm DF,sim}$. Among all BH mergers in the simulation, 5713 mergers ($\sim 1.4\%$ of the whole merger population) happen at the first encounter.

For the post-processed DF time $T_{\rm DF,post}$, we adopt the treatment from Merritt [2013] and Dosopoulou and Antonini [2017], who modifies the Chandrasekhar formalism [e.g. Binney and Tremaine, 2008, Chandrasekhar, 1943] to include the effect of the secondary BH embedded in a tight core of stars brought in from the secondary galaxy. The increased dynamical friction allows the secondary to sink faster towards the primary galaxy's center, and thus the resulting dynamical friction time is less than the prediction from the canonical Binney and Tremaine [2008] treatment assuming a bare BH. In Dosopoulou and Antonini [2017] the assumption is that the mass of stars bound to the secondary BH is 1000 times the mass of the BH itself, and the resulting dynamical friction timescale is:

$$t_{\rm DF,post} = 0.12\,{\rm Gyr}\left(\frac{r}{10{\rm kpc}}\right)^2\left(\frac{\sigma}{300{\rm km/s}}\right)\left(\frac{10^8 M_\odot}{M_2}\right)\frac{1}{\log(\Lambda)}, \tag{4.7}$$

where $\log(\Lambda)$ is the Coulomb logarithm, M_2 is the mass of the secondary black hole. For the initial separation r, we use the radius of the circular orbit that has the same energy as the last orbit of the binary before the (numerical) merger. Note that the model in Equation 4.7 does not account for the effect of non-circular orbits on the DF time. Taking the eccentricity into consideration can further reduce the estimated DF time [e.g. Taffoni et al., 2003]. Following the method in [Chen et al., 2021],we compute the Coulomb logarithm by:

$$\Lambda = \frac{b_{\rm max}}{(GM_2)/v_{\rm BH}^2},\ b_{\rm max} = 10\ {\rm ckpc}/h, \tag{4.8}$$

where M_2 is the mass of the secondary black hole and $v_{\rm BH}$ is the velocity of the secondary black hole with respect to the host galaxy center.

Figure 4.4.1 shows the comparison between the in-simulation dynamical friction time and the post-processed dynamical friction time from above. The top panel shows the overall distributions of the DF times. The two distributions are on the same order of magnitude at around 10^2 Myrs, with a range from 10 Myrs to 1 Gyrs. For most BH pairs, $T_{\rm DF,sim}$ is longer than $T_{\rm DF,post}$. This means that by accounting for dynamical friction in the simulation, we have already included about half of the total dynamical friction delay effects. Note that both DF timescales are shorter than 1 Gyr. In the case of the resolved DF time, this is mainly due to the fact that most of the black holes have not existed for more than 1 Gyr at $z = 3$.

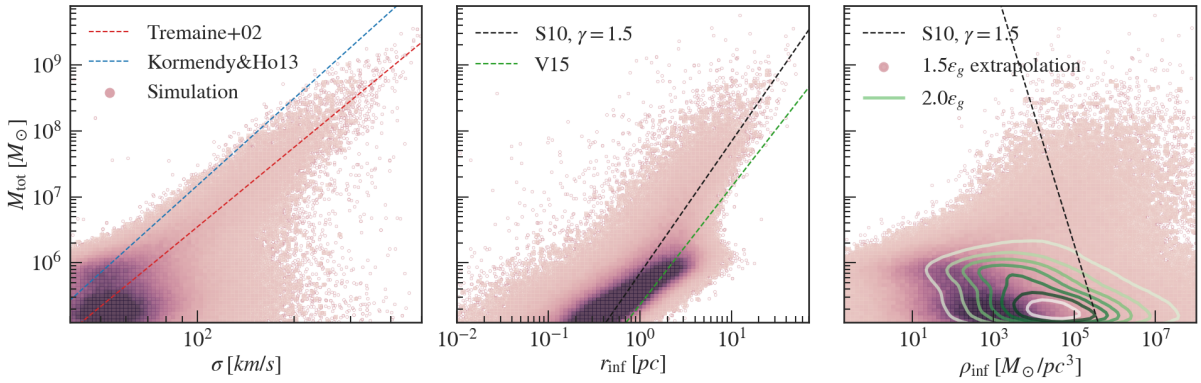

Figure 4.4.4: Variables used to calculate dynamical friction and binary hardening timescales. **Left:** $M_{\rm tot}-\sigma$ relation measured from all the binaries at the time of merger in the simulation, compared to the analytical relation given in Tremaine et al. [2002] and Kormendy and Ho [2013]. **Middle:** The influence radius derived from γ and σ measured the simulation, compared with the analytical model used in Vasiliev et al. [2015] (green dashed line), and in Sesana [2010] with $\gamma = 1.5$ (black dashed line). Our measured σ and $r_{\rm inf}$ are both close to the analytical models. **Right:** Density at influence radius extrapolated from the simulation. To illustrate the effect of extrapolation scales on $\rho_{\rm inf}$, we show the resulting extrapolation from both $1.5\epsilon_g$ (pink dots) and $2.0\epsilon_g$ (green contour). As was demonstrated in Figure 4.4.3, the density extrapolation is sensitive to the starting point of the extrapolation. However, even the extrapolated density from an outer radius is smaller compared with the analytical model used in Sesana [2010] with $\gamma = 1.5$ (black dashed line).

In the bottom panel of Figure 4.4.1, we show the relation between the two DF times and the binary mass ratio q. Here we only show the times involving at least one non-seed MBH, defined as mergers with $M_1 > 2M_{1,\rm seed}$. This is because our merger population is dominated by seed MBHs which have not grown out of their dynamical mass and thus the in-simulation DF time estimation is not exact. From Equation 4.7, we can see that the DF time is correlated with the mass of the primary galaxy (and MBH) through σ, and that it is inversely proportional to the secondary black hole mass. Hence, we expect that minor mergers will have longer decay timescales, and in the plot we do see a negative correlation between $T_{\rm DF,post}$ and q. For the in-simulation DF, although this relation is not imposed explicitly, we still observe a negative correlation between q and the DF time. This indicates that the negative correlation is still captured by the in-simulation dynamical friction modeling.

4.4.2 Loss Cone Scattering and Gravitational Wave Hardening

Once the two MBHs become gravitationally bound, the dynamical friction formalism is no longer a valid approximation, and individual interactions between singular stars and the

binary must be considered. These interactions extract angular momentum from the binary, driving them closer to each other [e.g. Merritt, 2013, Vasiliev and Merritt, 2013]. This regime is the loss-cone scattering (LC) regime, which refers to the specific cone in parameter space where stars have to exist in order to extract angular momentum from the binary [e.g. Frank and Rees, 1976, Lightman and Shapiro, 1977]. On even smaller scales, the binary will enter the gravitational wave regime where it will evolve until coalescence. Once the binary enters the gravitational wave regime, its dynamics follow the formalism of Peters [1964] at small separations of $10 - 1000$ Schwarzschild radii.

For the loss-cone scattering and gravitational-wave hardening phase, we adopt the analytical prescription in Vasiliev et al. [2015] (V15 hereafter). However, the time estimation in Equation (25) of V15 assumes a single family of $M_{\rm tot} - \sigma_{\rm inf} - r_{\rm inf}$ relation, and thus it may over-simplify the properties of the galaxies hosting the merger events. Hence we will adopt the V15 formalism but with some slight changes, so that we can use the host galaxy properties measured from the simulation. In this section, we first explain how we measure the relevant galaxy properties, then we give our binary hardening time estimation by combining analytic modeling with the measured properties.

Extrapolated Galaxy Properties

To compute the hardening time for the binaries, the important quantities to measure are: the influence radius $r_{\rm inf}$ defined as the radius containing a stellar mass equal to two times the binary mass, the velocity dispersion of stars at the influence radius $\sigma_{\rm inf}$, the power-law slope of the stellar density profile γ, and the stellar density at the influence radius $\rho_{\rm inf}$. Since the binary hardening phase begins after the dynamical friction phase, we use the snapshot immediately following the numerical merger to measure these properties.

Among the quantities above, the velocity dispersion can be measured directly from the simulation without extrapolation (for an isothermal sphere, the velocity dispersion is independent of radius). Therefore, we make the approximation that $\sigma_{\rm inf} = \sigma_{\rm gal}$, and use the measured velocity dispersion within the half-mass radius of the host galaxy.

The next galaxy property we measure from the simulation is the power-law slope γ of the stellar density profile. In Figure 4.4.2, we show three examples of the density profiles of dark matter, gas, and stars for galaxies hosting recently merged binaries. We show the profiles of a massive binary with $M_{\rm tot} = 5.6 \times 10^8 M_\odot$, a less massive one with $M_{\rm tot} = 7.6 \times 10^6 M_\odot$ at $z = 3$, and a seed-mass binary with $M_{\rm tot} = 1.9 \times 10^6 M_\odot$. For the most massive binary (top), the stellar density is the dominant component on scales below ~ 10 ckpc$/h$. The stellar density profile follows a power law down to the gravitational softening length ϵ_g, where the profile flattens due to gravitational softening. In the case of the medium-mass binary, the density of all three components is comparable at $r < 10$ ckpc$/h$, and the density profile flattens at a larger radius compared to the massive one. In the third case of a seed-seed merger, the mass of the host galaxy is high relative to the binary mass. The binary is not the most massive MBHs in this galaxy, but the merger still occurs in a relatively central region. We note that this binary belongs to the seed MBH population that still merges after

the post-processing delays.

As we do not resolve the scale of interest for the loss-cone scattering, we assume that below a scale $r_{\rm ext}$ close to the resolution limit ϵ_g, the stellar density profile follows a single power-law $\rho \propto r^{-\gamma}$. By doing so, we are able to extrapolate the stellar density to the inner region of the host galaxy. To measure the value of γ, we take the measured density from 10 bins just above $r_{\rm ext}$, and fit it to the power-law profile. Our choice of $r_{\rm ext}$ is motivated by the flattening of the profile at $\sim 1.5\epsilon_g$ in Figure 4.4.2 and the fact that gravity is not well-resolved within $\sim 2\epsilon_g$. Since the exact scale on which the simulation density becomes unrealistic is uncertain, we use both $r_{\rm ext} = 1.5\epsilon_g$ and $r_{\rm ext} = 2.0\epsilon_g$ to bracket our predictions. We also note that the modeling of the inner regions of the galaxy is a simple one, where a single power-law profile is assumed. In reality, the relation between the density of the inner core of the galaxy and the profile at kpc-scales may be more complicated. Therefore, we take into account the lack of resolution in our simulations by measuring the profiles at different radii and including a range in our final predictions (whereas in previous works this uncertainty is not explicitly considered, or often a constant power-law index is assumed).

The left panel of Figure 4.4.3 shows the measured stellar density profiles and extrapolations beyond $r_{\rm ext}$ for all binaries in `Astrid`. We show the median as well as the 95% contour of the measured density, and we compare the power-law extrapolation from $r_{\rm ext} = 1.5\epsilon_g$ and $r_{\rm ext} = 2.0\epsilon_g$. From the comparison, we see that the measurement of γ is sensitive to the extrapolation scale, and that larger $r_{\rm ext}$ results in a steeper power-law slope and thus a higher density at the inner region. However, we also note that the shift due to $r_{\rm ext}$ is comparable to the width of the distribution, and that both measurements are consistent with the values assumed in various binary hardening models.

This is further illustrated by the middle/right panel of Figure 4.4.3, where we show the distribution of the measured γ and the density extrapolated to 10 pc. For $r_{\rm ext} = 1.5\epsilon_g$, the distribution peaks at $\gamma = 1.4$, while for $r_{\rm ext} = 2.0\epsilon_g$, the distribution peaks at $\gamma = 1.9$. These values are consistent with the range of values used in most loss-cone scattering models [e.g. Merritt, 2013, Sesana, 2010, Sesana and Khan, 2015, Vasiliev et al., 2015]. In the figure, we also compared our distributions with the measured distribution in Kelley et al. [2017c] from the Illustris simulation. Compared to Kelley et al. [2017c], our measured profiles are significantly steeper, which also leads to a higher extrapolated density at $r = 10pc$. Our simulation has a higher resolution than Illustris, and thus resolves the stellar density profiles better on kpc scales. This is also due to the fact that we begin our extrapolation at different scales: Kelley et al. [2017c] uses the inner-most eight density bins that contain at least four particles, which could lie well below the gravitational softening. From the right panel, we see that the extrapolated density is sensitive to the change in $r_{\rm ext}$: $r_{\rm ext} = 1.5\epsilon_g$ gives a distribution centered at $10\,M_\odot/pc^3$, while $r_{\rm ext} = 2.0\epsilon_g$ gives a distribution centered at $100\,M_\odot/pc^3$. The order-of-magnitude difference motivates us to propagate the uncertainty in $r_{\rm ext}$ throughout subsequent analyses, as it may have non-trivial impacts on the final merger rate predictions from the simulation.

Finally, we compute $r_{\rm inf}$ and $\rho_{\rm inf}$ from the quantities measured above. As we cannot resolve the inner cusp of the galaxies in our simulation, a direct measurement of $r_{\rm inf}$ is not

possible. To estimate the influence radius, we adopt the analytical relation [e.g. Sesana, 2010]:

$$r_{\rm inf} = (3-\gamma)\frac{GM_{\rm tot}}{\sigma_{\rm inf}^2}, \tag{4.9}$$

where γ is the density power-law slope we just showed, and $\sigma_{\rm inf}$ is approximated by the measured galaxy velocity dispersion.

To get the density at the influence radius $\rho_{\rm inf}$, we extrapolate the power-law relation of the density profile down to $r_{\rm inf}$, using the measured γ and ρ. Note that our simulation does not resolve the high-density peaks below our resolution, or nuclear star clusters, and thus the extrapolated $\rho_{\rm inf}$ is likely a lower limit. Moreover, since the nuclear star clusters are not resolved, we do not account for effects such as tidal disruption, which can to a shorter binary hardening time [e.g. Arca-Sedda and Gualandris, 2018, Biava et al., 2019, Ogiya et al., 2020].

Figure 4.4.4 shows all of the measured or derived variables for computing the binary hardening timescales, and their relation with the binary mass. The $M_{\rm BH}-\sigma$ relation follows the relation in Tremaine et al. [2002] for binaries with $M_{\rm tot} > 2\times10^6 M_\odot$, but is flatter compared to the relation in Kormendy and Ho [2013]. There is a large scatter in σ for seed-mass binaries. Since the influence radius $r_{\rm inf}$ is derived from σ, γ, and the binary mass, we expect it to stay close to the analytical models from binary hardening papers. Here we compared it with the analytical model adopted in Sesana [2010] and Vasiliev et al. [2015]. Our values are in line with the Sesana [2010] model with a constant $\gamma = 1.5$, although the scatter is large. This is also consistent with the fact that our distribution in γ peaks around $\gamma = 1.4$ when measured at $r_{\rm ext} = 1.5\epsilon_g$.

Finally, in the right panel of Figure 4.4.4 we show the density at the influence radius extrapolated from the simulation. To illustrate the effect of extrapolation scales on $\rho_{\rm inf}$, we show the resulting extrapolation from both $1.5\epsilon_g$ and $2.0\epsilon_g$. As shown in Figure,4.4.3, the density extrapolation is very sensitive to the starting point of the extrapolation. Shifting the starting point by $0.5\epsilon_g = 0.75{\rm ckpc}/h$ can result in an order of magnitude difference in $\rho_{\rm inf}$. However, we note that even the density extrapolated from the outer radius is smaller than the analytical model used in Sesana [2010] with $\gamma = 1.5$.

Binary Hardening Timescales

After measuring the quantities of interest for computing the binary hardening time, we will proceed to describe the analytical model for estimating the hardening timescale. As was mentioned earlier, we base most of our model on Vasiliev et al. [2015] (V15), with appropriate changes to incorporate information from the simulation.

V15 models a separation-dependent LC hardening rate by:

$$S_*(a) = \mu S_{\rm inf}\left(\frac{a}{a_h}\right)^\nu, \tag{4.10}$$

where a is the binary separation, a_h is the hardening radius given by $a_h = \frac{q}{4(1+q)^2}r_{\rm inf}$, μ is the filling fraction of the loss cone, and ν characterizes the radial dependence of the hardening

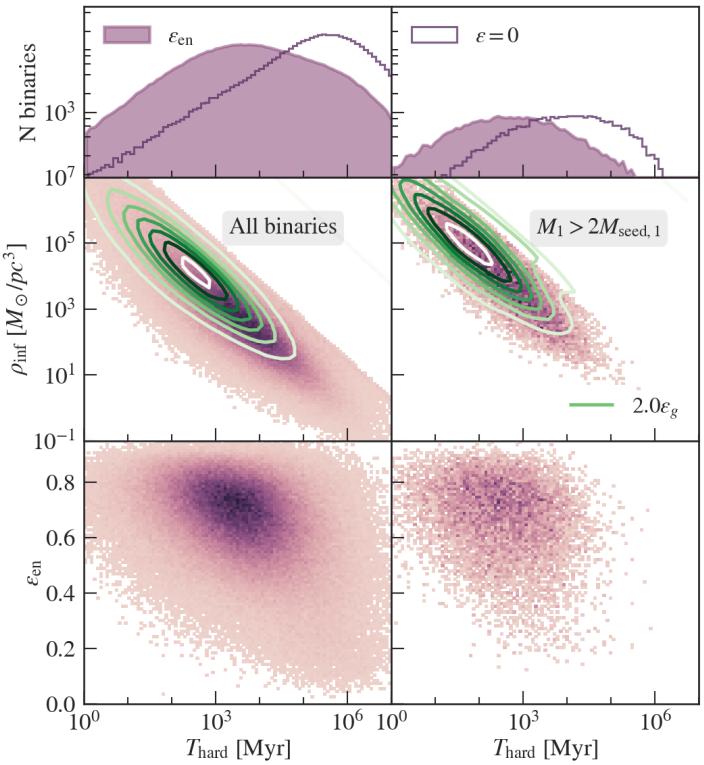

Figure 4.4.5: **Top:** The distribution of the loss-cone and gravitational-wave hardening time for all binaries in the simulation. Here we use r_{ext} from $1.5\epsilon_g$. The shaded distribution is computed using the measured eccentricity ϵ_{en}. If we assume $\epsilon = 0$ (unshaded), the decay timescales will generally be longer by a factor of ~ 100 and peak at 100 Gyr, which is much longer than a Hubble time. **Middle:** the relation between the hardening timescale and the density at influence radius ρ_{inf}. The timescale is negatively correlated with ρ_{inf}. Changing r_{ext} from $1.5\epsilon_g$ (pink dots) to $2.0\epsilon_g$ (green contours) shortens the hardening timescale. The right panel shows a clearer dependency when we remove the seed population. **Bottom:** the relation between the hardening timescale and the measured eccentricity. We see a weak negative correlation between T_{hard} and ϵ_{en}.

rate. We adopt the fiducial values of $\mu = 0.3$ and $\nu = 0.4$ from V15. $S_{\rm inf}$ is the full LC hardening rate at the influence radius given by:

$$S_{\rm inf} = H\frac{G\rho_{\rm inf}}{\sigma_{\rm inf}}, \tag{4.11}$$

where $\sigma_{\rm inf}$ and $\rho_{\rm inf}$ are the velocity dispersion and stellar density at the influence radius $r_{\rm inf}$, and H is a constant LC hardening rate given by $H = 2\pi A$, with $A = 4$ in V15. This value is slightly larger than the $H = 15$ rate given by Sesana and Khan [2015]. We note that this model is tested under the assumption that $\gamma \in [1, 2]$, and in the case of a shallower density profile from core depletion, the value of A may be smaller [e.g. Mannerkoski et al., 2019].

At a closer separation, GW emission becomes the dominant channel for binary energy loss. The hardening rate in the GW regime is given by [Peters, 1964], which considers the evolution of the Keplerian orbital due to the leading radiation reaction term at the PN2.5 level:

$$S_{\rm GW}(a) = \frac{1}{a^5}\frac{64G^3M_1M_2M_{\rm tot}F(\epsilon)}{5c^2}, \tag{4.12}$$

where ϵ is the eccentricity of the binary orbit and

$$F(\epsilon) = (1-\epsilon^2)^{-7/2}[1 + (73/24)\epsilon^2 + (37/96)\epsilon^4] \tag{4.13}$$

accounts for the eccentricity dependence of the GW hardening rate.

The separation at which the binary spends the most time, $a_{\rm gw}$, is calculated by setting $S_*(a) = S_{\rm GW}(a)$, which leads to:

$$a_{\rm GW} = \left(\frac{64G^3M_1M_2M_{\rm tot}F(\epsilon)}{5c^2}\frac{a_h^\nu\sigma_{\rm inf}}{\mu S_{\rm inf}}\right)^{1/(5+\nu)} \tag{4.14}$$

Finally, we can estimate the LC+GW hardening timescale by:

$$T_{\rm hard}^{\epsilon_{gw}} = \frac{1}{S_*(a_{\rm GW})\times a_{\rm GW}}. \tag{4.15}$$

Note that in this expression, we have only accounted for the eccentricity dependence during the GW hardening stage, and thus the superscript $\epsilon_{\rm gw}$. However, the orbital eccentricity also evolves during the LC scattering phase and can impact the hardening time. V15 models this effect by:

$$T_{\rm hard} = T_{\rm hard}^{\epsilon_{gw}=0}\times(1-\epsilon^2)[k + (1-k)(1-\epsilon^2)^4] \tag{4.16}$$

where $k = 0.4 + 0.1\log_{10}(M_{\rm tot}/10^8\,M_\odot)$. At higher eccentricities, Equation 4.15 and 4.16 give similar results, but for $\epsilon \sim 0$, the former underestimates the hardening timescale by a factor of ~ 3.

For the binaries in our simulation, we use the galaxy and binary properties shown in Section 4.4.2, together with the above formalism to estimate the binary hardening time. Note that the hardening timescale depends on the orbital eccentricity as the BHs enter the

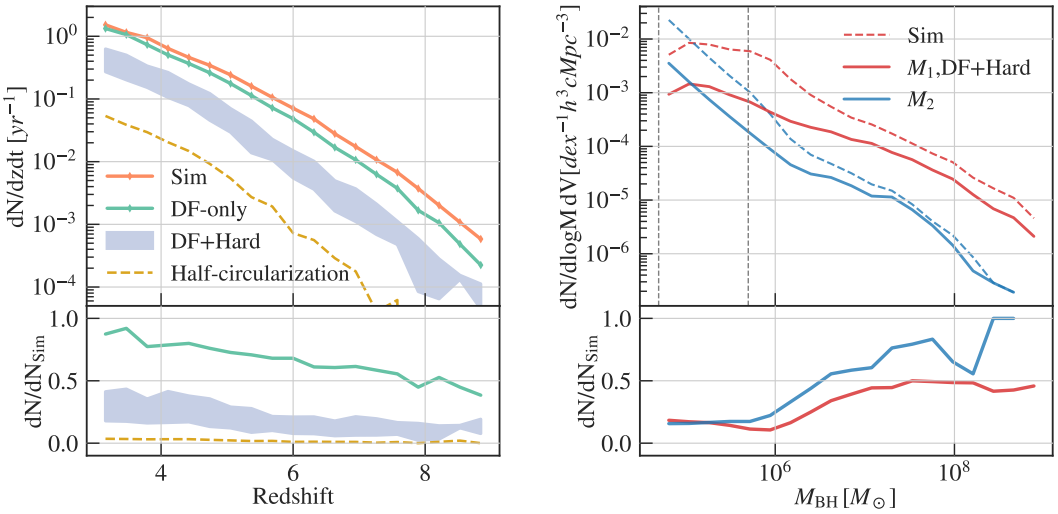

Figure 4.4.6: **Left:** The merger rates for all binaries in `Astrid` down to $z = 3$ with different levels of delays. Without considering any post-processing delays (**orange**), we expect a total of ~ 2 mergers per year of observation down to $z = 3$. The rate when considering only the DF delay (**green**) has an at most 50% decrease compared to the raw rate at the highest redshifts. The binary hardening time has the most significant effect in reducing the merger rate. The **purple** band shows the DF+hardening delayed merger rate estimated using the measured eccentricity $\epsilon_{\rm en}$. The upper limits of the bands assume $r_{\rm ext} = 2\epsilon_g$, and the lower limits assume $r_{\rm ext} = 1.5\epsilon_g$. The **yellow** dashed line shows the DF+hardening delayed merger rate estimated using the half-circularized eccentricity $0.5\epsilon_{\rm en}$, assuming $r_{\rm ext} = 1.5\epsilon_g$. The bottom panel shows the ratio between the delayed merger rates and the simulation merger rates. **Right:** The mass distribution of the two MBHs involved in the mergers. The red curves correspond to the more massive MBH and the blue curves correspond to the less massive MBH. The mass distribution of the simulation mergers is plotted in dashed lines, and that of the delayed mergers is plotted in solid lines. The bottom panel shows the ratio between the mass distributions of simulation mergers and delayed mergers. The seed-mass mergers (enclosed in the vertical dashed lines) are suppressed most strongly by a factor of ~ 6.

hardening regime: more eccentric orbits merge faster compare to circular ones. To take this effect into account, we use the orbital eccentricity shown in Section 4.3 as a proxy for the orbital eccentricity at the beginning of the binary hardening phase, assuming that the post-processed dynamical friction does not change the orbital eccentricity greatly [e.g. Colpi et al., 1999, Hashimoto et al., 2003]. There are many very recent works investigating the change in the orbital eccentricity during the dynamical friction and loss cone scattering evolution phases. Vasiliev et al. [2022] has shown that the orbital eccentricity tends to increase for the low-q, shallow-profile pairs, while Mannerkoski et al. [2021] and Gualandris et al. [2022] saw the circularization of the orbits during the dynamical friction phase. Nonetheless, all these simulations agree on the result that the initial eccentricity of the MBH orbit at $\sim 100\,\mathrm{pc}$ scales is high, and that the eccentricity by the end of the loss-cone scattering phase still traces the initial eccentricity of the MBH. Hence, our assumption of using the measured eccentricity $\epsilon_{\rm en}$ as a proxy for the eccentricity at the hardening phase still aligns with their results. In Section 4.5 and in Appendix 4.A, we will further discuss the change in the merger rate estimation due to possible circularization of the orbit during the unresolved dynamical friction phase.

We also note that the galaxy properties we put into the calculation are instantaneous properties from the simulation after the BHs go through the numerical merger. Given that the galaxy and central stellar densities will only grow with time (as well as the BH masses), our estimations are likely upper limits of the hardening time.

Figure 4.4.5 shows the relation between the binary hardening time and $\rho_{\rm inf}$ as well as the energy-based eccentricity $\epsilon_{\rm en}$. We also show the 1D distribution of hardening times. The left column includes all binaries in the catalog, while the right column only includes binaries with $M_1 > 2M_{\rm seed,1}$. For all binaries, given our measured initial eccentricities, the hardening timescale falls between 100 Myrs and 100 Gyrs, with a peak around 5 Gyrs. The timescale is strongly correlated with $\rho_{\rm inf}$ and therefore also $r_{\rm ext}$. Changing the value of $r_{\rm ext}$ from $1.5\epsilon_g$ to $2.0\epsilon_g$ leads to a shorter estimated hardening timescale. This is because higher stellar density leads to shorter hardening timescales, as the LC stars can more efficiently carry away the energy from the binary. In fact, we find that the inner stellar density is the most important property for determining the hardening timescale. Nonetheless, in both cases, the hardening timescale is much longer than the dynamical friction timescale. Note that if we do not account for the eccentricities of the binary orbits, the decay timescales will generally be longer by a factor of ~ 100 and peak at 100 Gyr, which is much longer than a Hubble time.

The bottom row of Figure 4.4.5 shows the relation between the hardening timescale and the measured eccentricity. When looking at the whole binary population, we see a negative correlation between $T_{\rm hard}$ and $\epsilon_{\rm en}$. This is expected as eccentric orbits have accelerated hardening rates. However, when we only focus on the non-seed mergers, the $\epsilon_{\rm en}$ dependence is washed out by the strong correlation with $\rho_{\rm inf}$.

Because of the strong dependence of the delay timescale on the uncertain variable $\rho_{\rm inf}$, we will propagate this uncertainty to the merger rate predictions in the next session, and characterize how the uncertainty due to numerical resolution affects the mergers in `Astrid`.

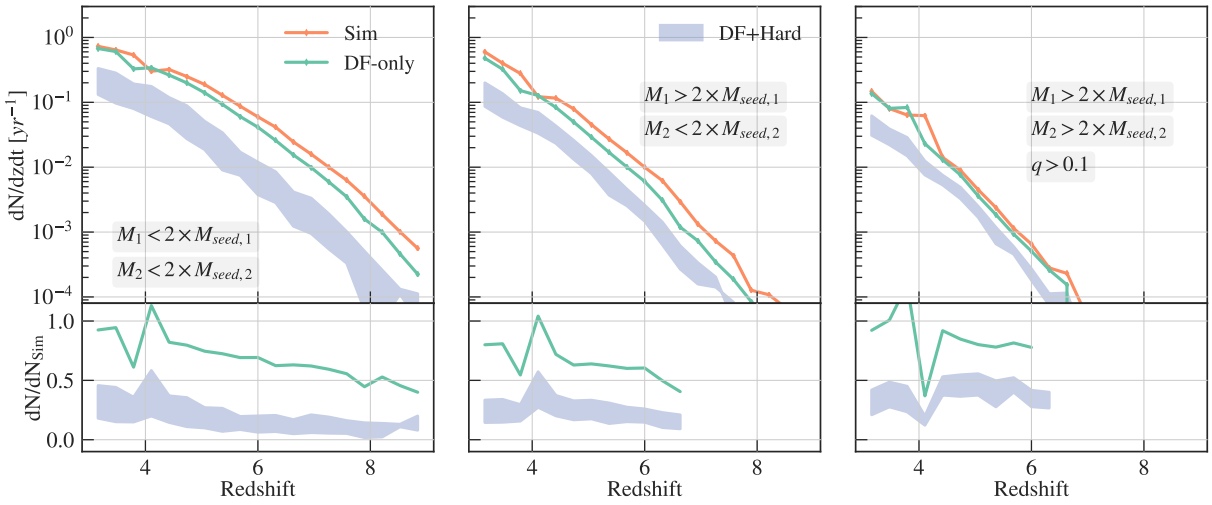

Figure 4.5.1: Merger rates for different mass cuts and mass-ratio cuts. **Left:** The merger rates for the seed-mass population, where the masses of both MBHs are less than two times their seed masses. The colors are the same as in Figure 4.4.6. Compared to 4.4.6, this population makes up $\sim 60\%$ of the mergers. **Middle:** Merger rate for MBHs with only one of the two grown out of the seed mass. This rate makes up $\sim 30\%$ of the entire merger population. Compared to the seed-seed mergers, here we see fewer mergers at high redshifts, but a similar rate at $z = 3$. **Right:** Mergers with both MBHs larger than two times their seed masses and with $q > 0.1$. When constrained to major and non-seed mergers, the effect of DF is barely noticeable. The DF+Hard delayed rate makes up 50% of the total rate. The lower panels show the ratio between the delayed merger rates and the simulation merger rates.

4.5 MBH merger rate and Host galaxy properties

After characterizing the delay time, in this section we present the rate at which GW signals from MBH mergers will reach the earth, taking into account the sub-resolution delay processes. We also examine how the DF and binary hardening delay affects the different populations of MBH mergers. Finally, we investigate the galaxy properties for different parts of the merger population.

4.5.1 Merger Rate Predictions

We calculate the rate by integrating the number of mergers in the simulation over redshifts, incorporating the cosmic volume at the given redshift:

$$\frac{\mathrm{d}N}{\mathrm{d}z\,\mathrm{d}t} = \frac{\mathrm{d}^2 n(z)}{\mathrm{d}z\,\mathrm{d}V_c}\frac{\mathrm{d}z}{\mathrm{d}t}\frac{\mathrm{d}V_c}{\mathrm{d}z}\frac{1}{1+z} \tag{4.17}$$

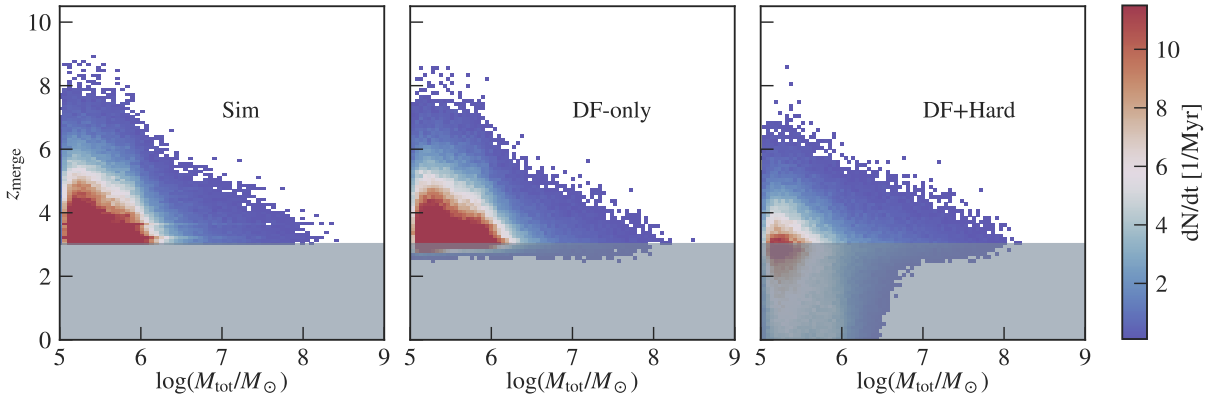

Figure 4.5.2: The distribution of mergers on the $M_{\rm tot} - z_{\rm merge}$ plane for the simulation and delayed mergers, color-coded by the number of mergers per Myr. **Left:** The distribution for all mergers without delays. **Middle:** The same merger population with the post-merger DF time added. Here, we see a slight shift of the merger population towards a lower redshift, but nothing gets delayed below $z = 2$. **Right:** The distribution after considering both the DF delay and the hardening time. Note that since the latest redshift of the simulation is $z = 3$, all the data points at $z < 3$ (masked in grey) are results of the delay from $z > 3$ numerical mergers, and are not representative of all merger events at $z < 3$. We see a significant shift of the mergers towards lower redshifts. The population most significantly shifted are the low-mass mergers with $M_{\rm tot} < 10^{6.5} M_\odot$, while the most massive binaries are still able to merge at relatively high redshifts.

where $\mathrm{d}V_c$ is the comoving volume element of the universe at a given redshift and $n(z)$ is the number of mergers at that redshift. The $1/(1+z)$ term redshifts the infinitesimal time element in $\mathrm{d}z/\mathrm{d}t$ to the observer frame time interval.

To calculate this rate from our simulation, we take the finite-interval approximation:

$$\frac{\mathrm{d}^2 n(z)}{\mathrm{d}z\,\mathrm{d}V_c} = \frac{N(z)}{\Delta z\, V_{\rm sim}}, \tag{4.18}$$

where Δz is the width of the redshift bin, $N(z)$ is the total number of mergers within that redshift bin, and $V_{\rm sim} = (250\,\mathrm{Mpc}/h)^3$ is the volume of our simulation in comoving units.

To clearly see the effect of each stage of the delay, we calculate three different rates. We first compute the "Sim" rate which uses the numerical merging time as the redshift of the merger [also see DeGraf et al., in prep]. Then we add the post-processed DF time to the numerical merger time to compute the "DF-only" rate. We further account for the binary hardening timescales and calculate the "DF+Hard" rate. Finally, to account for the possible circularization of the orbital eccentricity during the unresolved dynamical friction evolution, we compute the "half-circularization" rate assuming that binaries only retain 50% of their initial eccentricities at the beginning of the hardening phase. Our "half-circularization" model uses a simple assumption that all the binaries lose 50% of the initial measured eccentricities, regardless of the environment. In reality, the eccentricity evolution can depend on various factors such as the density profile and the mass ratio of the host galaxies, and could deviate from a simple linear relation. Nonetheless, due to the lack of an analytical model for eccentricity evolution in the dynamical friction phase, we choose this simplified linear relation in order to estimate the uncertainties.

In the left panel of Figure 4.4.6, we plot the merger rates with different levels of post-processed delays, for the whole merger population in `Astrid`. First, we notice that the number of mergers keeps increasing with decreasing redshift for all three models. This is because we keep seeding BHs as structures form and grow, and we have not reached the peak in seeding rate at $z = 3$. Without considering any post-processed delays ("Sim"), we expect a total of ~ 1.8 mergers per year of observation down to $z = 3$. The post-processed DF time does not significantly impact the total observed merger rate ("DF-only"), with a $\sim 50\%$ decrease at the highest redshift ($z \sim 8$). The binary hardening time has the most significant impact on the merger rate at all redshifts ("DF+Hard"). We see that the merger rate is reduced by a factor of $3 \sim 7$ after adding the delay from binary hardening. The resulting merger rate is $0.3 \sim 0.7$ at $z > 3$. Here the upper limit is given by assuming $r_{\rm ext} = 2\epsilon_g$ and the lower limit is given by $r_{\rm ext} = 1.5\epsilon_g$. Finally, if we further consider the circularization of MBH orbits during the unresolved dynamical friction evolution, the rate estimation decreases to $0.1 \sim 0.3$ per year at $z > 3$. This is again a factor of ~ 5 decrease in the merger rate, comparable to the uncertainties due to the density profile measurements. In Appendix 4.A, we will investigate in more details how various eccentricity assumptions affect our merger rate predictions. There we will show that the difference between a "half-circularizaiton model" and a "full-circularization" model (where all orbits are assumed to be circular) is within 15% in terms of the merger rate prediction. Thus by investigating the

"half-circularization" model here, we have approached the lower-bound in the merger rate due to orbital circularization. On the bottom panel, we show the ratio between the delayed merger rate and the simulation merger rate as a function of redshift. For both DF-only and DF+Hard delays, the fractional rates get higher at lower redshifts. This is a result of the high-redshift mergers being pushed down to low redshifts.

In the right panel, we show the mass distribution of the two MBHs involved in each merger. The dashed lines correspond to the simulation merger without any delays, and the solid lines show the distribution of the merger population after the DF+hardening delays. First, we can see that both before and after the delay, the merger population is dominated by seed-mass mergers (the ones enclosed by the vertical dashed lines), with M_1 evenly distributed across the seed masses and M_2 concentrated on the lower-mass end of the seeds. It is also this seed-mass merger population that gets suppressed the most by the delay. From the ratio between the mass functions shown in the bottom panel, we see that for the seed-mass mergers, only $\sim 15\%$ still merge at $z > 3$ after the delays, whereas at the high-mass end this fraction increases to 50%.

In order to disentangle different merger populations, in Figure 4.5.1 we further split the rate by how many seed MBHs are involved in the merger. The left panel shows the merger rates for the seed-mass population, where the masses of both MBHs are below two times their seed masses. This population makes up $\sim 60\%$ of the mergers. At $z > 5$, the seed-seed mergers are strongly suppressed by the binary hardening delays because the stellar density is relatively low. The middle panel shows the mergers with the only more massive MBH grown beyond two times its seed mass. At $z = 3$, the rate from this group is comparable to the rate from the seed-seed mergers. However, the number decreases more steeply as we go to higher redshifts. Compared to the seed-seed mergers, this group has a higher mass ratio and thus a longer DF time. The effect of the binary hardening delay, however, is smaller because of the higher density in the remnant galaxy. Finally, on the right panel, we show the more massive and major mergers. Compared to the previous two groups where at least one seed-mass MBH is involved in the merger, the mergers from this group are ~ 6 times lower. The effect of delay is also the smallest. In particular, we noticed that the DF-only rate is very similar to the simulation rate. Even for this group where the effect of delays is the smallest, the merger rate is still suppressed by $> 50\%$ at each redshift compared to the simulation merger rate.

Figure 4.5.2 shows the distribution of MBH mergers on the $M_{\rm tot} - z_{\rm merge}$ plane for both the simulation and delayed mergers, color-coded by the number of mergers per Myr. Without any delay, the majority of the merger events are seed-seed mergers around $z = 3 - 4$. As we would expect from the black hole mass growth over time, we see more massive mergers at lower redshifts. The middle panel shows the same merger population with the post-merger DF time added. As was discussed in the previous paragraph and in Section 4.4.1, the post-processed DF peaks around 200 Myrs and does not significantly delay the mergers. Here, we see a slight shift of the merger population towards a lower redshift.

In the right panel of Figure 4.5.2, we show the distribution after considering the DF delay and hardening phase. Note that since the final simulation output is at $z = 3$, all the data

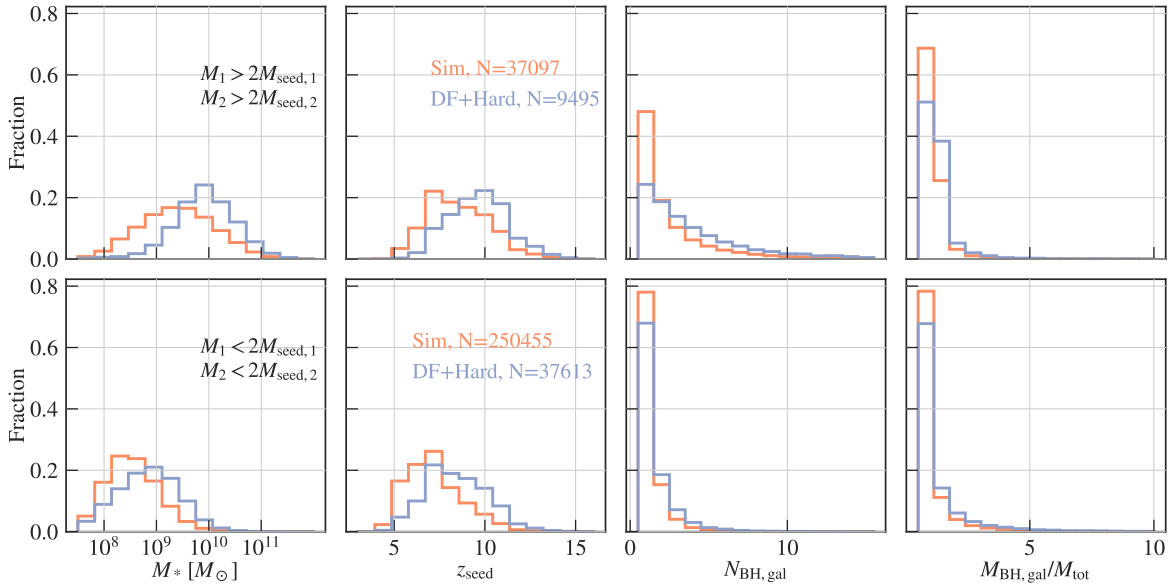

Figure 4.5.3: The fraction of the merger population in each bin of the galaxy stellar mass hosting the merger (**first column**), seeding redshifts of the merged MBHs (**second column**), number of MBHs in the host galaxy (**third column**), and the ratio between the total MBH mass in the host galaxy and the binary mass $M_{\rm tot}$ (**fourth column**). The top row shows the non-seed merger population, and the bottom row shows the seed-mass merger population. The simulation mergers are shown in orange and the DF+Hard delayed mergers are shown in purple. The total number of $z > 3$ mergers in each population is shown in the second column with corresponding colors.

points at $z < 3$ are the results of delayed $z > 3$ numerical mergers, and are not representative of all merger events at $z < 3$. Compared with the other two panels, we see a significant shift of the mergers towards lower redshifts. The population that is most significantly shifted are the low-mass mergers with $M_{\rm tot} < 10^{6.5} M_\odot$, while the most massive binaries are still able to merge at relatively high redshifts. This is a consequence of the large hardening time scale of smaller BHs associated with lower $\rho_{\rm inf}$.

4.5.2 Properties of High-z MBH Mergers

From the previous section, we have seen that while some low-mass mergers are significantly delayed and do not merge at $z > 3$, $\sim 15\%$ of them still do. For the non-seed mergers, although the delay is generally less significant, we still see a 50% decrease in merger rate when accounting for the delays. Now we will investigate which part of the merger population gets significantly delayed, and which still manages to merge at high redshifts.

In Figure 4.5.3 we show the properties of MBHs involved in both the simulation mergers and the delayed mergers. The top row shows the properties of the non-seed mergers, and the

bottom row shows the properties of the seed-seed mergers. We start by looking at the mass distribution of galaxies hosting the mergers (shown in the first column). For the simulation mergers consisting of two non-seed MBHs, the masses of the host galaxies peak at $4\times10^9 M_\odot$. For systems that still merge after the delays, we see a clear shift towards the higher-end in stellar masses with a peak at $\sim 10^{10} M_\odot$. This is because for more massive galaxies, the high stellar density enables more efficient hardening through loss-cone scattering, and thus the delay time is shorter (also see Figure 4.4.5). For mergers involving two MBH seeds shown on the bottom, we observe a similar trend. Overall, seed mergers reside in less massive galaxies with stellar masses below $4 \times 10^8\, M_\odot$. The delayed merger events also pick up the more massive galaxy population out of the simulation mergers with galaxy masses distributed around $10^9\, M_\odot$.

In addition to the stellar environment which plays an important role in the delay time estimation, the seeding redshift of the MBHs can also affect whether the two MBHs still merge at a high redshift after the delay. This is shown in the second column of Figure 4.5.3. While the seeding redshift of the simulation merger MBHs is $z \sim 7$, the MBHs involved in delayed mergers are seeded as early as $z = 10$. For the seed-seed mergers shown on the bottom, the overall seeding redshift is lower, but we also see a shift towards a higher redshift when comparing the delayed mergers to the simulation mergers. The bias towards early MBH seeding for delayed mergers is also correlated with the higher host galaxy mass we have seen earlier: because the delayed mergers favor earlier seeds, they also tend to reside in galaxies that are massive enough at high redshifts to host an MBH seed.

On the right two columns, we examine the properties of other MBHs embedded in the host galaxy of the mergers. The third column shows the total number of MBHs embedded in the host galaxy of the merger, in the snapshot immediately following the numerical merger (so the merging MBHs will be counted as one object). The fourth column is the mass ratio between all MBHs in the host galaxy and the merging system. For both the seed and non-seed merger populations, the merging system is the sole MBH in the host galaxy in the majority of mergers. For the non-seed population, there is still a $> 50\%$ fraction of mergers happening next to a third MBH (or more). Interestingly, the delayed merger systems favor galaxies with more MBHs near the merging ones (also correlated with larger galaxy masses). Nonetheless, the merging system is still the most massive MBH in its host galaxy in most cases when we look at the $M_{\rm BH,gal}/M_{\rm tot}$ ratio.

When constrained to seed-seed mergers, we see that $\sim 70\%$ of the mergers are the single MBH in the host galaxy. The delayed mergers also tend to pick out the galaxies with more MBHs compared to the simulation mergers. However, contrary to the non-seed case where the merging MBH is more massive than the other MBHs in the same galaxy, for seed-seed mergers that do occur near a third MBH, the mass of the third MBH is more likely to be larger. This can be seen from the fact that the $N_{\rm BH,gal}$ distribution is more peaked at $N_{\rm BH,gal} > 1$ compared to the $M_{\rm BH,gal}/M_{\rm tot} > 1$ distribution (it means that if there is a third MBH, its mass can be larger than $M_{\rm tot}$ in some cases, resulting in the longer tail of $M_{\rm BH,gal}/M_{\rm tot}$).

From the investigations above, we conclude that the $z > 3$ mergers after the DF and

hardening delay make up a small and biased sample of the simulation mergers. In particular, they are systems with MBHs seeded earlier and embedded in more massive galaxies compared to the overall simulation merger population. Moreover, the majority of the merger remnant is the only MBH in its host galaxy, especially for the seed-mass mergers. However, the delayed mergers tend to pick out more systems that have other nearby MBHs in the remnant galaxy compared to the overall simulation merger population.

4.6 Gravitational Wave Emission from MBH Mergers

With a catalog of merging binaries, their merging time, and orbital eccentricities, we can not only compute the rate of mergers reaching the Earth, but also predict the gravitational wave signal that can be observed from these sources. This section is dedicated to predicting the gravitational wave signal and detectability of the `Astrid` mergers with LISA. We first briefly describe the characteristic strain for circular sources, and then we generalize to the signal from eccentric sources. After that, we combine with the LISA sensitivity curve and compute the signal-to-noise ratio (SNR) for each merger in the simulation.

4.6.1 Characteristic Strain of Circular Orbits

MBH binaries provide a variety of signals measurable by LISA since their chirp evolution in the frequency domain occurs near the low-frequency band edge of the LISA sensitivity curve. Binaries with $10^5 - 10^7 M_\odot$ total mass will provide a measurable inspiral, merger, and ringdown leading to signals out to the cosmic horizon [Amaro-Seoane et al., 2017]. The binary inspiral is the initial stage of binary black hole coalescence when the two MBHs orbit one another at separations greater than the innermost stable circular orbit (ISCO; $R = 6GM_{\rm BH}/c^2$). At these separations, the orbit is usually treated with a post-Newtonian formalism. The merger stage follows the binary inspiral with a highly non-linear relativistic process. This process continues until the binary components form a single event horizon, leading to ringdown.

We use the characteristic strain, h_s, to model the binary signal which accounts for the time the binary spends in each frequency bin [Finn and Thorne, 2000]. The characteristic strain is given by [e.g. Moore et al., 2015]:

$$h_s(f) = 4f^2|\tilde{h}(f)|^2 \tag{4.19}$$

where $\tilde{h}(f)$ represents the Fourier transform of a time domain signal.

To generate the waveforms, we use the phenomenological waveform PhenomD [Husa et al., 2016, Khan et al., 2016] implemented within the `gwsnrcalc` Python package [Katz and Larson, 2019]. The input parameters are the binary masses, merging redshift, and the dimensionless spins of the binary. For the MBH masses, we do not account for mass growth after the numerical merger. However, we note that the MBH can potentially gain a significant fraction of its mass during the $> 1\,$Gyr of time in the dynamical friction [e.g. Banks et al.,

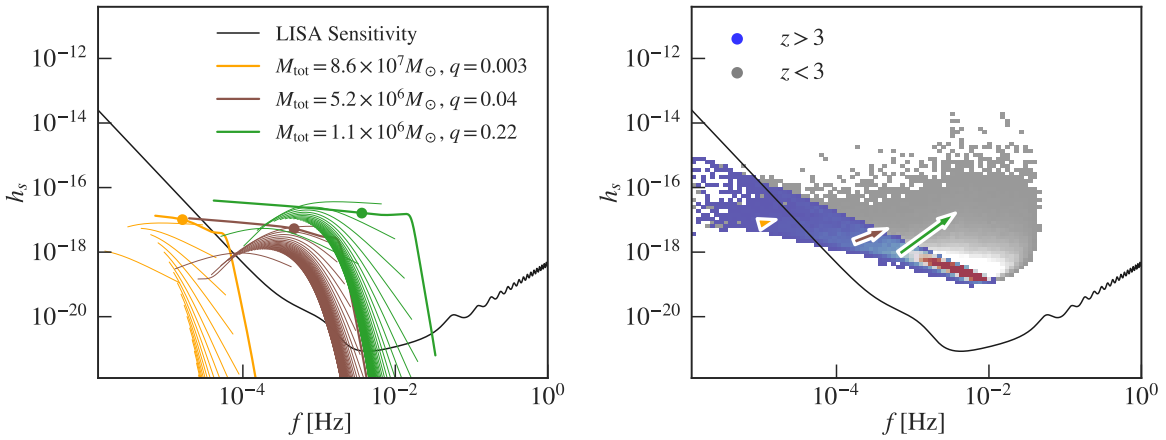

Figure 4.6.1: **Left:** Example waveforms for three binaries of different masses in `Astrid`. The thick curve shows the waveform assuming $\epsilon = 0$, while the thin lines are the waveform assuming eccentric orbits. We also show the LISA sensitivity curve from Amaro-Seoane et al. [2017] (black solid) for comparison. The numerical merging time of all example binaries is $z \sim 3.1$. **Right:** The $h-f$ distribution after applying the delay models. The arrows indicate the shifts in strain and frequency by the delay. Most signals are shifted to the upper-right due to the lower redshift of the merger after the delays. The light grey region shows the merger population delayed to $z < 3$, which is not part of our prediction.

2021] or loss-cone scattering phase. The dimensionless spin a characterizes the alignment of the spin angular momentum with the orbital angular momentum, and the value of a ranges from -1 to 1. However, we do not have any information on the spin of the SMBHs in our simulation. Therefore, following the argument in Katz et al. [2020], we assume a constant dimensionless spin of $a_1 = a_2 = 0.8$ for all binaries [e.g. Miller, 2007, Reynolds, 2013].

In Figure 4.6.1, we show the distribution of the merging frequency $f_{\rm merge}$ and the strain at this frequency for all binaries in the simulation, before and after applying the DF+Hardening delay models. To evaluate the detectability of the population with LISA, we also plot the proposed LISA sensitivity curves. We use the LISA sensitivity configuration from the LISA Mission Proposal [Amaro-Seoane et al., 2017], and we use $h_N = \sqrt{S_N}$ [Moore et al., 2015] to convert from the proposed power spectral density S_N to strain h_N.

In the left panel of Figure 4.6.1, we show example waveforms for binaries of different masses but similar numerical merging time. The thick curve shows the waveform assuming $\epsilon = 0$, with the dot representing the merging frequency $f_{\rm merge}$. We will discuss the thin lines with non-zero eccentricities in later sections. From the example waveforms, we see that at a fixed source redshift, the more massive binary has a higher strain amplitude. However, this does not necessarily lead to a more significant detection, because the lower frequency at which the wave is emitted falls into the region where the LISA sensitivity is worse. Out of these three binaries, the two least massive binaries are detectable by LISA while the most massive one is not. After the DF and hardening delays, all curves have higher strain

amplitudes, as the strength of the signal is negatively correlated with redshift.

After looking at individual cases, we turn to the whole binary population. On the right panel, we show the distribution of $f_{\rm merge}$ and $h_s(f_{\rm merge})$ for `Astrid` mergers, after the post-processed delays. We have masked the signals from $z < 3$ mergers in light grey, as they are purely due to the post-processed delays, and are not part of our simulation predictions. The majority of merger events within the simulation lie above the LISA sensitivity curve. From example waveforms, we see that once any given GW signal crosses the detector sensitivity curve, the ratio of the signal to the sensitivity curve rapidly increases by a few orders of magnitude. Since the merger population is dominated by seed-seed mergers, we see a peak around $f_{\rm merge} \sim 10^{-2}$Hz, corresponding to the example green curve. Finally, we demonstrate the shift of the signal due to the delay model by the colored arrows. The tail of the arrows indicates the location of the frequency/strain before the delays. The head of the arrows are the signals after the delays. We see that in the example cases, the signal shifts to the high-strain, high-frequency region of the plane. This is mainly because of the delay of the mergers from $z > 3$ to $z < 3$.

4.6.2 GW Signal from Eccentric Sources

In the previous section, we have shown a single $h_s - f$ relation by assuming circular orbits for the binaries. In this section, we will utilize the eccentricity measured from the simulation when calculating the strain and signal-to-noise ratio (SNR) for each binary.

The GW strain from an individual, eccentric source can be related to that of a circular source as [e.g. Amaro-Seoane et al., 2010, Kelley et al., 2017c]:

$$h_s^2(f_{\rm r}) = \left(\frac{2}{n}\right)^2 \sum_{n=1}^{\infty} h_{\rm r,circ}^2(f_{\rm h}) g(n,\epsilon)|_{f_{\rm h}=f_{\rm r}/n}, \tag{4.20}$$

where $h_{\rm r,circ}$ is the characteristic strain of a circular source given by Equation 4.19, $g(n,\epsilon)$ is the GW frequency distribution function given by Equation 20 in Peters and Mathews [1963] with $\sum_{n=1}^{\infty} g(n,\epsilon) = F(\epsilon)$, where $F(\epsilon)$ is defined by Equation 4.13.

During the GW-driven inspiral, the orbital eccentricity also evolves according to Peters [1964] Equation (5.7), such that it decays towards zero as the binary inspirals toward merger. This will affect the orbital frequency by:

$$\frac{f_{\rm orb}}{f_0} = \left[\frac{1-\epsilon_0^2}{1-\epsilon^2}\left(\frac{\epsilon}{\epsilon_0}\right)^{12/19}\left(\frac{1+\frac{121}{304}\epsilon^2}{1+\frac{121}{304}\epsilon_0^2}\right)^{870/2299}\right]^{-3/2}, \tag{4.21}$$

where ϵ_0 is the initial eccentricity at the reference frequency f_0.

In Figure 4.6.1, the multiple thin lines are the waveforms from higher-order harmonics assuming eccentric orbits. For circular orbits, the GW is emitted at a single frequency at a fixed separation, while the eccentric binaries emit GW at higher-order harmonics at a given time. One consequence of this is that the energy dissipated in higher-order harmonics

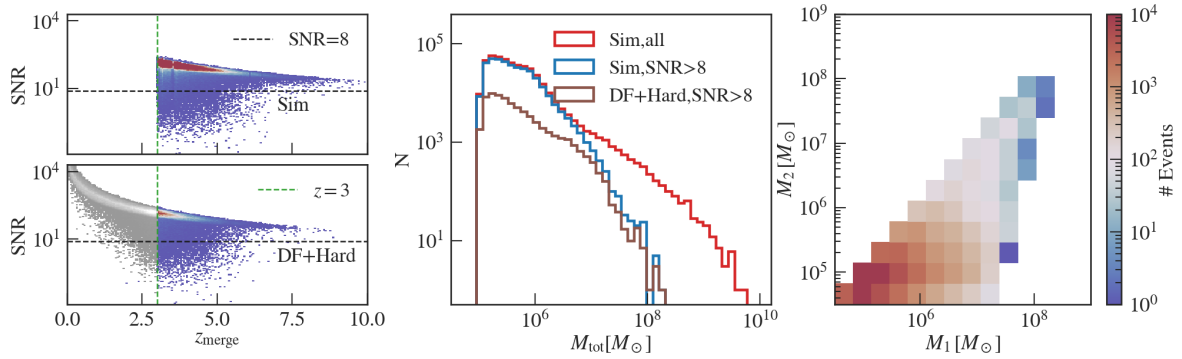

Figure 4.6.2: **Left:** the joint distribution of the SNR and redshift for `Astrid` mergers. The top row is the SNR computed before the DF and hardening delays, and the bottom row is the SNR after the delay time is applied. The mergers delayed to $z < 3$ are masked in grey. **Middle:** distribution of binary mass for all `Astrid` mergers (red), the ones with SNR>8 without the delay model (blue), and the ones that merge before $z = 3$ after the delays (brown). The SNR>8 cut eliminates all mergers with $M_{\rm tot} > 10^8 M_\odot$, while the drop in low-mass merger events is due to the delays. **Right:** the distribution of two MBH masses for LISA detectable merger events at $z > 3$. Most events are expected to involve two seed-mass MBHs.

is below the detection sensitivity, and thus the signal will be smaller compared with the circular orbits.

We note that by using the simulation measurement of the orbital eccentricity as the initial eccentricity in the inspiral phase, we did not account for any possible increase in ϵ during the loss-cone scattering phase [see, e.g. Sesana, 2010]. However, such changes mostly affect low initial eccentricity pairs [e.g. Kelley et al., 2017b]. Since the initial binary eccentricities of our MBH pairs are already very high, we expect the loss-cone scattering to have only a minor effect on the final eccentricity.

4.6.3 Detectability Prediction

Although the strain in Figure 4.6.1 is a good estimation of the detectability of a circular binary, for the eccentric case a more careful prediction comes from the signal-to-noise ratio (SNR). The SNR is estimated by integrating the ratio of the signal to the noise in the frequency domain. The sky, orientation, and polarization averaged SNR are given by :

$$\langle \mathrm{SNR} \rangle^2 = \frac{16}{5} \int_{f_{\rm start}}^{f_{\rm end}} \frac{h_s^2}{h_N^2} f^{-1} df, \tag{4.22}$$

where $f_{\rm start} = f(t_{\rm start})$ and $f_{\rm end} = f(t_{\rm end})$, with $t_{\rm start}$ and $t_{\rm end}$ representing the starting and ending time of when the signal is observed. Note that here we are assuming eccentric waveforms for the binaries, and thus h_s is given by the sum over different modes following Equation 4.20. As it is not computationally feasible to sum an infinite number of modes,

we truncate the sum in Equation 4.20 at $n = 50$ and we have checked that the difference between the first 50 and the first 100 modes is less than 5%.

For the current configuration, we assume that the LISA observation lasts for 4 years. We further assume a most optimistic SNR for all mergers by taking $t_{\rm end} = t_{\rm peak}$ and $t_{\rm start} = t_{\rm peak} - 4$yrs. Under this assumption, we are always integrating the part of the waveform where the strain is maximized. However, as was discussed in Salcido et al. [2016] and Katz et al. [2020], the actual SNR may be smaller if there is an offset between the LISA observation window and the merger time of the binary.

Figure 4.6.2 shows the distribution of the SNR computed for all mergers in the simulation. The left column shows the joint distribution of SNR and the merging redshift. The top row is the SNR computed with merging redshifts before the DF and hardening delays, and the bottom row is the SNR after the delay time is applied. As was expected from the simpler calculation shown in Figure 4.6.1, the majority of the binary population in the simulation has an SNR larger than the LISA detection threshold of 8 (plotted as dashed gray lines). The ones that fall below the SNR cut are mainly massive mergers with $M_{\rm tot} > 10^7\,M_\odot$. When we account for the delays, the mergers are pushed towards lower redshifts, and the resulting SNR is higher for each event.

The middle panel of Figure 4.6.2 shows the effect of delays and the SNR cut on mergers with different masses. The SNR cut removes all mergers with $M_{\rm tot} > 10^8\,M_\odot$ from the LISA-detectable population. On the low-mass end of MBH mergers, the reduction results from the DF and binary hardening delays. Combining both the delays and SNR cut, we see that the overall detectable mergers at $z > 3$ are $\sim 15\%$ of the original `Astrid` merger population across all masses. The seed-mass mergers still dominate over other events even though they are most strongly suppressed by the delays. Finally, on the right panel, we show the mass distribution of the two MBHs involved in each detectable event. The majority of these events are expected to be mergers from two seed-mass MBHs. On the high-mass end, the detectable events have a mass ratio of $q \sim 1$ (close to the diagonal line). Based on these results, the likelihood that a LISA detection comes from mergers of MBH seeds is high, but the detectable MBH seed mergers is only a small sample of the seed MBH pairs and the associated galaxy mergers.

Here, accounting for the delay time to merger affects the resulting SNR more than the eccentricity. The eccentricity itself, however, may affect the prospects for multi-messenger follow-up. For example, eccentric binaries may spend a shorter amount of time in the LISA band compared to circular binaries. Spin-orbit interactions in eccentric binaries may change the orbital inclination with respect to the line of sight, which may also play a role in detectability and sky localization. We will explore such effects and their implications for multi-messenger follow-up in a companion paper.

4.7 Conclusion and Discussion

In this work, we have made predictions for the MBH merger rate and associated LISA events for a cosmological population of MBHs with masses ranging between $5 \times 10^4 M_\odot$ and $10^{10} M_\odot$

down to $z = 3$, using the large volume cosmological simulation `Astrid`. At high redshifts, MBH mergers and the associated GW signal should provide strong constraints for models of seed black hole formation. In `Astrid` , MBH seeds range from $5 \times 10^4 M_\odot$ to $5 \times 10^5 M_\odot$, covering down to masses that LISA will be most sensitive to. Moreover, in `Astrid` we have included an on-the-fly subgrid dynamical friction prescription, which allows us to trace the MBH orbits down to the resolution limit.

Using the MBH orbits directly from the simulation, we estimated the (generalized) orbital eccentricity for unbounded MBH pairs that undergoDF-donimated orbital decay in the `Astrid` simulation. In addition, we use the most recent post-processing models to account for the additional delay in MBH mergers due to dynamical friction [Dosopoulou and Antonini, 2017] and binary hardening [Vasiliev et al., 2015] at scales not resolved directly by `Astrid`. This is done by accounting for the orbital eccentricities constrained by the simulation which is important for the loss-cone scattering and gravitational-wave hardening phase. After considering the effect of these processes in delaying the MBH merger, we made a detailed prediction of the expected number of mergers down to $z = 3$, the redshift that the simulation has currently reached. Finally, we computed the detectability of these events by LISA.

We find that most MBHs pairs in `Astrid` have eccentric orbits distributed near $\epsilon = 0.8$. We verify the eccentricity measurements by using both the shape and the dynamical information of the MBHs and find general agreement on the result. While some orbits circularize during the dynamical friction decay, the majority of them still maintain a high level of eccentricity at the time of the numerical merger. The orbital eccentricity is important in accelerating the binary hardening process. In particular, we show that the assumption of circular orbits for all binaries leads to estimates for the binary hardening time that can exceed 20 Gyrs for most `Astrid` binaries. Taking into account the measured orbital eccentricities, our estimated hardening times fall between $1 \sim 10$ Gyrs.

Even after considering the accelerated binary hardening rate due to eccentric orbits, for `Astrid` mergers close to the seed mass, the binary hardening (including LC and GW hardening) time typically provides the longest delay, and it remains more important than the dynamical friction component (including DF time modeled in `Astrid` directly and the estimated sub-resolution component). For MBH binaries above the seed mass, the hardening time becomes comparable to the DF time and always remains < 1 Gyrs. By comparing the DF directly modeled in `Astrid` with the post-processed (sub-resolution) DF time, we find that they are comparable, accounting for $100 \sim 300$ Myr of binary evolution. At the resolution of `Astrid`, the sub-grid DF added directly in the simulation is able to recover more than half of the dynamical friction decay process before the numerical merger.

Without accounting for any additional post-processed binary dynamics delays, we expect ~ 2 merger events per year [DeGraf et al., in prep] from the $z > 3$ MBH population in `Astrid`. With the post-processed dynamical friction and binary hardening taken into account, the expected merger rate reduces to $0.3 \sim 0.7$ per year at $z > 3$. `Astrid` predicts for merger rates that are higher than most previous predictions from hydro-dynamical simulations of comparable volumes [e.g. Katz et al., 2020, Salcido et al., 2016, Volonteri et al., 2020],

because `Astrid` accounts for a seed population [see DeGraf et al., in prep, for a more direct comparison] in halos about an order of magnitude lower in mass than e.g. Illustris ($M_{\rm halo,thr} = 7 \times 10^{10}\,M_\odot$) and EAGLE ($M_{\rm halo,thr} = 1.4 \times 10^{10}\,M_\odot$). Among the whole MBH merger population, the seed-mass mergers are most affected by the delays, with only $< 20\%$ of the original simulation mergers still merging at $z > 3$. Nonetheless, because the seed-mass mergers dominate the merger population in absolute numbers (250455 out of 440999), they still occupy a large fraction of the delayed mergers. Out of the delayed merger events at $z > 3$, $\sim 60\%$ involve two seed-mass MBHs, $\sim 30\%$ are mergers between one non-seed MBH and one seed-mass MBH, and $\sim 10\%$ are mergers between two large mass MBHs.

We use a 4-year LISA observation time to calculate an upper limit on the SNR for each merger event. Many of these high-z mergers result in SNRs around ~ 200. With a SNR$>$8 threshold, high-mass merger ($M_{\rm tot} > 10^8\,M_\odot$) events are removed from the detectable population at $z > 3$. The $M_{\rm tot} < 10^7\,M_\odot$ mergers are still detectable. As a result, the LISA detectable population is still dominated by seed MBH mergers, and the expected detection rate is similar to the total merger rate of $0.3 \sim 0.7$ per year at $z > 3$.

Based on these results, a LISA detection of merger events from MBH seeds population is highly feasible. However, the detectable MBH seed mergers are predicted to correspond to the sample of the seed MBH pairs that occur in hosts with stellar masses close to $10^9\,M_\odot$. This is about three times larger than the typical stellar mass at which seed-mass mergers are expected to occur if loss cone scattering was not accounted for. We also find that $\sim 80\%$ of the seed-seed merger remnants in the simulation are the only MBH residing in their host galaxies. Accounting for the DF and binary hardening delays slightly favors systems embedded in a larger galaxy with a more massive MBH around. This is because the more massive hosts tend to provide a higher stellar density and hence a more effective loss-cone scattering. However, sole MBH remnants still make up $\sim 70\%$ of the seed-seed merger population after the delays. Regardless, `Astrid` predicts the host galaxies of the detectable $z > 3$ mergers to be galaxies of $M_* \sim 10^9 - 10^{10}\,M_\odot$. These host galaxies are detectable with current and upcoming telescopes.

We note also that our estimation of the low-mass MBH merger rate is a lower-limit, since we do not resolve the MBHs residing in low-mass dwarf galaxies. Observations have provided evidence that dwarf galaxies host MBHs in their center [e.g. Lemons et al., 2015, Moran et al., 2014, Nguyen et al., 2019, Pardo et al., 2016, Reines et al., 2013, Sartori et al., 2015, Satyapal et al., 2014]. Simulations [e.g. Bellovary et al., 2019, Van Wassenhove et al., 2010, Volonteri et al., 2020] also shows that dwarf galaxies consistently merge into larger galaxies over time. Hence, missing the dwarf galaxy MBHs could bias our merger rate and detection rate estimation towards the lower end.

Moreover, in this work, we do not evolve the orbital eccentricity during the loss-cone scattering phase. Loss-cone scattering can increase the orbital eccentricity of the binary [e.g. Kelley et al., 2017c, Sesana, 2010], and may affect the detected GW signal. We also do not consider circumbinary-disk interactions [e.g. Haiman et al., 2009], since circumbinary-disk simulations for eccentric binaries have not yet been comprehensively explored for a wide-enough range of binary parameters and disk properties. A significant amount of progress,

however, has been made in the hydrodynamic modeling of such systems [e.g., D'Orazio and Duffell, 2021, Duffell et al., 2020, Tiede et al., 2020]. Binary-disk interactions may also affect the spin orientations of each MBH. It is also currently uncertain how a circumbinary disk would respond when an eccentric binary undergoes post-Newtonian spin-orbit interactions. We thus leave such analyses with our cosmological binary population for future work.

Despite the limitations in the modeling discussed above, we find that current simulations such as `Astrid` are getting closer to predicting DF timescales for the binary evolution. The estimation of the binary hardening timescale remains more uncertain as it depends on the properties of central stellar densities below the resolution limit. We have shown that changing the stellar density extrapolation starting point from $1.5\epsilon_g$ to $2\epsilon_g$ increases the estimated density at the influence radius by a factor of ~ 10, and thereby shortens the estimated binary hardening timescale by a factor of ~ 10. This translates to a factor of ~ 3 different in the merger rate predictions. To more confidently estimate the binary hardening timescale and thus the MBH merger rate in the context of cosmological simulations, better modeling of the inner region of the galaxy would be needed. Nonetheless, we still expect the merger rates to be within a factor of a few of what a cosmological simulation is able to predict (at the resolution of `Astrid`)

4.A Effect of Unresolved Eccentricity Evolution

As was discussed in Section 4.4.2 and Section 4.6.2, when computing the delay of mergers due to loss-cone scattering and when calculating the SNR for eccentric binaries, we have not taken into account possible circularization of the orbits during the unresolved dynamical friction phase. In this section, we will investigate the possible effect of orbit circularization on the merger rate predictions as well as on the SNR calculation.

We still assume simple models for binary circularization, because there is not yet a analytical model we can apply for the eccentricity evolution on $< 100\,\mathrm{pc}$ scales. We assume two scenarios for the orbit circularization: the first model is an extreme case, where we assume that all orbits are fully circularized before entering the loss-cone scattering phase. This model deviates from the results in previous works such as Mannerkoski et al. [2021], Vasiliev et al. [2022] and Gualandris et al. [2022], but we take it as a lower limit on our rate predictions. The second model is motivated by the result in Gualandris et al. [2022], who found that in the DF regime, the orbit goes through a certain degree of circularization, while still retaining a fraction of the high eccentricity at the beginning of the DF phase. Hence, we assume that by the end of the DF-dominated orbital decay, the binary retains half of its original eccentricity. This is in line with the median eccentricity loss in the simulations of Mannerkoski et al. [2021] and Gualandris et al. [2022], although these simulations also show a wide range of circularization.

In Figure 4.A.1, we show the merger rate similar to those calculated in Figure 4.4.6, but for different initial eccentricity assumptions. When we assume that all orbits have zero eccentricity before the loss-cone scattering phase, the binary hardening time is significantly longer, and the merger rate decreases by a order of magnitude compared with our original

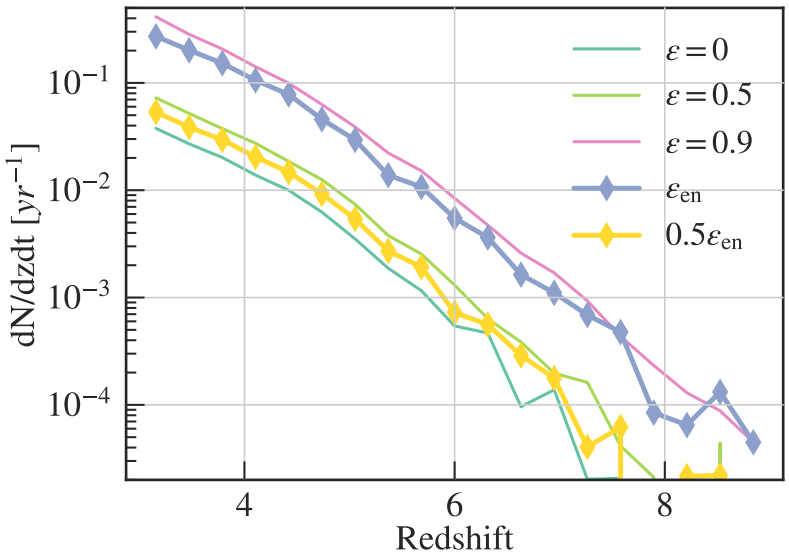

Figure 4.A.1: Merger rates after the DF and hardening delays when we assume different eccentricities for the binary population. We compare the constant-eccentricity cases with $\epsilon = 0$ (*thin blue*), $\epsilon = 0.5$ (*thin green*), and $\epsilon = 0.9$ (*thin pink*) with the merger rate assuming our measured eccentricity during the DF phase (*thick blue*). We also show the merger rate when assume that the eccentricity decreased by half during the unresolved DF phase (*thick yellow*), based on the conclusion of Gualandris et al. [2022].

predictions using the measured eccentricities. When assuming half-circularized orbit, the hardening time also increases, resulting in a 70% decrease in the merger rate before $z = 3$.

Figure 4.A.2 further shows the impact of the assumed initial eccentricity on the SNR predictions for LISA. In the top panel we reproduce our original predictions based on the measured eccentricities. The middel panel assume a full-circularization model. Note that here the eccentricity not only affects the merging redshifts throught the hardening time, but also affects the waveform of the final signals. We can see that the most of the mergers still have SNRs above the detection limit, but there are significantly less mergers before $z = 3$. The bottom panel shows the SNR for the half-circularizaiton model. Comparing with the full-circularization model, the overall SNR is slightly lower at high-redshifts, and the distribution of SNR better traces the measured-eccentricity model. In both cases, the assumed eccentricity does not have a large impact on the SNR for each merger event, but does affect the high-redshift merger rate.

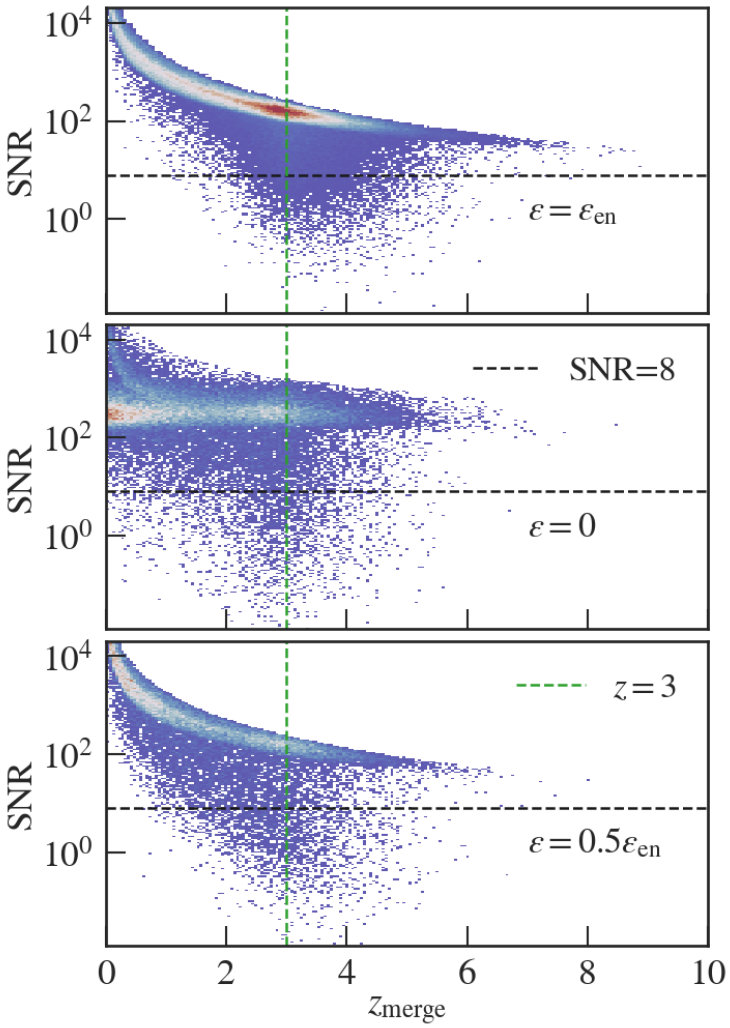

Figure 4.A.2: SNR and merging redshift distribution for different eccentricities assumed at the beginning of the loss-cone scattering phase. **Top:** same as the lower left panel of Figure 4.6.2, where we have used the eccentricity measured from the last orbit in the simulation. **Middle:** The merging time and SNR assuming that all orbits are completely circularized before entering the loss-cone scattering regime. **Bottom:** The merging time and SNR assuming that the orbits are half-circularized during the unresolved DF and the LC phase.

Chapter 5

Properties and Evolution of Dual and Offset AGN in the ASTRID Simulation at $z \sim 2$

Nianyi Chen,[11] Tiziana Di Matteo,[1,2] Yueying Ni,[1,2] Michael Tremmel,[3] Colin DeGraf,[4] Yue Shen,[5,6] A. Miguel Holgado,[1] Simeon Bird,[7] Rupert Croft,[1,2] Yu Feng [8]
[1] McWilliams Center for Cosmology, Department of Physics, Carnegie Mellon University, Pittsburgh, PA 15213
[2] NSF AI Planning Institute for Physics of the Future, Carnegie Mellon University, Pittsburgh, PA 15213, USA
[3] Astronomy Department, Yale University, P.O. Box 208120, New Haven, CT 06520, USA
[4] Department of Physics, Truman State University, Kirksville, MO 63501, USA
[5] Department of Astronomy, University of Illinois at Urbana-Champaign, Urbana, IL 61801, USA
[6] National Center for Supercomputing Applications, University of Illinois at Urbana-Champaign, Urbana, IL 61801, USA
[7] Department of Physics & Astronomy, University of California, Riverside, 900 University Ave., Riverside, CA 92521, USA
[8] Berkeley Center for Cosmological Physics and Department of Physics, University of California, Berkeley, CA 94720, USA

Abstract

We examine the dual (both BHs active) and offset (one BH active and in distinct galaxies) AGN population (comprising ~ 2000 pairs at $0.5\,\mathrm{kpc} \lesssim \Delta r < 30\,\mathrm{kpc}$) at $z = 2 \sim 3$ in the ASTRID simulation covering $(360\ \mathrm{cMpc})^3$. The dual (offset) AGN make up 3.0(0.5)% of all AGN at $z = 2$. The dual fraction is roughly constant while the offset fraction increases by a factor of ten from $z = 4 \sim 2$. Compared with the full AGN population, duals are characterized by low M_{BH}/M_* ratios, high specific star-formation rates (sSFR) of $\sim 1\,\mathrm{Gyr}^{-1}$, and high Eddington ratios (~ 0.05, double that of single AGN). Dual AGN are formed in

major galaxy mergers (typically involving $M_{\rm halo} < 10^{13}\,M_\odot$), with simular-mass BHs. At small separations (when host galaxies are in the late phase of the merger) duals become $2 \sim 8$ times brighter (albeit more obscured) than at larger separations. 80% of the bright, close duals would merge within $\sim 500\,$Myrs. Notably, the initially less-massive BHs in duals frequently become the brighter AGN during galaxy mergers. In offset AGN, the active BH is typically $\gtrsim 10$ times more massive than its non-active counterpart and than most BHs in duals. Offsets are predominantly formed in minor galaxy mergers with the active BH residing in the center of massive halos ($M_{\rm halo} \sim 10^{13-14}\,M_\odot$). In these deep potentials, gas stripping is common and the secondary quickly deactivates. The stripping also leads to inefficient orbital decay amongst offsets, which stall at $\Delta r \sim 5\,$kpc for a few hundred Myrs.

5.1 Introduction

Super-Massive Black Holes (SMBHs) are believed to reside in the center of most massive galaxies [e.g. Kormendy and Ho, 2013]. As a consequence of the hierarchical structure formation [e.g. Blumenthal et al., 1984], pairs of SMBHs were found in the merger remnant after mergers between two galaxies. These SMBH pairs slowly spiral toward the center of mass of the newly merged system and remain at a separation of $0.1 \sim 100\,$kpc for a few hundred Myrs [e.g. Begelman et al., 1980, Milosavljević and Merritt, 2001], during which dynamical friction is the major mechanism for driving the orbital decay, and enables the formation of a bound binary.

During the galaxy mergers, active galactic nuclei (AGN) can be triggered by the gas driven towards the center of the merger remnant and onto the SMBHs [e.g. Di Matteo et al., 2005b, Hopkins et al., 2008], making these SMBH pairs observable as either dual AGN [when both of the SMBHs are active, e.g. Comerford et al., 2009, Gerke et al., 2007], or offset AGN [when only one of the SMBHs is active, e.g. Steinborn et al., 2016]. Because of the tight connections between the galaxy assemblies and SMBH pairs, the detection and characterization of dual and offset AGN are fundamental for understanding the formation and accretion history of SMBHs across cosmic ages.

There have been significant observational efforts to search for these SMBH pairs using various techniques [see e.g. De Rosa et al., 2019, for a comprehensive review of recent observational works]. Candidates of dual AGN can be found by searching for double-peaked narrow AGN emission lines in optical spectroscopy [e.g. Barrows et al., 2013, Comerford et al., 2009], with follow-up confirmation through other bands [e.g. Fu et al., 2012, McGurk et al., 2011, Shen et al., 2011]. Hard X-ray observations are widely used to detect multiple AGN in a galaxy especially at high redshifts [e.g. Bianchi et al., 2008, Koss et al., 2018, Lanzuisi et al., 2018, Piconcelli et al., 2010], being less affected by contamination from stellar processes and absorption [e.g. Fragos et al., 2013, Lehmer et al., 2016]. Among the observed samples, some controversial conclusions arise likely due to the different selection functions from different observational techniques. For example, a number of studies find a higher fraction of dual AGN in galaxies with a closer separation, suggesting that galaxy interactions play a role in triggering of dual AGN [e.g. Ellison et al., 2011, Kocevski et al., 2015, Koss et al., 2012, 2018,

Liu et al., 2012, Satyapal et al., 2014, Silverman et al., 2011]. On the other hand, there are also studies showing no enhanced AGN activity in mergers compared to a matched control sample of inactive galaxies [e.g. Cisternas et al., 2011, Mechtley et al., 2016].

Despite the massive effort in catching AGN in their dual phase, there have been very limited number of $z \gtrsim 2$, close separation ($\Delta r \sim$ kpc) pairs, due to the limitation in spatial resolution to distinguish between the close pairs. However, very recently, several groups have been pushing the limit of detecting these high-redshift close pairs using novel observational techniques. For example, Chen et al. [2022d] uses `varstrometry` with Gaia DR2 [also see e.g. Hwang et al., 2020, Shen et al., 2019, 2021] to identify several $z \gtrsim 2$ dual/offset AGN candidates. Silverman et al. [2020] uses the double quasar samples from the Hyper Suprime-Cam (HSC) Subaru Strategic Program and identified 421 dual AGN candidates out to a redshift of 4.5. By looking for distinguished stellar bulges in a sample of AGN host galaxies, Stemo et al. [2021] put up a catalog of 204 offset and dual AGN candidates down to a separation of $< 4\,$kpc, among which a few are $z \gtrsim 2$ AGN. In recent works, Shen et al. [2022] characterizes the statistical properties of galactic-scale quasar pairs using a statistically large sample of 60 double quasars. Mannucci et al. [2022] uses the novel Gaia Multi-Peak method to select over 200 multiple AGN candidates between $z = 0.3 \sim 4$ down to ∼kpc separations.

In light of these recent observations of high redshift AGN pairs, a sample of simulated counterparts is needed to understand the observed sample and its astrophysical implications. In the realm of idealized galaxy-merger simulation, Blecha et al. [2013], Capelo et al. [2017], Van Wassenhove et al. [2012] studied AGN activation at various pair separations as well as the impact of the galaxy merger parameters such as the host galaxy mass ratio and morphology. Recent developments in cosmological hydrodynamical simulations also allow studies of dual and offset AGN and galaxy mergers in a cosmological context [e.g. Ricarte et al., 2021, Rosas-Guevara et al., 2019, Steinborn et al., 2016, Tremmel et al., 2017, Volonteri et al., 2016, 2022], where the number and the properties of dual AGN relative to all AGN can be calculated at different redshifts.

Among the cosmological simulations mentioned above, very few were able to produce a statistically large sample of kpc-separation AGN pairs at $z \gtrsim 2$, due to several reasons. First, because the dual and offset AGN only make up a few percent of the total AGN population [e.g. Fu et al., 2011, Liu et al., 2011], and because bright AGN are already rare at high redshifts, a large $(\gtrsim 100\,\mathrm{Mpc/h})^3$ cosmological volume is required to produce those pairs. Moreover, $\sim$ kpc spatial resolution is needed in order to resolve pairs separated by a few kpc. Finally, even for simulations satisfying the above resolution requirements, in most cosmological simulations BHs are pinned to the gravitational potential minimum to avoid artificial kicks of the BH. Consequently, during a galaxy merger, the two central MBHs merge too quickly to be captured at the $\sim$ kpc separation. The BH dynamics modeling after the host galaxy merger is even more important for studying offset pairs [e.g. Allen et al., 2015, Barth et al., 2008, Comerford et al., 2012, 2015, Müller-Sánchez et al., 2015] , which are thought to originate mostly from galaxy merger events.

The `Astrid` simulation is among the few cosmological simulations that meet the above requirements for studying high-redshift AGN pairs [Bird et al., 2022, Chen et al., 2022a, Ni

et al., 2022]. First, with a volume of $(250\,\mathrm{Mpc}/h)^3$, `Astrid` contains $> 10^4$ massive AGN already at $z = 2 \sim 3$, among which $\gtrsim 3\%$ are in pairs. More importantly, the high spatial resolution of $\sim 1.5\,\mathrm{ckpc}/h$ relative to the volume can resolve AGN pairs at close separations a few hundred Myrs after the host galaxy mergers. Finally, the dynamical-friction modeling in `Astrid` allows for one of the first studies of the evolution of $\Delta r \lesssim 1\,\mathrm{kpc}$ AGN pairs and their activation in the context of cosmological simulations (previously only done in idealized galaxy merger simulations).

This paper is organized as follows: in Section 6.2 we introduce the `Astrid` simulation, in particular the MBH modeling, and describe our selection criterion for the dual and offset AGN from the simulation; in Section 5.3, we focus on a sample of dual and offset AGN at $z = 2$, and investigate their properties such as the separation, mass/luminosity distributions, host galaxy mass, AGN activation levels and obscuration, with comparisons with high-redshift observations where possible; then, in Section 5.4, we characterize the evolution of AGN pairs at $z = 3$ during and after the host galaxy merger, with an emphasis on the effect of pericentric passages and the difference between the evolution of dual and offset AGN.

5.2 Simulation

The `Astrid` simulation is a large-scale cosmological hydrodynamic simulation in a $250\,\mathrm{Mpc}/h$ box with 2×5500^3 particles. `Astrid` contains a statistical sample of halos which can be compared to future survey data from JWST, while resolving galactic halos down to $10^9\,M_\odot$ (corresponding to 200 dark matter particles). The initial conditions are set at $z = 99$ and the current final redshift is $z = 2$. The cosmological parameters used are from Planck Collaboration et al. [2020], with $\Omega_0 = 0.3089$, $\Omega_\Lambda = 0.6911$, $\Omega_\mathrm{b} = 0.0486$, $\sigma_8 = 0.82$, $h = 0.6774$, $A_s = 2.142 \times 10^{-9}$, $n_s = 0.9667$. The mass resolution of `Astrid` is $M_\mathrm{DM} = 6.74 \times 10^6 h^{-1} M_\odot$ and $M_\mathrm{gas} = 1.27 \times 10^6 h^{-1} M_\odot$ in the initial conditions, and our star particles have a median mass of $10^{5.5}\,M_\odot$. The gravitational softening length is $\epsilon_\mathrm{g} = 1.5\,\mathrm{ckpc/h}$ for both DM and gas particles.

5.2.1 Black Hole Modeling

Here we briefly describe the BH modeling used in `Astrid` most relevant for the dual and offset AGN. For a thorough description of the sub-grid models and BH statistics, please refer to Bird et al. [2022], Ni et al. [2022], and Chen et al. [2022a].

`Astrid` contains models for inhomogeneous hydrogen and helium reionization, baryon relative velocities and massive neutrinos, as well as 'full-physics' galaxy formation models including star formation, BH accretion and the associated supernova and AGN feedback. The star formation model is unchanged from Feng et al. [2016], which followed the implementation of Springel and Hernquist [2003]. The BH model includes mergers driven by dynamic friction rather than repositioning. Our treatment of BHs largely follows the `BlueTides` simulation in terms of the BH accretion and feedback, which is based on the earlier work by Di Matteo et al. [2005b], Springel et al. [2005b]. The gas accretion rate onto the BH is estimated via the

Bondi-Hoyle-Lyttleton-like prescription applied to the smoothed properties of the 112 gas particles within the SPH kernel of the BH. We allow for short periods of super-Eddington accretion in the simulation, but limit the accretion rate to 2 times the Eddington accretion rate.

The BH radiates with a bolometric luminosity $L_{\rm bol}$ proportional to the accretion rate $\dot{M}_{\rm BH}$, with a mass-to-light conversion efficiency $\eta = 0.1$ in an accretion disk according to Shakura and Sunyaev [1973]. We include both thermal (or quasar-mode) feedback and kinetic AGN feedback. In quasar mode feedback, 5% of the radiated energy is thermally coupled to the gas residing within twice the radius of the SPH smoothing kernel of the BH particle. A BH switches to the kinetic mode only when the accretion rate drops below the Eddington ratio $\chi_{\rm thr,max} = 0.05$ and the BH mass is $M_{\rm BH} \gtrsim 10^{8.5} M_\odot$. The kinetic feedback follows Weinberger et al. [2017], with slightly different parameters. Kinetic feedback energy is deposited as $\Delta\dot{E}_{\rm kin} = \epsilon_{\rm f,kin}\dot{M}_{\rm BH}c^2$, where $\epsilon_{\rm f,kin}$ scales with the BH local gas density and has a maximum value of $\epsilon_{\rm f,kin,max} = 0.05$. The energy is accumulated over time and released in a bursty way once the accumulated kinetic feedback energy exceeds the threshold $E_{\rm inj,min} = f_{\rm re}\frac{1}{2}\sigma^2_{\rm DM} m_{\rm enc}$. $\sigma^2_{\rm DM}$ is the one-dimensional dark matter velocity dispersion around the BH, $m_{\rm enc}$ is the gas mass in the feedback sphere and $f_{\rm re} = 5$. The released kinetic energy kicks each gas particle in the feedback kernel in a random direction with a prescribed momentum weighted by the SPH kernel. Kinetic feedback is enabled in `Astrid` at $z < 2.4$.

To seed MBHs in the simulation, we periodically run a FOF group finder on the fly with a linking length of 0.2 times the mean particle separation, to identify halos with a total mass and stellar mass satisfying the seeding criteria $\{ M_{\rm halo,FOF} > M_{\rm halo,thr}; M_{*,\rm FOF} > M_{*,\rm thr}\}$. We apply a mass threshold value of $M_{\rm halo,thr} = 5 \times 10^9 h^{-1} M_\odot$ and $M_{*,\rm thr} = 2 \times 10^6 h^{-1} M_\odot$.

Instead of applying a uniform seed mass for all BHs, we probe a mass range of the BH seed mass $M_{\rm seed}$ drawn probabilistically from a power-law distribution:

$$P(M_{\rm seed}) = \begin{cases} 0 & M_{\rm seed} < M_{\rm seed,min} \\ \mathcal{N}(M_{\rm seed})^{-n} & M_{\rm seed,min} \leq M_{\rm seed} \leq M_{\rm seed,max} \\ 0 & M_{\rm seed} > M_{\rm seed,max} \end{cases} \tag{5.1}$$

where $\mathcal{N}$ is the normalization factor. The minimum seed mass is $M_{\rm seed,min} = 3 \times 10^4 h^{-1} M_\odot$ and the maximum seed mass is $M_{\rm seed,max} = 3 \times 10^5 h^{-1} M_\odot$, with a power-law index $n = -1$. For each halo that satisfies the seeding criteria but does not already contain at least one BH particle, we convert the densest gas particle into a BH particle.

Instead of repositioning the black hole towards the potential minimum, in Chen et al. [2021] we implemented and tested a model for sub-grid dynamical friction [similar to Tremmel et al., 2015, 2017], using a BH dynamical mass of $M_{\rm dyn} = 2 \times M_{\rm DM} = 1.3 \times 10^7\, M_\odot$. This means that we boost the mass of the BHs to $M_{\rm dyn} = 2 \times M_{\rm DM} = 1.3 \times 10^7\, M_\odot$ *only* when calculating the acceleration if the original mass of the BH is less than this threshold, in order to avoid the unphysical scattering off of dark matter particles. With this dynamical mass, the orbital decay timescale of seed-mass BHs is likely underestimated, but for the current work, since we focus on the massive BHs, the dynamical mass does not deviate

greatly from the true mass and thus should not affect the sinking timescale. We set the merging distance to be $2\epsilon_{\rm g} = 3\,{\rm ckpc}/h$, because the BH dynamics below this distance is not well resolved. We conserve the total momentum of the MBHs during the merger (i.e. $M_{\rm BH,1}\mathbf{v_1} + M_{\rm BH,2}\mathbf{v_2} = M_{\rm BH,rem}\mathbf{v}_{\rm rem}$). Moreover, as we do not have repositioning of the BHs to the nearby potential minimum, the BHs have well-defined velocities at each time step (this is true whether or not we add the dynamical friction). This allows us to apply further merging criteria based on the velocities and accelerations of the black hole pair, and thus avoid early mergers of gravitationally unbound pairs.

We follow Bellovary et al. [2011] and Tremmel et al. [2017], and use the criterion

$$\frac{1}{2}|\mathbf{\Delta v}|^2 < \mathbf{\Delta a}\cdot\mathbf{\Delta r} \tag{5.2}$$

to check whether two black holes are gravitationally bound. Here $\mathbf{\Delta a}$, $\mathbf{\Delta v}$ and $\mathbf{\Delta r}$ denote the relative acceleration, velocity and position of the black hole pair, respectively. Note that this expression is not strictly the total energy of the black hole pair, but an approximation of the kinetic energy and the work needed to get the black holes to merge. Because in the simulations the black hole is constantly interacting with surrounding particles, on the right-hand side we use the overall gravitational acceleration instead of the acceleration purely from the two-body interaction. We note, however, that the mergers in the simulation following the criterion above do not correspond to the real coalescence of the two MBHs: the typical separations between the MBH pairs are still ~ 1 kpc, and the MBH should experience further orbital decay by dynamical friction, loss-cone scattering and drags due to the circum-binary disk before the final coalescence.

5.2.2 AGN Pair Selection

Among all MBHs in the simulation at a fixed redshift, we define an MBH pair as two MBHs with a separation of $\Delta r < 30\,{\rm kpc}$ (proper). The upper limit in separation chosen here follows from previous simulation works such as Steinborn et al. [2016]. For this work, we only focus on the massive end of our population by restricting to MBH pairs with both MBHs above $10^7\,M_\odot$ for two main reasons: first, with the current dynamical-friction model in `Astrid`, there remain large uncertainties in the dynamics of lower-mass MBHs due to the introduction of the dynamical mass; second, the low-mass/faint-end luminosity function from most hydrodynamical simulations are high compared with observations, so that including the $M_{\rm BH} < 10^7\,M_\odot$ MBHs may lead to an over-estimation of dual AGN passing certain luminosity thresholds.

Among the large MBHs, we then define AGN as MBHs with bolometric luminosity $L_{\rm bol} > 10^{43}\,{\rm erg/s}$. Dual AGN are MBH pairs in which both of the MBHs are bright enough to be AGN. There is also a significant population of MBH pairs with only one MBH powering an AGN, while the other remains faint ($L_{\rm bol} < 10^{43}\,{\rm erg/s}$). We define such MBH pairs as "one-AGN pairs", indicating that these are still MBH pairs resulting from mergers between massive galaxies, but only one MBH is powering an AGN. If a one-AGN pair is in the

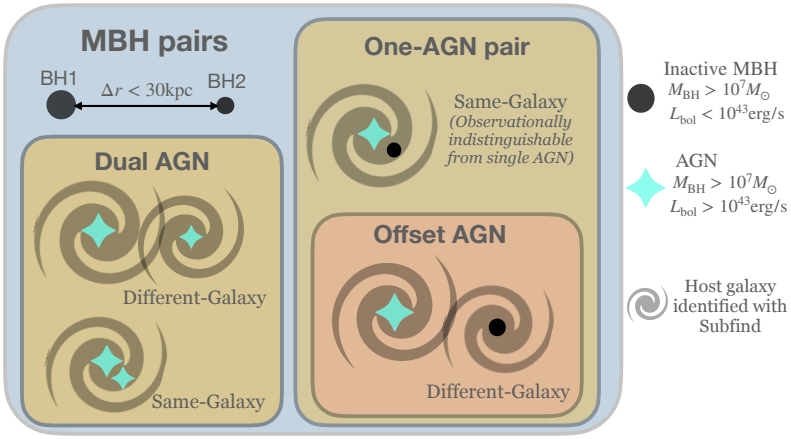

Figure 5.2.1: Illustration of different categories of MBH pairs defined in this work. Note that offset AGN are the subset of one-AGN pairs in which the two MBHs are found in distinct galaxies. See Section 5.2.2 for the detailed definitions.

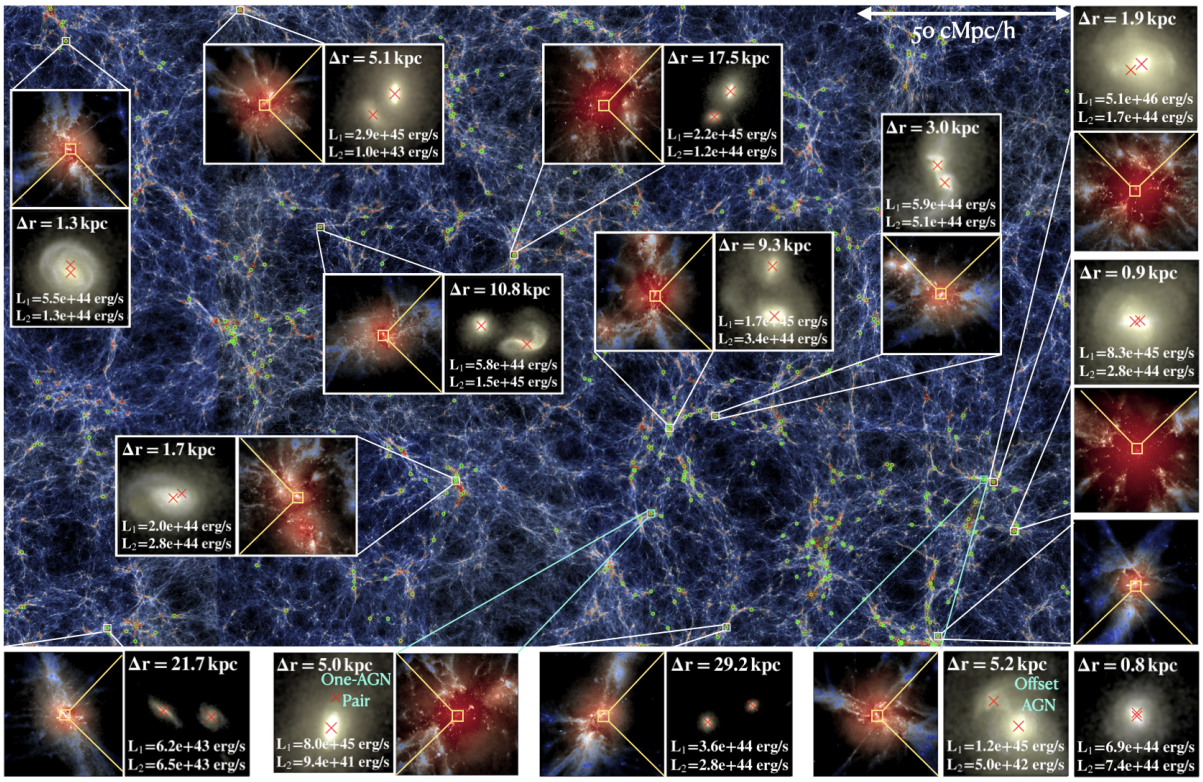

Figure 5.2.2: Dual AGN and one-AGN pairs in a $250\,\mathrm{cMpc}/h \times 150\,\mathrm{cMpc}/h \times 20\,\mathrm{cMpc}/h$ slice of the `Astrid` simulation. The background image shows the gas distribution of the simulation, color-coded by the gas temperature where warmer regions correspond to higher temperatures. For each dual AGN in the slice, we locate it with white squares in the snapshot and zoom in on their surrounding IGM and host galaxies. About half of the duals are in separated galaxies with $\Delta r > 10\mathrm{kpc}/h$, and the other half have already gone through galaxy mergers. Among all pairs shown, there are two one-AGN pairs, out of which one is an offset AGN (see the definitions in Figure 5.2.1), and we have labeled them in ***cyan*** text.

early stage of a galaxy merger, their host galaxies still retain distinguishable bulges, and the inactive MBH may be inferred by the presence of a second bulge close to the AGN host. Following the definition in previous works such as Comerford et al. [2015], De Rosa et al. [2019], and Stemo et al. [2021], we will refer to the one-AGN pairs hosted by two galaxies as "offset AGN". In contrast, some one-AGN pairs are found after their host galaxies have merged. Observationally, such pairs may be very hard to distinguish from a single AGN. We note that sometimes in the literature, "offset AGN" also refers to single AGNs which are found at a large distance from the galaxy center [e.g. Blecha et al., 2016], or AGN with kinematic offset from their host galaxies that can be observed through offsets in the spectral lines [Comerford and Greene, 2014]. Note that for the inactive MBHs in the offset pairs, we also require them to have masses $> 10^7\,M_\odot$. This is to separate the MBHs that only become inactive during the galaxy merger from a much larger population of low-mass companions around the bright AGN. To avoid confusion with definitions from various works in the literature, in Figure 5.2.1 we show a schematic diagram of each type of objects defined in this work.

After applying the above criterion, there are 2008 (439) MBH pairs with $M_{\rm BH} > 10^7\,M_\odot$ at $z = 2$ ($z = 3$), among which 1087 (329) are dual AGN, 842 (110) are one-AGN pairs, and 79 (10) are no-AGN pairs. For this work, we do not explicitly search for MBH multiplets, so our catalog is subject to double-counting in the case of multiplets. More specifically, $\sim 10\%$ of the AGN in the dual catalog are involved in triplets, and $< 1\%$ is involved in quadruplets. This means that there could be up to 20% decrease in our pair counts if those multiplets were to be removed from the pair catalog. However, here we did not remove these pairs entirely from our catalog, because these are still tracers of galaxy mergers, and they have shared features with the "pure" dual AGN. For these AGN mutiplets, when we show the mass/luminosity functions or the halo/galaxy mass for individual AGN in the pairs (e.g. in Figure 5.3.4), we avoid counting one AGN multiple times by counting the most massive one as the primary (only once) and the rest as secondaries. For statistics involving the pairs as a single object (e.g. Figure 5.3.2), we will use all three pairs in a triplet. For the two MBHs in the pair, we will refer to the more massive one *at the time of observation* as the primary MBH (or BH1), and the less massive one as the secondary MBH (or BH2). By the "time of observation", we refer to the fixed redshifts ($z = 2$ or $z = 3$) at which we measure the properties of the BHs and host galaxies. We note that the mass ratio may change before or after this fixed redshift, but we do not switch our notation of the primary and secondary with the change in redshift. Note that we assign the primaries and secondaries by the MBH masses instead of the luminosities. We will refer to the more luminous MBH as the brighter AGN, and the less luminous MBH as the fainter AGN.

We identify the host galaxies of the MBHs with `Subfind` [Springel et al., 2001], where MBHs are treated as baryons in the `Subfind` when assigned to host galaxies, and are therefore gravitationally bound to the corresponding subhalo. We note that during the close encounters of galaxies, `Subfind` may not be able to separate the merging systems well. This is especially the case for offset AGN hosts since the gas and stellar disruption is very strong. For this reason, in our analysis we show the properties of one-AGN pairs as well as offset AGN, as

some of secondaries among close one-AGN pairs may retain their stellar bulges that our simulation or `Subfind` is not able to resolve/identify. The observed offset AGN should be bracketed by our one-AGN pairs and offset AGN populations. Finally, when tracing the MBH and galaxy properties back in redshift, we always follow the more massive progenitor if the MBH of interest has gone through prior mergers.

In Figure 5.2.2, we show the dual AGN and one-AGN pairs in a $250\,\mathrm{cMpc}/h \times 150\,\mathrm{cMpc}/h \times 20\,\mathrm{cMpc}/h$ slice of the `Astrid` simulation. The background image shows the gas distribution of the simulation, color-coded by the gas temperature where warmer regions corresponds to higher temperatures. At the position of each pair, we zoom into the IGM and galaxies surrounding the AGN pairs. The green dots mark all AGN with $M_{\rm BH} > 10^7\,M_\odot$ and $L_{\rm bol} > 10^{43}\,\mathrm{erg/s}$. Note that we have shown all of the dual AGN and one-AGN pairs in this slice, and we can see that the pair distribution is a sparse representation of the underlying galaxy/AGN distribution.

5.3 Properties of High-z AGN in Pairs

In this section, we investigate the properties of the duals and one-AGN pairs at a fixed redshift $z = 2$. Specifically, we will look at the separation of the pairs, their mass/luminosity function, Eddington ratio, and host galaxy properties compared with the underlying AGN population.

5.3.1 Dual Fraction

The fraction of dual AGN relative to the underlying single AGN population could be a proxy for the number of massive galaxies undergoing galaxy mergers. Observational studies suggest that the fraction of dual AGN is small [e.g. Fu et al., 2011, Rosario et al., 2011]. The dual AGN fraction in the local Universe has been estimated from the dual AGN sample of Koss et al. [2012] detected with X-ray spectroscopy to be about 2%. Liu et al. [2011] used a sample from the Seventh Data Release of the SDSS survey at $z = 0.1$ based on diagnostic emission-line ratios and estimated a dual AGN fraction with $\Delta r < 30\,\mathrm{kpc}$ to be 1.3%. Constraint on the evolution of dual AGN fraction at higher redshifts is still an ongoing work: recently Silverman et al. [2020] found a dual quasar fraction of $0.26 \pm 0.18\%$ from $z = 3$ to $z = 1.5$, with no evidence for a redshift evolution [also see Shen et al., 2022, for the fraction of bright double quasars at $z \sim 2$]. Although our simulation contains a few double quasars by $z = 2$ with both quasars above $L_{\rm bol} > 10^{46}\,\mathrm{erg/s}$, the sample size is still too small for statistical comparison. Here, we still use a selection criterion consistent with previous simulation works and do not directly draw comparisons between our dual fraction and those computed from observations. We refer the readers to Shen et al. [2022] and Chen et al. [2022e] for more information of the bright double quasar pairs in `Astrid` and a direct comparison with recent observations.

In Figure 5.3.1, we show the redshift dependence of the dual AGN, one-AGN pair, and offset AGN fraction in the `Astrid` simulation. To compute the fraction, we take the number

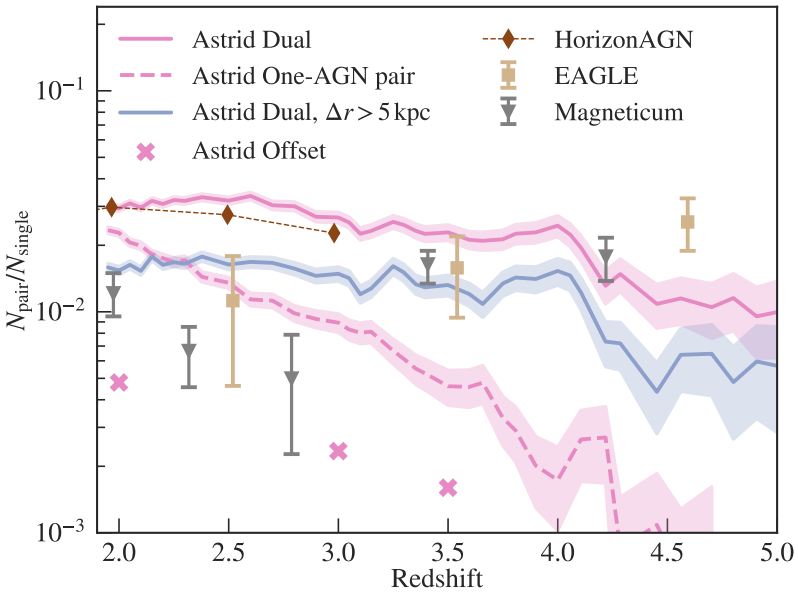

Figure 5.3.1: Fraction of dual AGN (***solid pink***), one-AGN pairs (***dashed pink***) and offset AGN (***pink cross***, we only show data points at redshifts where we have the subhalo information of the AGN) among the underlying massive AGN population. We also show the dual fraction with a selection criterion of $5\,\mathrm{kpc} < \Delta r < 30\,\mathrm{kpc}$ (***purple***). For comparison, we plot the dual fractions in recent simulation works of comparable box sizes including EAGLE (***beige square***), HorizonAGN (***brown diamond***), and Magneticum (***grey triangle***).

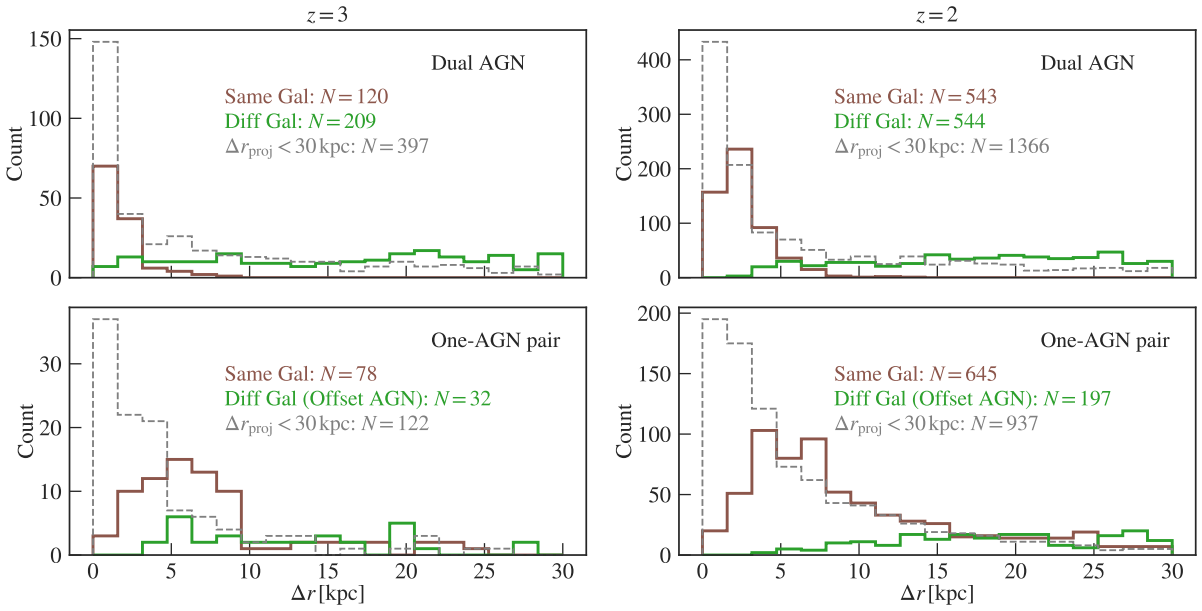

Figure 5.3.2: Distribution of the distance between the two MBHs in the dual AGN (***top***) and one-AGN pairs (***bottom***) at $z = 3$ (***left***) and $z = 2$ (***right***). Here we separate each population by whether the two MBHs are embedded in the same galaxy (***brown***) or not (***green***). Between $z = 3$ and $z = 2$, the number of duals goes through a three-fold increase, whereas the number of one-AGN pairs becomes seven times larger. We also show the dual AGN and one-AGN pairs selected based on the 2D projected distance instead of the true distance, to mimic the selection from observations (***grey dashed***). For those pairs, the x-axis represents the projected distance.

of dual AGN/one-AGN pairs/offset AGN selected based on the criterion in Section 5.2.2 as the numerator, and take all AGN with $M_{\rm BH} > 10^7\,M_\odot$, and $L_{\rm bol} > 10^{43}\,{\rm erg/s}$ as the denominator. From $z = 4$ to $z = 3$, the dual fraction shows no redshift dependence and remains $\sim 2.3\%$. After $z = 3$, we see a slight rise in the fraction of duals to $\sim 3\%$. Above $z = 4$, there is a drop in the dual fraction to $\sim 1\%$. The fraction of one-AGN pair increases significantly from $z = 4$ to $z = 2$, likely due to the increasing number of minor galaxy mergers which is the major sight for the one-AGN pairs [see e.g. Section 5.3.4, also Ricarte et al., 2021, Tremmel et al., 2018a]. Offset AGN make up $\sim 30\%$ of the one-AGN pairs from $z = 2 - 4$.

Also in Figure 5.3.1, we compare our result to the dual fraction estimates from previous numerical works at high redshifts [e.g. Rosas-Guevara et al., 2019, Steinborn et al., 2016, Volonteri et al., 2022]. Among the three simulations we compare with, HorizonAGN [Volonteri et al., 2022] uses the same distance/mass/luminosity criterion for the duals, and they also adopt dynamical-friction modeling of the MBH dynamics, and indeed our prediction of the dual fraction aligns closely with their predictions.

In contrast, the predictions from Steinborn et al. [2016] (using the Magneticum simulation) and Rosas-Guevara et al. [2019] (using the EAGLE simulation) show a lower fraction of the dual population, and they see a decrease in the dual fraction with redshift. The lower fraction in Steinborn et al. [2016] and Rosas-Guevara et al. [2019] is likely due to their exclusion of close pairs and lower spatial resolution of the MBH merger. To show the resolution dependence of the dual fraction, we also plot the fraction calculated only using duals separated by $\Delta r > 5\,{\rm kpc}$. With this selection criterion, the dual fraction systematically drops by $\sim 50\%$ at all redshifts, but compared with Steinborn et al. [2016] and Rosas-Guevara et al. [2019], our dual fraction remains higher at lower redshifts. This can be a result of the velocity-based merging criterion we have adopted, which was absent from most previous simulations: it has been shown that applying the velocity-based merging criterion can uniquely lead to long-lived pairs of MBHs at galaxy-scale separations [e.g. Chen et al., 2021, Tremmel et al., 2018a,b], such that a larger fraction of high-redshift pairs remains observable as dual AGNs at $z \sim 2$.

The different trend in redshift likely arises because the samples in Rosas-Guevara et al. [2019] are not subjected to the $M_{\rm BH} > 10^7\,M_\odot$ mass cut [see e.g. Volonteri et al., 2022, for the effect of applying various mass and luminosity cuts]. Finally, we note that the underlying AGN population is also different in their masses and luminosities, due to the BH model used in each simulation [e.g. Habouzit et al., 2022].

5.3.2 Pair Separations

In Figure 5.3.2, we plot the distributions of the separations between the two MBHs in the dual AGN and one-AGN pairs at $z = 3$ and $z = 2$. Among duals and one-AGN pairs, we further categorize the pairs as same and different galaxy duals (one-AGN pairs) according to whether the two MBHs are in the same galaxy or not, where the host galaxies are identified with the subhalo catalog generated by `Subfind`. Previously, Rosas-Guevara et al. [2019] and Volonteri

et al. [2022] also distinguish between the dual AGN before and after the host galaxy merger, in order to establish the relation between dual AGN activation and the host galaxy merger. In our case, we made this distinction both for the same reason as these works, and because this classification selects out the small-separation pairs which are of particular interest to the most recent observations. Since our simulation adopts a sub-grid dynamical friction model with a stricter merging criterion than most previous works of similar resolutions, we are able to identify more pairs at closer separations, down to $\Delta r < 1\,\mathrm{kpc}$.

On the top panels, we show the separation of dual AGN with $\Delta r < 30\,\mathrm{kpc}$. The same-galaxy dual AGN have separations below $\Delta r = 5\,\mathrm{kpc}$, with a peak near $\Delta r = 2\,\mathrm{kpc}$ for both $z = 2$ and $z = 3$. Within our sample, the probability of seeing a $\Delta r < 2\,\mathrm{kpc}$ dual AGN is five times the probability at larger separations. Finally, the distribution is flat at $\Delta r > 5\,\mathrm{kpc}$, showing no preferred separation for the different-galaxy duals during the galaxy merger. In previous works, Rosas-Guevara et al. [2019] find a peak of dual separations within $[20\,\mathrm{kpc}, 25\,\mathrm{kpc}]$, but they did not consider any pairs below 5 kpc. Steinborn et al. [2016] and Volonteri et al. [2022] also uses various models for the sub-grid dynamical friction, and found a higher probability density of duals at $\Delta r < 5\mathrm{kpc}$.

On the bottom panels of Figure 5.3.2, we show the separation distribution of the one-AGN pairs. Contrary to the dual AGN which accumulates near separation of 1 kpc, there are almost no one-AGN pairs at such close separations: most are found at separations around 5 kpc. As we will see in the later sections, this is mainly because the stripping of the secondary host galaxy is most severe when the two merging galaxies are separated by around 5 kpc, causing the secondary MBH to lose its gas supply and become inactive. When the separation of the MBHs gets closer to $\sim 1\,\mathrm{kpc}$, however, the secondary MBH begins to accrete from the gas in the primary galaxy, thereby turning the one-AGN pair into a dual at the 1 kpc separation.

We also see differences between the $z = 2$ and $z = 3$ populations. Only 30% of the dual AGN at $z = 3$ reside in the same host galaxy and are within $\Delta r < 5\,\mathrm{kpc}$ in separation, but this fraction becomes 50% at $z = 2$. The evolution from $z = 3$ to $z = 2$ also saw a large increase in the fraction of one-AGN pairs: while the number of duals has increased by $\sim 200\%$, the one-AGN pairs has grown by $\sim 700\%$. The growth of the same-galaxy, close duals as well as one-AGN pairs is a result of the dynamical friction model and merger criterion in `Astrid` which prevent dual AGNs from merging immediately after the host galaxy merger (also see the detailed discussion in Section 5.3.1). During the dynamical-friction dominated orbital decay, an increasing number of AGN go through gas stripping and become one-AGN pairs instead of duals.

Also in Figure 5.3.2, we show the pairs selected with the 2D projected separation Δr_{proj}, rather than the true separation, to mimic the selection function of observations. Here we take Δr_{proj} to be the projection of Δr on the $x-y$ plane, and we also limit the projection depth to be $|\Delta z| < 100\,\mathrm{kpc}$. Using the projected separation increases dual AGN by $\sim 30\%$, meaning that at separations of $\Delta r > 30\,\mathrm{kpc}$, there are still a significant number of pairs residing in separated galaxies. Furthermore, using projected separation also increases the probability of pairs at $\Delta r_{\mathrm{proj}} < 5\,\mathrm{kpc}$. For the one-AGN pairs, however, Δr_{proj}-based selection only

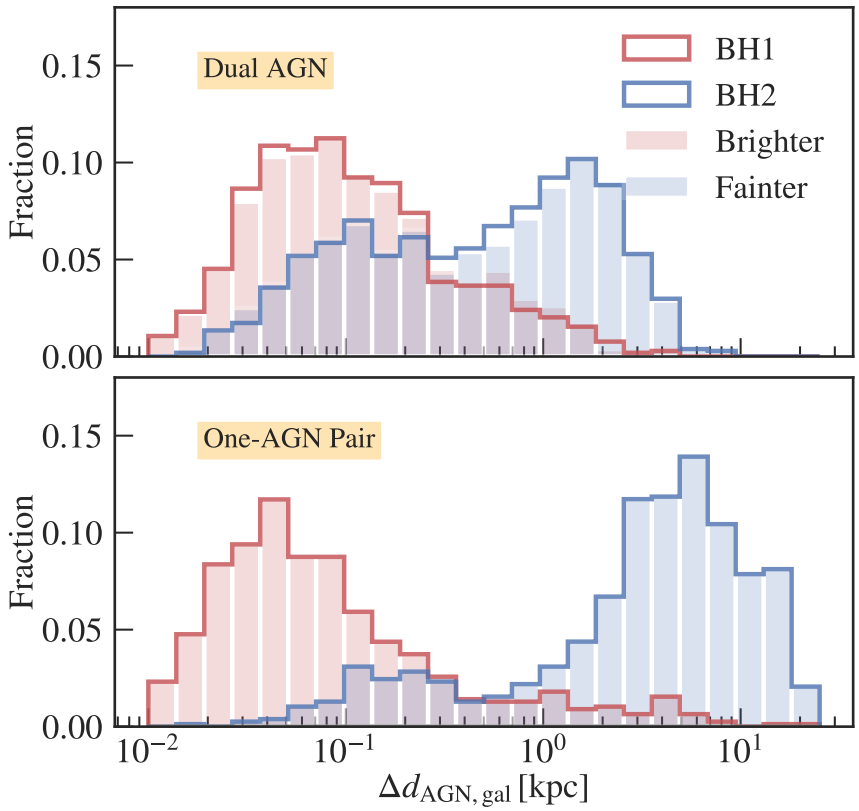

Figure 5.3.3: Distribution of the distances between the MBHs in duals (***top panel***)/one-AGN pairs (***bottom panel***) and their host galaxy centers (defined as the position of the particle at the potential minimum in each subhalo) at $z = 2$. While the primary AGN among duals and one-AGN pairs is usually within 1 kpc from the galaxy center, the majority of the secondaries are quite off-center ($\Delta r_{\mathrm{AGN,gal}} > 1\,\mathrm{kpc}$). We distinguish the BHs in pairs both by their masses (solid lines) and their luminosities (shaded). For one-AGN pairs, the more massive BH is always brighter, while for duals some of the brighter AGN is the less massive one (see Figure 5.3.4).

includes $< 10\%$ more pairs, which is a lot less compared with the increase in the dual AGN. With a mass cut of $M_{\mathrm{BH}} > 10^7 M_\odot$, the secondary MBHs rarely fall below $L_{\mathrm{bol}} < 10^{43}\,\mathrm{erg/s}$ without severe disruption of the gas during galaxy mergers (see e.g. Figure 5.3.5). Hence, at $\Delta r > 30\,\mathrm{kpc}$ and $\Delta r_{\mathrm{proj}} < 30\,\mathrm{kpc}$ when the host galaxies have barely interacted, massive but inactive secondaries are hard to find. Another consequence of the lack of large-separation one-AGN pairs is that using the projected distance will bias the observed distance separation towards the lower end and thus raise the resolution requirements.

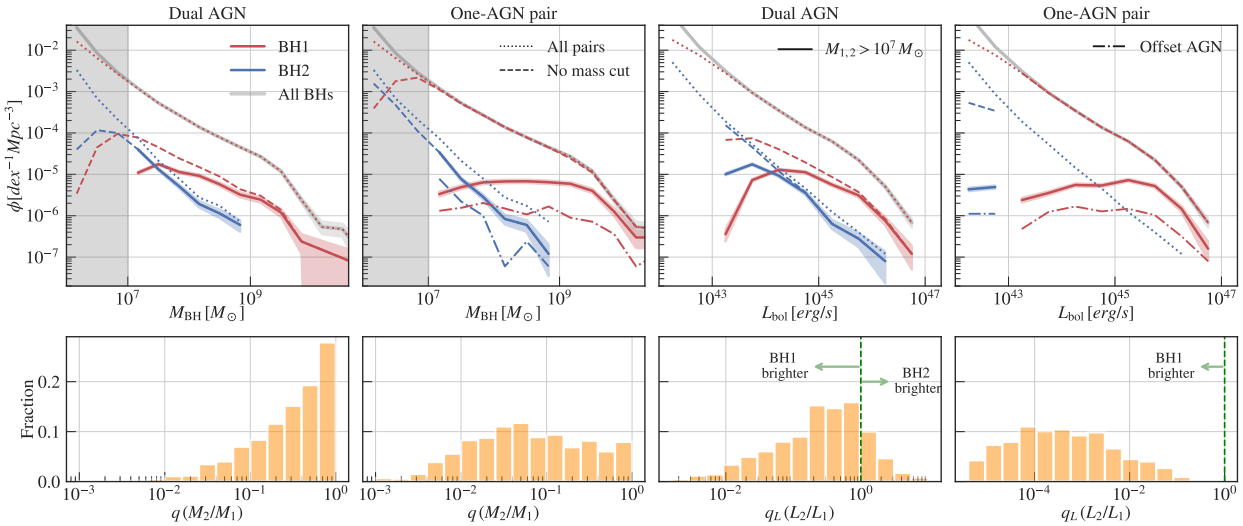

Figure 5.3.4: ***Top:*** Mass functions (***left two columns***) and luminosity functions (***right two columns***) of the dual AGN and one-AGN pairs, compared with the underlying MBH population and MBH pairs. The ***solid red (blue)*** shows the distribution of the more (less) massive MBH in the dual/one-AGN pairs. The mass and luminosity function of all MBHs are shown in ***solid grey*** (we start the bins at $M_{\rm BH} = 10^6\,M_\odot$ and $L_{\rm bol} = 10^{42}\,{\rm erg/s}$ for a clearer view of the high-mass end). To illustrate the effect of our mass threshold at $M_{\rm BH} > 10^7\,M_\odot$, we also show the "dual AGN" and "one-AGN pairs" without applying the mass threshold (***dashed***). Note that for such "duals", the luminosity threshold of $L_{\rm bol,1,2} > 10^{43}\,{\rm erg/s}$ is still present, while for the "one-AGN pairs", the only constraint is $L_{\rm bol,1} > 10^{43}\,{\rm erg/s}$. Finally, we show the mass and luminosity functions of all MBH pairs with $\Delta r < 30\,{\rm kpc}$ (***dotted***). ***Bottom:*** mass and luminosity ratio between the less massive MBHs and the more massive MBHs in the duals and one-AGN pairs. One-AGN pairs have greater mass and luminosity contrasts compared with duals. Also note that for duals, the more massive MBHs do not necessarily correspond to the brighter AGN.

5.3.3 Off-centered Pairs

As dual and offset AGN are typically found during/after mergers between massive galaxies, the associated MBHs are likely displaced from the host galaxy centers due to dynamical interactions. The distance between the MBH and the host galaxy centers could correlate with the accretion efficiency of the MBHs, and also indicate the existence of a hidden secondary in case only one AGN is observed.

In Figure 5.3.3, we show the distances between the MBHs in pairs and the centers of their host galaxies (identified by the minimum potential position). The more massive MBH in both duals and one-AGN pairs are usually found very close to the galaxy centers, with a typical separation of $\sim 0.1\,\mathrm{kpc}$ (we note that due to our resolution limit, we consider $\Delta d_{\mathrm{AGN,gal}} < 2\epsilon_g = 1\,\mathrm{kpc}$ to be "central"). The secondaries among duals are typically more perturbed, with about half of the population "off-center". Nonetheless, most of them are still within 5 kpc from the host galaxy center, which keeps them accreting relatively efficiently compared to the secondaries among one-AGN pairs. These secondaries among duals could potentially be detected as merger-induced off-center AGN if both the AGN and the host galaxy can be resolved.

We also show the separation distribution for the brighter and fainter BH in the pair, since it is possible for the less massive MBH to be brighter and visible. However, this is in fact never the case for one-AGN pairs, and even though around 15% of the duals have brighter secondaries (see Section 5.3.4 for details), the overall distribution of the distance to the host galaxy center does not change significantly.

5.3.4 Mass and Luminosity

Figure 5.3.4 shows the mass and luminosity functions of the two MBHs involved in duals and one-AGN pairs at $z = 2$, in comparison with the underlying single MBH population and the MBH pairs without the mass/luminosity cuts. By comparing the thin dotted lines which include all MBH pairs with the solid brown line showing the single MBH distribution, we can see that almost all MBHs with $M_{\mathrm{BH}} > 10^6\,M_\odot$ or $L_{\mathrm{bol}} > 10^{43}\,\mathrm{erg/s}$ have a companion black hole, typically with a much smaller mass. After applying a luminosity threshold of $L_{\mathrm{bol}} > 10^{43}\,\mathrm{erg/s}$ to both MBHs in the "dual" AGN case (note that since this is not how we define our dual AGN and one-AGN pair for this work, we have added quotes when referring to "duals" and "one-AGN pairs" selected only by their luminosities but not their masses.), we see a significant drop in the pair fraction shown by the dashed lines. This means that even though all massive MBHs have a close companion, only $\sim 10\%$ have a companion that is also luminous. For the "one-AGN pair", however, since we only apply the luminosity threshold to the more luminous MBH in the pair, the mass and luminosity distributions of the primary MBH are almost not affected at the high-mass end. For the less-luminous MBH in the "one-AGN pair", selecting only the luminous primary suppresses the mass and luminosity function of the secondary. Requiring the secondary to be under-luminous also suppresses the high-mass end, as these pairs would fall into the "dual AGN" category.

Finally, we show the mass and luminosity functions of our dual AGN and one-AGN

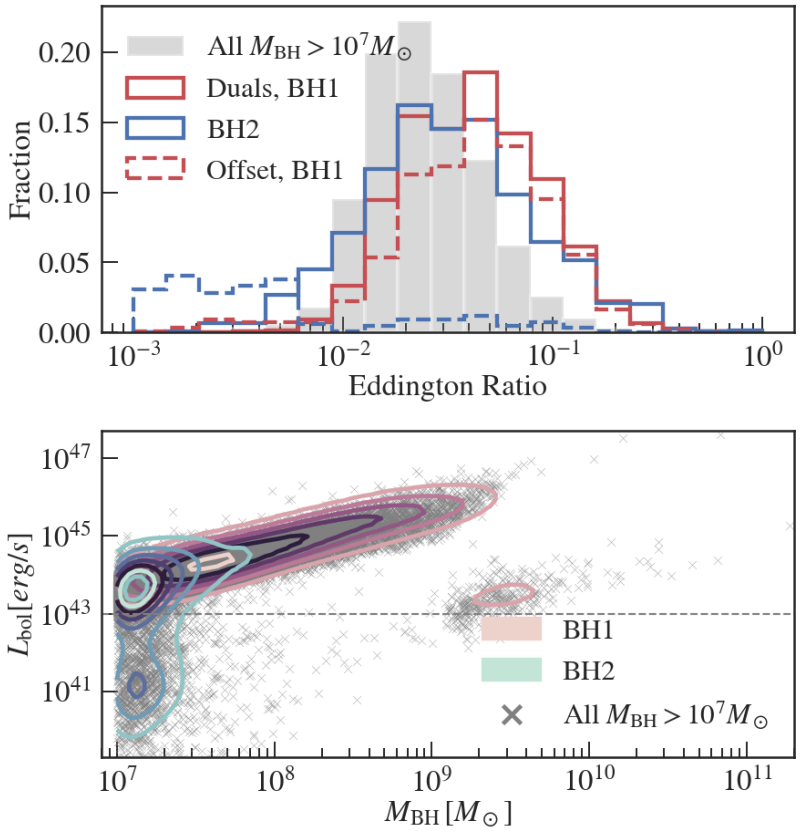

Figure 5.3.5: ***Top:*** Eddington ratio of the dual AGN and offset AGN (with the more massive one shown in ***red***, and the less massive one shown in ***blue***), compared with the underlying massive MBHs with $M_{\rm BH} > 10^7 M_\odot$ (***grey***, adding the extra $L_{\rm bol} > 10^{43}$ erg/s constraint does not affect the peak of the distribution). ***Bottom:*** Masses and luminosities of BH1 (***purple contour***) and BH2 (***blue contour***), plotted on top of all MBHs with masses above $10^7\,M_\odot$ (***grey cross***). The horizontal dashed line marks the threshold for an AGN, and the points below it are the secondary MBHs in a one-AGN pair. Almost all the $L_{\rm bol} < 10^{43}$ erg/s MBHs with $M_{\rm BH} > 10^7\,M_\odot$ are involved in a one-AGN pair.

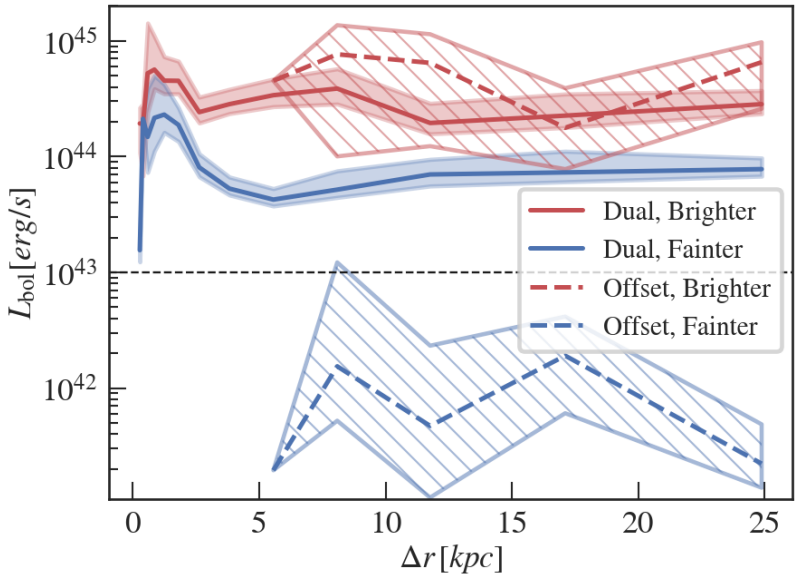

Figure 5.3.6: The relation between the pair separation and MBH luminosities. At large separations ($\Delta r > 10\,\mathrm{kpc}$), the luminosities are not sensitive to the separation. For closer pairs, the luminosity of the fainter MBH is inversely correlated with Δr.

pair catalog in solid lines. When adding the $M_{\rm BH} > 10^7\,M_\odot$ threshold to both MBHs in the pair, the dual fraction dropped to $\sim 3\%$. The change in the mass and luminosity functions are not greatly affected by the additional cut on the mass, since among MBHs with luminosities above $10^{43}\,{\rm erg/s}$, most already have $M_{\rm BH} > 10^7\,M_\odot$. The effect on the one-AGN pairs is more significant. Requiring the less luminous MBH in the one-AGN pair to have $M_{\rm BH} > 10^7\,M_\odot$, we are explicitly selecting out the rare population of massive but very under-luminous secondaries. By making this selection, we can separate the naturally low-luminosity secondaries due to their low mass, from the under-luminous secondaries that only become faint due to the galaxy merger events.

The mass and luminosity ratios between the two MBHs in the dual AGN and one-AGN pairs are shown in the bottom panels of each figure. Here we take the ratio of both the mass and the luminosity between the less massive and more massive MBHs (in particular, we do not take the luminosity ratio between the fainter and the brighter AGN). Dual AGN are mostly found in major mergers ($> 80\%$ duals have $q > 0.1$), while only $\sim 20\%$ one-AGN pairs have $q > 0.1$ and a significant fraction even has $q \sim 0.01$. The luminosity contrast between the two MBHs in the one-AGN pairs is even greater: the primary AGN are usually > 100 times brighter than the secondaries among all one-AGN pairs. For dual AGN, this feature has already been found in observational works such as Koss et al. [2012], and has been seen in various simulations [e.g. Callegari et al., 2009, Capelo et al., 2017, Steinborn et al., 2016]. Finally, we also note that in 20% of dual AGN, the less massive MBHs are brighter, but for one-AGN pairs (including offset AGN), the brighter or active AGN is always the more massive one.

The top panel of Figure 5.3.5 shows the distribution of the Eddington ratios of the pairs at $z = 2$ compared with all MBHs with $M_{\rm BH} > 10^7\,M_\odot$ (note that adding an extra $L_{\rm bol} > 10^{43}\,{\rm erg/s}$ threshold to the underlying single AGN population does not change our conclusion here, so we do not show an extra line for that population). Compared to the overall AGN population at the same masses with a typical Eddington ratio of ~ 0.025, the pairs have a higher level of activation, where the Eddington ratios peak above 0.05. On the bottom panel, we show the mass-luminosity relation for the dual and offset AGN, plotted on top of all MBHs. The primary MBHs follow the underlying MBH distribution but appear slightly over-luminous compared to the mean relation of the non-pair population. The blue contour marks the secondary MBHs in the pair, and the ones falling below the dashed line are the secondaries of one-AGN pairs. Comparing these secondaries to the overall MBH population, we can see that the inactive MBHs of the one-AGN pairs are extremely under-luminous. In fact, the secondaries among one-AGN pairs appear to be the majority of the $L_{\rm bol} < 10^{43}\,{\rm erg/s}$ MBHs with $M_{\rm BH} > 10^7\,M_\odot$. It is very rare for an $M_{\rm BH} > 10^7\,M_\odot$ MBH to have $L_{\rm bol} < 10^{43}\,{\rm erg/s}$ if it is not involved in a galaxy merger. Finally, we note that another group of low-Eddington ratio MBHs are the heaviest MBHs with $M_{\rm BH} \gtrsim 10^9\,M_\odot$ (the blob on the lower-right). This is due to the kinetic AGN feedback that actively suppresses the gas accretion among the most massive BHs.

The enhancement in the AGN activation among pairs shown above is usually attributed to the gas-inflow during galaxy mergers. Previous simulation works have seen peaks in the

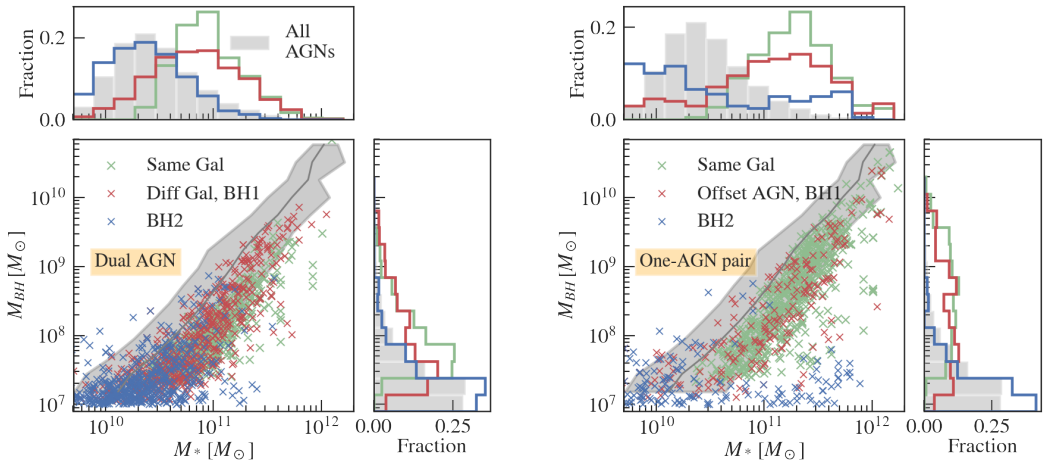

Figure 5.3.7: The $M_{\rm BH} - M_*$ relation of dual AGN (***left panels***) and one-AGN pairs(***right panels***). For different-galaxy pairs, we show the more massive MBH in each pair in *red* and the less massive one in *blue*. For same-galaxy pairs, we plot the sum of the MBH masses against their host galaxy mass in *green*. The *grey* line shows the median BH mass of all MBHs with $M_{\rm BH} > 10^7\,M_\odot$. The side panels show the 1D distribution of the MBH masses and galaxy masses.

pair activation at $1 \sim 10\,\mathrm{kpc}$ [Van Wassenhove et al., 2012] and $0.1 \sim 2\,\mathrm{kpc}$ [Blecha et al., 2013]. Recent observations by Stemo et al. [2021] have seen a bump in AGN activation at a bulge separation of $\sim 10 \sim 15\,\mathrm{kpc}$. Also in the nearby universe, enhanced AGN activation is seen in close pairs with less than tens of kpc separations [e.g. Ellison et al., 2011, Liu et al., 2012].

In Figure 5.3.6, we show the relationship between the dual/offset AGN luminosity and the pair separations. Here we log-binned the pairs by their separation, and for each bin, we plot the median luminosity enclosed by the interval including 80% of MBHs in that bin. The red (blue) lines correspond to the brighter (fainter) MBH, and the solid (dashed) curves represent the dual/offset pairs. For the dual AGN, both the brighter and the fainter AGN exhibit an increase in luminosity at separations below $\sim 4\,\mathrm{kpc}$. The median luminosities then drop slightly at a separation around 5 kpc, but then increase again at around 10 kpc. Because of the rise in AGN luminosity at $\Delta r < 5\mathrm{kpc}$, observations targeted at bright quasar pairs could see a larger fraction of close pairs than observations that also include fainter AGN pairs [see also the Appendix of Volonteri et al., 2022]. In the observation work by Shen et al. [2022], for example, we can see that using a higher luminosity threshold for the dual selection from our simulation than our sample here results in a larger contrast between the number of small-separation duals and large-separation duals.

For the offset AGN, the brighter MBH are overall more luminous than the duals, and the luminosity depends less on the pair separation. The fainter MBHs in the pair, however, show an increase in luminosity with smaller separations, and as a result, there are no offset secondaries at separations below 5 kpc. Our $\Delta r - L_{\mathrm{bol}}$ relation suggests that when observations only limit to $\Delta r > 5\,\mathrm{kpc}$ pairs, it may be hard to establish a relation between the AGN activation and the pair separation.

5.3.5 Host Galaxies

Figure 5.3.7 shows the $M_{\mathrm{BH}} - M_*$ relation for the dual AGN and one-AGN pairs and their host galaxies. For the pairs identified in the same galaxy, we plot the total mass of the MBH pair and the mass of their host, while for the different-galaxy pairs, we show the mass of each MBH and host separately. The central panels show the scattered relation between M_{BH} and M_*, while the top and right panels show the 1D distributions of the galaxy and MBH masses, respectively. To compare the dual AGNs and one-AGN pairs with the single AGN population, we show the distribution of all MBHs with $M_{\mathrm{BH}} > 10^7\,M_\odot$ in grey. For the middle panels, the solid curve shows the median galaxy mass within each M_{BH} bin, and the shaded region encloses the scatter of the middle 95% of the galaxy masses in that M_{BH} bin.

From the 1D distributions of the MBH and galaxy masses, we can see that the pairs favor the more massive MBHs and galaxies among the overall MBH population. For all MBHs selected with $M_{\mathrm{BH}} > 10^7\,M_\odot$, the galaxy masses center around $2 \times 10^{10} M_\odot$. For the dual AGN, the host galaxy masses peak near $10^{11}\,M_\odot$, regardless of whether the two MBHs are in the same galaxy. This is in general agreement with the findings of Rosas-Guevara et al.

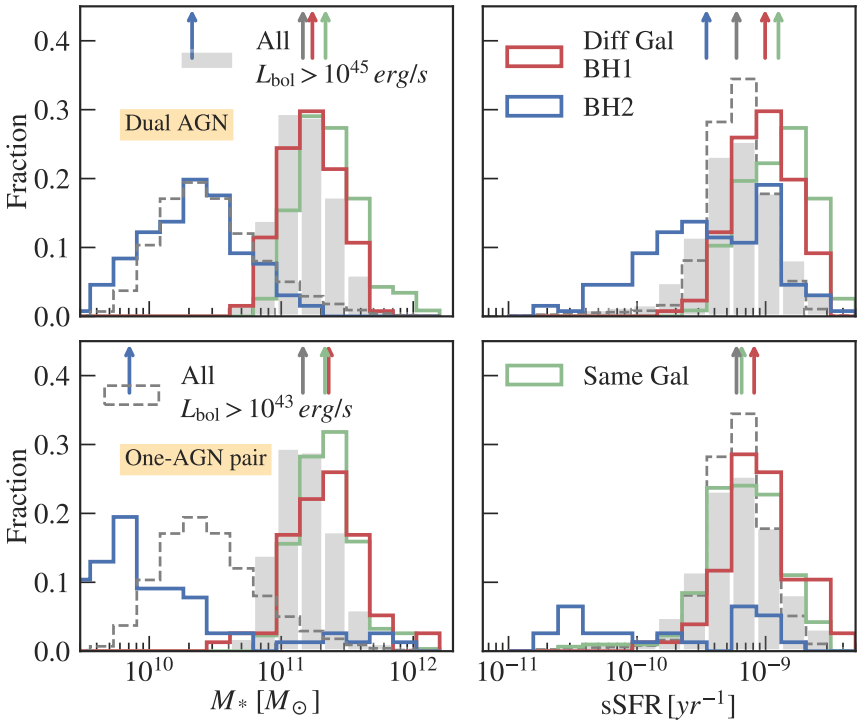

Figure 5.3.8: Comparisons between the galaxy mass (***left***) and specific star formation rate (***right***) of the dual AGN (***top***) and one-AGN pairs (***bottom***) AGN with those of all AGN with $L_{bol} > 10^{45}$ erg/s (***grey shadow***). For the dual and one-AGN pairs, we have added the $L_{bol} > 10^{45}$ erg/s luminosity threshold to the bright AGN in the pairs for a direct comparison with observations. For reference we also show the distributions of all AGN under our canonical definition ($M > 10^7 M_\odot$, $L_{bol} > 10^{43}$ erg/s) in ***dashed grey***. The vertical arrows on the top mark the median of each distribution (the grey arrow corresponds to the $L_{bol} > 10^{45}$ erg/s population).

[2019], although we see a greater difference between the dual AGN and single AGN host galaxy masses. From the $M_{\rm BH} - M_*$ relation of duals with that of all massive MBHs, we see that almost all pairs have galaxy masses above the median relation in the same MBH mass bin, meaning that MBHs in duals are under-massive relative to their host galaxies. A previous study by Steinborn et al. [2016] of the $z = 2$ pairs using the Magneticum simulation has found a similar trend, where their MBH in pairs are systematically under-massive with respect to the host galaxy masses. Volonteri et al. [2022] also examines the ratio between the MBH and galaxy masses for dual AGNs, and finds that before the host galaxy merger, stripping can lead to "overmassive" MBHs relative to the host galaxy among duals, while after the galaxy merger the MBH can be "undermassive" compared with the merger remnant. In our case, we find that both before and after the host galaxy mergers, the dual-hosting galaxies are generally "overmassive" relative to the MBHs.

For one-AGN pairs, the contrast of the host galaxy masses with those of the single AGN population is even greater. Most one-AGN pairs reside in galaxies of $M_* \sim 2 \times 10^{11}\, M_\odot$. This is again a consequence of two factors: the MBHs with a massive but under-luminous companion are among the most massive BHs, so they naturally reside in large galaxies; galaxy mergers also play a role, because even when compared with other AGN in the same $M_{\rm BH}$ mass bin, the host galaxies of one-AGN pairs are still larger than the median. A significant fraction even falls into the top 2.5% of the galaxy mass when compared with their similar-mass single-AGN counterparts.

We notice that there is a contrast between our comparisons of the single-AGN and AGN-pair population and the observational results shown in Stemo et al. [2021], who found that the MBH mass and galaxy mass distributions of the AGN pairs are not significantly different from the single AGN samples. One reason for the differences is that our underlying single-AGN samples have a lower $M_{\rm BH}$ distribution compared with their selection function, especially at high redshifts. To mitigate the difference in the underlying AGN sample, in Figure 5.3.8 we raise the luminosity threshold from $10^{43}\,$erg/s to $10^{45}\,$erg/s. We apply the same luminosity threshold to our dual AGN and one-AGN pair samples. The resulting galaxy-mass distribution of the single AGN is closer to the single AGN from Stemo et al. [2021], which peaks around $10^{11}\, M_\odot$. After the stricter luminosity cut, we find that the galaxy mass distribution of the duals is similar to that of the single AGN, with the primary galaxy mass slightly higher. The one-AGN pairs, however, still tend to reside in the high-mass galaxies compared to the underlying single AGN population.

In the right panels of Figure 5.3.8, we show the specific star-formation rate (sSFR) for the pairs with $L_{\rm bol,1} > 10^{45}\,$erg/s, compared with all AGN with $L_{\rm bol} > 10^{45}\,$erg/s. The sSFR is calculated by summing the gas star formation rate within the half-mass radius of the host galaxy, and then dividing it by the total stellar mass within the half-mass radius. For the $L_{\rm bol} > 10^{45}\,$erg/s AGN sample, the sSFR peaks around $0.6 \times 10^{-9}\, yr^{-1}$. The sSFR of the different-galaxy duals is similar to the AGN at similar luminosities and stellar masses, with the primary AGN's sSFR slightly higher. The hosts of the same-galaxy duals have an overall higher sSFR, with a peak around $10^{-9}\, yr^{-1}$. Our statistics are consistent with previous studies using idealized galaxy merger simulations [e.g. Van Wassenhove et al., 2012],

who saw peaks in the host galaxies' SFR after a few pericentric passages, when the duals are separated by a few kpcs. In our case, such duals mostly fall into the same-galaxy dual category. For the one-AGN pairs, even though the galaxy mass is generally higher compared to the overall luminous AGN, the sSFR of the host galaxies does not differ from the underlying AGN sample.

Comparing our sSFR with the observations from Stemo et al. [2021] with similar galaxy masses, we see that our sSFR peaks at a higher value. Moreover, Stemo et al. [2021] does not see an enhancement in the SFR among the pairs compared to their underlying AGN sample, whereas we see a shift towards higher SFR in our duals. One reason is that the sSFR increase is most significant for the same-galaxy duals, typically with separations of $\Delta r < 5\,\mathrm{kpc}$. However, the sample selected based on distinct galaxy bulges from Stemo et al. [2021] consists only of the different-galaxy pairs, among which the increase in star formation has not taken place.

5.3.6 Host Halo

Figure 5.3.9 shows the host FOF halo mass of the dual AGN, one-AGN pairs, and offset AGN at $z = 2$, together with the host halo mass of all MBHs with $M > 10^7\,M_\odot$. The fraction of pairs in each halo mass bin is shown on the bottom panel. Dual AGN prefer halos with masses ranging between $10^{12.3}\,M_\odot - 10^{13}\,M_\odot$, and are very rarely found in halos with $M_{\mathrm{halo}} > 10^{13.5}\,M_\odot$. The one-AGN pairs and offset AGN typically reside in more massive halos compared with the duals, with the majority of them found in halos in the mass range of $10^{13}\,M_\odot - 10^{14}\,M_\odot$. The fraction of one-AGN pairs increases significantly with the mass of the host halo: $< 0.1\%$ of the $\sim 10^{12.2}\,M_\odot$ halos host a one-AGN pair, whereas $\sim 40\%$ of the most massive halos with $M_{\mathrm{BH}} > 10^{13.5}\,M_\odot$ host a one-AGN pair. There is a similar trend in offset AGN, although the overall fraction is lower.

One explanation for why we find more one-AGN pairs than duals in the most massive halos is that the deep potential of such massive halos causes the most gas and stellar disruption of the secondary [also see e.g. Ricarte et al., 2021]. Therefore, even though the secondary MBH in the one-AGN pair is initially more massive (as we will show in Section 5.4.3 and Figure 5.4.8), it falls victim to the gravitational potential around the primary AGN and ends up lurking in the most massive halos for an extended period.

The fact that the most massive halos preferentially host one-AGN pairs instead of duals also has observational implications: one way to search for dual AGN is by looking for companion AGN around a sample of single AGN. At high redshift, the luminosity threshold for detecting AGN is typically high, and thus the resulting observed AGN sample could be embedded in the most massive halos. These most luminous AGN are more likely to be involved in one-AGN pairs rather than duals, such that its companion may not be detectable through EM observations albeit its high mass.

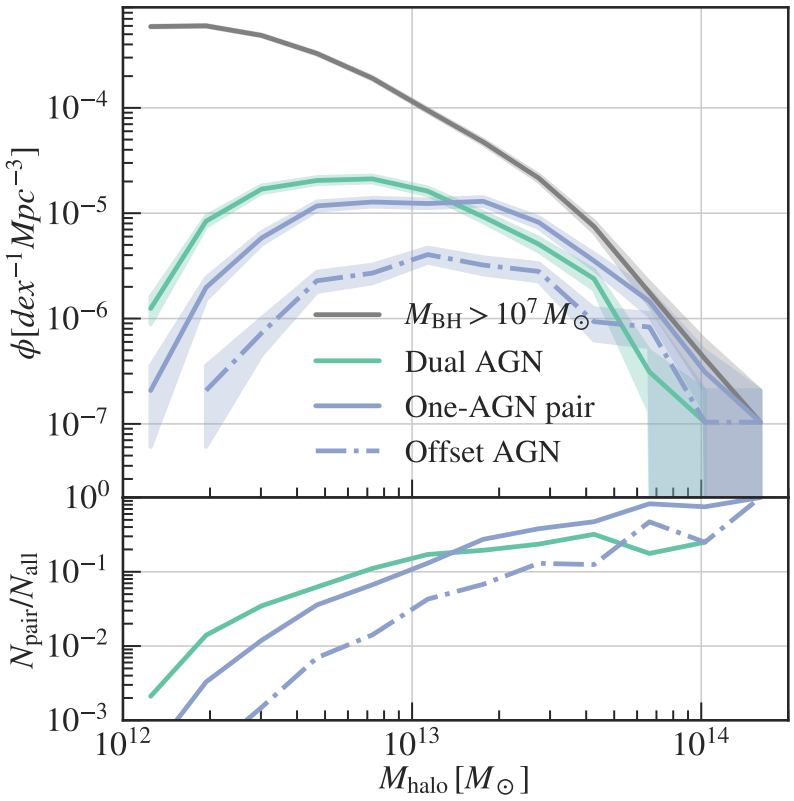

Figure 5.3.9: ***Top:*** Host halo mass functions of the same-galaxy dual AGN (***green***) and one-AGN pairs (***purple***), plotted with the mass function of all halos hosting at least one MBH with $M_{\rm BH} > 10^7\,M_\odot$ (***grey***, and we checked that adding the extra $L_{\rm bol} > 10^{43}\,{\rm erg/s}$ requirement results in a similar line). For hosts of duals and one- AGN pairs, we only count unique halos, but the fraction of halos hosting two pairs is less than 5%. ***Bottom:*** the ratio between the number of dual/one-AGN pair host halos and $M_{\rm BH} > 10^7\,M_\odot$ MBH host halos in each mass bin.

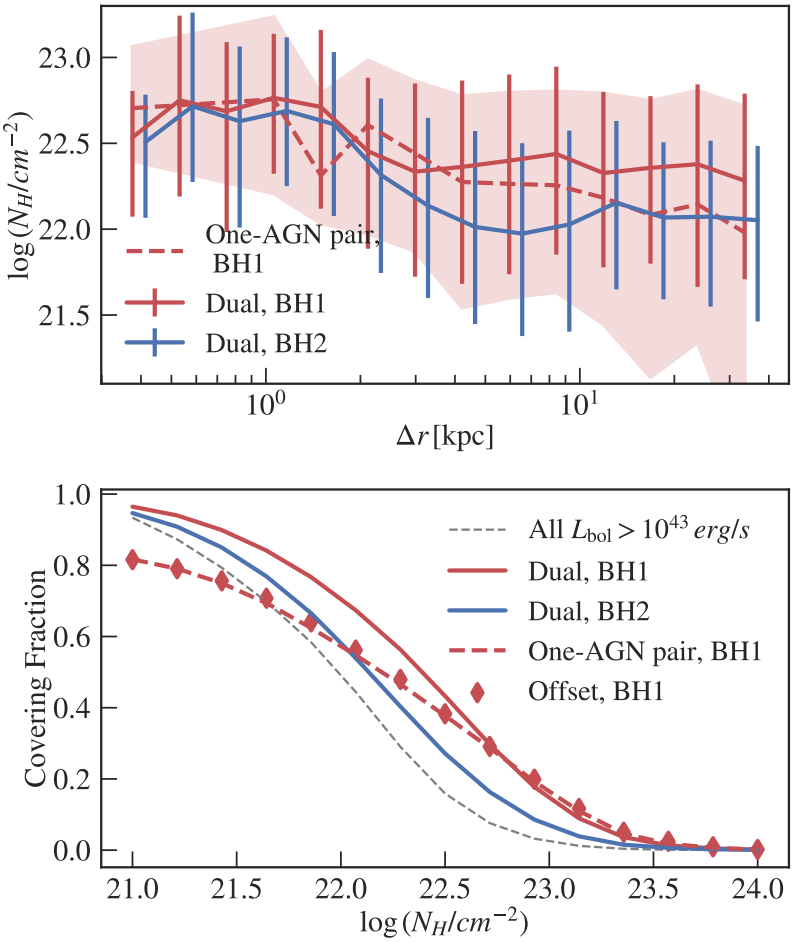

Figure 5.3.10: ***Top:*** The relation between gas column density N_H and pair separations for the dual AGN (the more luminous AGN in ***red solid***, the less luminous AGN in ***blue solid***) and one-AGN pairs (we only show the active AGN in ***red dashed***). For each AGN we compute $N_{\rm H}$ along 48 random sight lines. The curves show the median $N_{\rm H}$ of all lines-of-sight in each Δr bin, with the shaded area/vertical lines covering the 16 - 84th percentile of the distribution. ***Bottom:*** The AGN covering fraction of dual AGN, one-AGN pairs and offset AGN assuming various $N_{\rm H}$ thresholds. To compare with the underlying AGN sample (***grey***), we apply the same $L_{\rm bol}$ lower limit to the pairs. The covering fraction of pairs is higher than the underlying AGN population.

5.3.7 Obscuration of high-redshift pairs

Previous theoretical works have found that the offset in AGN triggering time and the dynamics of the merger are the main factors that explain the paucity of observed AGN pairs [e.g. Blecha et al., 2013, Van Wassenhove et al., 2012]. Besides these factors, AGN obscuration could also hinder the discovery of dual AGN. As was discussed in the recent review paper by De Rosa et al. [2019], some AGN in many confirmed dual systems show no (or very weak) explicit AGN evidence in their optical/near-infrared spectra, indicating that these AGN pairs are heavily dust-enshrouded, and there is also strong evidence that they are also heavily obscured in the X-rays. It is also known that $20-40\%$ of AGN are hidden behind Compton-thick column densities (with $N_{\rm H} > 10^{24}$ cm^{-2}) and $\sim 75\%$ of the remaining population are obscured, with $N_{\rm H} = 10^{22} \sim 10^{24}$cm^{-2} [e.g. Aird et al., 2015, Buchner et al., 2015, Ueda et al., 2014] at the peak of AGN activity at redshift $z = 0.5 - 3$. Meanwhile, Capelo et al. [2017] examined the effect of obscuration in hard X-ray luminosities on resolvable scales ($> 100\,$pc) in their idealized galaxy merger simulations, and found it to be negligible for $z = 3$ galaxies. In this section, we investigate the role of AGN obscuration in pair detection from our sample of dual AGN and one-AGN pairs.

To calculate the column density for each AGN, we follow the method in Ni et al. [2020], and estimate the contribution to the obscuration only due to the gas in the host galaxy. By doing so, we do not account for the AGN obscuration associated with the nuclear torus, on scales of ~ 10 pc surrounding the accretion disk of the BH, which is beyond the resolution of cosmological simulations.

In Figure 5.3.10, we show the gas column density of dual AGN and one-AGN pairs binned by the pair separation. For each AGN we compute $N_{\rm H}$ along 48 random sight lines, and for each Δr bin we show the median and the middle 68% of all lines-of-sight within that bin. For the one-AGN pairs, we only show the column density of the primary AGN, as the inactive MBH is likely not observable through EM signatures. We find that for both dual AGN and one-AGN pairs, the column density increases with decreasing pair separations. This is particularly true for dual AGN at separations below $\sim 2\,$kpc: at this separation, most duals have $N_{\rm H} > 10^{22.6}\,$cm^{-2}. Our finding is in line with the recent observational studies by e.g. Ricci et al. [2017], who find that AGN obscuration reaches its maximum at the late galaxy merger stage, when the nuclei of the two merging galaxies are at a projected distance of $< 10\,$kpc. Our results are also in broad agreement with the findings of Capelo et al. [2017], who used higher-resolution isolated galaxy merger simulations to evaluate N_H, and found that N_H around duals are close to $10^{23}\,$cm^{-2}. They also found such values of N_H only have minor effects on the hard X-ray flux of the $z = 3$ duals but may reduce the flux by half at low redshifts.

Between the two AGN in a dual, the secondary has a larger increase in the obscuration with decreasing pair separation, as it enters into the gas reservoir of the primary AGN. Moreover, we also find that the $N_{\rm H}$ of the secondary varies with the angle between the line-of-sight and the dual separation: the $N_{\rm H}$ integrated from the line-of-sight passing near the primary AGN can be three times higher than the $N_{\rm H}$ calculated from the opposite direction, or perpendicular to the dual separation. One implication is that pairs projected at a smaller

separation can have a more obscured secondary, compared to pairs viewed at their true separation.

The bottom panel of Figure 5.3.10 shows the AGN covering fraction at different $N_{\rm H}$ thresholds. Here we take the median overall line-of-sights for all the pairs to compute the covering fraction at each threshold. To do a fair comparison with the $\log(L_{\rm bol}) > 43$ AGN sample, we also apply a $\log(L_{\rm bol}) > 43$ lower limit to both AGN of the duals and the brighter AGN of the one-AGN pair. The AGN covering fraction for the duals is generally higher than that of the underlying AGN population, especially at higher $N_{\rm H}$ thresholds. At $\log(N_{\rm H}) > 23$, only $< 3\%$ of the sight lines among all AGN are covered, for dual AGN and one-AGN pairs the fraction ranges from 10% to 20%.

5.4 Evolution of Dual and Offset AGN

Up until now, we have focused on the properties of dual AGN, one-AGN pairs, and offset AGN at a fixed redshift of $z = 2$, in order to make comparisons with observational properties. In this section, we will take advantage of the simulation's access to the evolution of the pairs across different redshifts and the evolutionary stage of the pairs. For this purpose, we will use the 329 dual AGN and 110 one-AGN pair samples at $z = 3$, because we would like to trace the evolution of those pairs both before and after the time of observation. When studying the pairs across a range of redshifts, we do not single out offset AGN from one-AGN pairs for two reasons: first, we will focus our analysis on how the secondary becomes inactive during the galaxy merger, and this applies to both offset AGN and the entire one-AGN pair population; second, practically we cannot identify offset AGN at all redshifts, because we do not have the subhalo information in all simulation snapshots.

5.4.1 Connections between pairs across different redshifts

Previous simulations have associated AGN triggering with galaxy mergers, showing that the MBH pairs are observable as duals only during a small fraction of time during the host galaxy merger. Hence, a fraction of the observable duals at $z = 3$ could have been one-AGN pairs or inactive pairs in the past. Furthermore, some dual AGN may suffer suppression in activation during galaxy mergers, due to the gas outflows and heating induced by the galaxy mergers, and thus become a one-AGN pair at closer separations [e.g. Steinborn et al., 2016]. The future of the dual AGNs is also of great interest, as they are progenitors of the MBH merger event. Here we will look into the past and future of AGN in pairs, and draw connections between the pair population at different redshifts.

In Figure 5.4.1, we show the classification of the dual AGN and one-AGN pairs at $z = 3$ through different times. The top panels show the evolution of the same- and different-galaxy duals, where the width of each colored band shows the fraction of $z = 3$ duals falling into each category at different times. We have categorized the pairs into five categories: dual AGN and one-AGN pairs as defined throughout this paper, inactive pairs when the MBHs are separated by $< 30\,$kpc but do not fall into the dual AGN and one-AGN pair categories

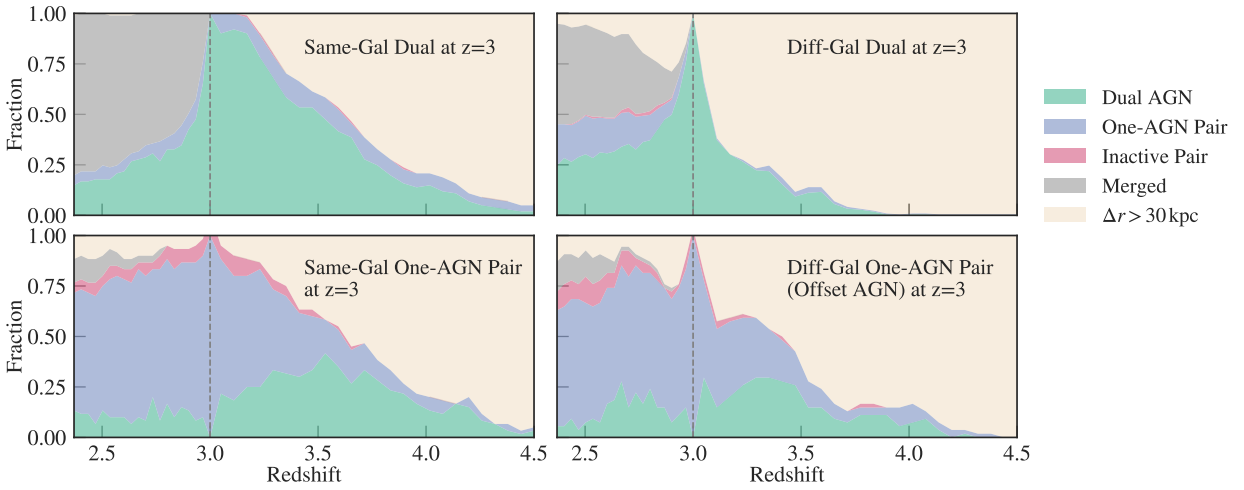

Figure 5.4.1: ***Top:*** the classification of same-galaxy dual AGN (***left***) and different-galaxy dual AGN (***right***) identified at $z = 3$, throughout $z = 2.4 \sim 4.5$. The width of each band corresponds to the fraction of dual AGN falling into each category. We have categorized the pairs into duals (***green***), one-AGN pairs (***purple***), inactive pairs (***pink***), mergers (***grey***) and non-pairs (***beige***) . Here the dual AGN and one-AGN pair categories have been previously defined for our work. Inactive pairs are pairs with both MBHs under $L_{\rm bol} < 10^{43}\,{\rm erg/s}$. The merger category refers to simulation mergers, with the merging criterion defined in Section 6.2. ***Bottom:*** the classification of same-galaxy one-AGN pairs (***left***) and offset AGN (***right***) identified at $z = 3$, across the same redshift range.

due to the luminosity threshold (not the mass threshold), mergers when the two MBHs merge in the simulation, and $\Delta r > 30$kpc when the two MBHs do not form a pair. For the same-galaxy duals at $z = 3$, the pairs were formed as early as $z = 4.5$, and 50% of those duals were observable as duals from $z = 3.5$ to $z = 3$. After $z = 3$, the same-galaxy duals go through rapid mergers because they are already very close at the time of observation, and also have similar masses compared to one-AGN pairs (so that the dynamical friction time is short). By $z = 2.4$, more than 80% of these duals would merge in the simulation. Volonteri et al. [2022] also investigated the connection between dual AGN and the subsequent MBH mergers, and they reached a similar conclusion that $\sim$ 80% of the same-galaxy duals at $z = 3$ would merge by $z = 2.5$. Moreover, most of the remaining 20% same-galaxy duals that do not merge by $z = 2.5$ never merge in their simulation even after that. We note that mergers in the simulation do not guarantee an MBH coalescence, due to the sub-resolution dynamical friction time [e.g. Chandrasekhar, 1943, Dosopoulou and Antonini, 2017, Pfister et al., 2019] and the binary hardening time [e.g. Sesana, 2010, Vasiliev et al., 2015], as well as the possibility of a three-body scattering. For example, Volonteri et al. [2022] showed that after considering these delays, only 40% instead of 80% of their same-galaxy duals would merge by $z = 0$. Nonetheless, the delay time calculation is largely model-dependent, and in the regime where both MBHs are massive, the delay due to the above mechanisms is expected to be within $\sim$ Gyr [see e.g. Chen et al., 2022a]. Finally, about 5% of the same-galaxy duals would fall into the one-AGN pair category at other redshifts. They may be observable as duals at $z = 3$ only because of the time variability of the AGN activation.

The different-galaxy duals at $z = 3$ have come to within 30 kpc of each other more recently, with more than 50% forming pairs after $z = 3.2$. The different-galaxy duals can be viewed as the progenitors of three distinct populations when we look at their evolution after $z = 3$. At $z = 2.5$, only $\sim$ 25% of the different-galaxy duals remain to be dual AGN, and most would become small-separation, same-galaxy duals. Another 25% of the different galaxy duals would evolve into one-AGN pairs, due to the gas disruption of the secondaries during the galaxy close encounters. Finally, an increasing fraction of the different-galaxy duals would first become same-galaxy duals, with $\sim$ 50% having merged at $z \sim 2.5$. Notably, 10% of the different galaxy duals would be separated by more than 30 kpc after $z = 2.5$, while $\sim$ 25% are separated to $>$ 30kpc shortly after $z = 3$, before getting closer again. This is because at $z = 3$, we happened to have caught those duals at their pericentric passage, and they will get into larger separations for some time before settling into $\Delta r < 30$ kpc orbits.

Next, we show the history of one-AGN pairs at $z = 3$ on the bottom panels of Figure 5.4.1. Among these pairs, at least 35% were once dual AGN at $z \sim 3.5$, and have only become one-AGN pairs between $z = 3$ and $z = 3.5$. In fact, if we trace the same-galaxy duals and one-AGN pairs back to $z = 3.5$, we see an equal fraction of them were once dual AGN, but these $z = 3.5$ duals then quickly parted ways and evolve into duals and one-AGN pairs at $z = 3$. We will investigate the reasons for the diverging paths of the duals and one-AGN pairs during this time in later sections.

When we follow these one-AGN pairs to lower redshifts, we can see that once the pair becomes a one-AGN pair, it will very likely remain so for a very long time, without going

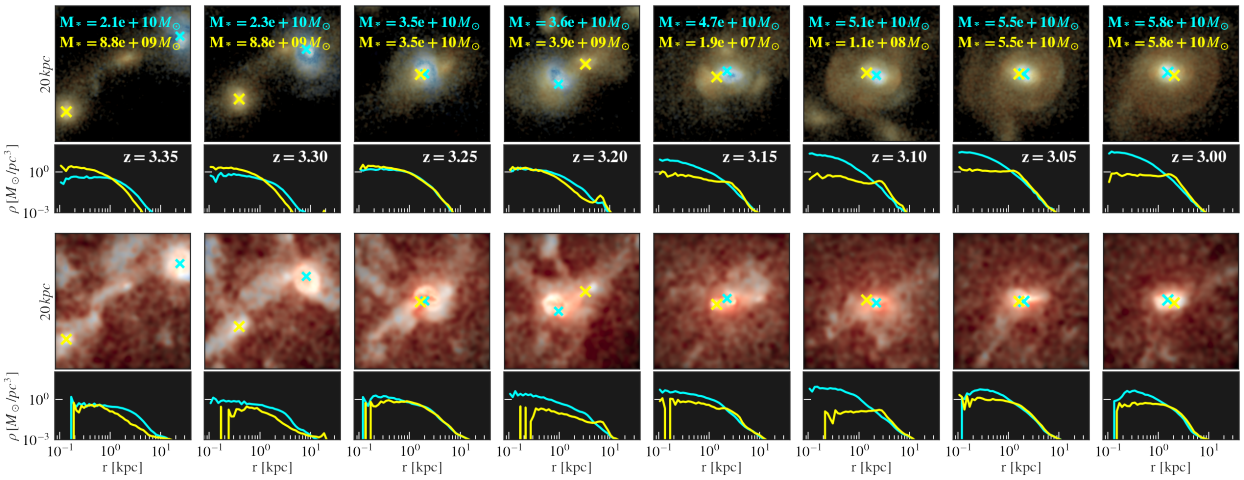

Figure 5.4.2: The galaxy (***top***) and gas (***bottom***) surrounding a dual AGN during the galaxy merger. The galaxies are color-coded by the stellar age (warmer colors correspond to older stars), and the gas is color-coded by the gas temperature (warmer colors correspond to higher temperature), with brightness representing the densities for both. The crosses mark the two MBHs. The bottom panels show the gas and stellar densities around the MBH with the corresponding color. The host galaxy masses of the two MBHs are marked with the corresponding color. The host galaxies merge between $z = 3.1$ and $z = 3.05$.

through mergers or both MBHs becoming active again. The stellar stripping of the inactive MBH leads to very inefficient orbital decay [also see e.g. Tremmel et al., 2018b], such that the MBH stalls at relatively large orbits for up to $>$ Gyrs. During this long period of in-fall time, we also see that $\sim 10\%$ of the same-galaxy one-AGN pair will be dissociated, likely due to the disruption from a third galaxy. Finally, only around 5% of the one-AGN pair will be observable as a dual at a given time, mostly during the pericentric passages when the secondary MBH passes through the high-density regions near the primary AGN.

5.4.2 Pair evolution during galaxy mergers: case studies

Previously, we have found that duals and one-AGN pairs are luminous at a closer pair separation, and that the high-mass ratio, different-galaxy duals may be the progenitor of one-AGN pairs at a closer separation. In this subsection, we will follow some of the $z = 3$ duals and one-AGN pairs throughout their formation histories, and investigate their surrounding environment and activation during different stages of the galaxy mergers.

In Figure 5.4.2, we show the evolution of the galaxy and gas surrounding the two MBHs in a $z = 3$ dual AGN during the pair formation, where the galaxies are color-coded by the stellar age (warmer colors correspond to older stars), and the gas is color-coded by the gas temperature (warmer colors correspond to higher temperature), with brightness representing the densities for both. The bottom panels show the density profiles of the stars and gas,

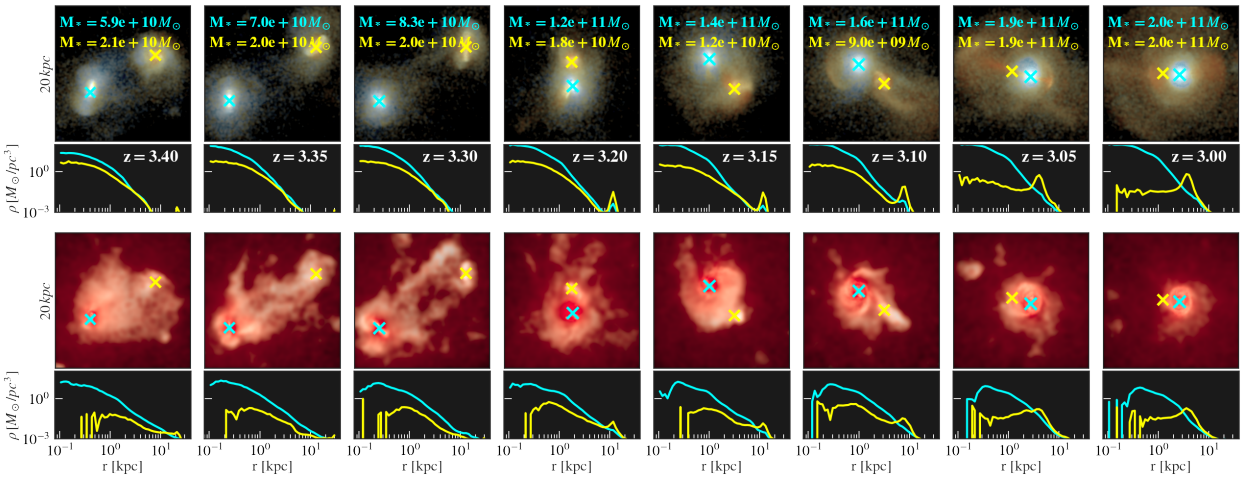

Figure 5.4.3: Similar to Figure 5.4.2, but for an MBH pair that evolved from a dual AGN to a one-AGN pair after the galaxy merger. The color ranges of the gas and galaxy images are the same as the dual pair for comparison. The host galaxies merge between $z = 3.1$ and $z = 3.05$. After $z = 3.1$, the secondary galaxy is almost completely disrupted and the secondary MBH becomes an inactive bare MBH. We also note that the gas temperature around the one-AGN pair is higher, and we find this to be generally true among one-AGN pairs.

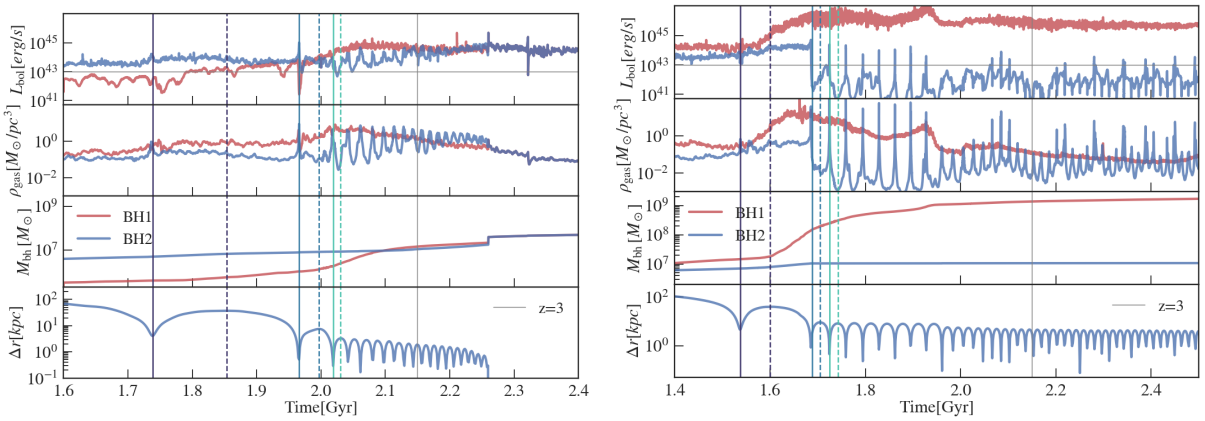

Figure 5.4.4: The evolution of a dual (***top***) and an one-AGN pair (***bottom***), where we traced their luminosity (*first panel*), surrounding gas density (*second panel*), masses (*third panels*) and the pair separation (*fourth panel*), throughout the pair formation time. We mark the time of the first (*dark blue*), second (*blue*) and third (*green*) pericentric (*solid*) and apocentric (*dashed*) passages by the vertical lines.

centered around the two MBHs. The evolution of the luminosities, gas densities, masses, and the separation between the two MBHs in the same pair are shown in the top panel of Figure 5.4.4. For this system, we see that the initially less-massive and inactive MBH (cyan in Figure 5.4.2 and red in Figure 5.4.4) was embedded in a galaxy with newly formed stars and a denser cold gas reservoir. During the galaxy merger, this less-massive MBH goes through very rapid growth by accreting from its surrounding gas and becomes the brighter AGN at the third pericentric passage. Then, after about 50 Myrs, its mass also catches up with the initially more massive MBH (yellow in Figure 5.4.2 and blue in Figure 5.4.4). In the meantime, the central density of its surrounding gas also grows by more than an order of magnitude.

The chosen dual AGN is typical among the few hundred duals, although there is a large variance among the population (see e.g. the distribution shown in Figure 5.4.8). The evolution of this pair is also in concordance with the cases of idealized galaxy mergers presented by Callegari et al. [2009, 2011] and Van Wassenhove et al. [2012] in many aspects: during the galaxy merger, there is a weaker SFR in the initially more massive MBH, while the initially lighter MBH has a higher central SFR during the galaxy merger, building up a dense cusp while outgrowing and disrupting the initially more massive MBH.

In Figure 5.4.3 and the bottom panels of Figure 5.4.4, we show the same information but for a one-AGN pair at $z = 3$. Compared with the dual AGN example, both MBHs in this one-AGN pair are more massive, but we note that the mass contrast between the two MBHs in this one-AGN pair before the encounter is actually smaller, indicating that minor mergers are not necessary conditions for forming a one-AGN pair. The large-scale environment can also play a key role: the gas temperature surrounding the one-AGN pair is hotter, and we find this to be generally true for the majority of one-AGN pairs, compared with the dual AGN. The hotter ISM/environment can be attributed to these objects being embedded in a more massive halo than a typical dual. This is illustrated in Figure 5.3.9.

From the luminosity and gas density shown on the bottom panel of Figure 5.4.4, we can see that between the first and the second pericentric passages, the primary AGN goes through a very rapid phase of gas accretion, when its surrounding gas density increases by two orders of magnitude, and its luminosity also increases by two orders of magnitude. On the other hand, there is a very clear gas stripping of the gas surrounding the secondary MBH immediately after the secondary pericentric passage (marked by the purple solid lines). After this point, the secondary MBH remains inactive for the majority of the time, although occasionally during the pericentric passages of the orbits, the inactive secondary comes very close to the primary, so that its luminosity peaks above 10^{43} erg/s.

From the pair separation shown in the fourth panel of Figure 5.4.4, we can also see that another effect of the complete star and gas stripping of the secondary is that the MBH orbit remains large for a very long time: even though the galaxy merger of the one-AGN pair takes place before the dual example shown in the top panel, the MBHs do not merge in the next Gyr.

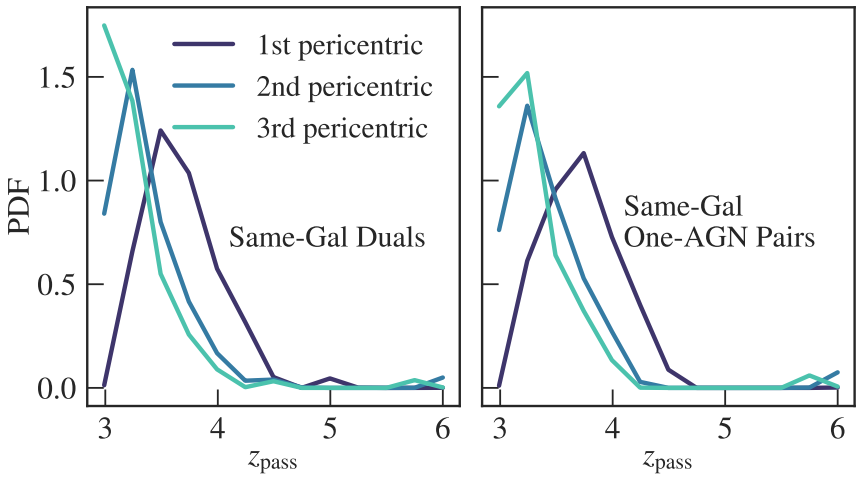

Figure 5.4.5: The redshift distribution of the first three pericentric passages between the same-galaxy dual AGN pairs (***left***) and one-AGN pairs (***right***) at $z = 3$. Duals and one-AGN pairs have similar pericentric passage times, but the orbital periods of one-AGN pairs are shorter, leading to an earlier third passage (as was illustrated in the cases of Figure 5.4.4).

5.4.3 Pair evolution during galaxy mergers: population statistics

From the previous section, we have selected two typical cases among the dual AGN and one-AGN pairs at $z = 3$ to illustrate the difference in their time evolution. Now we will apply a similar time-evolution analysis but for the whole dual and one-AGN pair population.

Similar to the case studies, the point at which the pericentric passage is identified is shown by the vertical lines of the same colors in the fourth panel of Figure 5.4.4. We show the redshift distribution of the first three pericentric passages for the same-galaxy duals and one-AGN pairs in Figure 5.4.5. Note that duals and one-AGN pairs have similar first-passage redshifts, but the orbital periods of one-AGN pairs are shorter, leading to an earlier third passage among one-AGN pairs (as was illustrated in the cases of Figure 5.4.4). When comparing the pair properties of duals and one-AGN pairs, the difference between the time of the third passage should also be noted, while the comparison between the first two passages is fair. Finally, the time before the encounter is defined to be the first time that the two MBHs are separated by less than the virial radius of the smaller subhalo, such that there has not been any significant dynamical interaction between the gas and stars surrounding the two MBHs.

In Figure 5.4.6, we show the Eddington ratio of two MBHs involved in the dual and one-AGN pairs at different stages of the galaxy merger. The top panels show the evolution of the primary MBH at $z = 3$ (but note that they are not necessarily more massive at all stages), and the bottom panel shows the evolution of the secondary MBH at $z = 3$. Here we trace the AGN activation before the galaxy merger and during the first, second, and third pericentric passages of the orbits.

For the dual AGN, both MBHs start at an Eddington ratio slightly above 0.1, but there are 20% in each population with Eddington ratios below 0.03. During the first pericentric encounter, we see an increase in AGN activity in both MBHs of the dual: a large fraction of the initially inactive tails activated with an Eddington ratio around 0.1. The divergence between the evolution of the two MBHs happens at the second pericentric passage: the primary AGN becomes more active with Eddington ratios peaking around 0.3, whereas some of the secondaries show a decrease in activity.

The effect of pericentric passages on the one-AGN pairs is more significant, as was shown in the right panels of Figure 5.4.6. From the plot on the left, we can see that the activation of the primary MBH of the one-AGN pairs steadily increases with each pericentric passage. The secondary MBHs (which are inactive at $z = 3$) start at a similar Eddington ratio as the primary, with an Eddington ratio of ~ 0.1, and maintain this Eddington ratio at the first pericentric passage. However, we see a sharp decrease in the Eddington ratio at the second pericentric passage, when half of the secondaries now have Eddington ratios below ~ 0.03. At the third passage, the gas stripping is more severe, and the majority of the secondary becomes inactive with Eddington ratios below 0.01. This is illustrated earlier in Figure 5.4.4, where we see a very sudden drop of the secondary MBH's surrounding gas density at exactly the second pericentric passage.

The strong gas stripping and the deactivation of the initially bright secondary among one-AGN pairs is a result of many factors. For example, Callegari et al. [2011] and Van

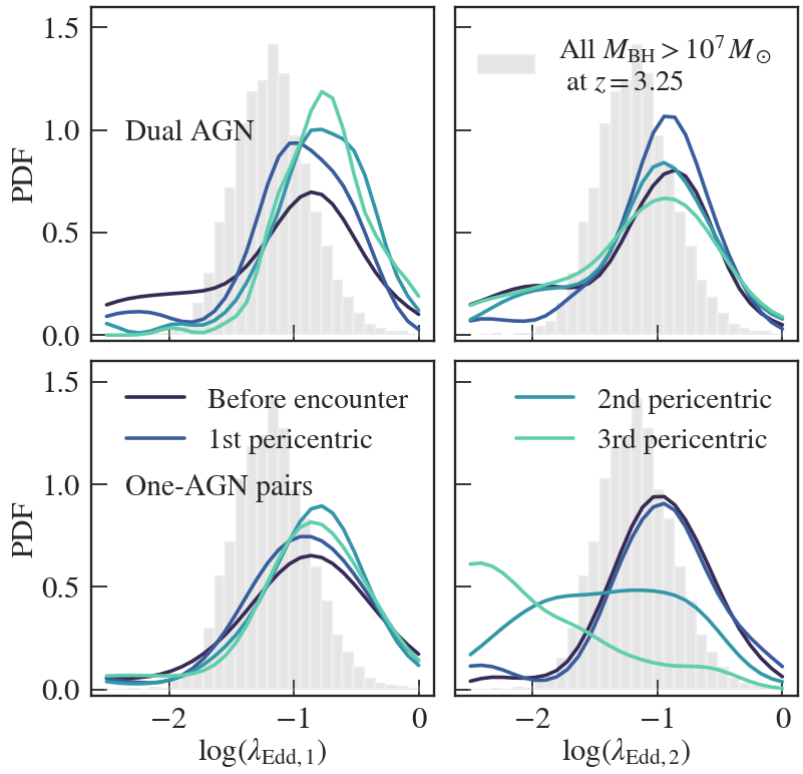

Figure 5.4.6: The distributions of the Eddington ratio of the $z = 3$ same-galaxy duals (***top***) and one-AGN pairs (***bottom***), traced back to before the encounter galaxies, and the first, second and third pericentric passages of the MBHs. The ***left column*** shows the Eddington ratio of the primary AGN, and the ***right column*** shows the Eddington ratio of the secondary AGN. We also plot the Eddington ratio of all MBHs with $M_{\rm BH} > 10^7\,M_\odot$ at $z = 3.25$ (250 Myrs before $z = 3$, *grey*) for reference.

Wassenhove et al. [2012] find that compared to coplanar galaxy mergers, inclined mergers can have less central star formation in the secondary, leading to disruption at $\sim$ kpc separations rather than efficient pairing. Here we investigate one specific factor that could affect the degree of gas stripping: the velocity difference between the two MBHs at their first pericentric passages. In Figure 5.4.7, we show the velocity difference $\Delta v_{\rm first}$ between the two MBHs in duals and one-AGN pairs, at their first passage. Compared with duals, one-AGN pairs have a larger velocity offset at the first encounter. This could also be a consequence of the deep potential associated with the large host halo of one-AGN pairs. The high potential energy is transformed into high kinetic energy during the pericentric passages. Since large ($\Delta v > 150\,$km/s) velocity offsets between AGN pairs are also important for pair detection, one-AGN pairs will more likely satisfy the velocity criterion than duals.

In Figure 5.4.8, we show the evolution of the MBH masses and host galaxy masses for the duals and one-AGN pairs, as well as the MBH and galaxy mass ratio between the host

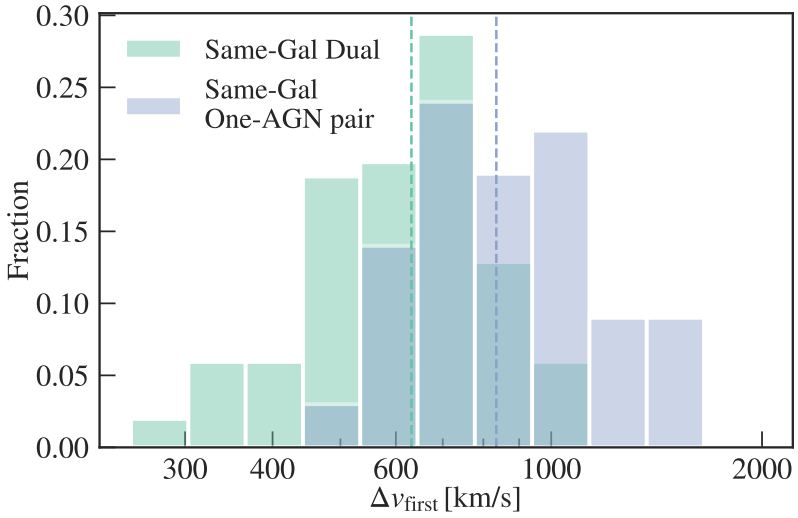

Figure 5.4.7: The distribution of the velocity difference between the two MBHs in the $z = 3$ same-galaxy duals (***green***) and one-AGN pairs (***purple***) at the first pericentric passage. The dashed lines show the median of each distribution. The one-AGN pairs generally have larger velocity offsets compared to duals.

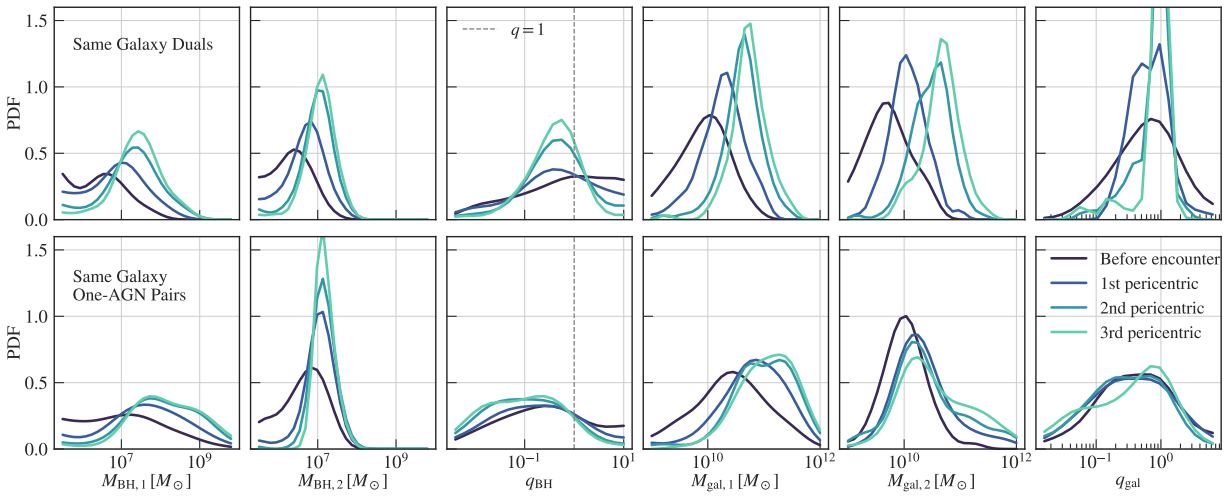

Figure 5.4.8: ***(a/b)***: the mass evolution of the two MBHs in the dual (***top***) and the one-AGN (***bottom***) pairs before the encounter of the host galaxies, and at the first, second and third pericentric passages between the MBH pair. Here BH1 is the more massive MBH at $z = 3$, and BH2 is the less massive MBH at $z = 3$. ***(c)***: mass ratio between the two MBHs in the pair. ***(d/e)***: the stellar mass of the host galaxies for each MBH in the dual and one-AGN pairs. If the galaxies of the two MBHs merged, then we show the mass of the merger remnant. ***(f):*** the evolution of the galaxy mass ratio between the galaxy hosting the secondary MBH and that hosting the primary MBH.

galaxies. Here we denote the more massive MBH at $z = 3$ as the primary (BH1) and its host as gal1, and the less massive MBH at $z = 3$ as the secondary (BH2) and its host as gal2.

Before the encounter of their host galaxies, MBHs in duals have typical BH masses below $10^7\,M_\odot$, and a subset as low as $M_{\rm BH} < 10^6\,M_\odot$. The one-AGN pairs start with typically higher masses than duals, with about 50% of one-AGN pairs with BH masses above $10^7\,M_\odot$ before their host's first encounter. During the interaction of their host galaxies, the primary MBHs, in both the duals and one-AGN pairs, accrete a significant amount of mass, and by the end of the third pericentric passage, the peaks, in the respective BH mass distributions, shift up by an order of magnitude. This is expected from the high Eddington ratio of the primary BH in duals and one-AGN pairs during this period shown in Figure 5.4.6. As for the secondary MBHs in duals, the BH mass growth is less significant, but most secondaries still reach a mass of $10^7\,M_\odot$ by the second passage. However, after this point, the growth stalls, and the masses of the secondaries do not go much beyond $10^7\,M_\odot$. Notably, $\gtrsim 50\%$ of duals have a mass ratio greater than unity before the host galaxy encounter, meaning that the initially less massive MBH among duals ends up accreting more mass during the galaxy merger and becomes the primary at $z = 3$.

We also see similar trends for the respective host galaxy masses of duals and one-AGN pairs. Before the first encounter, the primary MBHs of the duals reside in galaxies with masses between $10^9\,M_\odot$ and $10^{11}\,M_\odot$. The secondary galaxy is generally slightly less massive, with distribution peaked near $5 \times 10^9\,M_\odot$. Notably, none of the dual pairs has a galaxy mass above $10^{11}\,M_\odot$ before the encounter. Now looking at the time evolution of the masses, we see that the primary galaxy mass grows by an order of magnitude during the few hundred Myrs of the orbital passages. The galaxy mass of the secondary grows even faster, and by the time of the third pericentric passage, the majority of the two hosts have already merged and thus share the same galaxy mass.

The evolution of the mass ratio between the two MBHs in the pairs and between their host galaxies is particularly worth noting. Observational studies such as Comerford et al. [2015] found that all dual AGN and dual AGN candidates in their sample share the feature that the MBH in the less luminous galaxy always has the highest Eddington ratio. From the host galaxy mass ratio of our dual AGN sample, we see that although the distribution of the secondary's host galaxies does initially peak at a lower value (consistent with observations), about 30% of the duals have an original galaxy mass ratio above unity. This means that 30% of the more massive MBH in the duals at $z = 3$ starts off residing in the smaller galaxy, which then picks up a lot of its mass during the galaxy merger. Steinborn et al. [2016] also saw a similar trend in their sample of one-AGN pairs. Volonteri et al. [2022] also studies the galaxy mass evolution of the dual AGN hosts before the galaxy merger by looking at the evolution of a sample of dual AGNs at $z = 1$. In their sample, $q_{\rm gal}$ almost always decreases with time before the galaxy mergers, whereas we see a larger mass growth in the galaxy that hosts the secondary AGN. Our result is in agreement with high-resolution hydrodynamical simulations of galaxy mergers, which find that the Eddington rate is higher for the AGN in the less massive of the two merging galaxies [Capelo et al., 2015]. Van Wassenhove et al. [2012] also produced situations where the less massive black hole accretes at a higher

Eddington fraction until the less massive galaxy's gas is lost to ram pressure stripping. The higher mass gain in the less massive galaxies can happen if the less massive galaxies have higher gas fractions, or if the gas accretion is more efficient in less massive galaxies due to their stronger gravitational instabilities during mergers.

5.5 Conclusion

In this work, we characterize the properties and evolution of dual AGN, one-AGN pairs, and offset AGN at $z = 2 \sim 3$ within the `Astrid` simulation, identified with the canonical $L_{\rm bol,12} > 10^{43}\,{\rm erg/s}$, $M_{\rm BH,12} > 10^7\,M_\odot$ and $\Delta r < 30\,{\rm kpc}$ thresholds ($L_{\rm bol,2} < 10^{43}\,{\rm erg/s}$ for one-AGN pairs, and offset AGN are one-AGN pairs residing in separate galaxies). At these redshifts, dual and offset AGN pairs are very rare (with a number density of $\sim 10^{-5}\,{\rm cMpc}^{-3}$), but with the large volume of `Astrid`, we are able to identify a statistically large sample of AGN pairs (1087 duals, 842 one-AGN pairs, and 197 offsets at $z = 2$; 329 duals, 110 one-AGN pairs, and 32 offsets at $z = 3$). Having included an on-the-fly subgrid dynamical friction prescription in `Astrid`, we can trace the MBH orbits down to the resolution limit of $\sim 3\,{\rm ckpc/h}$ ($\sim 1\,{\rm kpc}$ at $z = 2$), and capture tens of dual AGN at (small) kpc separations.

Among the massive ($M_{\rm BH} > 10^7\,M_\odot$) and luminous ($L_{\rm bol} > 10^{43}\,{\rm erg/s}$) AGN at $z = 2$, the dual fraction is 3% with separations below 30 kpc. Another 2.2% (0.5%) of the AGN are involved in one-AGN (offset) pairs, where the secondary is massive but not luminous (with $L_{\rm bol} < 10^{43}\,{\rm erg/s}$). We do not see a strong redshift dependence in the dual fraction from $z = 2$ to $z = 4$, but the fraction drops below 2% above $z = 4$.

Out of the $z = 2$ dual AGN, $\sim 50\%$ are AGN within the same galaxy and separated by $< 5\,{\rm kpc}$. The number of duals increases with decreasing separation, and over half of the same-galaxy duals are found at separations below 2 kpc. For the dual AGN residing in different galaxies, we do not see a strong separation dependence in the number of duals. Among the offset pairs, over 80% are found at separations between $5 - 10\,{\rm kpc}$. Offset pairs are rare at smaller or larger separations because their formation involves both strong gas stripping which becomes most effective at $< 10\,{\rm kpc}$ scales, and large enough separation between the pair such that the two MBHs are not accreting from the same gas reservoir (which would equalize their luminosities).

The luminosities of both AGN in duals increase by up to an order of magnitude with decreasing separation below $\Delta r = 5\,{\rm kpc}$, indicating that observations with high luminosity threshold could bias towards close pairs (if the spatial resolution allows for detection of those pairs). Nonetheless, we find that the gas column density of duals also increases with decreasing separation, which adds complication to the detection of the close pairs. At larger separations, we find indications of an enhancement in the dual luminosities at $\Delta r = 10 - 15\,{\rm kpc}$, similar to the result shown in Stemo et al. [2021]. We then confirm with the time evolution analysis of the duals AGN that there is an enhanced AGN activity among both AGN in the pair following the first pericentric passage, which could lead to this bump.

The details in dynamical interaction during galaxy mergers play a crucial role in explaining the emergence of the dual AGN, one-AGN pair, and offset AGN populations. Compared

with the typical Eddington ratio of ~ 0.025 among the MBHs with $M_{\rm BH} > 10^7\,M_\odot$ in the simulation, both the dual AGN and the active AGN in the offset AGN correspond to BHs with an increased level of activity with Eddington ratios peaking around 0.05. Following each pair through the initial stages of galaxy mergers, we find that the AGN activity of the primary BH in both duals and one-AGN pairs increases with each pericentric encounter of the pair due to the enhanced gas supply brought in by the galaxy merger, whereas the secondaries suffer from various degrees of gas stripping mostly starting from the second pericentric passage and are thus tend to be less active over time. The secondary MBHs of the one-AGN pairs experience the most severe/complete stripping, and typically remain inactive on orbits with $\Delta r > 2\,$kpc for a few hundred Myrs. For the secondaries among duals, the central stellar bulges are not completely disrupted during the galaxy merger. Thus, $> 80\%$ these secondaries can go through more efficient orbital decays towards a simulation merger, usually within 500 Myrs. The host-galaxy disruption among one-AGN pairs also implies that dual/offset candidates selected through distinguishable galaxy bulges[e.g. Stemo et al., 2021] are more likely dual AGN pairs with one of the AGN hidden.

By further investigating the host galaxies of the dual and offset AGN, we find that MBHs involved in duals and offsets are under-massive relative to their hosts, with an $M_{\rm BH}/M_*$ ratio below the median value of the similar-mass MBHs. One possible reason is that the triggering of star formation preludes the phase of high MBH accretion during galaxy mergers [also see e.g. Callegari et al., 2011, Van Wassenhove et al., 2012]. Indeed, we find that the pair-hosting galaxies show an enhanced specific star-formation rate compared with galaxies of similar masses, especially after the merger of the two hosts.

Notably, there is a switch between the primary and the secondary MBH as well as in their host galaxy mass in $\sim 50\%$ of dual AGN during the galaxy merger: the initially less massive MBH embedded in the smaller galaxy ends up becoming the primary AGN shortly after the galaxy merger. This switch mostly takes place after the second pericentric passage between the two BHs/AGN. Our finding is in concordance with higher-resolution galaxy merger simulations [e.g. Capelo et al., 2015] as well as recent observation results [e.g. Comerford et al., 2015]. This may give rise to a significant population of bright off-center AGN in the smaller companion galaxy.

The large separation, different-galaxy dual AGNs are progenitors to both duals and one-AGN pairs at closer separations. Whether a large-separation dual evolves into a close-separation dual or one-AGN pair depends largely on the level of gas and star stripping during the first three pericentric passages. The secondary in one-AGN pairs started with a similar level of activation as the secondary of dual AGN, and are even more massive before the galaxy mergers, but they show a sudden decrease in the AGN activity by the third pericentric passage. One reason for the more severe gas stripping among one-AGN pairs is that they preferentially reside in some of the most massive halos and have the deepest gravitational potential. The velocity difference between the one-AGN pairs at the first pericentric passage is higher compared with the duals. Other factors such as the rotation of the galaxies relative to the orbit, and the angle of the initial galaxy merger also play important roles, but we do not explicitly quantify these effects from our samples.

In this work, we do not explicitly separate the multiple AGN systems from the pairs as in e.g. Volonteri et al. [2022]. Nonetheless, we have checked that the multiple AGN systems make up $< 10\%$ of all pairs and do not have a large impact on the overall statistics. We defer further study of triples and quadruple systems in `Astrid` to upcoming work.

Chapter 6

MAGICS I. The First Few Orbits Encode the Fate of Seed Massive Black Hole Pairs

[1]

[1] McWilliams Center for Cosmology, Department of Physics, Carnegie Mellon University, Pittsburgh, PA 15213
[2] NSF AI Planning Institute for Physics of the Future, Carnegie Mellon University, Pittsburgh, PA 15213, USA
3 Harvard-Smithsonian Center for Astrophysics, 60 Garden Street, Cambridge, MA 02138, USA
4 Department of Physics and Astronomy, University of California Riverside, 900 University Ave, Riverside, CA 92521

Abstract

The elusive massive black hole (MBH) seeds stand to be revealed by the Laser Space Antenna Interferometer through mergers. As an aftermath of galaxy mergers, MBH coalescence is a vastly multi-scale process connected to galaxy formation. We introduce the "Massive black hole Assembly in Galaxies Informed by Cosmological Simulations" (MAGICS) suite, with galaxy/MBH properties and orbits recovered from large-volume cosmological simulation ASTRID. The simulations include subgrid star formation, supernovae feedback, and MBH accretion/feedback. In this first suite, we extract fifteen representative galaxy mergers with seed MBHs to examine their dynamics at an improved mass and spatial resolution (by ~ 2000 and ~ 20) and follow MBH orbits down to $\sim 10\,\mathrm{pc}$. We find that the seed MBH energy loss and orbital decay are largely governed by global torques induced by the galaxy merger process on scales resolvable by cosmological simulations. Specifically, pairs sink quickly if their orbits shrink rapidly below 1 kpc during the first $\sim 200\,\mathrm{Myr}$ of pairing due to effective energy loss in major galaxy mergers, whereas MBHs gaining energy in minor galaxy mergers with close passages are likely to stall. High initial eccentricities ($e_{\mathrm{init}} > 0.5$) and high stellar

densities at kpc scales ($\rho_{\rm star} > 0.05\,M_\odot/{\rm pc}^3$) also lead to most efficient decays. $\sim 50\%$ high-redshift seed MBH pairs experience consecutive galaxy mergers and are more likely to stall at $\sim 1\,$kpc. For a subset of systems, we carry out N-Body re-simulations until binary formation and find that some systems merge at high-z when embedded in sufficient nuclear star clusters.

6.1 Introduction

Observations of local galaxies suggest that a supermassive black hole (SMBH) is harbored in almost all galactic centers [e.g. Kormendy and Ho, 2013, Tremaine et al., 2002]. These SMBHs has already grown to $\gtrsim 10^7\,M_\odot$ and some even to $\gtrsim 10^9\,M_\odot$ at high redshift ($z \sim 6$) through observations of high-redshift quasars [e.g. Bañados et al., 2018, Fan et al., 2001, Wang et al., 2021, Wu et al., 2015]. They are thought to have formed in the high-redshift Universe ($z \sim 20$), but the exact seeding mechanism remains largely unconstrained [e.g. Woods et al., 2019] due to their low masses and faint electromagnetic emissions [e.g. Reines and Comastri, 2016].

Recently, an MBH was found at $z \sim 11$ [Maiolino et al., 2023], and more high-redshift MBHs have been revealed by JWST [e.g. Harikane et al., 2023, Kocevski et al., 2023, Matthee et al., 2023, Übler et al., 2023]. These MBHs are found to be over-massive compared to their host galaxies compared with the low-redshift relation [e.g. Pacucci et al., 2023]. Such over-massive MBHs pose new challenges to the growth of MBHs in early galaxies, especially for MBH seeding by Pop-III stars, or runaway stellar growth in dense star clusters, since they usually need to grow at super-Eddington rates to reach the mass of the observed high-redshift MBHs.

Gravitational waves (GWs) from MBH mergers offer a promising way to observe the first MBH seeds [e.g. Barausse, 2012, Klein et al., 2016, Ricarte and Natarajan, 2018, Sesana et al., 2005], especially when combined with observations of the electromagnetic (EM) counterparts [DeGraf and Sijacki, 2020, Natarajan et al., 2017]. The gravitational waves of MBH mergers with masses in the range $10^4 - 10^7\,M_\odot$ have a frequency around mHz, and they are primary targets for the Laser Interferometer Space Antenna (LISA), which can detect MBHs with such masses out to $z > 20$ [Amaro-Seoane et al., 2017]. Compared to electromagnetic observations, GWs not only allow us to probe MBH seeds at higher redshift, but also provide MBH mass estimations independent of their instantaneous accretion state. However, modeling of MBH mergers depends heavily on the dynamics during the formation and shrinking of black hole (BH) binaries which are poorly constrained from kpc [e.g. Pfister et al., 2019, Tremmel et al., 2017], to pc [e.g. Colpi, 2014] scales. This can lead to a large spread in detection rates for LISA depending on the assumptions made [e.g. Klein et al., 2016, Sesana, 2010]. Therefore, an accurate understanding of the dynamical journey of seed MBHs in the early galaxy assembly is key to robust constraints on the seed MBH population with GW detections.

The dynamics of MBH pairs towards coalescence are first summarized in Begelman et al. [1980]. During galaxy mergers, the central MBHs start at a large separation in the remnant

galaxy (a few tens of kpc). The MBHs then gradually lose their orbital energy and sink to the center of the remnant galaxy due to the dynamical friction exerted by the gas, stars, and dark matter around them [e.g. Chandrasekhar, 1943, Ostriker, 1999]. When their separation is $\lesssim 1$ parsec, an MBH binary forms, and other energy-loss channels begin to dominate, such as scattering with stars [e.g. Berczik et al., 2006, Berentzen et al., 2009, Khan et al., 2011, 2013, Quinlan, 1996, Sesana et al., 2007a, Vasiliev et al., 2015], gas drag from the circumbinary disk [e.g. Haiman et al., 2009, Lai and Muñoz, 2023], and three-body scattering with a third black hole [e.g. Bonetti et al., 2018, Mannerkoski et al., 2021].

Currently, our most accurate understanding of the MBH binary population and its relation with galaxy evolution comes from cosmological simulations [see e.g. Amaro-Seoane et al., 2023, for an overview]. Cosmological simulations self-consistently follow the coevolution of MBHs with host galaxies, and contain rich information about the environments where MBH interactions and mergers take place [e.g. Katz et al., 2020, Kelley et al., 2017c, Salcido et al., 2016, Tremmel et al., 2017, Volonteri et al., 2020, **?**]. These environments include a wide range of scenarios from isolated dwarf galaxies to infalling satellites of a massive central galaxy in a cluster. However, realistic and large-volume modeling comes at the cost of limited resolutions, and at best they can follow MBH dynamics to $\sim$ kpc scales. These simulations are also subject to the simplistic subgrid-seeding mechanism that only considers the higher end of the MBH seed mass [out of these, Dubois et al., 2014, Tremmel et al., 2015, probes relatively low MBH seeds at high-redshifts]. To compensate for the resolution limit in large-volume simulations, cosmological "zoom-in" simulations are also applied to study the sinking behavior of specific merging systems [e.g. Bortolas et al., 2020, Pfister et al., 2019], but they are also subjected to high-computational cost and low flexibilities in configuration and subgrid models. Only a few galaxies and the MBHs can be studied at a time.

To accurately model the MBH orbital evolution on sub-kpc scales, high-resolution, idealized galaxy merger simulations, and direct N-body simulations are often used to investigate the detailed dynamical processes of galaxy/MBH mergers [e.g. Gualandris et al., 2022, Liao et al., 2023b, **?**]. These methods have great flexibility in varying the galaxy properties, orbital configurations, and subgrid models, and allow us to gain a detailed understanding of how different physics mechanisms impact the orbital decay and hardening of the MBH pairs and binaries. Most of the idealized merger simulations, however, do not account for the fully realistic scenario of the orbital properties of the MBH pairing and consecutive galaxy mergers frequent at high redshifts.

Very recently, many emerging works have started to consider the more realistic scenarios of MBH dynamics. This realism is approached in various ways. For example, Mannerkoski et al. [2021] and Koehn et al. [2023] directly recover the initial condition of cosmological mergers with accurate, high-resolution N-body methods and study the dynamics of binary and triple SMBHs across a wide dynamical range. Partmann et al. [2023] considers the scenario of multiple infalling satellites with seed MBH, which is typical for a high-redshift massive galaxy, and studies the many-body interactions with a treatment of gravitational recoils. Liao et al. [2023a,b] used realistic subgrid models of hydrodynamics simulations in combination with small-scale treatment of binary hardening to study the impact of galaxy

types and physics modeling on the merging timescale of SMBH binaries.

To truly bridge the gap between cosmological simulations and small-scale MBH dynamics, we introduce the "Massive Black Hole Assembly in Galaxies Informed by Cosmological Simulations" (MAGICS) suite, which combines the realistic MBH and galaxy population from the state-of-the-art cosmological hydrodynamics simulation `ASTRID` with the idealized galaxy merger simulations. This suite (also referred to as "resimulations" hereafter) directly recovers the high-redshift galaxy merger properties to include both isolated and multiple galaxy mergers, and uses the "full-physics" hydrodynamical subgrid modeling with star formation and various feedback channels. This is the first work to recover not only the collisionless component (e.g. dark matter and stars) in cosmological MBH merger events but also the full hydrodynamics evolution of the merging system. The importance of the latter in gas-rich environments (typical of high-redshift galaxies) has already been pointed out in e.g. Fiacconi et al. [2013], Tamburello et al. [2017], Liao et al. [2023a].

This paper is organized as follows. Section 6.2 introduces the simulation code and the subgrid models used in the simulations. Section 6.3 gives an overview of the high-redshift MBH merger population in `ASTRID`, which is the base population for the high-resolution resimulation suite. We also show the detailed properties of the systems selected for the first suite of high-resolution resimulations in this work. In Section 6.4, we describe how we set up galaxy merger initial conditions to directly mimic the original cosmological system. Finally, in Section 6.5 we present the results for the dynamical friction time scales of seed MBH mergers in various environments, and the correlation with large-scale galaxy and orbital properties. We also investigate the effect of multiple galaxy mergers on the MBH sinking and the inclusion of nuclear star clusters.

6.2 Idealized Galaxy Simulation with MP-Gadget

6.2.1 The subgrid physics model for galaxy formation

The subgrid gas, black hole, and galaxy-formation physics in the resimulations largely follow from the model in the `Astrid`cosmological simulation [Bird et al., 2022, Ni et al., 2022]. We summarize the key components here. In our simulations, gas cools via primordial radiative cooling [Katz et al., 1996] and via metal line cooling, with the gas and stellar metallicities traced following Vogelsberger et al. [2014]. In the context of isolated-galaxy simulation, we do not include the patchy reionization model. The ionizing ultra-violet background from Faucher-Giguère [2020] is employed with gas self-shielding being factored in as outlined in Rahmati et al. [2013]. Star formation is based on a multi-phase model for stellar formation as described in Springel and Hernquist [2003], accounting for the influence of molecular hydrogen [**?**]. Type II supernova wind feedback is incorporated into the simulation in accordance with Okamoto et al. [2010], with wind speeds proportional to the local one-dimensional dark matter velocity dispersion.

MBHs are represented by particles that can accrete gas, merge, and apply feedback to the surrounding gas medium. For this work, we do not seed extra BHs during the resimulation,

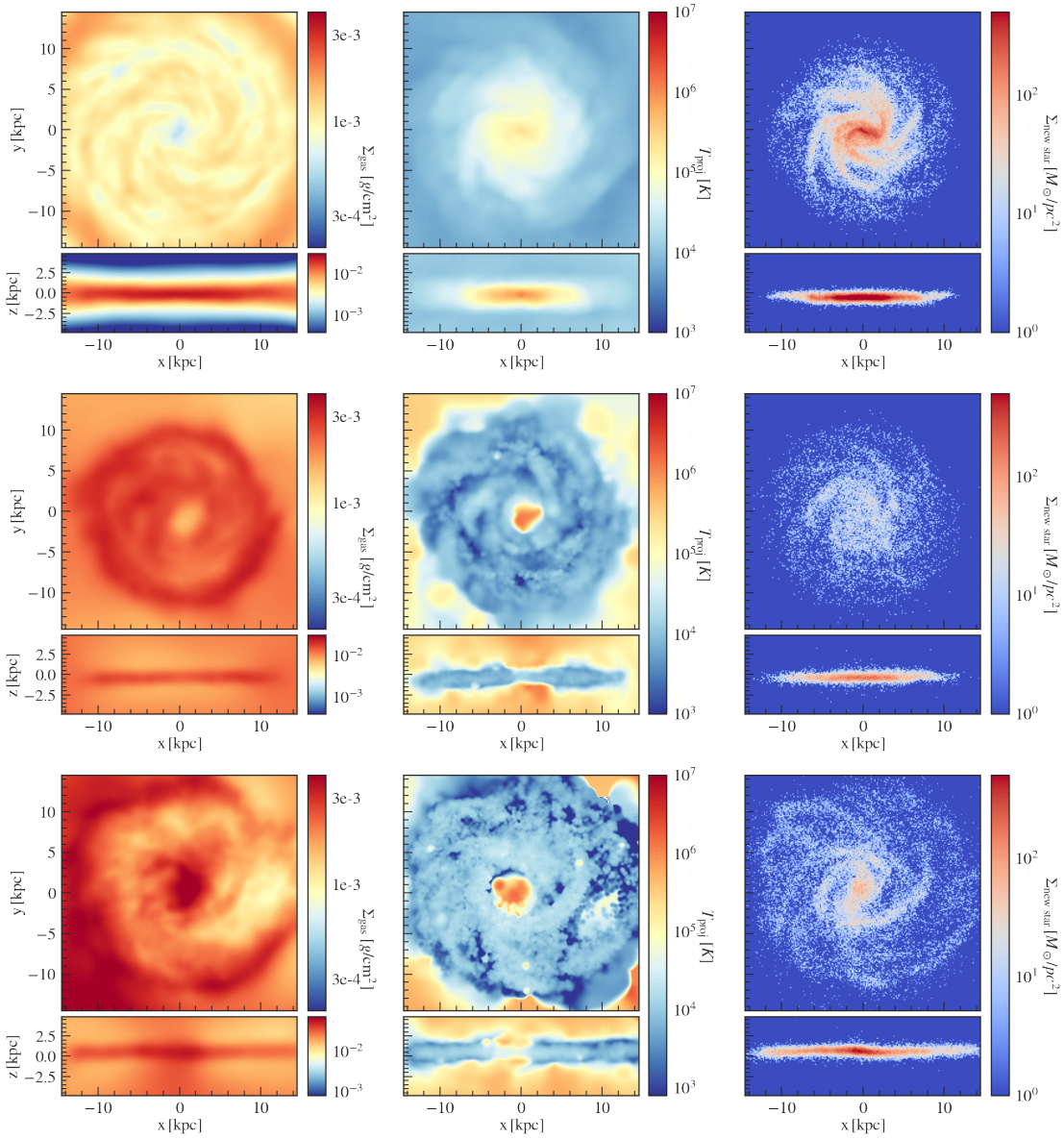

Figure 6.2.1: *Top Row:* Evolution of a disk galaxy with the "SH03" model in `MP-Gadget` after 500 Myrs. 2D projected gas density (*left*), density-weighted temperature (*middle*) and 2D projected density of newly-formed stars (*right*). *Middle Row:* Evolution of the same disk galaxy run with the `ASTRID` subgrid model in `MP-Gadget` after 500 Myrs. *Bottom Row:* evolution of the same disk galaxy as the middle row run with the `ASTRID` subgrid model, but with 50% of the gas put into the gas halo component.

but include them in the initial conditions. Gas accretion onto BHs is modeled with a Bondi-Hoyle-Lyttleton-like prescription [Di Matteo et al., 2005a]:

$$\dot{M}_{\rm B} = \frac{4\pi\alpha G^2 M_{\rm BH}^2 \rho}{(c_s^2 + v_{\rm rel}^2)^{3/2}} \tag{6.1}$$

where c_s and ρ are the local sound speed and density of the gas, $v_{\rm rel}$ is the relative velocity of the BH with respect to the nearby gas, and $\alpha = 100$ is a dimensionless fudge parameter to account for the underestimation of the accretion rate due to the unresolved cold and hot phase of the subgrid interstellar medium in the surrounding. We allow for short periods of super-Eddington accretion in the simulation but limit the accretion rate to two times the Eddington accretion rate. The BH radiates with a bolometric luminosity $L_{\rm bol}$ proportional to the accretion rate $\dot{M}_\bullet$, with a mass-to-energy conversion efficiency $\eta = 0.1$ in an accretion disk according to Shakura and Sunyaev [1973].

$$L_{\rm Bol} = \eta \dot{M}_{\rm BH} c^2 \tag{6.2}$$

5% of the radiated energy is coupled to the surrounding gas as the AGN feedback.

The dynamics of the BHs are modeled with a sub-grid dynamical friction model [Chen et al., 2021, Tremmel et al., 2015] in both `ASTRID` and the resimulations. This model provides an improved treatment for calculating BH trajectories and velocities. Two BHs merge if their separation is within two times the spatial resolution $2\epsilon_{\rm g,BH}$ (this is $\sim 500\,$pc in `ASTRID` at $z = 6$, and 20 pc in the resimulations), once their kinetic energy is dissipated by dynamical friction, and they are gravitationally bound to the local potential. We note that since we numerically merge the MBHs at 20 pc in the resimulations, our modeling ends before the MBH pairs become a bound binary. Therefore we do not attempt to model binary formation and binary hardening process (except in Section 6.5.5). In the `ASTRID` simulation, we use a separate mass tracer $M_{\rm dyn}$ to reduce the noisy gravitational forces (dynamical heating) acting on the small seed mass black holes during the force calculations of BHs (gravity and dynamical friction). When a new BH is seeded, $M_{\rm dyn}$ is set to $M_{\rm dyn,seed} = 10^7 h^{-1} M_\odot$, which is about $1.5 M_{\rm DM}$. $M_{\rm dyn}$ is kept at its seeding value until $M_{\rm BH} > M_{\rm dyn,seed}$. After that, $M_{\rm dyn}$ grows following the BH mass accretion.

Although this approach is a necessary step to alleviate dynamic heating and stabilize the BH motion in the early growth phase, it can also lead to underestimation of the DF timescale and over-predict high-redshift seed MBH mergers. In the high-resolution resimulations, with a stellar particle mass of $2000\,M_\odot$, we alleviate the boost of the dynamical mass of BH particles in the original simulation and use $M_{\rm dyn} = 2 \times 10^5\,M_\odot$. This is ~ 100 times smaller than the values used in `ASTRID` and gives a more faithful estimation of the true merging timescale. In future works, we will further push the resolution limit to directly model the true mass of seed MBHs. This typically requires a mass ratio of > 10 between dark matter and MBH particles with moderate softening and the inclusion of DF subgrid modeling, and ~ 1000 without [Ma et al., 2021, Pfister et al., 2019].

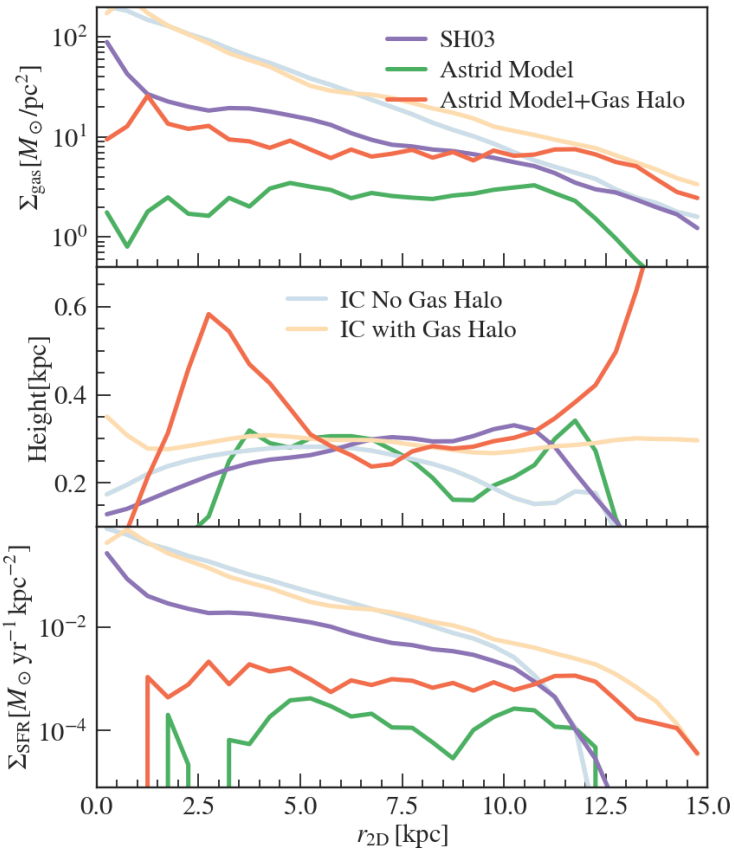

Figure 6.2.2: Comparison between the gas surface density profile (*top panel*), gas disk height (*middle panel*), and star-formation rate (SFR) surface density between the three runs. The lines with light colors show the gas properties in the initial conditions, and the lines with dark colors show the properties after 1 Gyr of evolution. The "SH03" run (purple) and the "Astrid Model" run (green) share the same IC (light blue). The "Astrid Model+Gas Halo" run (orange) has 50% gas in the disk and 50% gas in the halo for the initial condition (light orange).

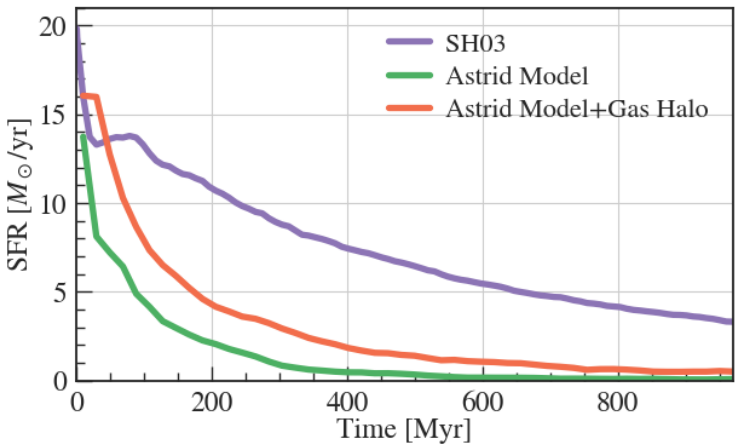

Figure 6.2.3: Evolution of the total star formation rate in the three validation runs. Without wind and AGN feedback, the "SH03" run has the most (up to ~ 4 times higher) star formation throughout the simulation.

6.2.2 Code Validation

Disk Galaxy with Star Formation

We first validate the physical models and implementations in `MP-Gadget` in the context of an isolated disk galaxy. We set up the initial condition (IC) following the Agora code comparison suite [Kim et al., 2014, 2016], using the `MakeDisk` IC generator Springel et al. [2005b], with parameters matching with Table 3 of Kim et al. [2016], except that we use a disk gas fraction of 0.4 to match our high-redshift application. We model the multiphase interstellar medium following the prescription of Springel and Hernquist [2003] that incorporates gas cooling, star formation, and SN thermal feedback. (this run is denoted as "SH03"). In this first validation step, we did not match the full `ASTRID` physical models: we did not include the wind feedback from TypeII supernova and the influence of molecular hydrogen on star-formation; we also did not include BHs in this run, so there is no BH accretion and feedback. We run the simulation for 1 Gyr and observe a stable disk throughout the simulation.

In the top row of Figure 6.2.1, we show the 2D projected density and density-weighted temperature of the gas, along with the projected density of newly formed stars after 500 Myrs of evolution. In this model, the central star formation is high because we do not include feedback mechanisms to mitigate the gas condensation. In Figure 6.2.2, we show the 2D profiles of gas properties in the initial condition and after 1 Gyr of evolution for this run (light blue and purple lines). The gas surface density is computed as the total gas mass in each radial bin divided by the area of the bin. The disk height is the mass-weighted distance to the x-y plane for particles in each radial bin. We note that to compare with runs with feedback and a gas halo, where the disk component is only a fraction of the total particle, we only take the star-forming gas with $|z| < 2\,\mathrm{kpc}$ in the disk height computation. Finally, the star-formation rate (SFR) surface density is the total SFR in each radial bin divided by the area of the bin. The gas density and SFR decrease throughout 1 Gyr due to the gradual depletion of gas, while we can maintain a thin disk throughout the evolution.

Figure 6.2.3 shows the total SFR in the isolated galaxy over 1 Gyr. Since our initial gas fraction in the disk is two times larger than the Agora suite, the SFR is also higher. After 500 Myrs of evolution, 18% of the stars are newly formed out of 26% of disk gas, mostly residing at the center of the galaxy, as can be seen from the top-right panel of Figure 6.2.1.

Disk Galaxy with ASTRID Models

To match the physical models used in the `ASTRID` simulation, as a further validation of the resimulation subgrid modeling we include a BH with an initial mass of $4 \times 10^6\,M_\odot$ and turn on all the `ASTRID` subgrid physics models described in Section 6.2. Compared with the vanilla SH03 modeling shown in the previous section, adding wind and AGN feedback is expected to remove the dense gas at the galaxy center and regulate the star formation in the disk [e.g. Di Matteo et al., 2005b, Okamoto et al., 2010, Weinberger et al., 2017]. We use two different initial conditions for this "Astrid-Model" run: we first keep the same IC as the "SH03" run in the previous section, with only the addition of a central BH. Then, to match more closely

with the high-redshift gas environments where only a small fraction of the total gas in the halo is star-forming and in disk structure ($\sim 10-40\%$, see e.g. Table **??** in Appendix **??**), we use a modified version of `MakeDisk` to put 50% of the total gas into the gaseous halo component, following the method laid out in Su et al. [2019]. We set up the gas halo in thermal equilibrium following a β profile with $\beta = 0.66$ and $R_c/R_s = 0.5$. We adiabatically relax the IC for 250 Myrs until it becomes stable, before turning on other subgrid models.

In Figure 6.2.1 we show comparisons of projected gas properties and newly formed stars in the SH03 run, the "Astrid Model" run with all gas in the disk, and the "Astrid Model" run with a gas halo ("Astrid Model+Gas Halo"). With feedback models turned on, we see a significant drop in central star formation (the right column), and the disk gas can cool to much lower temperatures (middle column). We find that the supernova wind feedback is more efficient at removing gas from the galaxy center and thus lowering the central SFR, compared with AGN feedback. Figure 6.2.2 shows the comparisons between the gas profiles in the three runs, along with their corresponding ICs (note that the "SH03" run and the "Astrid Model" run share the same IC so it is only shown once by the light blue curve). We see that the disk height and a high star-formation rate are maintained throughout the "SH03" run. The "Astrid Model+Gas Halo" run has a flattened star-formation surface density and gas surface density after a Gyr of evolution.

Finally, Figure 6.2.3 shows the total SFR in the isolated galaxies in the three runs during 1 Gyr. The "SH03" run has the most (up to ~ 4 times higher) star formation throughout the simulation. The model with a gaseous halo displays more efficient star formation compared to the no-halo run because more central gas is pushed to further distances by wind feedback in the disk-only model. In the "Astrid Model+Gas Halo" run we observe a continuous inflow of cold gas clumps, which sustains the star formation in the disk for a longer time. These clumps can also impact the dynamics of seed MBHs. We will use the "Astrid Model+Gas Halo" modeling in all of the resimulations in this work.

6.3 High-Redshift MBH Mergers

Previous works have shown that the dynamical friction timescales are long for MBH seeds, but with MBH seeds modeled down to $5 \times 10^4\, M_\odot$, we should still expect order unity mergers per year, dominated by seed-seed mergers [e.g. Tremmel et al., 2017, Volonteri et al., 2020, **?**]. However, the seed-seed merger is also the regime where the current simulation lacks prediction confidence due to the limited particle resolution. In this section, we examine the high-z merger population in the `ASTRID` simulation and select typical cases from the population for comparison with high-resolution resimulation.

6.3.1 $z \sim 6$ merger population in ASTRID

We focus on resimulating the population of $z \sim 6$ merger events in the `ASTRID` simulation, to study the sub-kpc scale sinking and merger timescales of seed MBHs. Here we give a brief overview of this population and their environments. There are 2107 MBH mergers between

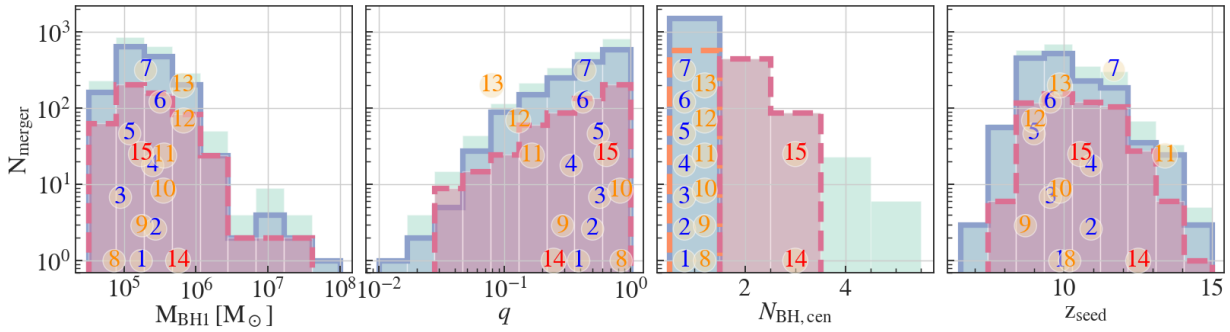

Figure 6.3.1: The $z = 6$ MBH merger population in `Astrid`. From left to right: the mass distribution of the more massive MBH among the pair (**first panel**); the distribution of the mass ratio between the two merging MBHs (**second panel**); the number of MBHs in the central region ($<$ 3kpc from the galaxy center) of the remnant galaxy (**third panel**); the seeding redshift of the more massive BH in the pair (**fourth panel**). The background **green** histogram shows the entire merger population, and we also show two sub-populations: the **blue** histogram is the "isolated" mergers with no third MBH coming into the central region of the host galaxy before $z = 6$, and the **red** histogram shows the "complex" mergers with multiple MBH in the host galaxy center already at $z = 6$. The numbers overlaid on each plot label where the resimulated systems lie within each distribution (only the x-values are meaningful, and the y-values are randomly taken).

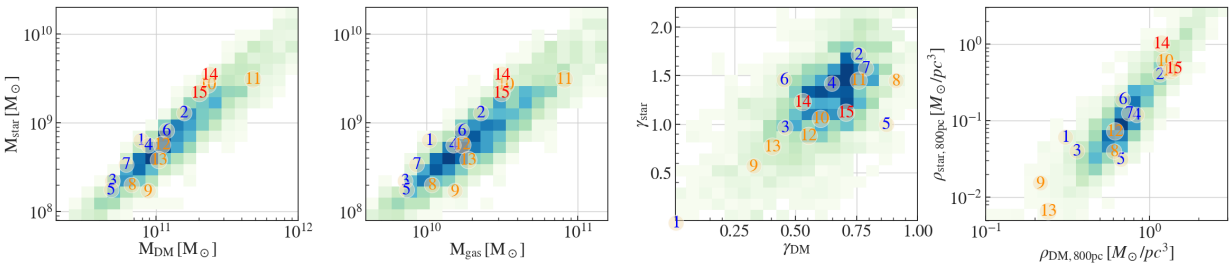

Figure 6.3.2: Host galaxy properties of the $z = 6$ MBH merger remnant in `Astrid`. *First and second panels:* the 2D distribution of the galaxy mass with the dark matter halo and total gas mass in the halo. *Third panel:* power-law index of the dark matter and stellar density profiles measured at the `ASTRID` resolution. *Fourth panel:* dark matter and stellar densities measured at at the `ASTRID` resolution (0.8 kpc from the galaxy center).

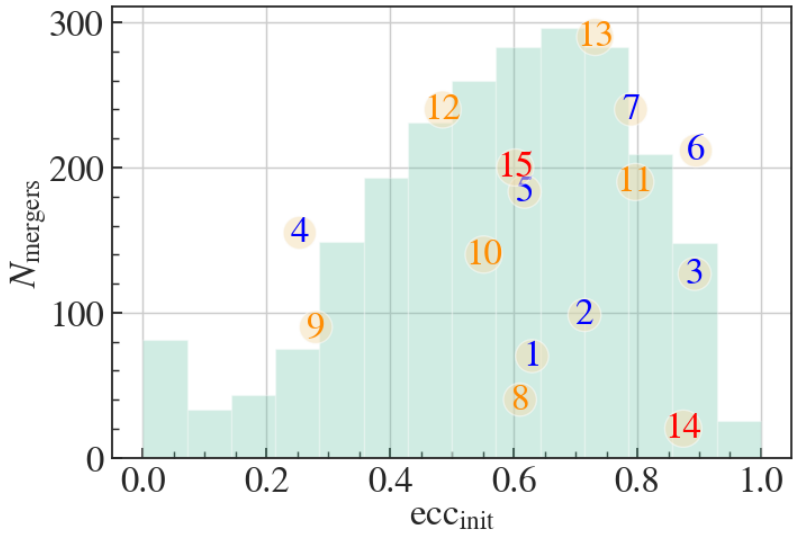

Figure 6.3.3: Initial orbital eccentricities of the merging MBH pair in `ASTRID`, calculated from the first periapsis and the first apoapsis. The overall distribution peaks at ~ 0.7, and the selected resimulation systems (scattered numbers) cover a range of eccentricities from 0.2 to 0.9 (similar to Figure 6.3.1, the y-values are randomly chosen for readability).

$z = 6 - 6.2$ in ASTRID. We collect their host galaxy properties from the $z = 6$ snapshot (i.e. shortly after the merger).

In Figure 6.3.1, we show the MBH properties of all mergers in this redshift bin, including the primary mass, mass ratio, the total number of MBHs in the remnant galaxy, and the seeding redshift of the primary MBH. We subdivide the merger population into three groups, according to the total number of MBHs in the remnant galaxy at $z = 6$ (we take this as a proxy for the complexity of the host environment). The first group is the "isolated mergers" which have no new infalling structures interacting with the merging MBHs at least until $z = 6$ (blue population in Figure 6.3.1). This group consisted of the majority of high-z mergers (1531/2107), with the merger remnant being the only MBH in its host galaxy. Within these "isolated mergers", however, a significant fraction will have new infalling MBHs/galaxies soon after the ASTRID merger at $z = 6$ (i.e. we found new structures on the outskirts of the remnant halo at $z = 6$). Although these new infalls will not impact MBHs that already merged in ASTRID by $z = 6$, they may interfere with the binary formation in the high-resolution resimulations. Hence, we treat these systems separately (shown as the orange bar in the third panel of Figure 6.3.1) when setting up resimulations.

The second group consists of "multiple MBH" systems (the red population), where at $z = 6$, the galaxy remnant has $1 - 2$ other MBHs besides the merging pair. This means that the orbits of the pair go through more complex interactions already before $z = 6$ with other galaxies/MBHs. From Figure 6.3.1, we see that about 25% (542 out of 2107) of $z = 6$ MBH pairs reside in these multiple galaxy interaction environments. This highlights the importance of considering multiple MBH interactions when modeling the dynamics of MBHs even in such high-redshift mergers. Finally, we leave out a group of the most complex (with > 3 MBHs in the remnant galaxy) merger systems for this work. This group makes up a very small fraction of the total merger population (34 out of 2107). In future works, it is still worthwhile to study these systems, as they often reside in the high-density peaks of the Universe and may trace the merger events during the formation of the first quasars.

In Figure 6.3.2, we show the host galaxy/halo information of the $z \sim 6$ mergers. The left two panels show the mass distribution of the dark matter, gas, and stellar components of the merger remnant at $z = 6$. The majority of $z = 6$ mergers are between MBH seeds in dwarf galaxies, with a host halo mass of $10^{10} - 10^{12}\,M_\odot$, and a host galaxy mass of $10^8 - 10^{10}\,M_\odot$. At $z = 6$, the merger host halos are often rich in gas, with the total gas fraction about ten times that of stars. Previous works have shown that in such environments, the clumpy cold gas can result in the ejection of MBHs at kpc scales [e.g. Fiacconi et al., 2013, Tamburello et al., 2017] and result in early wandering MBHs. Therefore, it is important to take gas physics into account when simulating mergers between the MBH seeds.

The right two panels of Figure 6.3.2 show the power-law index of the density profiles and the densities measured at the ASTRID resolution limit [similar to the method used in ?]. Specifically, we assume that below a scale $r_{\rm ext}$ close to the resolution limit $2.8 \times \epsilon_g = 0.85\,{\rm kpc}$, the stellar density profile follows a single power-law $\rho \propto r^{-\gamma}$. To measure the value of γ, we take the measured density from 10 bins just above $r_{\rm ext}$, and fit it to the power-law profile. The gravitational potential of high-redshift galaxies is dominated by the dark matter halo

Table 6.3.1: Properties of the ASTRID galaxy/MBH merger systems selected for high-resolution resimulations (Also see Figures 6.3.1, 6.3.2, 6.3.3). Column 1 is the label of each system used throughout the paper. Columns 2-4 are the two MBH and host properties measured before the galaxy merger (at $z_{\rm init}$). Column 5 is the eccentricity of the first orbit in ASTRID. Column 6 is the redshift when we initialized the resimulations. Columns 7-10 are the host properties of the merger remnant at $z = 6$. The last column is the number of MBHs in the remnant galaxy. The horizontal lines divide mergers in isolation until at least $z = 4$ (systems 1-7), mergers in isolation from $z = 9 - 6$ but with new infalling galaxies soon after $z = 6$ (systems 8-13), and mergers between multiple galaxies and MBHs (systems 14-15).

Name	$M_{\rm BH\,1,2}$ $[10^5\,h^{-1}{\rm M}_\odot]$	$M_{\rm halo\,1,2}$ $[h^{-1}{\rm M}_\odot]$	$M_{\rm gal\,1,2}$ $[h^{-1}{\rm M}_\odot]$	$e_{\rm init}$	$z_{\rm init}$	$\rm M_{halo,rem}$ $[h^{-1}{\rm M}_\odot]$	$M_{\rm gas,rem}$ $[h^{-1}{\rm M}_\odot]$	$M_{\rm gal,rem}$ $[h^{-1}{\rm M}_\odot]$	$\rm SFR_{rem}$ $[M_\odot/{\rm yr}]$	$N_{\rm BHs,rem}$
system1	1.7, 0.7	1e10, 2e10	8e6, 4e7	0.63	9	7e10	1e10	6e8	3.0	1
system2	2.7, 1.4	4e10, 4e10	2e8, 6e7	0.71	7.6	1e11	2e10	1e9	9.1	1
system3	0.9, 0.5	1e10, 9e9	9e6, 1e7	0.90	9	5e10	7e9	2e8	0.86	1
system4	2.5, 0.8	3e10, 7e9	4e7, 2e7	0.26	9	9e10	2e10	5e8	7.8	1
system5	1.2, 0.7	2e10, 5e9	1e7, 1e7	0.60	7.6	5e10	7e9	2e8	1.1	1
system6	3.2, 1.3	2e10, 7e9	1e7, 8e6	0.89	9	1e11	2e10	8e8	6.2	1
system7	2.0, 0.9	2e10, 7e9	2e7, 7e6	0.79	9	6e10	9e9	3e8	1.1	1
system8	0.7, 0.6	2e10, 2e9	2e7, 1e7	0.61	7.6	7e10	1e10	2e8	3.3	1
system9	1.8, 0.5	1e10, 1e10	3e6, 7e6	0.29	7.6	9e10	2e10	2e8	1.6	1
system10	3.5, 3.0	3e10, 3e10	3e7, 3e7	0.55	9	2e11	3e10	2e9	15	1
system11	3.6, 0.6	1e11, 1e10	2e8, 3e7	0.80	7.6	5e11	8e10	3e9	53	1
system12	6.7, 0.9	2e10, 1e10	2e7, 2e7	0.46	7.6	1e11	2e10	5e8	3.2	1
system13	6.5, 0.5	1e10, 3e9	1e7, 1e7	0.74	9	1e11	2e10	4e8	3.5	1
system14	5.6, 1.4	3e10, 6e10	8e7, 2e8	0.88	9	2e11	3e10	4e9	13	3
system15	1.7, 1.1	8e10, 4e9	2e8, 2e7	0.59	9	2e11	3e10	1e9	10	3

Table 6.3.2: Mass and spatial resolutions of the resimulation suite. The maximum separation for two MBHs to merge in the simulation is $2 \times \epsilon_{\rm BH}$.

$M_{\rm DM}$	$M_{\rm gas}$	$M_{\rm star}$	$M_{\rm BH,dyn}$	$\epsilon_{\rm DM}$	$\epsilon_{\rm gas}$	$\epsilon_{\rm star}$	$\epsilon_{\rm BH}$
8000 $M_\odot$	8000 $M_\odot$	2000 $M_\odot$	$2 \times 10^5\, M_\odot$	80 pc	80 pc	20 pc	10 pc

above kpc scales. In most cases, the dark matter density exceeds the stellar density by a factor of ~ 10. However, these galaxies are gas-rich and mergers can also trigger a phase of rapid star formation. Therefore, as we will also show later, the stellar densities are subjected to growth by a factor of ~ 10 over the timescale of a few hundred Myrs, and can dominate over dark matter on sub-kpc scales.

Finally, Figure 6.3.3 shows eccentricities of the first orbit between the MBH pairs during the galaxy merger in `ASTRID`. This is measured from the pericentric and apocentric separation between the MBH pair, and may be different from the Keplerian orbital parameters of the galaxy mergers. The initial eccentricities have a wide distribution, with most ranging between 0.5 and 0.8. We note that about $\sim 20\%$ of the pair has an initial eccentricity below 0.5, and these pairs may experience much longer time (up to ~ 2 times longer than a pair with an initial eccentricity of ~ 0.8) in the dynamical friction phase before the formation of a hard binary [e.g. Gualandris et al., 2022]. It is therefore important to include this population in the study of the seed sinking time.

6.3.2 Resimulation System Selection

As was described in the previous section, we categorize the merger systems according to the host environment complexity and use the number of MBHs in the merger remnants' host halo as a proxy for the complexity. To obtain a good representation of different seed MBH merging environments, we sample merger events from all three categories for high-resolution idealized galaxy merger simulations. We will resimulate a total of 15 `ASTRID` $z \sim 6$ mergers, including 7 in isolated galaxies, 6 in galaxies with new infalls at $z = 6$, and 2 in multiple-galaxy interactions. These systems are all chosen randomly from each population, to cover a statistical representation of all the merger events.

We show the sampled merger events on top of the overall $z \sim 6$ MBH merger population in Figures 6.3.1, 6.3.2, 6.3.3 with the corresponding labels. The colors represent the sub-population that each system belongs to (isolated, isolated with new infall, multiple galaxies). For Figures 6.3.1 and 6.3.3, the y-values are randomly chosen to spread out the data points for better visibility, while the x-values represent the MBH and orbital properties of the systems. All the selected systems are mergers between two seed-mass MBHs with $M_{\rm BH} < 10^6\,M_\odot$. They cover a wide range of galaxy, MBH, and orbital properties with high probability density in the parameter space.

In Table 6.3.1, we list the detailed properties of the resimulation systems before and after the galaxy mergers. For each system with an MBH merger at $z \sim 6$, we trace the host galaxies back to the snapshot before their interactions at $z_{\rm init}$ to initialize the resimulation IC. For the selected systems, this corresponds to either $z = 9$ or $z = 7.6$. During the galaxy merger, the total dark matter mass in the halo grows by a factor of ~ 2 for most systems due to further matter clustering. The galaxy masses grow more significantly because of star formation: the galaxy remnant mass is usually an order of magnitude higher than the sum of the two parent galaxies. We found that the SFR grew most rapidly during the galaxy merger. Finally, all of the host galaxies are gas-dominated, with gas masses much larger

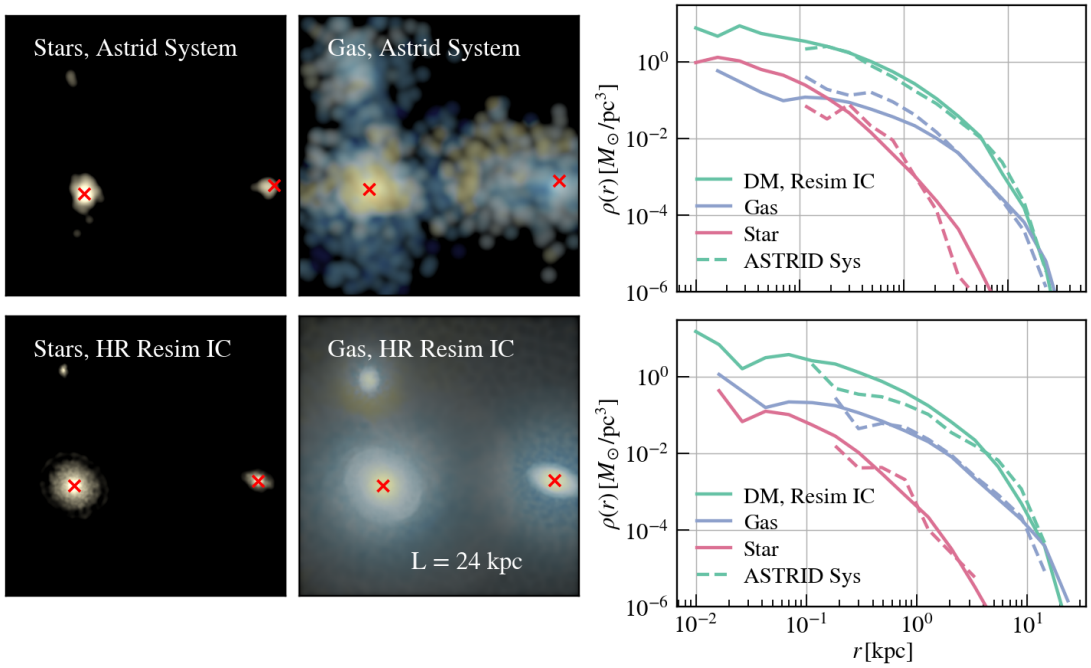

Figure 6.4.1: *Left column:* visualization of stars in the `Astrid` merging galaxies and MBHs (**top**) compared with the IC of the high-resolution resimulation (**bottom**). The background brightness corresponds to the stellar density, with matched color scales between the top and bottom panels. Two merging MBHs are shown as **red crosses** on top of their host galaxies. *Middle column:* Visualization of the gas environment in the `Astrid` system and the resimulation IC. The brightness represents gas density, and the colors represent the temperature (bluer colors are colder gas). *Right column:* density profile comparisons between the `Astrid` galaxies (**dashed lines**) and the resimulation galaxies (**solid lines**). We compare the profiles of all three components (dark matter in **green**, gas in **blue**, and stars in **pink**), and show that the resimulation profiles matched well with the original profiles, but with extrapolations down to > 10 times smaller scales than the original system.

than the stellar masses.

6.4 Resimulation Set-up

6.4.1 Initial Conditions

As was described in Section 6.2, in our idealized simulations, each subhalo consists of a dark matter halo component characterized by an NFW profile, a gaseous halo component with a beta profile, an exponential gaseous disk and stellar disk, and a stellar bulge following a Hernquist profile. To best mimic the original `ASTRID` systems, we initialize each idealized halo/galaxy in the resimulation IC according to the measured properties of the subhalos

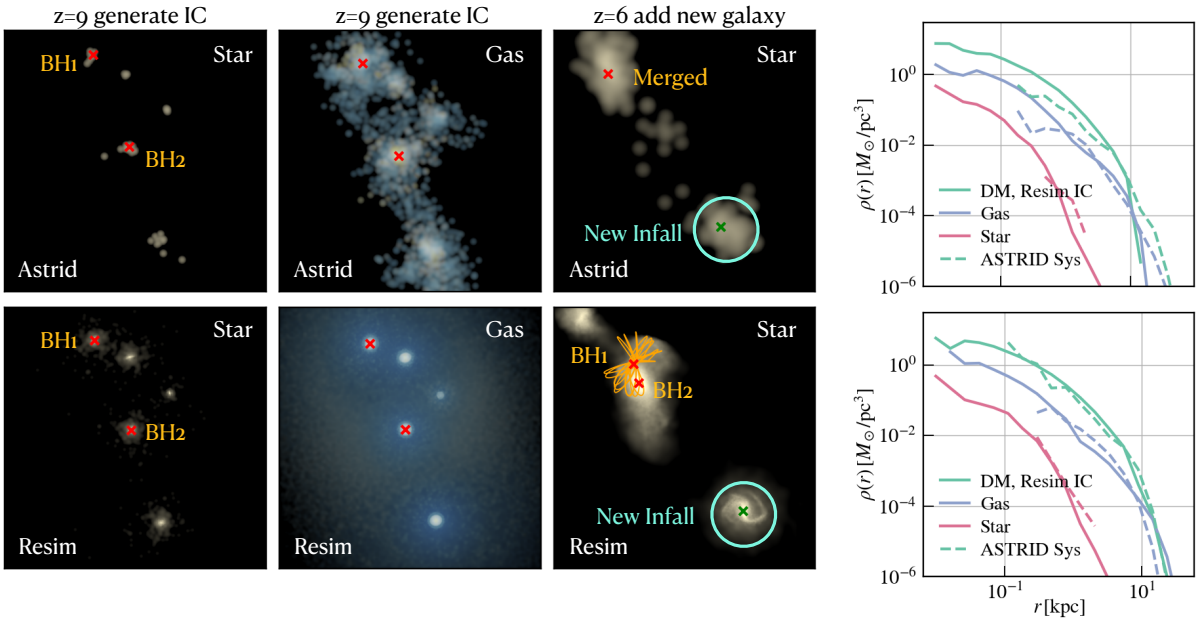

Figure 6.4.2: Similar to Figure 6.4.1, but for a more complex system with multiple galaxies in the IC as well as two new infalling MBHs and galaxies before the MBH pairs merge in the simulation. *Right column*: The density profiles of the two infalling galaxies in `Astrid` and the resimulation.

from a snapshot of the ASTRID simulation. Here we describe how we set the parameters in idealized galaxy ICs.

We initialize an idealized galaxy for each subhalo identified by Subfind in the ASTRID merging systems with stellar mass $> 10^6\,M_\odot$ and dark matter mass $> 10^9\,M_\odot$. We set $M_{\rm vir}$ as the total subhalo mass of the ASTRID subhalo. The dark matter halo is initialized with an NFW density profile, with the inner slope controlled by the concentration parameter c, and with the halo spin initialized to a constant value 0.033. We find that at the current ASTRID resolution and for the dwarf galaxies, we do not have enough information in the central region to provide a good fit for c. Thus we set $c = 4$ to fit with the dark matter density profile at the high-redshift regime of this work [see e.g. Prada et al., 2012] and find that this value fits the profiles well on the Astrid-resolved scales. We note that the sinking time of seed MBHs can be sensitive to the inner DM density profiles [e.g. Tamfal et al., 2018], and can potentially be used to distinguish between different dark matter models. However, this should not affect our major conclusions as we are only sampling from a single cosmology.

In ASTRID, there is no explicit gas disk (especially at high redshifts), and so we set the mass of disk gas according to the fraction of star-forming gas in the ASTRID subhalo. The rest of the gas is put into the gaseous halo component. We assume exponential, rotation-supported disk gas with scale lengths fitted to the original system's density profile, and we fix the scale height at 0.2 times the scale length. The gas temperatures are initialized to pressure equilibrium Springel et al. [2005b]. We also initialize a hydrostatic gas halo according to a beta profile with $R_c/R_s = 0.5$ and $\beta = 0.4$ (we tested that the dynamics of MBHs are not very sensitive to this choice, and defer the detailed study of its effect to future works).

The stellar disk and bulge fraction are decomposed following the kinematic decomposition algorithm in [e.g. Abadi et al., 2003, Scannapieco et al., 2009]. The stellar disk follows the same profile as the gas disk, and the stellar bulge follows the Herquist profile with scale length set according to the half-mass radius of the ASTRID galaxy: $a = r_{\rm half}/(1+\sqrt{2})$ [Hernquist, 1990]. We relax the initial conditions for each galaxy adiabatically and in isolation for 200 Myrs, before assembling the merging system and putting in the MBHs. After relaxation, we assemble all galaxies in the system according to their relative positions, velocities, and the direction of the rotation vectors originally found in ASTRID. We also add MBH particles according to their positions, velocities, and masses in ASTRID.

Figure 6.4.1 shows the comparisons between the ASTRID merging system and the resimulation initial conditions generated as described above. In the left and middle columns, we show visualizations of the host galaxies and gas environments, with matched color scales between Astrid and the resimulation (brightness corresponds to the density, and gas is color-coded by temperature with blue corresponding to cold gas). The resimulation IC resembles the morphologies, stellar densities, and gas temperature of the original system, but shows significant improvement in mass and spatial resolution. The improvement in resolution can be seen more clearly from the left column, where we show the density profiles of the original halos and the resimulation halos (measured after the adiabatic relaxation, just before we start the resimulations). The detailed properties of all components in each recovered galaxy are shown in Appendix **??**.

6.4.2 Other In-falling Galaxies/BHs During the MBH Pairing

When we resimulate the cosmological merging MBHs at a much higher resolution, the resolved DF timescale between galaxy mergers and MBH mergers may lengthen, both because we do not boost the dynamical mass of the BH particles and because we use a stricter merging criterion with smaller softening lengths. One result of the longer DF timescale is the infall of other galaxies and BHs to the merging system that may either intervene or accelerate the orbital decay of the original pair. To fully mimic the cosmological system, we need to take these newcomers into account, as they can both interfere with the original mergers and alter the properties of the remnant host galaxies.

To treat this scenario, we put new galaxies into the resimulated system at the time (t_1) when we see another galaxy with a BH coming within two times the virial radius of the original system. Similar to how we set up the original system's initial condition, we first initialize the new galaxies based on the properties of their cosmological counterpart at t_1. Then we compute the position ($\Delta\mathbf{x}(t_1)$) and orientation ($\Delta\theta(t_1)$) of the new galaxy relative to the original galaxy. To keep the total momentum of the new system at zero, we compute the velocities of both the original galaxy ($\Delta\mathbf{v}_{\rm old}(t_1)$) and the new galaxy ($\Delta\mathbf{v}_{\rm new}(t_1)$) with respect to the COM of the combined system. Finally we add the new galaxy at ($\Delta\mathbf{x}(t_1)$, $\Delta\mathbf{v}_{\rm new}(t_1)$, $\Delta\theta(t_1)$) to the resimulation, and modify the total velocity of the original galaxy to be $\Delta\mathbf{v}_{\rm old}(t_1)$.

Figure 6.4.2 shows an example system where we add new infalling galaxies and BHs during the resimulation, based on the information from the `ASTRID` system. This system originally consists of a merger between five dwarf galaxies with two seed MBHs. After we evolve the resimulation for $\sim 300\,$Myrs down to $z = 6$, we observe a new infalling galaxy that is about to merge with the original system in `ASTRID` (the green cross and the galaxy associated with it in the top row, third column of Figure 6.4.2). We initialize this galaxy following the procedures described above and add it into the resimulation (bottom row, third column), so that it will start to interact with the original MBH pair. The right columns show the density profiles of the new galaxies in the simulation compared with `ASTRID`, and again we can see that we match the `ASTRID` galaxy/halo profiles well on the $>$ kpc scale, while achieving more than ten times better spatial resolution.

We note that during the resimulation, the mass of the original system does not grow, and hence the new galaxies may fall into different potentials in the cosmological simulation and the resimulation. In general, we verify that the total mass of the original system does not grow by more than a factor of three before the injection of new galaxies. We defer more detailed investigations of this effect and careful treatments of the mass growth to future works.

6.5 Results

Using the method described in Section 6.4, we set up a total of 15 galaxies and MBH merger initial conditions for the chosen `ASTRID` merging systems shown in Section 6.3, and with the

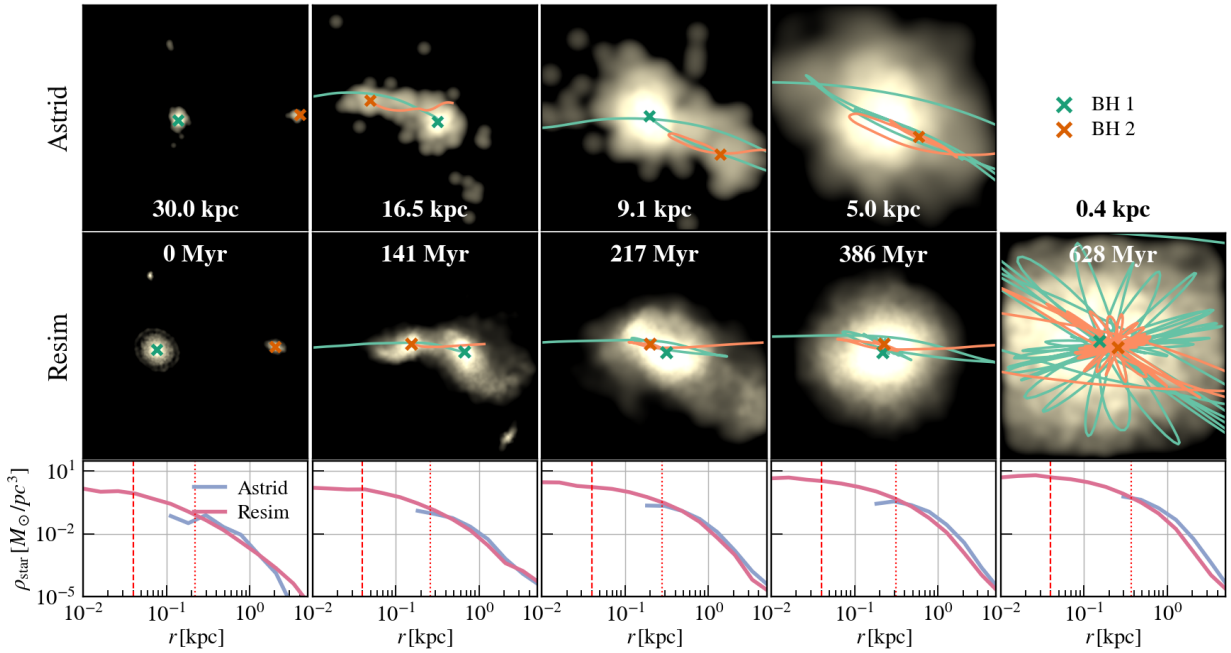

Figure 6.4.3: *Top row:* trajectories of the MBH pair (crosses) plotted on top of the merging host galaxies in `ASTRID system3`. The simulation merger happens between the third and fourth frames. *Middle row:* evolution of the same system in the high-resolution resimulation. The large-scale galaxy merger and MBH orbital properties are paralleled, but the orbits are resolved down to $\sim 20\,$pc scales, close to the binary hardening (last frame). *Bottom row:* comparison between the stellar density profiles of the primary galaxy (first two frames) and the remnant galaxy (last three frames) in `ASTRID` (**purple**) and the resimulation (**pink**). The density profiles in the resimulation match well with the `ASTRID` system, with an extrapolation to >10 times smaller scales.

"full-physics" subgrid physics models depicted in Section 6.2. In this section, we show the results from these high-resolution resimulations.

.

6.5.1 Evolution of the host galaxies

Although the initial conditions for the resimulations are set to match the ASTRID system as closely as possible, it is not guaranteed that their subsequent evolution will be similar. As a first test, we want to make sure that the general properties of the galaxies and MBH orbits in the resimulations still mimic the evolution in ASTRID to at least the ASTRID MBH merger time. Only in this case can we draw further comparisons and connections between the cosmological simulation and idealized galaxy merger simulations.

In Figure 6.4.3, we show a parallel comparison between the galaxy merger and BH orbits in ASTRID and in the resimulation system for an isolated galaxy merger (system1). On large scales, we find a good match between the progress of the galaxy merger and MBH orbits between the two systems (also shown later in Figure 6.5.3). The ASTRID system merged in the fourth frame, while in the resimulation we further evolve the orbits down to $\sim 20\,\mathrm{pc}$, and the sinking timescale is much longer (fifth frame). The bottom panels show the evolution of the stellar density profiles in both systems. The overall density profile evolution of the resimulation system matches well with the ASTRID system over $\sim 1\,\mathrm{Gyr}$, because we also try to match the gas properties in the resimulation initial conditions. More importantly, we note that the central density grows by a factor of ~ 10 during the orbital decay time of the MBH pair. The growth in central stellar density can significantly impact the dynamics of the BHs on sub-kpc scales.

Figure 6.5.1 shows the galaxy merger comparison for a more complex system with multiple galaxies merging (system15). In this case, the ASTRID system goes through two consecutive MBH mergers within $\sim 350\,\mathrm{Myrs}$(between BH1 with BH2, then with BH4). In the resimulation system, the MBHs have a difficult time merging: BH3 and BH4 (and their host galaxies) will start to interfere with the orbits of BH1 and BH2 before they can merge. As a result, BH2 is disrupted to a wider orbit (column 4) where the dynamical friction becomes inefficient.

We summarize the evolution in central stellar density across all resimulated systems in Figure 6.5.2, from the start of the resimulation ($\sim 300\,\mathrm{Myrs}$ before the ASTRID merger) to the resimulation merger time. The thick colored lines show the systems that merged in the resimulation, while the thin grey lines show the systems that stall at $\sim kpc$ scales for more than $1.5\,\mathrm{Gyr}$. For almost all systems the stellar densities increase by an order of magnitude during the MBH sinking. After the ASTRID merger, the stellar density still increases by a factor of $2 \sim 3$. This direct comparison implies that one should account for the newly formed stars when using post-processed analytical models to compute the binary hardening time for mergers in cosmological simulations, and the resulting hardening efficiency may increase. We also note that for the system with the steepest increase in central stellar density (system11, shown in light brown), the MBH sinks even more efficiently in the resimulation system and

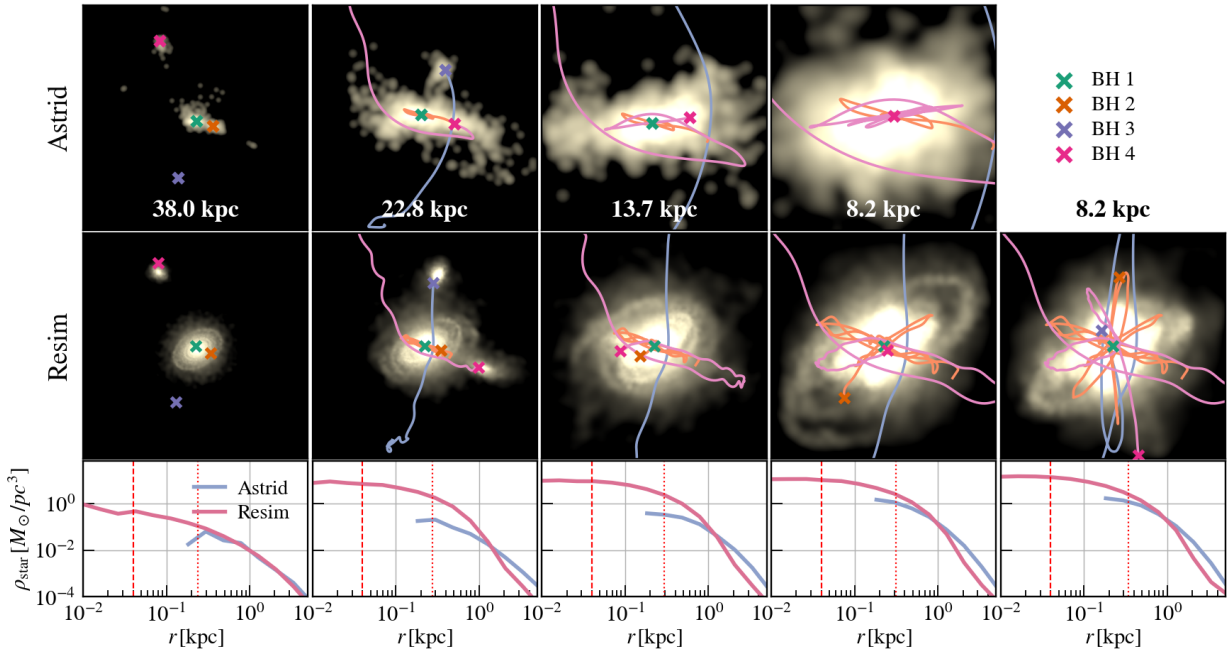

Figure 6.5.1: Similar to Figure 6.4.3 but for a system with multiple galaxy mergers (`system15`). The MBH orbits are more stochastic for this system, and the orbit of BH2 (orange) widens with the infall of BH3/BH4 and their host galaxies.

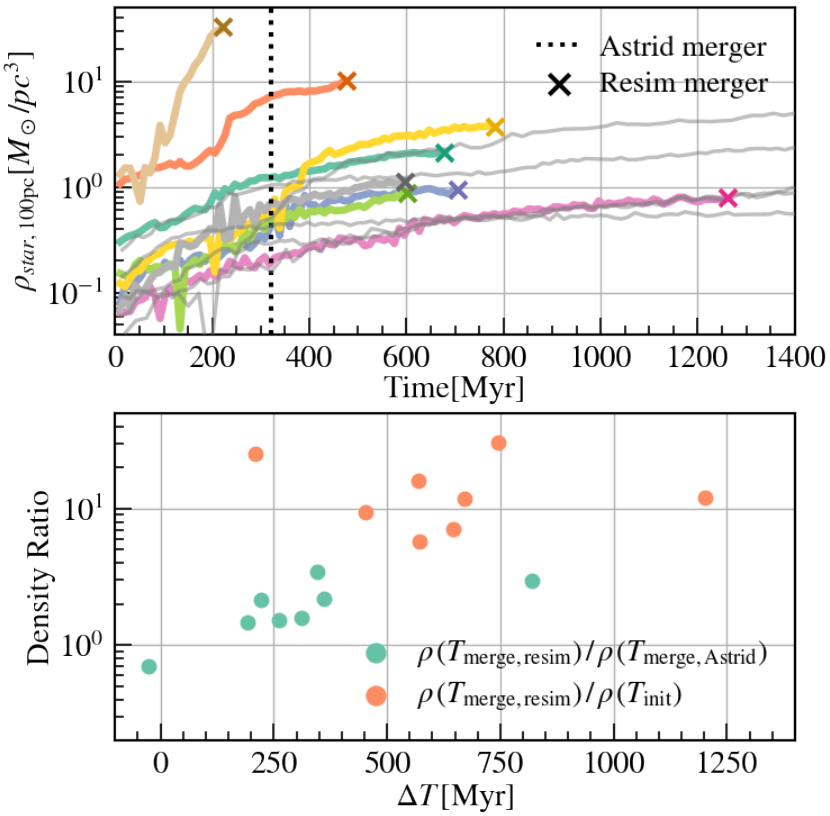

Figure 6.5.2: *Top panel:* Evolution of the central stellar density (measured at 100 pc from the most massive galaxy center) during the MBH inspiral and merger in the simulations.The colored lines show the density evolution until the resimulation merger time (**crosses**) for systems that merged in the resimulations. The **thin grey lines** are systems that stall in the resimulations. The vertical dotted line marks the `ASTRID` merger time. *Bottom panel:* the ratio between stellar density measured at the resimulation merger and the initial condition (**green**), and between the resimulation merger and the `ASTRID` merger (**orange**).

merges before the `ASTRID` merger takes place.

The recent work by Liao et al. [2023a] has shown that the increase in central stellar density and the development of a nuclear stellar core can significantly increase the binary hardening efficiency in SMBHs. Our result again highlights the effect of central star formation on MBH sinking timescales, in the context of high-redshift seed-mass MBH mergers. In the resimulation runs, we include the “full-physics" modeling of both star formation and AGN feedbacks (thermal and kinetic), and thus the stellar density profile flattens (similar to the “CoolStarKinAGN" modeling in Liao et al. [2023a]). Nonetheless, we still find very high star formation rates (up to $50\,M_\odot$/yr) and the development of stellar nuclei when the merging galaxies are compact enough (e.g. `system11`), and the MBH seeds can sink very efficiently in these cases.

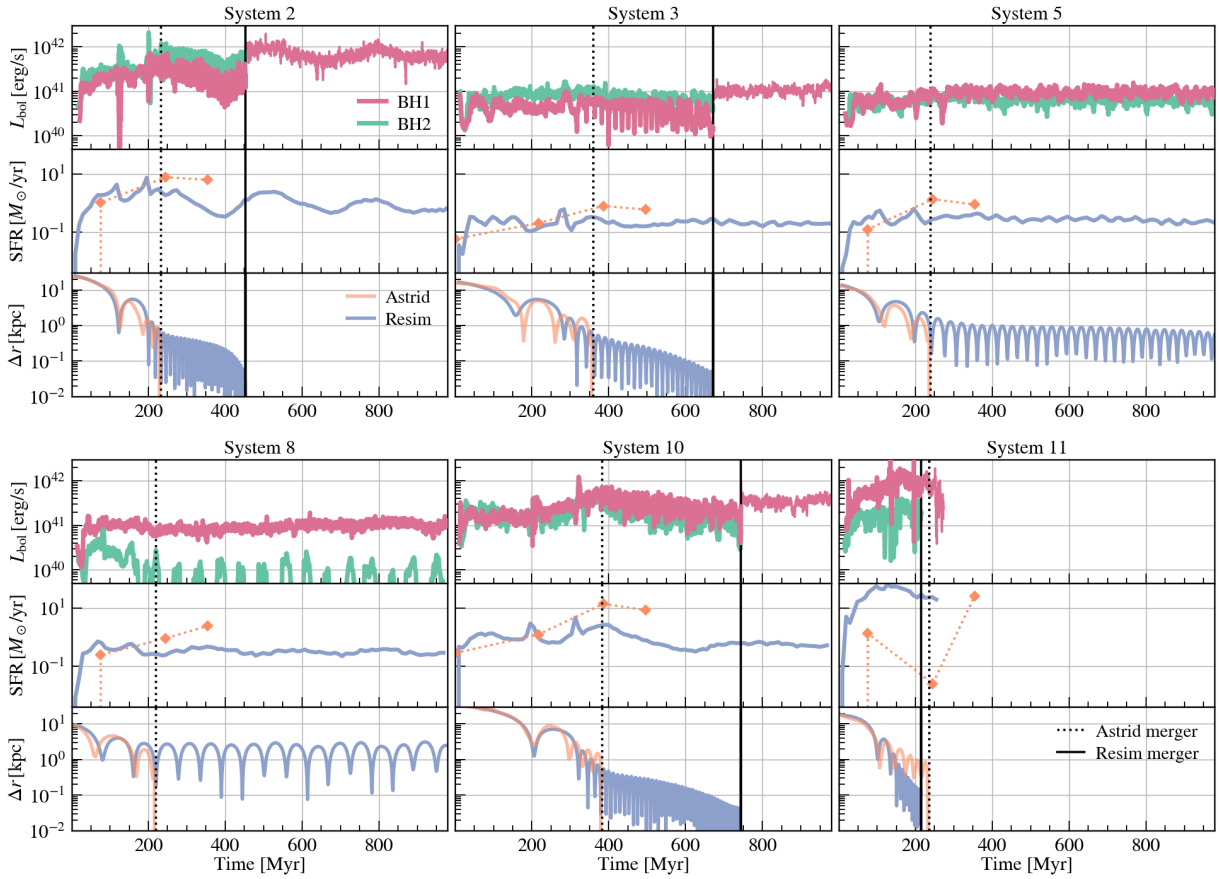

Figure 6.5.3: Evolution of the AGN luminosities (top row in each panel), star formation rate (middle row in each panel), and MBH pair separation (bottom row in each panel) in the resimulation. For the SFR and orbital separation we also compare the resimulation (**purple**) with the original `ASTRID` systems (**orange**). We show six systems representative of the orbital properties of the fifteen resimulations. `system2`, `system3`, `system10`, and `system11` go through efficient orbital decay, while `system5`, `system8` stall at the kpc scale. The SFRs in the resimulations resemble those of the `ASTRID` system well during and after the `ASTRID` merger. The initial few orbits also show a good resemblance to the `ASTRID` orbits.

6.5.2 Seed MBH merging timescale

In `ASTRID`, MBH orbits are resolved down to scales of ~ 1 kpc, and so MBH pairs are assumed to "merge" after that. However, in high-redshift dwarf galaxies, it is typical for seed MBHs to stall on kpc scale orbits for over a few Gyrs [e.g. Ma et al., 2021, Partmann et al., 2023, Pfister et al., 2019]. In this section, we study the merging timescales and the stalling of MBH seeds of the systems in the resimulation, and the correlation with large-scale orbital and galaxy properties.

Figure 6.5.3 shows the AGN luminosities, star-formation rate, and MBH pair separation

of six resimulation systems. These systems are chosen to cover the range of galaxy and the orbit properties across the 15 resimulated systems. Out of the six systems, four go through relatively fast orbital decay and merge within the resimulation after $< 800\,\mathrm{Myrs}$, while two systems show stalling at kpc separations for over a Gyr. Notably, the initial few orbits of the resimulation agree well with the `ASTRID` pair, even though we alleviate the boost in dynamical mass on the seeds (as we will show later, this is because the first few orbits are governed by the gravitational potential). This agreement indicates that cosmological simulations with well-calibrated dynamical friction treatment faithfully model the initial orbital properties of the MBH pairing. Such orbital properties can provide useful initial conditions for subsequent orbital evolution or analytical modeling of the MBH merging timescales [Gualandris et al., 2022].

The middle panels in Figure 6.5.3 compare the resimulation SFR with that of the corresponding `ASTRID` systems. We find general agreement between the two before and after the `ASTRID` merger. In almost all systems, we find an increase in AGN activity and star formation rate associated with the first few pericentric passages. In particular, fast orbital decays are associated with stronger AGN activities (`system2`, `system10`, `system11`). This comes as no surprise since these systems are also on the high-mass, high-density end of the galaxy population (see e.g. Figure 6.3.2).

We note that in the resimulation we still do not resolve the full dynamical range until the MBH coalescence, and so the MBHs "merge" when their orbital separation is $\sim 20\,\mathrm{pc}$. To validate that the MBHs' motion is not affected by numerical noise above the merging distance, we measure the wandering radius of the merger remnant following Bortolas et al. [2016], by averaging the mean displacement of the merger remnant from the galaxy center over time. We find that for all systems that merged, the remnant MBH has a mean displacement of $\sim 20\,\mathrm{pc}$. By numerically merging the MBH at this separation, we pick out systems that will likely form a bound binary, since the stalling in the dynamical friction regime is seen at $\sim$ kpc scales [e.g. Gualandris et al., 2022, Koehn et al., 2023, Partmann et al., 2023]. Further stalling may happen at $\sim pc$ scales due to the depletion of the loss cone, but here we only focus on the pair evolution in the dynamical friction regime and defer the smaller scale dynamics to future works.

The left panel of Figure 6.5.4 summarizes the correlation between galaxy properties and seed MBH merging timescales in all resimulation systems. Each system is labeled with the corresponding number in the plot. Out of 13 resimulated systems in isolation, 8 MBH pairs will merge within 1.5 Gyrs (i.e. before $z \sim 3$). We find a strong correlation between the merging timescales and the central stellar density, both at the `ASTRID` merging time and the resimulation merging time. We note that in our simulations, we do not hold any other galaxy or MBH properties constant while varying the stellar densities. Therefore, this correlation is a result of marginalizing over other parameters in the merger [see also e.g. Tremmel et al., 2018a]. In this plot, we leave out the two systems with multiple MBHs (`system14` and `system15`), as the MBH dynamics are more complex in those cases and a simple scaling with stellar density may not apply. We will discuss these systems in a later section.

Besides the stellar density, it is known that the orbital eccentricity also has a large im-

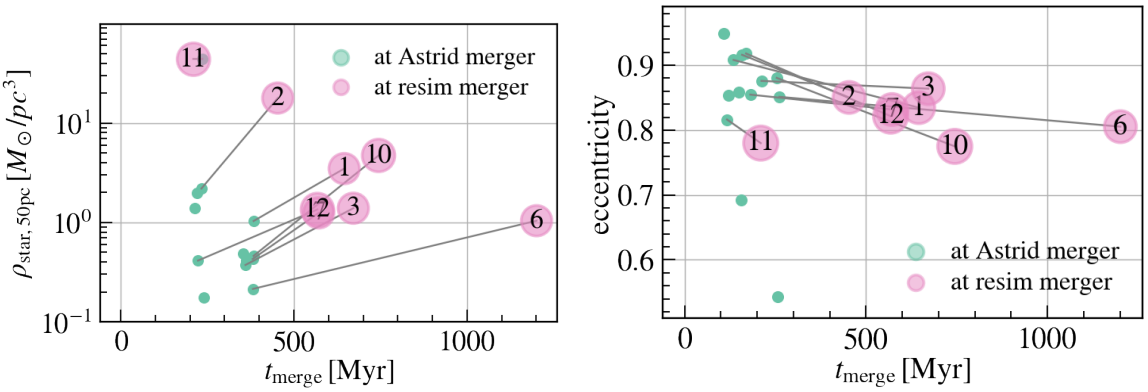

Figure 6.5.4: *Left panel:* relation between MBH merging timescale and stellar density at 50 pc from the galaxy center. We measure density both at the `ASTRID` merger time (**green**) and at the resimulation merger time (**pink**). We see a tight correlation between the merging timescale and stellar densities. We plot densities in systems that do not merge within 1.5 Gyrs in the resimulation on the right of the box. *Right panel:* initial (**green**) and final (**pink**) orbital eccentricity of MBH pairs in the resimulation and the correlation with the merging timescale. The eccentricity clusters around 0.8 when the pair starts entering into the hardening phase.

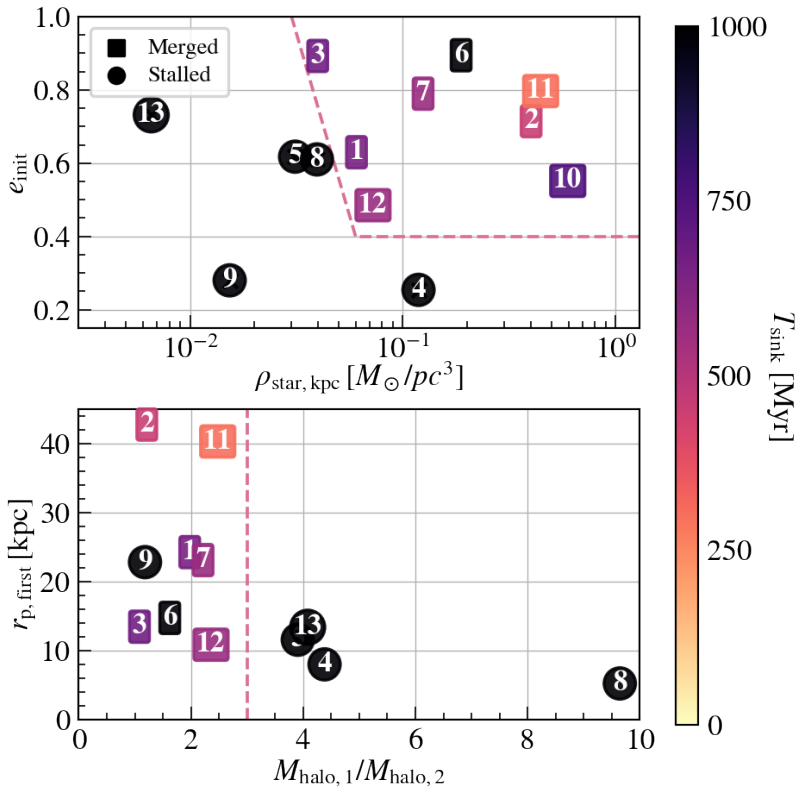

Figure 6.5.5: Sinking time of MBH seed pairs for the thirteen mergers simulated in isolation. *Top panel*: sinking time on the plane of stellar density and initial eccentricity of the MBH pair in `ASTRID`. *Bottom panel*: sinking time on the plane of halo mass ratio and pericentric radius between the galaxies (computed based on relative velocities and positions). In eight systems (**squares**) the MBH merges in the resimulation in $\sim 1.2 Gyr$ (i.e. by $z \sim 3.5$). The colors indicate the sinking time of each system that merged. Five pairs do not merge in the simulation (**black circles**). The merged systems are mostly characterized by high stellar density, high orbital eccentricity, and major halo mergers.

pact on the MBH merging timescales, both in the dynamical friction regime [e.g. Gualandris et al., 2022, Taffoni et al., 2003] and in the loss-cone scattering regime [e.g. Sesana, 2010]. In the right panel of Figure 6.5.4, we show the eccentricity evolution between the `ASTRID` MBH merger time and the resimulation merger time. For the systems that merged efficiently, the orbital eccentricity from at `ASTRID` merger falls above 0.8, and we find slight circularization during the subsequent dynamical friction phase. At the resimulation merger time, the eccentricities of the MBHs all fall close to a value of ~ 0.8. The two systems with $e < 0.8$ at the `ASTRID` merger time do not merge in the resimulation within 1.5 Gyr (`system4` and `system9`). These results imply that the high-redshift seed mergers more likely come from MBH pairs with high initial orbital eccentricities, and would retain these high e values by the end of the dynamical friction phase.

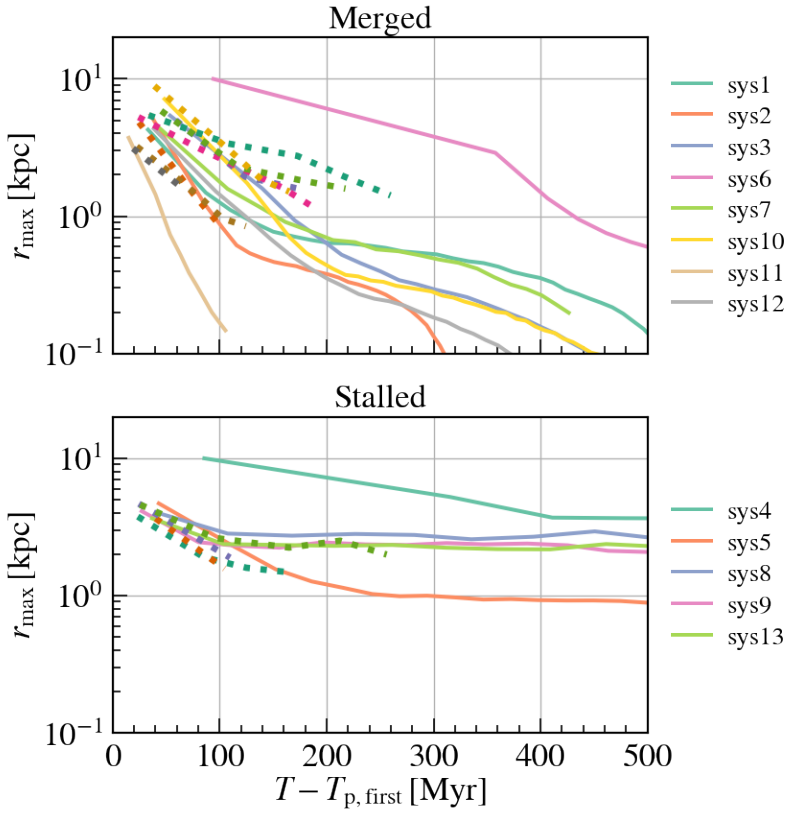

Figure 6.5.6: Evolution of apocentric distances of the secondary MBH $r_{\rm max}$ since the first pericentric passage in systems that merged in the simulation (*top*) and systems that stalled (*bottom*). We show the comparison between the distances in the original `ASTRID` systems (**dotted lines**) and the resimulated systems (**solid lines**).

6.5.3 MBH mergers and large-scale properties

One main motivation for using cosmological simulations to set up resimulations of galaxy and MBH mergers is to understand whether we can use the information from cosmological simulations to predict the dynamics of MBHs at sub-resolution scales. In this section, we connect each resimulation and the MBH merging time back to properties of the ASTRID-resolved quantities and investigate what would be a good indicator for the sub-resolution dynamical behavior of MBH seeds.

Figure 6.5.5 shows the quantities from the `ASTRID` system that we found most correlated with the orbital decay timescale in the resimulation. From the top panel, we see that systems that merge in the resimulation are characterized by high initial eccentricity between the MBH pair ($\gtrsim 0.4$), and high stellar density at $\sim$ kpc scales ($\gtrsim 5 \times 10^{-2}\, M_\odot/pc^3$). The bottom panel shows the relation between the sinking timescale and the properties of the host halo mergers. $r_{\rm first}$ is the pericentric radius of the initial galaxy merger, computed from the halo masses, initial relative positions and velocities of the two galaxies. We note that in some

cases there are more than two halos involved in the merger, and so the orbits cannot be exactly characterized by a Keplerian orbit. The stalled seeds are mostly found in minor halo mergers with small pericentric radii. In these mergers, the host halo and galaxy of the secondary MBH are most quickly disrupted, leaving the MBH completely bare from the very early stages.

We further investigate if the resolved first orbits in ASTRID show an indication of the subsequent orbital properties. In Figure 6.5.6, we plot the evolution of the apocentric radius $r_{\rm max}$ in all resimulated systems, since the first pericentric passage between the two galaxies. We separate the systems by whether the MBH pair merged or stalled in the resimulation. A comparison between the top and bottom panels shows that the merged systems typically started with lower orbital energies at the beginning of MBH pairing, and sink to $r_{\rm max} < 1\,{\rm kpc}$ within $\sim 200\,{\rm Myr}$ of the first pericentric passage. For systems that stalled in the resimulation, none of the MBH sink to $r_{\rm max} < 1\,{\rm kpc}$ within the first $\sim 300\,{\rm Myr}$. If the MBHs' initial orbital sizes are larger, they would experience less efficient dynamical-friction-driven decay due to the lower local densities, and as a result will stall on $r_{\rm max} \sim 1\,{\rm kpc}$ for longer than a Gyr.

Motivated by the study in Bortolas et al. [2020], we calculate the torque onto the MBHs at different times of the pairing, and from large-scale gravitational force to the local dynamical friction force. In Figure 6.5.7, we show the magnitude of the total gravitational torque on the sinking MBHs from all resimulations compared with the dynamical friction torque. The torque is calculated as a cross product between $\mathbf{r}$ (distance to the primary galaxy center or the remnant galaxy) and $\mathbf{F}_{\rm grav}$ or $\mathbf{F}_{\rm DF}$. $\mathbf{F}_{\rm grav}$ is taken as the total resolved gravitational force on the MBH in the simulation, and $\mathbf{F}_{\rm grav}$ is the subgrid-dynamical friction force computed at each MBH time step. Corroborating the results shown in Bortolas et al. [2020], we also find that the large-scale gravitational torque dominates the local dynamical friction force by ~ 2 orders of magnitude. This is true both during the galaxy merger and during the subsequent sinking of the MBHs. By splitting again between merged and stalled resimulation systems, we find that during the initial pairing stage ($\sim 200\,{\rm Myrs}$ since the first pericentric passage), the stalled systems generally experience less $\tau_{\rm grav}$, but not significantly. We also compare the gravitational and dynamical friction torque from ASTRID (before the MBH merger) with the torque from the resimulation, to evaluate if we miss any influence of the large-scale structures on the MBH dynamics. In general, we find that the $\tau_{\rm grav,resim}$ matches well with the $\tau_{\rm grav,ASTRID}$ values. Because the dynamical mass of BH particles in ASTRID is boosted by ~ 100, its magnitude is closer to the gravitational torque and may have a larger impact on the dynamics. This can also possibly lead to the early merger of the five systems that stalls in the resimulation.

Finally, Figure 6.5.8 shows the change in the total energy of the secondary MBH after the first pericentric passage between the pairs, compared with the energy loss due to dynamical friction (in the resimulation). We find a striking contrast between the merged and stalled system at the very early stage of the merger: the merged MBHs lost most of their energy within the first $\sim 100\,{\rm Myrs}$. The energy loss due to dynamical friction then begins to take effect after $\sim 200\,{\rm Myrs}$ to further drive the merger. In contrast, the stalled MBHs gained energy in this beginning phase from the gravitational torque. As a result, the MBHs never

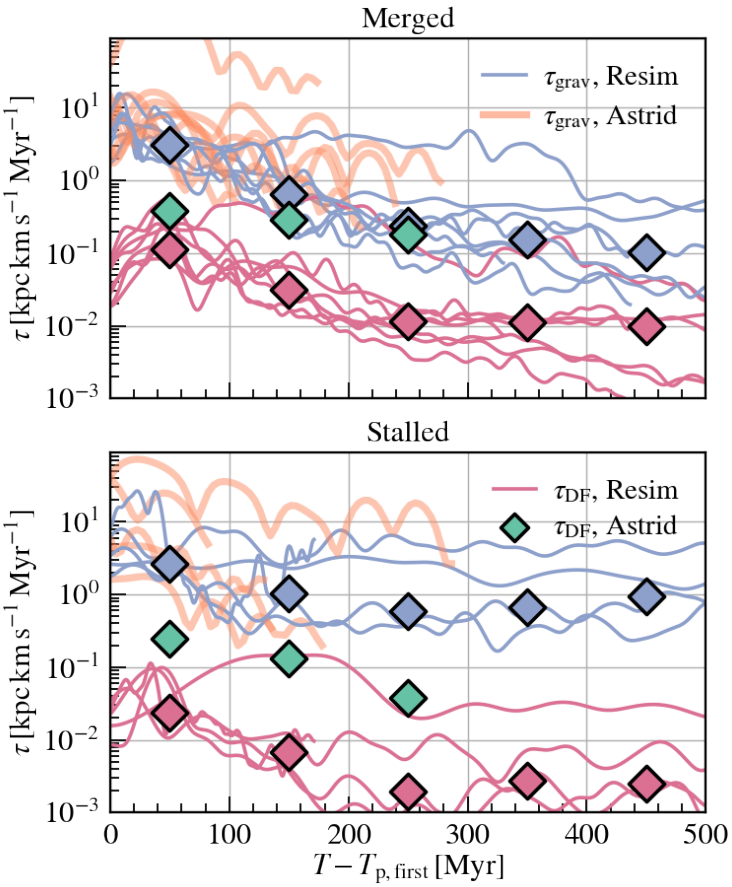

Figure 6.5.7: Time evolution of the gravitational torque on the secondary MBH since the first pericentric passage in ASTRID (**thick orange**) and the resimulation (**thin blue**). The **pink lines** show the dynamical friction torque from the resimulations. The gravitational torque in ASTRID is recovered by the resimulation in most systems, and it is two orders of magnitude larger than the dynamical friction torque, as was also shown in Bortolas et al. [2020]. The *diamonds* show the median torque among each group within time bins of 100 Myrs. The **green diamonds** are the median DF torque from ASTRID.

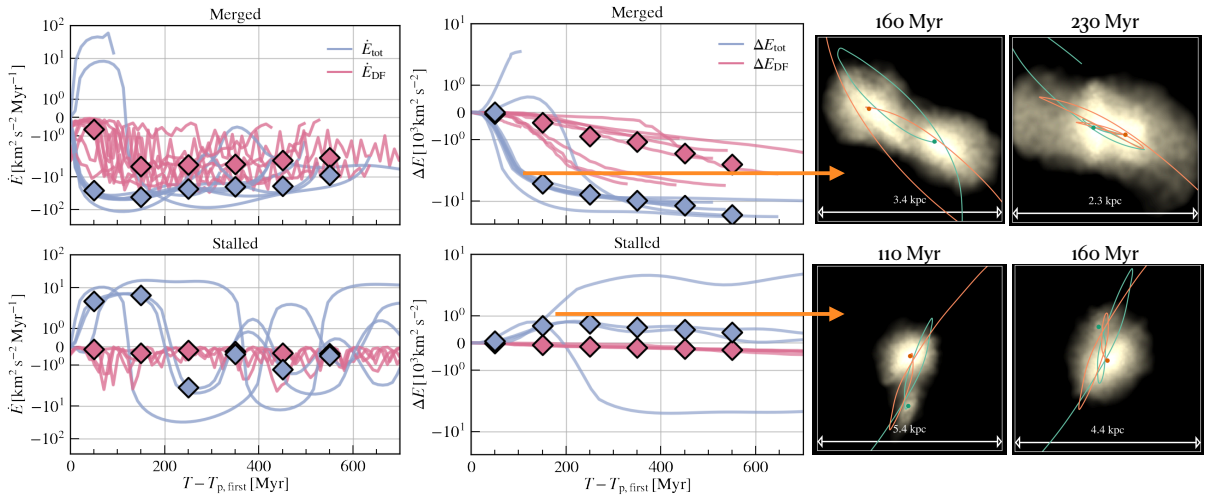

Figure 6.5.8: *Left column:* Rate of total energy change of the secondary MBH (**blue**) compared with the energy loss rate due to dynamic friction (**pink**). The **lines** show each system and the **diamonds** are the median across all systems in each time bin. We plot the systems that merged in the resimulation in the *top panel* and the systems that stalled in the *bottom panel*. The merged MBHs experience loss of energy dominated by gravity, while the stalled MBHs gain energy during the first ~ 200 Myrs of the galaxy merger. *Middle column:* Cumulative change in the MBH energy since the first pericentric passage between the pair. *Right column:* visualization of two galaxy mergers that lead to a merged pair (*top*) and a stalled pair (*bottom*). The stalled MBHs are mostly found in head-on collisions of minor galaxy mergers, in which the secondary host is quickly dissolved.

made their way into the central region where dynamical friction acts effectively. On the right, we show a typical example of both the merged and stalled scenarios. Consistent with the picture in Figure 6.5.5, the MBHs in major mergers experience energy loss at the potential center of their hosts, whereas those in minor mergers with head-on collisions gain energy from the tidal disruption of their host galaxies. In future development of subgrid merger models in cosmological simulations, it will be useful to measure the energy change rates of MBHs as an indication of the merging timescales and the likelihood of stalling.

6.5.4 Effect of new infalling galaxies and MBHs

The results shown for the seed MBH merging timescale so far exclude the effect of a third galaxy and MBH on the evolution of the original MBH pair. Recall that in the system selection in Section 6.3, 6 systems (8-13) will start to have new infalling MBHs at $z \sim 6$, and two systems (14 and 15) are already in the multiple-MBH environment at $z \sim 9$. In this section, we study the MBH pairing and orbits with considerations of multiple MBHs.

Figure 6.5.9 shows the bolometric luminosities and the orbits of all MBHs in four systems undergoing close interactions between multiple MBHs and galaxies. In all four cases, we find stalling of all MBHs on kpc scales. In particular, for the systems with new infalls (`system8` and `system9`), the third MBH/galaxy does not accelerate the sinking of the initial secondary. In `system8` the secondary orbit widens with the infall of a new galaxy. For the systems with simultaneous merger between several MBH-hosting galaxies, the MBHs exhibits more chaotic orbits except for the primary MBH. These multiple MBH mergers lead to many wandering MBH seeds that do not grow efficiently in the remnant galaxy. This picture is also consistent with the earlier findings that the seed dynamics are governed by large-scale torques. The galaxy structure is often more complicated with changing potentials for the multiple merger case and can lead to energy increases of seed MBHs.

6.5.5 Effect of nuclear star clusters

Recent works suggest that if MBHs are embedded in extended stellar systems such as NSCs, the sinking and formation of MBH binaries can be enhanced. This enhancement arises from the additional mass, which aids in dynamical friction, and the tidal effects exerted by the cluster [e.g., Mukherjee et al., 2023, Ogiya et al., 2020]. Our objective is to understand how resolving these clusters using N-body methods influences the outcomes obtained from the resimulations and compare the inspiral time obtained from the subgrid dynamical friction prescription used in `ASTRID` resimulations.

We use the Fast Multipole Method (FMM) based N-body code `Taichi` [Mukherjee et al., 2021, 2023, Zhu, 2021] to perform N-body simulations of the resimulated `ASTRID` systems. `Taichi` has explicit error control with time-symmetrized adaptive timesteps that allow the code to produce accurate results, even at mpc scales, and consistent with those obtained from direct summation-based N-body codes. `Taichi` is highly efficient at simulating large-N systems owing to the $\mathcal{O}(N)$ force calculations rather than $\mathcal{O}(N^2)$ that is typical of direct

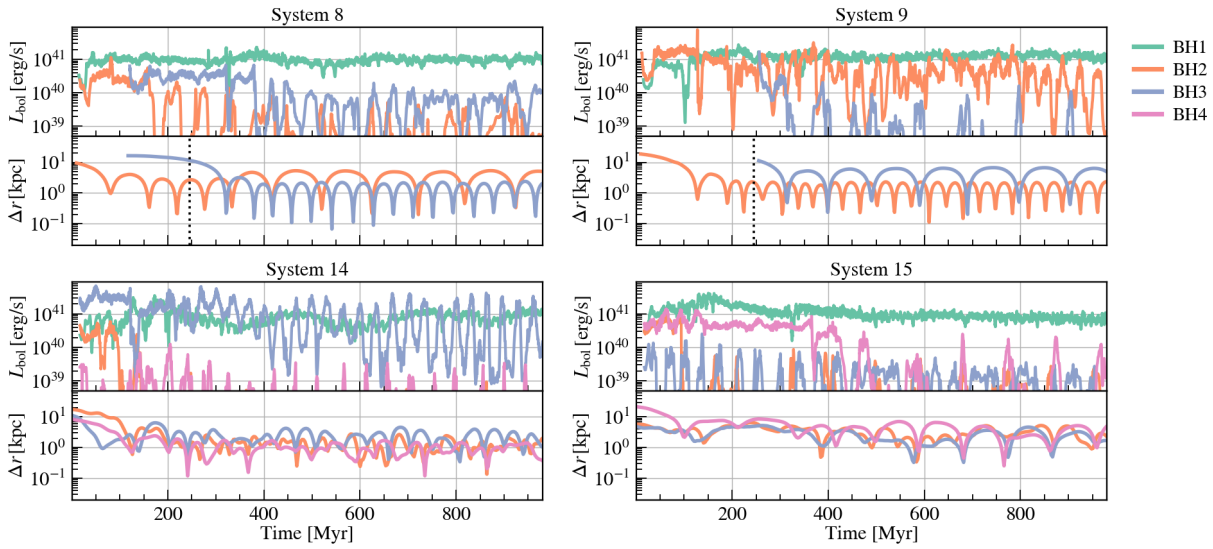

Figure 6.5.9: The bolometric luminosities and the orbits of all MBHs in four systems undergoing close interactions between multiple MBHs and galaxies. In all four cases, interactions between > 2 galaxies and infalling MBHs lead to wandering MBHs on kpc scales.

summation based N-body codes.

We perform preliminary investigations of two systems - `system5` and `system8`. These systems are chosen since they lie at the density and energy criterion boundary separating merged systems from stalled ones. We are motivated to understand if embedding the MBHs in these systems in stellar clusters allows them to sink to sub-pc scales where the binary enters the hard-binary limit.

The particle data is obtained at $t = 968.2$ Myr for `system5` and $t = 500$ Myr for `system8`. We take the particle data from the resimulations and perform radial cuts of 3 kpc and 5 kpc respectively from the centers of potentials of both systems. This was done to reduce the computational expenses. Cropping the systems results in $N = 1.3 \times 10^6$ particles being retained from `system5` and $N = 2.4 \times 10^6$ particles being retained from `system8`. We ensured that the cropping did not affect the overall dynamics of the MBHs and simulations were performed with non-cropped and cropped systems to verify consistency.

We infer the total mass present in clusters by extrapolating the stellar density profile obtained from the resimulations beyond 100 pc. Since the mass is sensitive to the profile used for extrapolation, we use three different slopes to generate three different models for each system: a shallow cusp with $\rho(r) \propto r^{-1}$, a slightly steeper cusp with $\rho(r) \propto r^{-1.5}$, and a steep cusp with $\rho(r) \propto r^{-2}$. The mass of each cluster, M_c, is then calculated by subtracting the mass present within the inner 100 pc and dividing it by two.

To ensure that the masses of the clusters are physically realistic, we compare the initial cluster mass in each of the three models to the initial stellar mass present within 100 pc of the MBHs in each of the galaxies before they get disrupted. For `system5`, we find that the lowest mass cluster is about $2\times$ the mass contained around the primary MBH. For the highest mass cluster, we find that the cluster mass is about $5\times$ that contained around the primary MBH initially. Similar values are obtained in the case of `system8`. The lower initial mass inferred from the galaxies is caused due to the suppression in the density profile within 100 pc of the MBHs owing to softening. In general, we would expect cusps to form around the MBHs leading to a larger stellar mass which would be more consistent with the masses of the clusters that we used in this study. Additionally, we note that the total cluster mass to stellar mass in the galaxy ranges from 1-3%, which is quite consistent with NSC to bulge stellar masses of some known nucleated dwarf galaxies [e.g., Khan and Holley-Bockelmann, 2021].

Since `Taichi` cannot handle gas effects, the gas particles are treated as stellar particles. We do not expect this to affect our overall results since gas is subdominant in the region of interest. N-body realizations of the stellar clusters are generated using the galactic modeling toolkit `Agama` [Vasiliev, 2019] by taking into account the potentials of the cluster, the MBH, and the galaxy. We use a Dehnen density profile [Dehnen, 1993] to model the cluster with a shallow inner cusp of $\gamma = 0.5$ and scale radius $a = 1.4$ pc. All of the generated clusters have a half-mass radius of about 4.3 pc. The cluster particles are assigned masses of $10^3 M_\odot$ each. Ideally, even smaller cluster particles are desirable to model the tidal effects accurately. While that is beyond the scope of this work, future work will include clusters that have a mass resolution of $10 - 100 M_\odot$. We summarize the initial conditions for our N-body simulations

System	Cluster model	$M_c[M_\odot]$
	Low mass	2.1×10^6
`system5`	Intermediate mass	3.1×10^6
	High mass	6.3×10^6
	Low mass	2.5×10^6
`system8`	Intermediate mass	3.7×10^6
	High mass	7.5×10^6

Table 6.5.1: A summary of the different stellar cluster models used in the N-body simulations and the masses of each individual cluster.

in Table 6.5.1.

The systems are evolved for ~ 500 Myr beyond the initial time or until the formation of a hard binary. Plummer softening is used while calculating the forces. The softening used for the cluster particles is 0.01 pc, while that for the stellar and gas particles is 25 pc. When the separation of the MBHs decreases below 100 pc, we decrease the softening of the stellar and gas particles to 1 pc. Dark matter particles are assigned a softening length of 50 pc. The interactions between the MBHs are never softened. The softening lengths were varied to understand the effects on the sinking time and no major differences were noticed. In scenarios that result in the sinking of the MBHs to sub-pc length scales, convergence is ensured by running the simulations again after splitting the particles such that the overall mass resolution of the non-cluster particles is $2 \times 10^3 M_\odot$. Particle splitting is performed using the same procedure as used in some previous studies [e.g., Khan et al., 2012]. In the split-particle cases, the softening of the DM particles is reduced to 25 pc. For `system5`, particle splitting results in a total of $N \approx 3 \times 10^6$ particles. While the mass resolution used in this work is somewhat insufficient to resolve the three-body hardening phase accurately, we want to note that the main objective of this preliminary study is to compare the sinking timescales between the ASTRID resimulations and the N-body simulations. A more detailed analysis is in preparation which includes additional prescriptions for relativistic effects, MBH spin, and GW recoil.

We use the fourth-order hierarchical Hamiltonian splitting integrator `HHS-FSI` [Rantala et al., 2021]. We set a force error tolerance parameter of $\epsilon = 2 \times 10^{-5}$, multipole parameter of $p = 12$, and timestep parameter of $\eta = 0.3$. This results in an overall relative energy error of $\sim 10^{-5}$ at the end of the simulations. For more information on the parameters, we refer the interested reader to Mukherjee et al. [2021]. The simulations are run using 32-48 threads on a single `AMD Epyc 7742` machine.

Examining Figure 6.5.10 where we plot the relative separation of the MBHs Δr as a function of time for our different N-body models, we find interesting results. For `system5`, our high mass cluster helps the MBHs efficiently sink to the potential minimum of the galaxy and form a hard binary within 1.2 Gyr. The initial periastron separation between the MBHs is ≈ 800 pc. The separation drops primarily due to DF on the extended system until the MBHs have a ~ 50 pc separation after which tidal forces from the clusters helps the MBHs

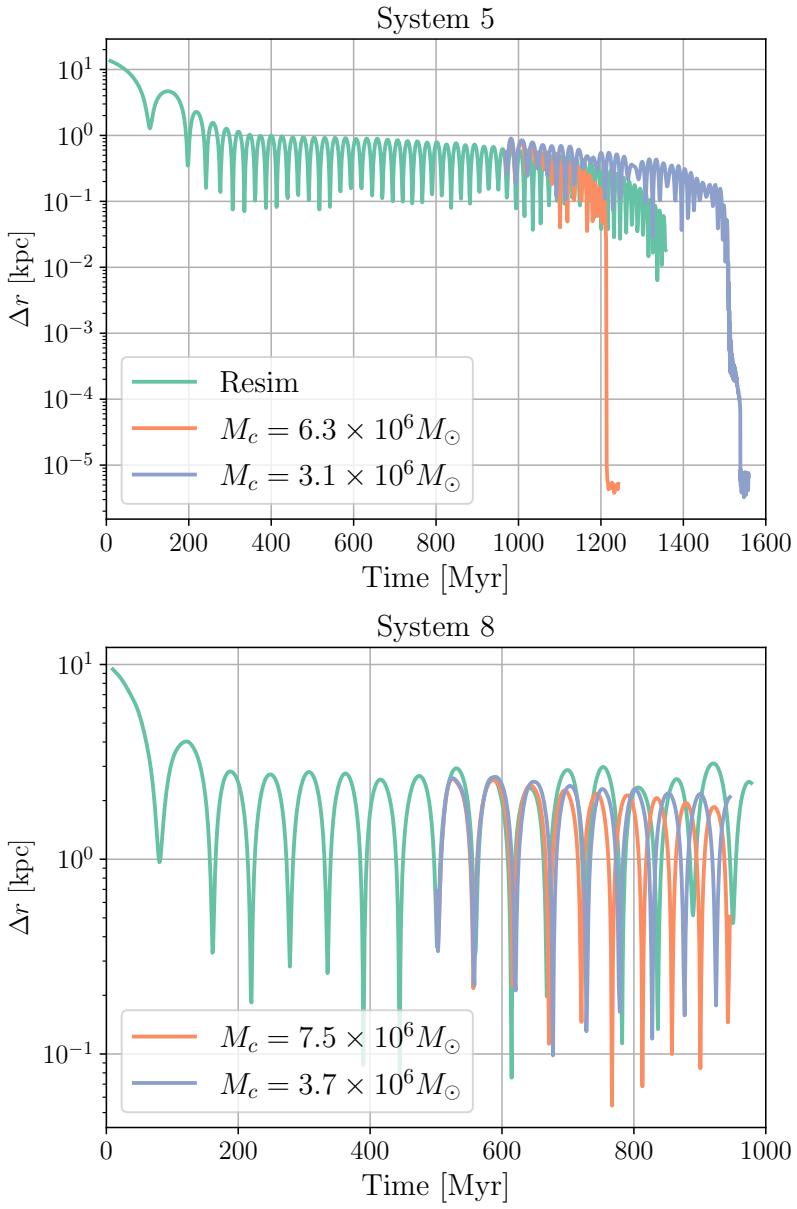

Figure 6.5.10: Relative separation between the MBHs Δr as a function of the time for resimulations and models with MBHs embedded in NSCs for `system5` (*top*) and `system8` (*bottom*). In the high mass cluster model (*orange*) in `system5`, the MBHs can sink efficiently and form a hard binary by 1.2 Gyr. The sinking time is almost twice as long for the intermediate mass cluster model (*blue*) owing to the lower mass in the cluster. The DF prescription in the resimulations (*green*) predicts an inspiral time somewhere within the two models. In `system8`, despite the added mass due to the clusters, the MBHs are unable to sink and form a hard binary. Even in the large mass cluster model, the separation between the MBHs reduces very slowly. This is quite consistent with the evolution in the resimulations.

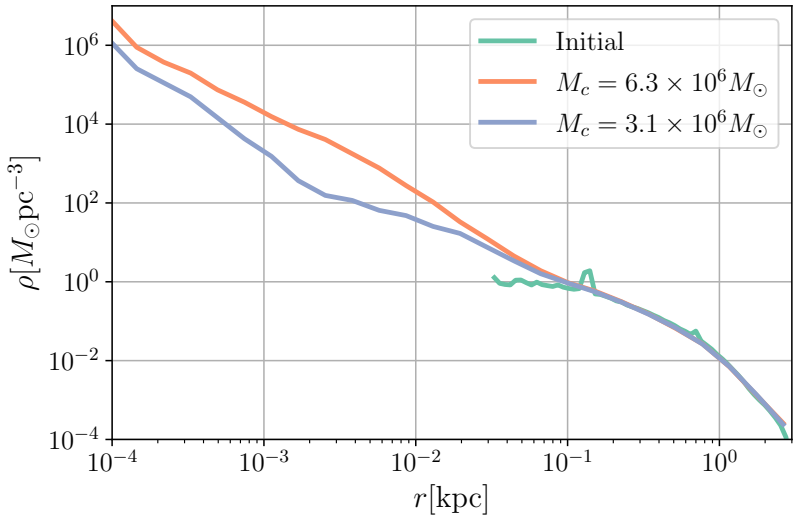

Figure 6.5.11: The stellar density profile upon the formation of a hard binary in the intermediate mass (*blue*) and high mass cluster models (*orange*) in `system5`. The bumps in the initial stellar density profile (green) represent the positions of the NSCs initially. Consistent with our initial conditions, the density profile after the clusters have sunk form a $\rho(r) \propto r^{-1.5}$ profile in the inner 100 pc in the intermediate mass model and a $\rho(r) \propto r^{-2}$ profile in the high mass model. The central density at 10^{-4} kpc is quite consistent with stellar density values of known nucleated dwarf galaxies such as M32 or NGC 5102.

sink rapidly to sub-pc separations, consistent with previous studies [Mukherjee et al., 2023, Ogiya et al., 2020]. The semi-major axis of the formed binary is around 5×10^{-3}pc whereas its eccentricity is $\sim 0.3 - 0.4$. We caution the reader, however, that a better estimation of eccentricity would require finer resolution in the last few Myrs before sinking, a work in progress. In the intermediate mass cluster model, the inspiral takes twice as long owing to the lower mass of the cluster, and some mass loss from the cluster due to tidal stripping. Similar to the high mass model, the separation between the MBHs rapidly drops when the separation reduces to ≤ 50 pc, and a hard binary is formed quite efficiently. Although not presented here, we find that the low mass cluster model is not able to sink the MBHs to sub-pc scales within ~ 500 Myr of evolution but a decrease in the separation is noticed. We notice that the inspiral time predicted by the `ASTRID` resimulation model is approximately in between our intermediate and large cluster models.

The cluster models in `system8` do not show the same signs of rapid inspiral as those observed in `system5`. Even in the high mass cluster model `system8`, the MBHs are only able to reduce their periastron separation from 2.6 kpc to 2 kpc within 500 Myr. The decrease is even smaller in the case of the intermediate mass cluster model. Since `system5` and `system8` share similar initial MBH orbits and stellar density profiles, it suggests that NSCs become an effective method of sinking only when the periastron separation between the MBHs is $\lesssim 1$ kpc. This underscores the importance of taking into account the global effects and the necessity of `ASTRID`-like simulations where the initial orbits of the MBHs are modeled accurately. The first few kpc scale orbits contain very useful information on the subsequent orbital evolution and the fate of the binary.

We also examine the overall stellar profile of the galaxy once a hard binary has formed in Figure 6.5.11. Consistent with the initial conditions used, once the clusters have merged, we find that a $\rho(r) \propto r^{-1.5}$ profile forms in the inner 100 pc in the intermediate mass cluster model while a $\rho(r) \propto r^{-2}$ profile forms in the high mass cluster model. Since the softening of the cluster particles is quite small and they dominate the mass at $r \lesssim 0.1$ kpc, the density profile is accurate to $\approx 10^{-4}$ kpc. The stellar profile is quite consistent with those from known nucleated dwarf galaxies such as M32, NGC 5012, and NGC 5206 [Khan and Holley-Bockelmann, 2021], especially in the inner-pc. The stellar profiles are obtained at the beginning of the hard-binary stage and no core scouring has taken place. With time, due to core-scouring, we expect the density within the influence radius of the binary ($\sim$ 1pc) to become shallower.

6.6 Discussion

The dynamics of MBHs in the dynamical friction regime (from a few kpc to < 10 pc scales) have not been understood in great detail, partly due to the intrinsic stochasticity [e.g. Nasim et al., 2020, Rawlings et al., 2023] and the wide range of physics processed involved [e.g. Banik and van den Bosch, 2021, Dosopoulou and Antonini, 2017, Park and Bogdanović, 2017, Tamburello et al., 2017]. Recently, several works have been focusing on bridging this gap in the dynamical range by following the dynamics of MBH pairs from galaxy mergers to

binary hardening, and some even to binary coalescence. Here we briefly discuss our work in the context of these emerging literatures.

Probably most relevant to our work are the recent studies by Koehn et al. [2023] and Partmann et al. [2023], both of which take into account realistic consecutive galaxy mergers with > 2 MBHs. The former uses a similar resimulation approach to resimulate triple SMBHs in the `Romulus` simulation, with a focus on the massive galaxies. The latter considers the infall of several seed MBHs in satellite halos into the main halo, and finds that a seed mass of $\sim 10^5\,M_\odot$ is needed for MBHs to merge in these low-mass galaxies. Compared to these works, our study uniquely considers the effect of gas physics in high-redshift galaxies, and shows that the growth in stellar density due to star formation allows seed MBHs to enter into the hardening phase within $\sim 1\,\mathrm{Gyr}$. However, we currently lack the self-consistent treatments of triple MBH interactions and gravitational recoil, which have been shown to lead to a high fraction of MBH ejections according to these works. Despite the differences in the subgrid models, the three works reach agreements on the production of numerous wandering MBHs due to various mechanisms in multiple-MBH systems. We also explicitly show that such systems are numerous as a result of the high-redshift early galaxy assemblies, and so it is important to understand such systems in greater detail and implications for early MBH growths.

Other works on the seed MBH dynamics include Tamfal et al. [2018], Pfister et al. [2019], Ma et al. [2021]. In particular, both Pfister et al. [2019] and Ma et al. [2021] considered the effect of clumpy gas on the sinking of MBH seeds. The key finding is that seed-mass MBHs cannot sink efficiently in clumpy high-redshift galaxies, or even in idealized cases. By taking initial conditions from cosmologically merged systems instead of putting MBHs on more *ad hoc* orbits, our resimulations naturally favor the initial orbital parameters and galaxy configurations (such as rotation angles) that are more likely to sink the MBHs efficiently. With initial conditions that favor efficient orbital decay, it is still likely that the MBHs can migrate into the dense central star-forming regions before they get significantly scattered. In future works, we will explore if more detailed ISM modeling significantly impacts our conclusion.

6.7 Conclusion

We present a suite of the MAGICS simulations, consisting of 15 idealized high-resolution galaxy merger simulations with initial conditions directly reproducing the configurations of galaxy mergers in the large-volume cosmological simulation `ASTRID`. This suite encapsulates a wide range of realistic galaxy merger environments directly drawn from `ASTRID`, with both isolated dwarf galaxy mergers with an MBH pair and consecutive galaxy mergers with multiple MBHs. The simulation suite is run with the full subgrid physics model of the `ASTRID` simulation using `MP-Gadget` to include realistic gas and star-formation physics, the feedback from the supernova, as well as the accretion onto MBHs and the AGN feedback.

We use these simulations to study the merger and sinking of high-redshift ($z \sim 6$) mergers between MBH seeds ($5 \times 10^4\,M_\odot < M_{\rm BH} < 10^6\,M_\odot$), in early gas-rich, star-forming galaxies

with a typical gas fraction > 1, galaxy mass between $\sim 10^8\,M_\odot$ and $\sim 3\times10^9\,M_\odot$, and halo mass between $\sim 5\times10^{10}\,M_\odot$ and $\sim 5\times10^{11}\,M_\odot$. For selected systems with inefficient orbital decay, we continue the galaxy merger simulation during the evolution of the final $\sim$ kpc scale with the FMM-based N-body code `Taichi` with MBHs embedded in NSCs.

We show that the resimulation method can create galaxy merger initial conditions and orbital configurations that resemble the original galaxy merger system in cosmological simulation. Furthermore, the subsequent evolution of the cosmological merger is also paralleled in the resimulations regarding the MBH orbits, host galaxy density profiles, and host galaxy star formation rates. We find a good match between the MBH orbits of the `ASTRID` mergers and the resimulation mergers above the `ASTRID` resolution limit (the first ~ 3 orbits). This validates using cosmological simulations with dynamical friction modeling for setting the initial distribution of MBH orbital eccentricities and separations for idealized galaxy/MBH mergers simulations and analytical models.

In 8 out of 15 resimulated `ASTRID` mergers, the MBH pairs can sink efficiently to separations below 20 pc in 1.5 Gyrs and before other galaxies start to interfere with the binary system. `ASTRID` mergers with high initial eccentricity ($e_{\rm init} > 0.5$), high density at kpc scales ($\rho_{\rm star} > 0.05\,M_\odot/pc^3$), and low halo mass ratio ($q_{\rm halo} < 0.3$) will sink efficiently to ~ 20 pc in the resimulation. The MBH will stall at $0.1-1$ kpc orbits if any of these conditions are not satisfied. Moreover, the central stellar density can grow by a factor of $2\sim3$ between the cosmological merger and the end of the dynamical friction regime and over a factor of ~ 10 from before the galaxy merger to the binary hardening. We find that all merger remnant galaxies have a central stellar density of $\rho_{\rm star,50pc} > 1\,M_\odot/pc^3$ and orbital eccentricity of ~ 0.8 when the MBHs begin entering into the binary hardening regime. Our predicted eccentricity is in broad agreement with the results in Gualandris et al. [2022].

By directly linking the resimulation MBH mergers (or non-mergers) with the cosmological system, we find that galaxy and orbital properties at the `ASTRID` MBH merger time and resolution are already good indicators of whether the MBH pair can sink efficiently or not. Specifically, the energy loss of the seed MBH that leads to fast sinking is dominated by gravitational torque during the first ~ 200 Myrs of galaxy merger, and dynamical friction plays a subdominant role. The seed MBHs in merged systems lose energy at a rate of $\sim 10-100\,{\rm km\,s^{-2}\,Myr^{-1}}$ during the galaxy merger, whereas the stalled seeds gain energy in this phase. As a result of the initial energy loss driven by large-scale torques, some seeds experience efficient orbital decay during the first few orbits of MBH paring, with apocentric orbital sizes below 1 kpc in ~ 200 Myrs after the first pericentric passage between the MBHs.

Consecutive mergers between multiple galaxies and MBHs are common ($\sim 50\%$) among high-redshift seed MBH mergers, and thus need to be taken into account when modeling the merging between MBH seeds. We find that the consecutive merger scenario generally hinders the sinking of MBH seeds. The 4 resimulated systems with multiple galaxy mergers involving > 2 MBHs all lead to the stalling of several MBHs at ~ 1 kpc from the remnant galaxy center, with only one MBH sinking and accreting efficiently at the galaxy center. In particular, we find that the orbit of the initial MBH pairs widens with the infall of new galaxies.

Finally, by resimulating the sub-kpc evolution of MBH pairs for two systems with the secondary MBHs stalling on $\sim 1\,\mathrm{kpc}$ scales with MBH embedded in NSCs, we find that a cluster mass of $\sim 3 \times 10^6\,M_\odot$ facilitate the sinking of the secondary and allows for a rapid formation of a hard binary in the case where the orbital size is already below 1 kpc. By applying the criterion of rapid MBH sinking derived in this work (high-density and high-eccentricity mergers in isolation) to the properties of `ASTRID` MBH mergers shown in **?**, we find that about $\sim 10 - 20\%$ MBH seeds that pair at $z \sim 9$ will enter into the binary hardening phase before $z \sim 3$. Since binary hardening is also relatively efficient for dense and high-eccentricity mergers, we expect that these pairs will be detected by LISA around $z \sim 3$.

Chapter 7

Conclusion

In this thesis, I have used a combination of hydrodynamical simulations (in an idealized and a cosmological context) and semi-numerical simulations to study the evolution of galaxies and massive black holes since cosmic dawn, with a particular focus on cosmic reionization and massive black hole binaries.

Using the semi-numerical code for reionization AMBER, I model the patchy kinetic Sunyaev-Zel'dovich (kSZ) effect by directly specifying the reionization history with the redshift midpoint $z_{\rm mid}$, duration $\Delta_{\rm z}$, and asymmetry $A_{\rm z}$. I constrain the redshift midpoint $6.0 < z_{\rm mid} < 8.9$ using the Planck2018 Thomson optical depth result, and find that the amplitude of $D^{\rm pkSZ}_{\ell=3000}$ is consistent with the 1σ upper limit from the South Pole Telescope results up to $\Delta_z < 5.1$. I show that constraints on the asymmetry require $\sim 0.1\,\mu k^2$ measurement accuracy at multipoles other than $\ell = 3000$. Finally, the amplitude and shape of the kSZ spectrum are only weakly sensitive to M_h under a fixed reionization history and radiation mean-free path. This means that using only the two-point statistics at a few multipole values of the patchy kSZ map gives limited constraints on the detailed reionization history and morphology. Higher-order statistics or map-level information can be useful in providing more information about the reionization process.

Another probe of galaxy formation comes from the observation of massive black holes or AGNs. Specifically, massive black hole binaries are promising for understanding the growth and accretion of MBHs, especially given the current and future gravitational wave observations targeting BHs on the massive end. Aiming for accurate theoretical modeling of the MBH binary population, I developed and validated the numerical modeling of MBH dynamics within cosmological simulations, which allows for a more physical and accurate prediction of the MBH binary formation and merger rate. Compared with previous simulations, this model takes into account the MBH orbital decay process after galaxy mergers and postpones binary formation by a few hundred Myrs to several Gyrs.

Using the state-of-the-art large-volume cosmological simulation ASTRID with the new dynamical modeling, I compute the initial eccentricities of MBH orbits directly from the simulation at kpc-scales, and find orbital eccentricities above 0.7 for most MBH pairs before the numerical merger. After accounting for the full evolution stages of MBH binaries, only

$\lesssim 20\%$ of seed MBH pairs merge at $z > 3$. These $z > 3$ seed-mass mergers are hosted in a biased population of galaxies with the highest stellar masses of $> 10^9\,M_\odot$. With the high initial eccentricity prediction, we estimate an expected merger rate of $0.3-0.7$ per year from the $z > 3$ MBH population. This is a factor of ~ 7 higher than the prediction using the circular orbit assumption.

Then I also investigate the electromagnetic signatures of MBH pairs. ASTRID provides one of the largest statistical samples of the rare quasar pairs down to kpc scales. I search for the distinctive features of AGN pairs compared to the underlying single AGN population, and find that dual AGN have an overall high-accretion efficiency and obscurations. Following the evolution of the pair systems during and after the galaxy merger, I show that in the most massive halos, MBH pairs often exist in the offset AGN form, with the secondary deactivated by severe gas stripping and stall at 5kpc for a few hundred Myrs. On the contrary, the pairing to GW emission timescales of dual AGN is typically less than 1 Gyrs, and could be as short as 100 Myrs for the brightest duals. These pairs can lead to the majority of gravitational wave sources in LISA and PTA observations.

Finally, noticing that the current dynamics model still fails to accurately model the dynamics and merger of seed-mass MBHs at the resolution of cosmological simulations, I developed idealized galaxy merger simulations with initial conditions informed by cosmological merger events to study the binary evolution of high-redshift MBH seeds at high-resolution. I find that the initial orbital configuration of the galaxy merger and the galaxy mass ratio play a major role in the subsequent dynamical evolution of the binary, by either adding or decreasing the orbital energy of the MBHs. These simulations showed that current cosmological simulations potentially overpredict seed-mass MBH mergers, and most MBH seeds may end up wandering in the host galaxy at different radii.

This thesis constitutes a step forward in refined modeling of the high-redshift galaxies, particularly the progress of cosmic reionization and the evolution of massive black hole binaries. More importantly, it made several theoretical predictions based on our current understanding of high-redshift galaxy formation, which is testable through current and future observations. It is now an exciting era for studying the galaxy evolution in the high-redshift Universe, and relate it spatially to the evolution of instruction on larger scales, and temporally to the present-day galaxies. The state of the field rapidly changing change due to a suite of instruments and telescopes that are operating now or will become available in the next few years. On the theory side, there has been a lot of progress since the recent cosmological galaxy formation simulations used in this work in all aspects of the physics involved. In the future, we should incorporate those developments in cosmological simulations, and understand how the resulting prediction compared against the new observations.

Bibliography

Mario G. Abadi, Julio F. Navarro, Matthias Steinmetz, and Vincent R. Eke. Simulations of Galaxy Formation in a Λ Cold Dark Matter Universe. I. Dynamical and Photometric Properties of a Simulated Disk Galaxy. *ApJ*, 591(2):499–514, July 2003. doi: 10.1086/375512.

B. P. Abbott, R. Abbott, T. D. Abbott, M. R. Abernathy, F. Acernese, K. Ackley, C. Adams, T. Adams, P. Addesso, R. X. Adhikari, V. B. Adya, C. Affeldt, M. Agathos, K. Agatsuma, N. Aggarwal, O. D. Aguiar, L. Aiello, A. Ain, P. Ajith, B. Allen, A. Allocca, P. A. Altin, S. B. Anderson, W. G. Anderson, K. Arai, M. A. Arain, M. C. Araya, C. C. Arceneaux, J. S. Areeda, N. Arnaud, K. G. Arun, S. Ascenzi, G. Ashton, M. Ast, S. M. Aston, P. Astone, P. Aufmuth, C. Aulbert, S. Babak, P. Bacon, M. K. M. Bader, P. T. Baker, F. Baldaccini, G. Ballardin, S. W. Ballmer, J. C. Barayoga, S. E. Barclay, B. C. Barish, D. Barker, F. Barone, B. Barr, L. Barsotti, M. Barsuglia, D. Barta, J. Bartlett, M. A. Barton, I. Bartos, R. Bassiri, A. Basti, J. C. Batch, C. Baune, V. Bavigadda, M. Bazzan, B. Behnke, M. Bejger, C. Belczynski, A. S. Bell, C. J. Bell, B. K. Berger, J. Bergman, G. Bergmann, C. P. L. Berry, D. Bersanetti, A. Bertolini, J. Betzwieser, S. Bhagwat, R. Bhandare, I. A. Bilenko, G. Billingsley, J. Birch, R. Birney, O. Birnholtz, S. Biscans, A. Bisht, M. Bitossi, C. Biwer, M. A. Bizouard, J. K. Blackburn, C. D. Blair, D. G. Blair, R. M. Blair, S. Bloemen, O. Bock, T. P. Bodiya, M. Boer, G. Bogaert, C. Bogan, A. Bohe, P. Bojtos, C. Bond, F. Bondu, R. Bonnand, B. A. Boom, R. Bork, V. Boschi, S. Bose, Y. Bouffanais, A. Bozzi, C. Bradaschia, P. R. Brady, V. B. Braginsky, M. Branchesi, J. E. Brau, T. Briant, A. Brillet, M. Brinkmann, V. Brisson, P. Brockill, A. F. Brooks, D. A. Brown, D. D. Brown, N. M. Brown, C. C. Buchanan, A. Buikema, T. Bulik, H. J. Bulten, A. Buonanno, D. Buskulic, C. Buy, R. L. Byer, M. Cabero, L. Cadonati, G. Cagnoli, C. Cahillane, J. Calderón Bustillo, T. Callister, E. Calloni, J. B. Camp, K. C. Cannon, J. Cao, C. D. Capano, E. Capocasa, F. Carbognani, S. Caride, J. Casanueva Diaz, C. Casentini, S. Caudill, M. Cavaglià, F. Cavalier, R. Cavalieri, G. Cella, C. B. Cepeda, L. Cerboni Baiardi, G. Cerretani, E. Cesarini, R. Chakraborty, T. Chalermsongsak, S. J. Chamberlin, M. Chan, S. Chao, P. Charlton, E. Chassande-Mottin, H. Y. Chen, Y. Chen, C. Cheng, A. Chincarini, A. Chiummo, H. S. Cho, M. Cho, J. H. Chow, N. Christensen, Q. Chu, S. Chua, S. Chung, G. Ciani, F. Clara, J. A. Clark, F. Cleva, E. Coccia, P. F. Cohadon, A. Colla, C. G. Collette, L. Cominsky, M. Constancio, A. Conte, L. Conti, D. Cook, T. R. Corbitt, N. Cornish, A. Corsi, S. Cortese, C. A. Costa, M. W. Coughlin, S. B. Coughlin, J. P. Coulon, S. T. Countryman, P. Couvares, E. E. Cowan, D. M. Coward, M. J. Cowart, D. C. Coyne, R. Coyne, K. Craig, J. D. E. Creighton, T. D. Creighton, J. Cripe, S. G. Crowder, A. M. Cruise, A. Cumming, L. Cunningham, E. Cuoco, T. Dal Canton, S. L. Danilishin, S. D'Antonio, K. Danzmann, N. S. Darman, C. F. Da Silva Costa, V. Dattilo, I. Dave, H. P. Daveloza, M. Davier, G. S. Davies, E. J. Daw, R. Day, S. De, D. DeBra, G. Debreczeni, J. Degallaix, M. De Laurentis, S. Deléglise, W. Del Pozzo, T. Denker, T. Dent, H. Dereli, V. Dergachev, R. T. DeRosa, R. De Rosa, R. DeSalvo, S. Dhurandhar, M. C. Díaz, L. Di Fiore, M. Di Giovanni, A. Di Lieto, S. Di Pace, I. Di Palma, A. Di Virgilio, G. Dojcinoski, V. Dolique, F. Donovan, K. L. Dooley, S. Doravari, R. Douglas, T. P. Downes, M. Drago, R. W. P. Drever, J. C. Driggers, Z. Du, M. Ducrot, S. E. Dwyer, T. B. Edo, M. C. Edwards, A. Effler, H. B. Eggenstein, P. Ehrens, J. Eichholz, S. S. Eikenberry, W. Engels, R. C. Essick, T. Etzel, M. Evans, T. M. Evans, R. Everett, M. Factourovich, V. Fafone, H. Fair, S. Fairhurst, X. Fan, Q. Fang, S. Farinon, B. Farr, W. M. Farr, M. Favata, M. Fays, H. Fehrmann, M. M. Fejer, D. Feldbaum, I. Fer-

rante, E. C. Ferreira, F. Ferrini, F. Fidecaro, L. S. Finn, I. Fiori, D. Fiorucci, R. P. Fisher, R. Flaminio, M. Fletcher, H. Fong, J. D. Fournier, S. Franco, S. Frasca, F. Frasconi, M. Frede, Z. Frei, A. Freise, R. Frey, V. Frey, T. T. Fricke, P. Fritschel, V. V. Frolov, P. Fulda, M. Fyffe, H. A. G. Gabbard, J. R. Gair, L. Gammaitoni, S. G. Gaonkar, F. Garufi, A. Gatto, G. Gaur, N. Gehrels, G. Gemme, B. Gendre, E. Genin, A. Gennai, J. George, L. Gergely, V. Germain, Abhirup Ghosh, Archisman Ghosh, S. Ghosh, J. A. Giaime, K. D. Giardina, A. Giazotto, K. Gill, A. Glaefke, J. R. Gleason, E. Goetz, R. Goetz, L. Gondan, G. González, J. M. Gonzalez Castro, A. Gopakumar, N. A. Gordon, M. L. Gorodetsky, S. E. Gossan, M. Gosselin, R. Gouaty, C. Graef, P. B. Graff, M. Granata, A. Grant, S. Gras, C. Gray, G. Greco, A. C. Green, R. J. S. Greenhalgh, P. Groot, H. Grote, S. Grunewald, G. M. Guidi, X. Guo, A. Gupta, M. K. Gupta, K. E. Gushwa, E. K. Gustafson, R. Gustafson, J. J. Hacker, B. R. Hall, E. D. Hall, G. Hammond, M. Haney, M. M. Hanke, J. Hanks, C. Hanna, M. D. Hannam, J. Hanson, T. Hardwick, J. Harms, G. M. Harry, I. W. Harry, M. J. Hart, M. T. Hartman, C. J. Haster, K. Haughian, J. Healy, J. Heefner, A. Heidmann, M. C. Heintze, G. Heinzel, H. Heitmann, P. Hello, G. Hemming, M. Hendry, I. S. Heng, J. Hennig, A. W. Heptonstall, M. Heurs, S. Hild, D. Hoak, K. A. Hodge, D. Hofman, S. E. Hollitt, K. Holt, D. E. Holz, P. Hopkins, D. J. Hosken, J. Hough, E. A. Houston, E. J. Howell, Y. M. Hu, S. Huang, E. A. Huerta, D. Huet, B. Hughey, S. Husa, S. H. Huttner, T. Huynh-Dinh, A. Idrisy, N. Indik, D. R. Ingram, R. Inta, H. N. Isa, J. M. Isac, M. Isi, G. Islas, T. Isogai, B. R. Iyer, K. Izumi, M. B. Jacobson, T. Jacqmin, H. Jang, K. Jani, P. Jaranowski, S. Jawahar, F. Jiménez-Forteza, W. W. Johnson, N. K. Johnson-McDaniel, D. I. Jones, R. Jones, R. J. G. Jonker, L. Ju, K. Haris, C. V. Kalaghatgi, V. Kalogera, S. Kandhasamy, G. Kang, J. B. Kanner, S. Karki, M. Kasprzack, E. Katsavounidis, W. Katzman, S. Kaufer, T. Kaur, K. Kawabe, F. Kawazoe, F. Kéfélian, M. S. Kehl, D. Keitel, D. B. Kelley, W. Kells, R. Kennedy, D. G. Keppel, J. S. Key, A. Khalaidovski, F. Y. Khalili, I. Khan, S. Khan, Z. Khan, E. A. Khazanov, N. Kijbunchoo, C. Kim, J. Kim, K. Kim, Nam-Gyu Kim, Namjun Kim, Y. M. Kim, E. J. King, P. J. King, D. L. Kinzel, J. S. Kissel, L. Kleybolte, S. Klimenko, S. M. Koehlenbeck, K. Kokeyama, S. Koley, V. Kondrashov, A. Kontos, S. Koranda, M. Korobko, W. Z. Korth, I. Kowalska, D. B. Kozak, V. Kringel, B. Krishnan, A. Królak, C. Krueger, G. Kuehn, P. Kumar, R. Kumar, L. Kuo, A. Kutynia, P. Kwee, B. D. Lackey, M. Landry, J. Lange, B. Lantz, P. D. Lasky, A. Lazzarini, C. Lazzaro, P. Leaci, S. Leavey, E. O. Lebigot, C. H. Lee, H. K. Lee, H. M. Lee, K. Lee, A. Lenon, M. Leonardi, J. R. Leong, N. Leroy, N. Letendre, Y. Levin, B. M. Levine, T. G. F. Li, A. Libson, T. B. Littenberg, N. A. Lockerbie, J. Logue, A. L. Lombardi, L. T. London, J. E. Lord, M. Lorenzini, V. Loriette, M. Lormand, G. Losurdo, J. D. Lough, C. O. Lousto, G. Lovelace, H. Lück, A. P. Lundgren, J. Luo, R. Lynch, Y. Ma, T. MacDonald, B. Machenschalk, M. MacInnis, D. M. Macleod, F. Magaña-Sandoval, R. M. Magee, M. Mageswaran, E. Majorana, I. Maksimovic, V. Malvezzi, N. Man, I. Mandel, V. Mandic, V. Mangano, G. L. Mansell, M. Manske, M. Mantovani, F. Marchesoni, F. Marion, S. Márka, Z. Márka, A. S. Markosyan, E. Maros, F. Martelli, L. Martellini, I. W. Martin, R. M. Martin, D. V. Martynov, J. N. Marx, K. Mason, A. Masserot, T. J. Massinger, M. Masso-Reid, F. Matichard, L. Matone, N. Mavalvala, N. Mazumder, G. Mazzolo, R. McCarthy, D. E. McClelland, S. McCormick, S. C. McGuire, G. McIntyre, J. McIver, D. J. McManus, S. T. McWilliams, D. Meacher, G. D. Meadors, J. Meidam, A. Melatos, G. Mendell, D. Mendoza-Gandara, R. A. Mercer, E. Merilh, M. Merzougui, S. Meshkov, C. Messenger, C. Messick, P. M. Meyers, F. Mezzani, H. Miao, C. Michel, H. Middleton, E. E. Mikhailov, L. Milano, J. Miller, M. Millhouse, Y. Minenkov, J. Ming, S. Mirshekari, C. Mishra, S. Mitra, V. P. Mitrofanov, G. Mitselmakher, R. Mittleman, A. Moggi, M. Mohan, S. R. P. Mohapatra, M. Montani, B. C. Moore, C. J. Moore, D. Moraru, G. Moreno, S. R. Morriss, K. Mossavi, B. Mours, C. M. Mow-Lowry, C. L. Mueller, G. Mueller, A. W. Muir, Arunava Mukherjee, D. Mukherjee, S. Mukherjee, N. Mukund, A. Mullavey, J. Munch, D. J. Murphy, P. G. Murray, A. Mytidis, I. Nardecchia, L. Naticchioni, R. K. Nayak, V. Necula, K. Nedkova, G. Nelemans, M. Neri, A. Neunzert, G. Newton, T. T. Nguyen, A. B. Nielsen, S. Nissanke, A. Nitz, F. Nocera, D. Nolting, M. E. N. Normandin, L. K. Nuttall, J. Oberling, E. Ochsner, J. O'Dell, E. Oelker, G. H. Ogin, J. J. Oh, S. H. Oh, F. Ohme, M. Oliver, P. Oppermann, Richard J. Oram, B. O'Reilly, R. O'Shaughnessy, C. D. Ott, D. J. Ottaway, R. S. Ottens, H. Overmier, B. J. Owen, A. Pai, S. A. Pai, J. R. Palamos, O. Palashov, C. Palomba, A. Pal-Singh, H. Pan, Y. Pan, C. Pankow, F. Pannarale, B. C. Pant, F. Paoletti, A. Paoli, M. A. Papa, H. R. Paris, W. Parker, D. Pascucci, A. Pasqualetti, R. Passaquieti, D. Passuello, B. Patricelli, Z. Patrick,

B. L. Pearlstone, M. Pedraza, R. Pedurand, L. Pekowsky, A. Pele, S. Penn, A. Perreca, H. P. Pfeiffer, M. Phelps, O. Piccinni, M. Pichot, M. Pickenpack, F. Piergiovanni, V. Pierro, G. Pillant, L. Pinard, I. M. Pinto, M. Pitkin, J. H. Poeld, R. Poggiani, P. Popolizio, A. Post, J. Powell, J. Prasad, V. Predoi, S. S. Premachandra, T. Prestegard, L. R. Price, M. Prijatelj, M. Principe, S. Privitera, R. Prix, G. A. Prodi, L. Prokhorov, O. Puncken, M. Punturo, P. Puppo, M. Pürrer, H. Qi, J. Qin, V. Quetschke, E. A. Quintero, R. Quitzow-James, F. J. Raab, D. S. Rabeling, H. Radkins, P. Raffai, S. Raja, M. Rakhmanov, C. R. Ramet, P. Rapagnani, V. Raymond, M. Razzano, V. Re, J. Read, C. M. Reed, T. Regimbau, L. Rei, S. Reid, D. H. Reitze, H. Rew, S. D. Reyes, F. Ricci, K. Riles, N. A. Robertson, R. Robie, F. Robinet, A. Rocchi, L. Rolland, J. G. Rollins, V. J. Roma, J. D. Romano, R. Romano, G. Romanov, J. H. Romie, D. Rosińska, S. Rowan, A. Rüdiger, P. Ruggi, K. Ryan, S. Sachdev, T. Sadecki, L. Sadeghian, L. Salconi, M. Saleem, F. Salemi, A. Samajdar, L. Sammut, L. M. Sampson, E. J. Sanchez, V. Sandberg, B. Sandeen, G. H. Sanders, J. R. Sanders, B. Sassolas, B. S. Sathyaprakash, P. R. Saulson, O. Sauter, R. L. Savage, A. Sawadsky, P. Schale, R. Schilling, J. Schmidt, P. Schmidt, R. Schnabel, R. M. S. Schofield, A. Schönbeck, E. Schreiber, D. Schuette, B. F. Schutz, J. Scott, S. M. Scott, D. Sellers, A. S. Sengupta, D. Sentenac, V. Sequino, A. Sergeev, G. Serna, Y. Setyawati, A. Sevigny, D. A. Shaddock, T. Shaffer, S. Shah, M. S. Shahriar, M. Shaltev, Z. Shao, B. Shapiro, P. Shawhan, A. Sheperd, D. H. Shoemaker, D. M. Shoemaker, K. Siellez, X. Siemens, D. Sigg, A. D. Silva, D. Simakov, A. Singer, L. P. Singer, A. Singh, R. Singh, A. Singhal, A. M. Sintes, B. J. J. Slagmolen, J. R. Smith, M. R. Smith, N. D. Smith, R. J. E. Smith, E. J. Son, B. Sorazu, F. Sorrentino, T. Souradeep, A. K. Srivastava, A. Staley, M. Steinke, J. Steinlechner, S. Steinlechner, D. Steinmeyer, B. C. Stephens, S. P. Stevenson, R. Stone, K. A. Strain, N. Straniero, G. Stratta, N. A. Strauss, S. Strigin, R. Sturani, A. L. Stuver, T. Z. Summerscales, L. Sun, P. J. Sutton, B. L. Swinkels, M. J. Szczepańczyk, M. Tacca, D. Talukder, D. B. Tanner, M. Tápai, S. P. Tarabrin, A. Taracchini, R. Taylor, T. Theeg, M. P. Thirugnanasambandam, E. G. Thomas, M. Thomas, P. Thomas, K. A. Thorne, K. S. Thorne, E. Thrane, S. Tiwari, V. Tiwari, K. V. Tokmakov, C. Tomlinson, M. Tonelli, C. V. Torres, C. I. Torrie, D. Töyrä, F. Travasso, G. Traylor, D. Trifirò, M. C. Tringali, L. Trozzo, M. Tse, M. Turconi, D. Tuyenbayev, D. Ugolini, C. S. Unnikrishnan, A. L. Urban, S. A. Usman, H. Vahlbruch, G. Vajente, G. Valdes, M. Vallisneri, N. van Bakel, M. van Beuzekom, J. F. J. van den Brand, C. Van Den Broeck, D. C. Vander-Hyde, L. van der Schaaf, J. V. van Heijningen, A. A. van Veggel, M. Vardaro, S. Vass, M. Vasúth, R. Vaulin, A. Vecchio, G. Vedovato, J. Veitch, P. J. Veitch, K. Venkateswara, D. Verkindt, F. Vetrano, A. Viceré, S. Vinciguerra, D. J. Vine, J. Y. Vinet, S. Vitale, T. Vo, H. Vocca, C. Vorvick, D. Voss, W. D. Vousden, S. P. Vyatchanin, A. R. Wade, L. E. Wade, M. Wade, S. J. Waldman, M. Walker, L. Wallace, S. Walsh, G. Wang, H. Wang, M. Wang, X. Wang, Y. Wang, H. Ward, R. L. Ward, J. Warner, M. Was, B. Weaver, L. W. Wei, M. Weinert, A. J. Weinstein, R. Weiss, T. Welborn, L. Wen, P. Weßels, T. Westphal, K. Wette, J. T. Whelan, S. E. Whitcomb, D. J. White, B. F. Whiting, K. Wiesner, C. Wilkinson, P. A. Willems, L. Williams, R. D. Williams, A. R. Williamson, J. L. Willis, B. Willke, M. H. Wimmer, L. Winkelmann, W. Winkler, C. C. Wipf, A. G. Wiseman, H. Wittel, G. Woan, J. Worden, J. L. Wright, G. Wu, J. Yablon, I. Yakushin, W. Yam, H. Yamamoto, C. C. Yancey, M. J. Yap, H. Yu, M. Yvert, A. ZadroŻny, L. Zangrando, M. Zanolin, J. P. Zendri, M. Zevin, F. Zhang, L. Zhang, M. Zhang, Y. Zhang, C. Zhao, M. Zhou, Z. Zhou, X. J. Zhu, M. E. Zucker, S. E. Zuraw, J. Zweizig, LIGO Scientific Collaboration, and Virgo Collaboration. Observation of Gravitational Waves from a Binary Black Hole Merger. *Phys. Rev. Lett.*, 116(6):061102, February 2016. doi: 10.1103/PhysRevLett.116.061102.

G. E. Addison, J. Dunkley, and J. R. Bond. Constraining thermal dust emission in distant galaxies with number counts and angular power spectra. *MNRAS*, 436(2):1896–1917, Dec 2013. doi: 10.1093/mnras/stt1703.

J. Aird, A. L. Coil, A. Georgakakis, K. Nandra, G. Barro, and P. G. Pérez-González. The evolution of the X-ray luminosity functions of unabsorbed and absorbed AGNs out to z$\sim$ 5. *MNRAS*, 451(2):1892–1927, August 2015. doi: 10.1093/mnras/stv1062.

J. T. Allen, A. L. Schaefer, N. Scott, L. M. R. Fogarty, I. T. Ho, A. M. Medling, S. K. Leslie, J. Bland-

Hawthorn, J. J. Bryant, S. M. Croom, M. Goodwin, A. W. Green, I. S. Konstantopoulos, J. S. Lawrence, M. S. Owers, S. N. Richards, and R. Sharp. The SAMI Galaxy Survey: unveiling the nature of kinematically offset active galactic nuclei. *MNRAS*, 451(3):2780–2792, August 2015. doi: 10.1093/mnras/stv1121.

M. A. Alvarez. The Kinetic Sunyaev-Zeldovich Effect from Reionization: Simulated Full-sky Maps at Arcminute Resolution. *ApJ*, 824:118, June 2016. doi: 10.3847/0004-637X/824/2/118.

Marcelo A. Alvarez, Simone Ferraro, J. Colin Hill, Renée Hložek, and Margaret Ikape. Mitigating the optical depth degeneracy using the kinematic Sunyaev-Zel'dovich effect with CMB-S4 data. *Phys. Rev. E*, 103 (6):063518, March 2021. doi: 10.1103/PhysRevD.103.063518.

Pau Amaro-Seoane, Alberto Sesana, Loren Hoffman, Matthew Benacquista, Christoph Eichhorn, Junichiro Makino, and Rainer Spurzem. Triplets of supermassive black holes: astrophysics, gravitational waves and detection. *MNRAS*, 402(4):2308–2320, March 2010. doi: 10.1111/j.1365-2966.2009.16104.x.

Pau Amaro-Seoane, Sofiane Aoudia, Stanislav Babak, Pierre Binétruy, Emanuele Berti, Alejandro Bohé, Chiara Caprini, Monica Colpi, Neil J. Cornish, Karsten Danzmann, Jean-François Dufaux, Jonathan Gair, Oliver Jennrich, Philippe Jetzer, Antoine Klein, Ryan N. Lang, Alberto Lobo, Tyson Littenberg, Sean T. McWilliams, Gijs Nelemans, Antoine Petiteau, Edward K. Porter, Bernard F. Schutz, Alberto Sesana, Robin Stebbins, Tim Sumner, Michele Vallisneri, Stefano Vitale, Marta Volonteri, and Henry Ward. Low-frequency gravitational-wave science with eLISA/NGO. *Classical and Quantum Gravity*, 29 (12):124016, June 2012. doi: 10.1088/0264-9381/29/12/124016.

Pau Amaro-Seoane, Heather Audley, Stanislav Babak, John Baker, Enrico Barausse, Peter Bender, Emanuele Berti, Pierre Binetruy, Michael Born, Daniele Bortoluzzi, Jordan Camp, Chiara Caprini, Vitor Cardoso, Monica Colpi, John Conklin, Neil Cornish, Curt Cutler, Karsten Danzmann, Rita Dolesi, Luigi Ferraioli, Valerio Ferroni, Ewan Fitzsimons, Jonathan Gair, Lluis Gesa Bote, Domenico Giardini, Ferran Gibert, Catia Grimani, Hubert Halloin, Gerhard Heinzel, Thomas Hertog, Martin Hewitson, Kelly Holley-Bockelmann, Daniel Hollington, Mauro Hueller, Henri Inchauspe, Philippe Jetzer, Nikos Karnesis, Christian Killow, Antoine Klein, Bill Klipstein, Natalia Korsakova, Shane L Larson, Jeffrey Livas, Ivan Lloro, Nary Man, Davor Mance, Joseph Martino, Ignacio Mateos, Kirk McKenzie, Sean T McWilliams, Cole Miller, Guido Mueller, Germano Nardini, Gijs Nelemans, Miquel Nofrarias, Antoine Petiteau, Paolo Pivato, Eric Plagnol, Ed Porter, Jens Reiche, David Robertson, Norna Robertson, Elena Rossi, Giuliana Russano, Bernard Schutz, Alberto Sesana, David Shoemaker, Jacob Slutsky, Carlos F. Sopuerta, Tim Sumner, Nicola Tamanini, Ira Thorpe, Michael Troebs, Michele Vallisneri, Alberto Vecchio, Daniele Vetrugno, Stefano Vitale, Marta Volonteri, Gudrun Wanner, Harry Ward, Peter Wass, William Weber, John Ziemer, and Peter Zweifel. Laser Interferometer Space Antenna. *arXiv e-prints*, art. arXiv:1702.00786, February 2017.

Pau Amaro-Seoane, Jeff Andrews, Manuel Arca Sedda, Abbas Askar, Quentin Baghi, Razvan Balasov, Imre Bartos, Simone S. Bavera, Jillian Bellovary, Christopher P. L. Berry, Emanuele Berti, Stefano Bianchi, Laura Blecha, Stéphane Blondin, Tamara Bogdanović, Samuel Boissier, Matteo Bonetti, Silvia Bonoli, Elisa Bortolas, Katelyn Breivik, Pedro R. Capelo, Laurentiu Caramete, Federico Cattorini, Maria Charisi, Sylvain Chaty, Xian Chen, Martyna Chruślińska, Alvin J. K. Chua, Ross Church, Monica Colpi, Daniel D'Orazio, Camilla Danielski, Melvyn B. Davies, Pratika Dayal, Alessandra De Rosa, Andrea Derdzinski, Kyriakos Destounis, Massimo Dotti, Ioana Dutan, Irina Dvorkin, Gaia Fabj, Thierry Foglizzo, Saavik Ford, Jean-Baptiste Fouvry, Alessia Franchini, Tassos Fragos, Chris Fryer, Massimo Gaspari, Davide Gerosa, Luca Graziani, Paul Groot, Melanie Habouzit, Daryl Haggard, Zoltan Haiman, Wen-Biao Han, Alina Istrate, Peter H. Johansson, Fazeel Mahmood Khan, Tomas Kimpson, Kostas Kokkotas, Albert Kong, Valeriya Korol, Kyle Kremer, Thomas Kupfer, Astrid Lamberts, Shane Larson, Mike Lau, Dongliang Liu, Nicole Lloyd-Ronning, Giuseppe Lodato, Alessandro Lupi, Chung-Pei Ma, Tomas Maccarone, Ilya Mandel, Alberto Mangiagli, Michela Mapelli, Stéphane Mathis, Lucio Mayer, Sean McGee, Barry McKernan,

M. Coleman Miller, David F. Mota, Matthew Mumpower, Syeda S. Nasim, Gijs Nelemans, Scott Noble, Fabio Pacucci, Francesca Panessa, Vasileios Paschalidis, Hugo Pfister, Delphine Porquet, John Quenby, Angelo Ricarte, Friedrich K. Röpke, John Regan, Stephan Rosswog, Ashley Ruiter, Milton Ruiz, Jessie Runnoe, Raffaella Schneider, Jeremy Schnittman, Amy Secunda, Alberto Sesana, Naoki Seto, Lijing Shao, Stuart Shapiro, Carlos Sopuerta, Nicholas C. Stone, Arthur Suvorov, Nicola Tamanini, Tomas Tamfal, Thomas Tauris, Karel Temmink, John Tomsick, Silvia Toonen, Alejandro Torres-Orjuela, Martina Toscani, Antonios Tsokaros, Caner Unal, Verónica Vázquez-Aceves, Rosa Valiante, Maurice van Putten, Jan van Roestel, Christian Vignali, Marta Volonteri, Kinwah Wu, Ziri Younsi, Shenghua Yu, Silvia Zane, Lorenz Zwick, Fabio Antonini, Vishal Baibhav, Enrico Barausse, Alexander Bonilla Rivera, Marica Branchesi, Graziella Branduardi-Raymont, Kevin Burdge, Srija Chakraborty, Jorge Cuadra, Kristen Dage, Benjamin Davis, Selma E. de Mink, Roberto Decarli, Daniela Doneva, Stephanie Escoffier, Poshak Gandhi, Francesco Haardt, Carlos O. Lousto, Samaya Nissanke, Jason Nordhaus, Richard O'Shaughnessy, Simon Portegies Zwart, Adam Pound, Fabian Schussler, Olga Sergijenko, Alessandro Spallicci, Daniele Vernieri, and Alejandro Vigna-Gómez. Astrophysics with the Laser Interferometer Space Antenna. *Living Reviews in Relativity*, 26(1):2, December 2023. doi: 10.1007/s41114-022-00041-y.

Daniel Anglés-Alcázar, Romeel Davé, Claude-André Faucher-Giguère, Feryal Özel, and Philip F. Hopkins. Gravitational torque-driven black hole growth and feedback in cosmological simulations. *MNRAS*, 464 (3):2840–2853, January 2017. doi: 10.1093/mnras/stw2565.

Daniel Anglés-Alcázar, Eliot Quataert, Philip F. Hopkins, Rachel S. Somerville, Christopher C. Hayward, Claude-André Faucher-Giguère, Greg L. Bryan, Dušan Kereš, Lars Hernquist, and James M. Stone. Cosmological Simulations of Quasar Fueling to Subparsec Scales Using Lagrangian Hyper-refinement. *ApJ*, 917(2):53, August 2021. doi: 10.3847/1538-4357/ac09e8.

Fabio Antonini and David Merritt. Dynamical Friction around Supermassive Black Holes. *ApJ*, 745(1):83, January 2012. doi: 10.1088/0004-637X/745/1/83.

Manuel Arca-Sedda and Alessia Gualandris. Gravitational wave sources from inspiralling globular clusters in the Galactic Centre and similar environments. *MNRAS*, 477(4):4423–4442, July 2018. doi: 10.1093/mnras/sty922.

Eduardo Bañados, Bram P. Venemans, Chiara Mazzucchelli, Emanuele P. Farina, Fabian Walter, Feige Wang, Roberto Decarli, Daniel Stern, Xiaohui Fan, Frederick B. Davies, Joseph F. Hennawi, Robert A. Simcoe, Monica L. Turner, Hans-Walter Rix, Jinyi Yang, Daniel D. Kelson, Gwen C. Rudie, and Jan Martin Winters. An 800-million-solar-mass black hole in a significantly neutral Universe at a redshift of 7.5. *Nature*, 553(7689):473–476, January 2018. doi: 10.1038/nature25180.

Uddipan Banik and Frank C. van den Bosch. A Self-consistent, Time-dependent Treatment of Dynamical Friction: New Insights Regarding Core Stalling and Dynamical Buoyancy. *ApJ*, 912(1):43, May 2021. doi: 10.3847/1538-4357/abeb6d.

Samuel Banks, Katharine Lee, Nazanin Azimi, Kendall Scarborough, Nikolai Stefanov, Indra Periwal, Colin DeGraf, and Tiziana Di Matteo. On the detectability of massive black hole merger eventsby LISA. *arXiv e-prints*, art. arXiv:2107.09084, July 2021.

Enrico Barausse. The evolution of massive black holes and their spins in their galactic hosts. *MNRAS*, 423 (3):2533–2557, July 2012. doi: 10.1111/j.1365-2966.2012.21057.x.

Enrico Barausse, Irina Dvorkin, Michael Tremmel, Marta Volonteri, and Matteo Bonetti. Massive Black Hole Merger Rates: The Effect of Kiloparsec Separation Wandering and Supernova Feedback. *ApJ*, 904 (1):16, November 2020. doi: 10.3847/1538-4357/abba7f.

Josh Barnes and Piet Hut. A hierarchical O(N log N) force-calculation algorithm. *Nature*, 324(6096):446–449, December 1986. doi: 10.1038/324446a0.

R. Scott Barrows, Claud H. Sandberg Lacy, Julia Kennefick, Julia M. Comerford, Daniel Kennefick, and Joel C. Berrier. Identification of Outflows and Candidate Dual Active Galactic Nuclei in SDSS Quasars at z = 0.8-1.6. *ApJ*, 769(2):95, June 2013. doi: 10.1088/0004-637X/769/2/95.

R. Scott Barrows, Julia M. Comerford, and Jenny E. Greene. Spatially Offset Active Galactic Nuclei. III. Discovery of Late-stage Galaxy Mergers with the Hubble Space Telescope. *ApJ*, 869(2):154, December 2018. doi: 10.3847/1538-4357/aaedb6.

Aaron J. Barth, Misty C. Bentz, Jenny E. Greene, and Luis C. Ho. An Offset Seyfert 2 Nucleus in the Minor Merger System NGC 3341. *ApJ*, 683(2):L119, August 2008. doi: 10.1086/591905.

N. Battaglia, A. Natarajan, H. Trac, R. Cen, and A. Loeb. Reionization on Large Scales. III. Predictions for Low-l Cosmic Microwave Background Polarization and High-l Kinetic Sunyaev-Zel'dovich Observables. *ApJ*, 776:83, October 2013a. doi: 10.1088/0004-637X/776/2/83.

N. Battaglia, H. Trac, R. Cen, and A. Loeb. Reionization on Large Scales. I. A Parametric Model Constructed from Radiation-hydrodynamic Simulations. *ApJ*, 776:81, October 2013b. doi: 10.1088/0004-637X/776/2/81.

G. D. Becker, J. S. Bolton, P. Madau, M. Pettini, E. V. Ryan-Weber, and B. P. Venemans. Evidence of patchy hydrogen reionization from an extreme Lyα trough below redshift six. *MNRAS*, 447:3402–3419, March 2015. doi: 10.1093/mnras/stu2646.

M. C. Begelman, R. D. Blandford, and M. J. Rees. Massive black hole binaries in active galactic nuclei. *Nature*, 287(5780):307–309, September 1980. doi: 10.1038/287307a0.

Jillian Bellovary, Marta Volonteri, Fabio Governato, Sijing Shen, Thomas Quinn, and James Wadsley. The First Massive Black Hole Seeds and Their Hosts. *ApJ*, 742(1):13, November 2011. doi: 10.1088/0004-637X/742/1/13.

Jillian M. Bellovary, Fabio Governato, Thomas R. Quinn, James Wadsley, Sijing Shen, and Marta Volonteri. Wandering Black Holes in Bright Disk Galaxy Halos. *ApJ*, 721(2):L148–L152, October 2010. doi: 10.1088/2041-8205/721/2/L148.

Jillian M. Bellovary, Colleen E. Cleary, Ferah Munshi, Michael Tremmel, Charlotte R. Christensen, Alyson Brooks, and Thomas R. Quinn. Multimessenger signatures of massive black holes in dwarf galaxies. *MNRAS*, 482(3):2913–2923, January 2019. doi: 10.1093/mnras/sty2842.

Peter Berczik, David Merritt, Rainer Spurzem, and Hans-Peter Bischof. Efficient Merger of Binary Supermassive Black Holes in Nonaxisymmetric Galaxies. *ApJ*, 642(1):L21–L24, May 2006. doi: 10.1086/504426.

Ingo Berentzen, Miguel Preto, Peter Berczik, David Merritt, and Rainer Spurzem. Binary Black Hole Merger in Galactic Nuclei: Post-Newtonian Simulations. *ApJ*, 695(1):455–468, April 2009. doi: 10.1088/0004-637X/695/1/455.

Edmund Bertschinger. Multiscale Gaussian Random Fields and Their Application to Cosmological Simulations. *ApJS*, 137(1):1–20, November 2001. doi: 10.1086/322526.

Aklant K. Bhowmick, Tiziana Di Matteo, Yu Feng, and Francois Lanusse. The clustering of z $>$ 7 galaxies: predictions from the BLUETIDES simulation. *MNRAS*, 474(4):5393–5405, March 2018. doi: 10.1093/mnras/stx3149.

Stefano Bianchi, Marco Chiaberge, Enrico Piconcelli, Matteo Guainazzi, and Giorgio Matt. Chandra unveils a binary active galactic nucleus in Mrk 463. *MNRAS*, 386(1):105–110, May 2008. doi: 10.1111/j.1365-2966.2008.13078.x.

Nadia Biava, Monica Colpi, Pedro R. Capelo, Matteo Bonetti, Marta Volonteri, Tomas Tamfal, Lucio Mayer, and Alberto Sesana. The lifetime of binary black holes in Sérsic galaxy models. *MNRAS*, 487(4):4985–4994, August 2019. doi: 10.1093/mnras/stz1614.

Pawel Biernacki, Romain Teyssier, and Andreas Bleuler. On the dynamics of supermassive black holes in gas-rich, star-forming galaxies: the case for nuclear star cluster co-evolution. *MNRAS*, 469(1):295–313, July 2017. doi: 10.1093/mnras/stx845.

James Binney and Scott Tremaine. *Galactic Dynamics: Second Edition*. 2008.

Simeon Bird, Yueying Ni, Tiziana Di Matteo, Rupert Croft, Yu Feng, and Nianyi Chen. The ASTRID Simulation: Galaxy Formation and Reionization. *arXiv e-prints*, art. arXiv:2111.01160, November 2021.

Simeon Bird, Yueying Ni, Tiziana Di Matteo, Rupert Croft, Yu Feng, and Nianyi Chen. The ASTRID simulation: galaxy formation and reionization. *MNRAS*, 512(3):3703–3716, May 2022. doi: 10.1093/mnras/stac648.

Laura Blecha, Abraham Loeb, and Ramesh Narayan. Double-peaked narrow-line signatures of dual supermassive black holes in galaxy merger simulations. *MNRAS*, 429(3):2594–2616, March 2013. doi: 10.1093/mnras/sts533.

Laura Blecha, Debora Sijacki, Luke Zoltan Kelley, Paul Torrey, Mark Vogelsberger, Dylan Nelson, Volker Springel, Gregory Snyder, and Lars Hernquist. Recoiling black holes: prospects for detection and implications of spin alignment. *MNRAS*, 456(1):961–989, February 2016. doi: 10.1093/mnras/stv2646.

G. R. Blumenthal, S. M. Faber, J. R. Primack, and M. J. Rees. Formation of galaxies and large-scale structure with cold dark matter. *Nature*, 311:517–525, October 1984. doi: 10.1038/311517a0.

J. R. Bond, S. Cole, G. Efstathiou, and N. Kaiser. Excursion set mass functions for hierarchical Gaussian fluctuations. *ApJ*, 379:440–460, October 1991. doi: 10.1086/170520.

Matteo Bonetti, Francesco Haardt, Alberto Sesana, and Enrico Barausse. Post-Newtonian evolution of massive black hole triplets in galactic nuclei - II. Survey of the parameter space. *MNRAS*, 477(3):3910–3926, July 2018. doi: 10.1093/mnras/sty896.

Matteo Bonetti, Alberto Sesana, Francesco Haardt, Enrico Barausse, and Monica Colpi. Post-Newtonian evolution of massive black hole triplets in galactic nuclei - IV. Implications for LISA. *MNRAS*, 486(3):4044–4060, July 2019. doi: 10.1093/mnras/stz903.

C. M. Booth and Joop Schaye. Cosmological simulations of the growth of supermassive black holes and feedback from active galactic nuclei: method and tests. *MNRAS*, 398(1):53–74, September 2009. doi: 10.1111/j.1365-2966.2009.15043.x.

E. Bortolas, A. Gualandris, M. Dotti, M. Spera, and M. Mapelli. Brownian motion of massive black hole binaries and the final parsec problem. *MNRAS*, 461(1):1023–1031, September 2016. doi: 10.1093/mnras/stw1372.

Elisa Bortolas, Pedro R. Capelo, Tommaso Zana, Lucio Mayer, Matteo Bonetti, Massimo Dotti, Melvyn B. Davies, and Piero Madau. Global torques and stochasticity as the drivers of massive black hole pairing in the young Universe. *MNRAS*, 498(3):3601–3615, November 2020. doi: 10.1093/mnras/staa2628.

R. J. Bouwens, G. D. Illingworth, P. A. Oesch, M. Trenti, I. Labbé, L. Bradley, M. Carollo, P. G. van Dokkum, V. Gonzalez, B. Holwerda, M. Franx, L. Spitler, R. Smit, and D. Magee. UV Luminosity Functions at Redshifts z $\sim$ 4 to z $\sim$ 10: 10,000 Galaxies from HST Legacy Fields. *ApJ*, 803:34, April 2015. doi: 10.1088/0004-637X/803/1/34.

Johannes Buchner, Antonis Georgakakis, Kirpal Nandra, Murray Brightman, Marie-Luise Menzel, Zhu Liu, Li-Ting Hsu, Mara Salvato, Cyprian Rangel, James Aird, Andrea Merloni, and Nicholas Ross. Obscuration-dependent Evolution of Active Galactic Nuclei. *ApJ*, 802(2):89, April 2015. doi: 10.1088/0004-637X/802/2/89.

Simone Callegari, Lucio Mayer, Stelios Kazantzidis, Monica Colpi, Fabio Governato, Thomas Quinn, and James Wadsley. Pairing of Supermassive Black Holes in Unequal-Mass Galaxy Mergers. *ApJ*, 696(1): L89–L92, May 2009. doi: 10.1088/0004-637X/696/1/L89.

Simone Callegari, Stelios Kazantzidis, Lucio Mayer, Monica Colpi, Jillian M. Bellovary, Thomas Quinn, and James Wadsley. Growing Massive Black Hole Pairs in Minor Mergers of Disk Galaxies. *ApJ*, 729(2):85, March 2011. doi: 10.1088/0004-637X/729/2/85.

Pedro R. Capelo, Marta Volonteri, Massimo Dotti, Jillian M. Bellovary, Lucio Mayer, and Fabio Governato. Growth and activity of black holes in galaxy mergers with varying mass ratios. *MNRAS*, 447(3):2123–2143, March 2015. doi: 10.1093/mnras/stu2500.

Pedro R. Capelo, Massimo Dotti, Marta Volonteri, Lucio Mayer, Jillian M. Bellovary, and Sijing Shen. A survey of dual active galactic nuclei in simulations of galaxy mergers: frequency and properties. *MNRAS*, 469(4):4437–4454, August 2017. doi: 10.1093/mnras/stx1067.

John E. Carlstrom, Gilbert P. Holder, and Erik D. Reese. Cosmology with the Sunyaev-Zel'dovich Effect. , 40:643–680, January 2002. doi: 10.1146/annurev.astro.40.060401.093803.

S. Chandrasekhar. Dynamical Friction. I. General Considerations: the Coefficient of Dynamical Friction. *ApJ*, 97:255, March 1943. doi: 10.1086/144517.

Damien Chapon, Lucio Mayer, and Romain Teyssier. Hydrodynamics of galaxy mergers with supermassive black holes: is there a last parsec problem? *MNRAS*, 429(4):3114–3122, March 2013. doi: 10.1093/mnras/sts568.

Nianyi Chen, Aristide Doussot, Hy Trac, and Renyue Cen. SCORCH. III. Analytical Models of Reionization with Varying Clumping Factors. *ApJ*, 905(2):132, December 2020. doi: 10.3847/1538-4357/abc890.

Nianyi Chen, Yueying Ni, Michael Tremmel, Tiziana Di Matteo, Simeon Bird, Colin DeGraf, and Yu Feng. Dynamical Friction Modeling of Massive Black Holes in Cosmological Simulations and Effects on Merger Rate Predictions. *arXiv e-prints*, art. arXiv:2104.00021, March 2021.

Nianyi Chen, Yueying Ni, A. Miguel Holgado, Tiziana Di Matteo, Michael Tremmel, Colin DeGraf, Simeon Bird, Rupert Croft, and Yu Feng. Massive black hole mergers with orbital information: predictions from the ASTRID simulation. *MNRAS*, May 2022a. doi: 10.1093/mnras/stac1432.

Nianyi Chen, Yueying Ni, A. Miguel Holgado, Tiziana Di Matteo, Michael Tremmel, Colin DeGraf, Simeon Bird, Rupert Croft, and Yu Feng. Massive black hole mergers with orbital information: predictions from the ASTRID simulation. *MNRAS*, 514(2):2220–2238, August 2022b. doi: 10.1093/mnras/stac1432.

Nianyi Chen, Yueying Ni, Michael Tremmel, Tiziana Di Matteo, Simeon Bird, Colin DeGraf, and Yu Feng. Dynamical friction modelling of massive black holes in cosmological simulations and effects on merger rate predictions. *MNRAS*, 510(1):531–550, February 2022c. doi: 10.1093/mnras/stab3411.

Nianyi Chen, Tiziana Di Matteo, Yueying Ni, Michael Tremmel, Colin DeGraf, Yue Shen, A. Miguel Holgado, Simeon Bird, Rupert Croft, and Yu Feng. Properties and evolution of dual and offset AGN in the ASTRID simulation at z 2. *MNRAS*, 522(2):1895–1913, June 2023a. doi: 10.1093/mnras/stad834.

Nianyi Chen, Diptajyoti Mukherjee, Tiziana Di Matteo, Yueying Ni, Simeon Bird, and Rupert Croft. MAGICS I. The First Few Orbits Encode the Fate of Seed Massive Black Hole Pairs. *arXiv e-prints*, art. arXiv:2312.09183, December 2023b. doi: 10.48550/arXiv.2312.09183.

Nianyi Chen, Hy Trac, Suvodip Mukherjee, and Renyue Cen. Patchy Kinetic Sunyaev-Zel'dovich Effect with Controlled Reionization History and Morphology. *ApJ*, 943(2):138, February 2023c. doi: 10.3847/1538-4357/ac8481.

Yu-Ching Chen, Hsiang-Chih Hwang, Yue Shen, Xin Liu, Nadia L. Zakamska, Qian Yang, and Jennifer I. Li. Varstrometry for Off-nucleus and Dual Subkiloparsec AGN (VODKA): Hubble Space Telescope Discovers Double Quasars. *ApJ*, 925(2):162, February 2022d. doi: 10.3847/1538-4357/ac401b.

Yu-Ching Chen, Xin Liu, Adi Foord, Yue Shen, Nianyi Chen, Miguel Holgado, Tiziana Di Matteo, Masamune Oguri, Hsiang-Chih Hwang, and Nadia Zakamska. A Close Quasar Pair in a Disk-Disk Galaxy Merger at z = 2.17. *arXiv e-prints*, art. arXiv:2209.11249, September 2022e.

Tirthankar Roy Choudhury, Suvodip Mukherjee, and Sourabh Paul. Cosmic microwave background constraints on a physical model of reionization. *MNRAS*, 501(1):L7–L11, January 2021. doi: 10.1093/mnrasl/slaa185.

Mauricio Cisternas, Knud Jahnke, Katherine J. Inskip, Jeyhan Kartaltepe, Anton M. Koekemoer, Thorsten Lisker, Aday R. Robaina, Marco Scodeggio, Kartik Sheth, Jonathan R. Trump, René Andrae, Takamitsu Miyaji, Elisabeta Lusso, Marcella Brusa, Peter Capak, Nico Cappelluti, Francesca Civano, Olivier Ilbert, Chris D. Impey, Alexie Leauthaud, Simon J. Lilly, Mara Salvato, Nick Z. Scoville, and Yoshi Taniguchi. The Bulk of the Black Hole Growth Since z ~1 Occurs in a Secular Universe: No Major Merger-AGN Connection. *ApJ*, 726(2):57, January 2011. doi: 10.1088/0004-637X/726/2/57.

Monica Colpi. Massive Binary Black Holes in Galactic Nuclei and Their Path to Coalescence. *Space Sci. Rev.*, 183(1-4):189–221, September 2014. doi: 10.1007/s11214-014-0067-1.

Monica Colpi, Lucio Mayer, and Fabio Governato. Dynamical Friction and the Evolution of Satellites in Virialized Halos: The Theory of Linear Response. *ApJ*, 525(2):720–733, November 1999. doi: 10.1086/307952.

Julia M. Comerford and Jenny E. Greene. Offset Active Galactic Nuclei as Tracers of Galaxy Mergers and Supermassive Black Hole Growth. *ApJ*, 789(2):112, July 2014. doi: 10.1088/0004-637X/789/2/112.

Julia M. Comerford, Roger L. Griffith, Brian F. Gerke, Michael C. Cooper, Jeffrey A. Newman, Marc Davis, and Daniel Stern. 1.75 h $^{-1}$ kpc Separation Dual Active Galactic Nuclei at z = 0.36 in the Cosmos Field. *ApJ*, 702(1):L82–L86, September 2009. doi: 10.1088/0004-637X/702/1/L82.

Julia M. Comerford, Brian F. Gerke, Daniel Stern, Michael C. Cooper, Benjamin J. Weiner, Jeffrey A. Newman, Kristin Madsen, and R. Scott Barrows. Kiloparsec-scale Spatial Offsets in Double-peaked Narrow-line Active Galactic Nuclei. I. Markers for Selection of Compelling Dual Active Galactic Nucleus Candidates. *ApJ*, 753(1):42, July 2012. doi: 10.1088/0004-637X/753/1/42.

Julia M. Comerford, David Pooley, R. Scott Barrows, Jenny E. Greene, Nadia L. Zakamska, Greg M. Madejski, and Michael C. Cooper. Merger-driven Fueling of Active Galactic Nuclei: Six Dual and Offset AGNs Discovered with Chandra and Hubble Space Telescope Observations. *ApJ*, 806(2):219, June 2015. doi: 10.1088/0004-637X/806/2/219.

Robert A. Crain, Joop Schaye, Richard G. Bower, Michelle Furlong, Matthieu Schaller, Tom Theuns, Claudio Dalla Vecchia, Carlos S. Frenk, Ian G. McCarthy, John C. Helly, Adrian Jenkins, Yetli M. Rosas-Guevara, Simon D. M. White, and James W. Trayford. The EAGLE simulations of galaxy formation: calibration of subgrid physics and model variations. *MNRAS*, 450(2):1937–1961, June 2015. doi: 10.1093/mnras/stv725.

Romeel Davé, Daniel Anglés-Alcázar, Desika Narayanan, Qi Li, Mika H. Rafieferantsoa, and Sarah Appleby. SIMBA: Cosmological simulations with black hole growth and feedback. *MNRAS*, 486(2):2827–2849, June 2019. doi: 10.1093/mnras/stz937.

Roger de Belsunce, Steven Gratton, William Coulton, and George Efstathiou. Inference of the optical depth to reionization from low multipole temperature and polarization Planck data. *MNRAS*, 507(1):1072–1091, October 2021. doi: 10.1093/mnras/stab2215.

Alessandra De Rosa, Cristian Vignali, Tamara Bogdanović, Pedro R. Capelo, Maria Charisi, Massimo Dotti, Bernd Husemann, Elisabeta Lusso, Lucio Mayer, Zsolt Paragi, Jessie Runnoe, Alberto Sesana, Lisa Steinborn, Stefano Bianchi, Monica Colpi, Luciano del Valle, Sándor Frey, Krisztina É. Gabányi, Margherita Giustini, Matteo Guainazzi, Zoltan Haiman, Noelia Herrera Ruiz, Rubén Herrero-Illana, Kazushi Iwasawa, S. Komossa, Davide Lena, Nora Loiseau, Miguel Perez-Torres, Enrico Piconcelli, and Marta Volonteri. The quest for dual and binary supermassive black holes: A multi-messenger view. , 86:101525, December 2019. doi: 10.1016/j.newar.2020.101525.

David R. DeBoer, Aaron R. Parsons, James E. Aguirre, Paul Alexander, Zaki S. Ali, Adam P. Beardsley, Gianni Bernardi, Judd D. Bowman, Richard F. Bradley, Chris L. Carilli, Carina Cheng, Eloy de Lera Acedo, Joshua S. Dillon, Aaron Ewall-Wice, Gcobisa Fadana, Nicolas Fagnoni, Randall Fritz, Steve R. Furlanetto, Brian Glendenning, Bradley Greig, Jasper Grobbelaar, Bryna J. Hazelton, Jacqueline N. Hewitt, Jack Hickish, Daniel C. Jacobs, Austin Julius, MacCalvin Kariseb, Saul A. Kohn, Telalo Lekalake, Adrian Liu, Anita Loots, David MacMahon, Lourence Malan, Cresshim Malgas, Matthys Maree, Zachary Martinot, Nathan Mathison, Eunice Matsetela, Andrei Mesinger, Miguel F. Morales, Abraham R. Neben, Nipanjana Patra, Samantha Pieterse, Jonathan C. Pober, Nima Razavi-Ghods, Jon Ringuette, James Robnett, Kathryn Rosie, Raddwine Sell, Craig Smith, Angelo Syce, Max Tegmark, Nithyanandan Thyagarajan, Peter K. G. Williams, and Haoxuan Zheng. Hydrogen Epoch of Reionization Array (HERA). *PASP*, 129(974):045001, April 2017. doi: 10.1088/1538-3873/129/974/045001.

C. DeGraf and D. Sijacki. Cosmological simulations of massive black hole seeds: predictions for next-generation electromagnetic and gravitational wave observations. *MNRAS*, 491(4):4973–4992, February 2020. doi: 10.1093/mnras/stz3309.

C. DeGraf et al. High-redshift supermassive black hole mergers insimulations with dynamical friction modelling. *MNRAS*, in prep.

W. Dehnen. A Family of Potential-Density Pairs for Spherical Galaxies and Bulges. *MNRAS*, 265:250, November 1993. doi: 10.1093/mnras/265.1.250.

A. M. Derdzinski, D. D'Orazio, P. Duffell, Z. Haiman, and A. MacFadyen. Probing gas disc physics with LISA: simulations of an intermediate mass ratio inspiral in an accretion disc. *MNRAS*, 486(2):2754–2765, June 2019. doi: 10.1093/mnras/stz1026.

T. Di Matteo, V. Springel, and L. Hernquist. Energy input from quasars regulates the growth and activity of black holes and their host galaxies. *Nature*, 433:604–607, February 2005a. doi: 10.1038/nature03335.

Tiziana Di Matteo, Volker Springel, and Lars Hernquist. Energy input from quasars regulates the growth and activity of black holes and their host galaxies. *Nature*, 433(7026):604–607, February 2005b. doi: 10.1038/nature03335.

Tiziana Di Matteo, Rupert A. C. Croft, Yu Feng, Dacen Waters, and Stephen Wilkins. The origin of the most massive black holes at high-z: BlueTides and the next quasar frontier. *MNRAS*, 467(4):4243–4251, June 2017. doi: 10.1093/mnras/stx319.

Tiziana Di Matteo, Daniel Angles-Alcazar, and Francesco Shankar. Massive black holes in galactic nuclei: Theory and Simulations. *arXiv e-prints*, art. arXiv:2304.11541, April 2023. doi: 10.48550/arXiv.2304.11541.

Scott Dodelson. *Modern Cosmology*. 2003.

Daniel J. D'Orazio and Paul C. Duffell. Orbital Evolution of Equal-mass Eccentric Binaries due to a Gas Disk: Eccentric Inspirals and Circular Outspirals. *ApJ*, 914(1):L21, June 2021. doi: 10.3847/2041-8213/ac0621.

Fani Dosopoulou and Fabio Antonini. Dynamical Friction and the Evolution of Supermassive Black Hole Binaries: The Final Hundred-parsec Problem. *ApJ*, 840(1):31, May 2017. doi: 10.3847/1538-4357/aa6b58.

Aristide Doussot, Hy Trac, and Renyue Cen. SCORCH. II. Radiation-hydrodynamic Simulations of Reionization with Varying Radiation Escape Fractions. *ApJ*, 870(1):18, Jan 2019. doi: 10.3847/1538-4357/aaef75.

Y. Dubois, C. Pichon, C. Welker, D. Le Borgne, J. Devriendt, C. Laigle, S. Codis, D. Pogosyan, S. Arnouts, K. Benabed, E. Bertin, J. Blaizot, F. Bouchet, J. F. Cardoso, S. Colombi, V. de Lapparent, V. Desjacques, R. Gavazzi, S. Kassin, T. Kimm, H. McCracken, B. Milliard, S. Peirani, S. Prunet, S. Rouberol, J. Silk, A. Slyz, T. Sousbie, R. Teyssier, L. Tresse, M. Treyer, D. Vibert, and M. Volonteri. Dancing in the dark: galactic properties trace spin swings along the cosmic web. *MNRAS*, 444(2):1453–1468, October 2014. doi: 10.1093/mnras/stu1227.

Yohan Dubois, Christophe Pichon, Julien Devriendt, Joseph Silk, Martin Haehnelt, Taysun Kimm, and Adrianne Slyz. Blowing cold flows away: the impact of early AGN activity on the formation of a brightest cluster galaxy progenitor. *MNRAS*, 428(4):2885–2900, February 2013. doi: 10.1093/mnras/sts224.

Paul C. Duffell, Daniel D'Orazio, Andrea Derdzinski, Zoltan Haiman, Andrew MacFadyen, Anna L. Rosen, and Jonathan Zrake. Circumbinary Disks: Accretion and Torque as a Function of Mass Ratio and Disk Viscosity. *ApJ*, 901(1):25, September 2020. doi: 10.3847/1538-4357/abab95.

J. Dunkley, E. Calabrese, J. Sievers, G. E. Addison, N. Battaglia, E. S. Battistelli, J. R. Bond, S. Das, M. J. Devlin, R. Dünner, J. W. Fowler, M. Gralla, A. Hajian, M. Halpern, M. Hasselfield, A. D. Hincks, R. Hlozek, J. P. Hughes, K. D. Irwin, A. Kosowsky, T. Louis, T. A. Marriage, D. Marsden, F. Menanteau, K. Moodley, M. Niemack, M. R. Nolta, L. A. Page, B. Partridge, N. Sehgal, D. N. Spergel, S. T. Staggs, E. R. Switzer, H. Trac, and E. Wollack. The Atacama Cosmology Telescope: likelihood for small-scale CMB data. *J. Cosmology Astropart. Phys.*, 2013(7):025, Jul 2013. doi: 10.1088/1475-7516/2013/07/025.

M. Efroimsky and P. Goldreich. Gauge freedom in the N-body problem of celestial mechanics. *A&A*, 415: 1187–1199, March 2004. doi: 10.1051/0004-6361:20034058.

Sara L. Ellison, David R. Patton, J. Trevor Mendel, and Jillian M. Scudder. Galaxy pairs in the Sloan Digital Sky Survey - IV. Interactions trigger active galactic nuclei. *MNRAS*, 418(3):2043–2053, December 2011. doi: 10.1111/j.1365-2966.2011.19624.x.

Andrés Escala, Richard B. Larson, Paolo S. Coppi, and Diego Mardones. The Role of Gas in the Merging of Massive Black Holes in Galactic Nuclei. I. Black Hole Merging in a Spherical Gas Cloud. *ApJ*, 607(2): 765–777, June 2004. doi: 10.1086/386278.

Xiaohui Fan, Vijay K. Narayanan, Robert H. Lupton, Michael A. Strauss, Gillian R. Knapp, Robert H. Becker, Richard L. White, Laura Pentericci, S. K. Leggett, Zoltán Haiman, James E. Gunn, Željko Ivezić, Donald P. Schneider, Scott F. Anderson, J. Brinkmann, Neta A. Bahcall, Andrew J. Connolly, István Csabai, Mamoru Doi, Masataka Fukugita, Tom Geballe, Eva K. Grebel, Daniel Harbeck, Gregory Hennessy, Don Q. Lamb, Gajus Miknaitis, Jeffrey A. Munn, Robert Nichol, Sadanori Okamura, Jeffrey R. Pier, Francisco Prada, Gordon T. Richards, Alex Szalay, and Donald G. York. A Survey of z>5.8 Quasars in the Sloan Digital Sky Survey. I. Discovery of Three New Quasars and the Spatial Density of Luminous Quasars at z~6. *AJ*, 122(6):2833–2849, December 2001. doi: 10.1086/324111.

Claude-André Faucher-Giguère. A cosmic UV/X-ray background model update. *MNRAS*, 493(2):1614–1632, April 2020. doi: 10.1093/mnras/staa302.

Yu Feng, Tiziana Di-Matteo, Rupert A. Croft, Simeon Bird, Nicholas Battaglia, and Stephen Wilkins. The BlueTides simulation: first galaxies and reionization. *MNRAS*, 455(3):2778–2791, January 2016. doi: 10.1093/mnras/stv2484.

Simone Ferraro and Kendrick M. Smith. Characterizing the epoch of reionization with the small-scale CMB: Constraints on the optical depth and duration. *Phys. Rev. E*, 98(12):123519, December 2018. doi: 10.1103/PhysRevD.98.123519.

Davide Fiacconi, Lucio Mayer, Rok Roškar, and Monica Colpi. Massive Black Hole Pairs in Clumpy, Self-gravitating Circumnuclear Disks: Stochastic Orbital Decay. *ApJ*, 777(1):L14, November 2013. doi: 10.1088/2041-8205/777/1/L14.

S. L. Finkelstein, R. E. Ryan, Jr., C. Papovich, M. Dickinson, M. Song, R. S. Somerville, H. C. Ferguson, B. Salmon, M. Giavalisco, A. M. Koekemoer, M. L. N. Ashby, P. Behroozi, M. Castellano, J. S. Dunlop, S. M. Faber, G. G. Fazio, A. Fontana, N. A. Grogin, N. Hathi, J. Jaacks, D. D. Kocevski, R. Livermore, R. J. McLure, E. Merlin, B. Mobasher, J. A. Newman, M. Rafelski, V. Tilvi, and S. P. Willner. The Evolution of the Galaxy Rest-frame Ultraviolet Luminosity Function over the First Two Billion Years. *ApJ*, 810:71, September 2015. doi: 10.1088/0004-637X/810/1/71.

Lee Samuel Finn and Kip S. Thorne. Gravitational waves from a compact star in a circular, inspiral orbit, in the equatorial plane of a massive, spinning black hole, as observed by LISA. *Phys. Rev. E*, 62(12): 124021, December 2000. doi: 10.1103/PhysRevD.62.124021.

T. Fragos, B. Lehmer, M. Tremmel, P. Tzanavaris, A. Basu-Zych, K. Belczynski, A. Hornschemeier, L. Jenkins, V. Kalogera, A. Ptak, and A. Zezas. X-Ray Binary Evolution Across Cosmic Time. *ApJ*, 764(1):41, February 2013. doi: 10.1088/0004-637X/764/1/41.

J. Frank and M. J. Rees. Effects of massive black holes on dense stellar systems. *MNRAS*, 176:633–647, September 1976. doi: 10.1093/mnras/176.3.633.

Hai Fu, Adam D. Myers, S. G. Djorgovski, and Lin Yan. Mergers in Double-peaked [O III] Active Galactic Nuclei. *ApJ*, 733(2):103, June 2011. doi: 10.1088/0004-637X/733/2/103.

Hai Fu, Lin Yan, Adam D. Myers, Alan Stockton, S. G. Djorgovski, G. Aldering, and Jeffrey A. Rich. The Nature of Double-peaked [O III] Active Galactic Nuclei. *ApJ*, 745(1):67, January 2012. doi: 10.1088/0004-637X/745/1/67.

S. R. Furlanetto, M. Zaldarriaga, and L. Hernquist. The Growth of H II Regions During Reionization. *ApJ*, 613:1–15, September 2004. doi: 10.1086/423025.

Lehman H. Garrison, Daniel J. Eisenstein, Douglas Ferrer, Marc V. Metchnik, and Philip A. Pinto. Improving initial conditions for cosmological N-body simulations. *MNRAS*, 461(4):4125–4145, October 2016. doi: 10.1093/mnras/stw1594.

Shy Genel, Mark Vogelsberger, Volker Springel, Debora Sijacki, Dylan Nelson, Greg Snyder, Vicente Rodriguez-Gomez, Paul Torrey, and Lars Hernquist. Introducing the Illustris project: the evolution of galaxy populations across cosmic time. *MNRAS*, 445(1):175–200, November 2014. doi: 10.1093/mnras/stu1654.

E. M. George, C. L. Reichardt, K. A. Aird, B. A. Benson, L. E. Bleem, J. E. Carlstrom, C. L. Chang, H. M. Cho, T. M. Crawford, A. T. Crites, T. de Haan, M. A. Dobbs, J. Dudley, N. W. Halverson, N. L. Harrington, G. P. Holder, W. L. Holzapfel, Z. Hou, J. D. Hrubes, R. Keisler, L. Knox, A. T. Lee, E. M. Leitch, M. Lueker, D. Luong-Van, J. J. McMahon, J. Mehl, S. S. Meyer, M. Millea, L. M. Mocanu, J. J. Mohr, T. E. Montroy, S. Padin, T. Plagge, C. Pryke, J. E. Ruhl, K. K. Schaffer, L. Shaw, E. Shirokoff, H. G. Spieler, Z. Staniszewski, A. A. Stark, K. T. Story, A. van Engelen, K. Vanderlinde, J. D. Vieira, R. Williamson, and O. Zahn. A Measurement of Secondary Cosmic Microwave Background Anisotropies from the 2500 Square-degree SPT-SZ Survey. *ApJ*, 799(2):177, Feb 2015. doi: 10.1088/0004-637X/799/2/177.

Brian F. Gerke, Jeffrey A. Newman, Jennifer Lotz, Renbin Yan, P. Barmby, Alison L. Coil, Christopher J. Conselice, R. J. Ivison, Lihwai Lin, David C. Koo, Kirpal Nandra, Samir Salim, Todd Small, Benjamin J. Weiner, Michael C. Cooper, Marc Davis, S. M. Faber, and Puragra Guhathakurta. The DEEP2 Galaxy Redshift Survey: AEGIS Observations of a Dual AGN at z = 0.7. *ApJ*, 660(1):L23–L26, May 2007. doi: 10.1086/517968.

D. Glazer, M. M. Rau, and H. Trac. The Reionization Parameter Space Consistent with the Thomson Optical Depth from Planck. *Research Notes of the American Astronomical Society*, 2(3):135, August 2018. doi: 10.3847/2515-5172/aad68a.

A. Gorce, S. Ilić, M. Douspis, D. Aubert, and M. Langer. Improved constraints on reionisation from CMB observations: A parameterisation of the kSZ effect. *A&A*, 640:A90, August 2020. doi: 10.1051/0004-6361/202038170.

K. M. Górski, E. Hivon, A. J. Banday, B. D. Wandelt, F. K. Hansen, M. Reinecke, and M. Bartelmann. HEALPix: A Framework for High-Resolution Discretization and Fast Analysis of Data Distributed on the Sphere. *ApJ*, 622:759–771, April 2005. doi: 10.1086/427976.

F. Governato, M. Colpi, and L. Maraschi. The fate of central black holes in merging galaxies. *MNRAS*, 271:317, November 1994. doi: 10.1093/mnras/271.2.317.

L. Greengard and V. Rokhlin. A Fast Algorithm for Particle Simulations. *Journal of Computational Physics*, 73(2):325–348, December 1987. doi: 10.1016/0021-9991(87)90140-9.

Alessia Gualandris, Fazeel Mahmood Khan, Elisa Bortolas, Matteo Bonetti, Alberto Sesana, Peter Berczik, and Kelly Holley-Bockelmann. Eccentricity evolution of massive black hole binaries from formation to coalescence. *MNRAS*, 511(4):4753–4765, April 2022. doi: 10.1093/mnras/stac241.

Minghao Guo, James M. Stone, Chang-Goo Kim, and Eliot Quataert. Toward Horizon-scale Accretion onto Supermassive Black Holes in Elliptical Galaxies. *ApJ*, 946(1):26, March 2023. doi: 10.3847/1538-4357/acb81e.

Mélanie Habouzit, Yuan Li, Rachel S. Somerville, Shy Genel, Annalisa Pillepich, Marta Volonteri, Romeel Davé, Yetli Rosas-Guevara, Stuart McAlpine, Sébastien Peirani, Lars Hernquist, Daniel Anglés-Alcázar, Amy Reines, Richard Bower, Yohan Dubois, Dylan Nelson, Christophe Pichon, and Mark Vogelsberger. Supermassive black holes in cosmological simulations I: M_{BH} - $M_\star$ relation and black hole mass function. *MNRAS*, 503(2):1940–1975, May 2021. doi: 10.1093/mnras/stab496.

Mélanie Habouzit, Masafusa Onoue, Eduardo Bañados, Marcel Neeleman, Daniel Anglés-Alcázar, Fabian Walter, Annalisa Pillepich, Romeel Davé, Knud Jahnke, and Yohan Dubois. Co-evolution of massive black holes and their host galaxies at high redshift: discrepancies from six cosmological simulations and the key role of JWST. *MNRAS*, 511(3):3751–3767, April 2022. doi: 10.1093/mnras/stac225.

M. G. Haehnelt. Low-Frequency Gravitational Waves from Supermassive Black-Holes. *MNRAS*, 269:199, July 1994. doi: 10.1093/mnras/269.1.199.

Oliver Hahn and Tom Abel. Multi-scale initial conditions for cosmological simulations. *MNRAS*, 415(3): 2101–2121, August 2011. doi: 10.1111/j.1365-2966.2011.18820.x.

Zoltán Haiman, Bence Kocsis, and Kristen Menou. The Population of Viscosity- and Gravitational Wave-driven Supermassive Black Hole Binaries Among Luminous Active Galactic Nuclei. *ApJ*, 700(2):1952–1969, August 2009. doi: 10.1088/0004-637X/700/2/1952.

Yuichi Harikane, Yechi Zhang, Kimihiko Nakajima, Masami Ouchi, Yuki Isobe, Yoshiaki Ono, Shun Hatano, Yi Xu, and Hiroya Umeda. A JWST/NIRSpec First Census of Broad-Line AGNs at z=4-7: Detection of 10 Faint AGNs with M_BH~10^{6}-10^{8} M_sun and Their Host Galaxy Properties. *arXiv e-prints*, art. arXiv:2303.11946, March 2023. doi: 10.48550/arXiv.2303.11946.

Yoshikazu Hashimoto, Yoko Funato, and Junichiro Makino. To Circularize or Not To Circularize?-Orbital Evolution of Satellite Galaxies. *ApJ*, 582(1):196–201, January 2003. doi: 10.1086/344260.

Yizhou He, Hy Trac, and Nickolay Y. Gnedin. A Hydro-Particle-Mesh Code for Efficient and Rapid Simulations of the Intracluster Medium. *arXiv e-prints*, art. arXiv:2107.04606, July 2021.

Lars Hernquist. An Analytical Model for Spherical Galaxies and Bulges. *ApJ*, 356:359, June 1990. doi: 10.1086/168845.

G. Hinshaw, D. Larson, E. Komatsu, D. N. Spergel, C. L. Bennett, J. Dunkley, M. R. Nolta, M. Halpern, R. S. Hill, N. Odegard, L. Page, K. M. Smith, J. L. Weiland, B. Gold, N. Jarosik, A. Kogut, M. Limon, S. S. Meyer, G. S. Tucker, E. Wollack, and E. L. Wright. Nine-year Wilkinson Microwave Anisotropy Probe (WMAP) Observations: Cosmological Parameter Results. *ApJS*, 208:19, October 2013. doi: 10.1088/0067-0049/208/2/19.

Michaela Hirschmann, Klaus Dolag, Alexandro Saro, Lisa Bachmann, Stefano Borgani, and Andreas Burkert. Cosmological simulations of black hole growth: AGN luminosities and downsizing. *MNRAS*, 442(3):2304–2324, August 2014. doi: 10.1093/mnras/stu1023.

Y. Hoffman and E. Ribak. Constrained realizations of Gaussian fields - A simple algorithm. *ApJ*, 380:L5–L8, October 1991. doi: 10.1086/186160.

Philip F. Hopkins. A general class of Lagrangian smoothed particle hydrodynamics methods and implications for fluid mixing problems. *MNRAS*, 428(4):2840–2856, February 2013. doi: 10.1093/mnras/sts210.

Philip F. Hopkins, Lars Hernquist, Thomas J. Cox, and Dušan Kereš. A Cosmological Framework for the Co-Evolution of Quasars, Supermassive Black Holes, and Elliptical Galaxies. I. Galaxy Mergers and Quasar Activity. *ApJS*, 175(2):356–389, April 2008. doi: 10.1086/524362.

Kuan-Wei Huang, Tiziana Di Matteo, Aklant K. Bhowmick, Yu Feng, and Chung-Pei Ma. BLUETIDES simulation: establishing black hole-galaxy relations at high redshift. *MNRAS*, 478(4):5063–5073, August 2018. doi: 10.1093/mnras/sty1329.

Sascha Husa, Sebastian Khan, Mark Hannam, Michael Pürrer, Frank Ohme, Xisco Jiménez Forteza, and Alejandro Bohé. Frequency-domain gravitational waves from nonprecessing black-hole binaries. I. New numerical waveforms and anatomy of the signal. *Phys. Rev. E*, 93(4):044006, February 2016. doi: 10.1103/PhysRevD.93.044006.

Hsiang-Chih Hwang, Yue Shen, Nadia Zakamska, and Xin Liu. Varstrometry for Off-nucleus and Dual Subkiloparsec AGN (VODKA): Methodology and Initial Results with Gaia DR2. *ApJ*, 888(2):73, January 2020. doi: 10.3847/1538-4357/ab5c1a.

Ilian T. Iliev, Ue-Li Pen, J. Richard Bond, Garrelt Mellema, and Paul R. Shapiro. The Kinetic Sunyaev-Zel'dovich Effect from Radiative Transfer Simulations of Patchy Reionization. *ApJ*, 660(2):933–944, May 2007. doi: 10.1086/513687.

A. H. Jaffe and D. C. Backer. Gravitational Waves Probe the Coalescence Rate of Massive Black Hole Binaries. *ApJ*, 583(2):616–631, February 2003. doi: 10.1086/345443.

Fredrick A. Jenet, Andrea Lommen, Shane L. Larson, and Linqing Wen. Constraining the Properties of Supermassive Black Hole Systems Using Pulsar Timing: Application to 3C 66B. *ApJ*, 606(2):799–803, May 2004. doi: 10.1086/383020.

Fredrick A. Jenet, George B. Hobbs, K. J. Lee, and Richard N. Manchester. Detecting the Stochastic Gravitational Wave Background Using Pulsar Timing. *ApJ*, 625(2):L123–L126, June 2005. doi: 10.1086/431220.

Adrian Jenkins. Second-order Lagrangian perturbation theory initial conditions for resimulations. *MNRAS*, 403(4):1859–1872, April 2010. doi: 10.1111/j.1365-2966.2010.16259.x.

Michael L. Katz and Shane L. Larson. Evaluating black hole detectability with LISA. *MNRAS*, 483(3):3108–3118, March 2019. doi: 10.1093/mnras/sty3321.

Michael L. Katz, Luke Zoltan Kelley, Fani Dosopoulou, Samantha Berry, Laura Blecha, and Shane L. Larson. Probing massive black hole binary populations with LISA. *MNRAS*, 491(2):2301–2317, January 2020. doi: 10.1093/mnras/stz3102.

N. Katz, L. Hernquist, and D. H. Weinberg. The Clustering of High-Redshift Galaxies in the Cold Dark Matter Scenario. *ApJ*, 523:463–479, October 1999. doi: 10.1086/307744.

Neal Katz, David H. Weinberg, and Lars Hernquist. Cosmological Simulations with TreeSPH. *ApJS*, 105:19, July 1996. doi: 10.1086/192305.

Stelios Kazantzidis, Lucio Mayer, Monica Colpi, Piero Madau, Victor P. Debattista, James Wadsley, Joachim Stadel, Thomas Quinn, and Ben Moore. The Fate of Supermassive Black Holes and the Evolution of the M_{BH}-σ Relation in Merging Galaxies: The Effect of Gaseous Dissipation. *ApJ*, 623(2):L67–L70, April 2005. doi: 10.1086/430139.

Laura C. Keating, Lewis H. Weinberger, Girish Kulkarni, Martin G. Haehnelt, Jonathan Chardin, and Dominique Aubert. Long troughs in the Lyman-α forest below redshift 6 due to islands of neutral hydrogen. *arXiv e-prints*, art. arXiv:1905.12640, May 2019.

Luke Zoltan Kelley, Laura Blecha, and Lars Hernquist. Massive black hole binary mergers in dynamical galactic environments. *MNRAS*, 464(3):3131–3157, January 2017a. doi: 10.1093/mnras/stw2452.

Luke Zoltan Kelley, Laura Blecha, and Lars Hernquist. Massive black hole binary mergers in dynamical galactic environments. *MNRAS*, 464(3):3131–3157, January 2017b. doi: 10.1093/mnras/stw2452.

Luke Zoltan Kelley, Laura Blecha, and Lars Hernquist. Massive black hole binary mergers in dynamical galactic environments. *MNRAS*, 464(3):3131–3157, January 2017c. doi: 10.1093/mnras/stw2452.

Fazeel Mahmood Khan and Kelly Holley-Bockelmann. Extremely efficient mergers of intermediate-mass black hole binaries in nucleated dwarf galaxies. *MNRAS*, 508(1):1174–1188, November 2021. doi: 10.1093/mnras/stab2646.

Fazeel Mahmood Khan, Andreas Just, and David Merritt. Efficient Merger of Binary Supermassive Black Holes in Merging Galaxies. *ApJ*, 732(2):89, May 2011. doi: 10.1088/0004-637X/732/2/89.

Fazeel Mahmood Khan, Ingo Berentzen, Peter Berczik, Andreas Just, Lucio Mayer, Keigo Nitadori, and Simone Callegari. Formation and Hardening of Supermassive Black Hole Binaries in Minor Mergers of Disk Galaxies. *ApJ*, 756(1):30, September 2012. doi: 10.1088/0004-637X/756/1/30.

Fazeel Mahmood Khan, Kelly Holley-Bockelmann, Peter Berczik, and Andreas Just. Supermassive Black Hole Binary Evolution in Axisymmetric Galaxies: The Final Parsec Problem is Not a Problem. *ApJ*, 773(2):100, August 2013. doi: 10.1088/0004-637X/773/2/100.

Sebastian Khan, Sascha Husa, Mark Hannam, Frank Ohme, Michael Pürrer, Xisco Jiménez Forteza, and Alejandro Bohé. Frequency-domain gravitational waves from nonprecessing black-hole binaries. II. A phenomenological model for the advanced detector era. *Phys. Rev. E*, 93(4):044007, February 2016. doi: 10.1103/PhysRevD.93.044007.

Nishikanta Khandai, Tiziana Di Matteo, Rupert Croft, Stephen Wilkins, Yu Feng, Evan Tucker, Colin DeGraf, and Mao-Sheng Liu. The MassiveBlack-II simulation: the evolution of haloes and galaxies to z $\sim$ 0. *MNRAS*, 450(2):1349–1374, June 2015. doi: 10.1093/mnras/stv627.

Ji-hoon Kim, Tom Abel, Oscar Agertz, Greg L. Bryan, Daniel Ceverino, Charlotte Christensen, Charlie Conroy, Avishai Dekel, Nickolay Y. Gnedin, Nathan J. Goldbaum, Javiera Guedes, Oliver Hahn, Alexander Hobbs, Philip F. Hopkins, Cameron B. Hummels, Francesca Iannuzzi, Dusan Keres, Anatoly Klypin, Andrey V. Kravtsov, Mark R. Krumholz, Michael Kuhlen, Samuel N. Leitner, Piero Madau, Lucio Mayer, Christopher E. Moody, Kentaro Nagamine, Michael L. Norman, Jose Onorbe, Brian W. O'Shea, Annalisa Pillepich, Joel R. Primack, Thomas Quinn, Justin I. Read, Brant E. Robertson, Miguel Rocha, Douglas H. Rudd, Sijing Shen, Britton D. Smith, Alexander S. Szalay, Romain Teyssier, Robert Thompson, Keita Todoroki, Matthew J. Turk, James W. Wadsley, John H. Wise, Adi Zolotov, and the AGORA Collaboration29. The AGORA High-resolution Galaxy Simulations Comparison Project. *ApJS*, 210(1):14, January 2014. doi: 10.1088/0067-0049/210/1/14.

Ji-hoon Kim, Oscar Agertz, Romain Teyssier, Michael J. Butler, Daniel Ceverino, Jun-Hwan Choi, Robert Feldmann, Ben W. Keller, Alessandro Lupi, Thomas Quinn, Yves Revaz, Spencer Wallace, Nickolay Y. Gnedin, Samuel N. Leitner, Sijing Shen, Britton D. Smith, Robert Thompson, Matthew J. Turk, Tom Abel, Kenza S. Arraki, Samantha M. Benincasa, Sukanya Chakrabarti, Colin DeGraf, Avishai Dekel, Nathan J. Goldbaum, Philip F. Hopkins, Cameron B. Hummels, Anatoly Klypin, Hui Li, Piero Madau, Nir Mandelker, Lucio Mayer, Kentaro Nagamine, Sarah Nickerson, Brian W. O'Shea, Joel R. Primack, Santi Roca-Fàbrega, Vadim Semenov, Ikkoh Shimizu, Christine M. Simpson, Keita Todoroki, James W. Wadsley, John H. Wise, and AGORA Collaboration. The AGORA High-resolution Galaxy Simulations Comparison Project. II. Isolated Disk Test. *ApJ*, 833(2):202, December 2016. doi: 10.3847/1538-4357/833/2/202.

Antoine Klein, Enrico Barausse, Alberto Sesana, Antoine Petiteau, Emanuele Berti, Stanislav Babak, Jonathan Gair, Sofiane Aoudia, Ian Hinder, Frank Ohme, and Barry Wardell. Science with the space-based interferometer elisa: Supermassive black hole binaries. *Phys. Rev. D*, 93:024003, Jan 2016. doi: 10.1103/PhysRevD.93.024003. URL `https://link.aps.org/doi/10.1103/PhysRevD.93.024003`.

Steffen R. Knollmann and Alexander Knebe. AHF: Amiga's Halo Finder. *ApJS*, 182(2):608–624, June 2009. doi: 10.1088/0067-0049/182/2/608.

Dale D. Kocevski, Murray Brightman, Kirpal Nandra, Anton M. Koekemoer, Mara Salvato, James Aird, Eric F. Bell, Li-Ting Hsu, Jeyhan S. Kartaltepe, David C. Koo, Jennifer M. Lotz, Daniel H. McIntosh, Mark Mozena, David Rosario, and Jonathan R. Trump. Are Compton-thick AGNs the Missing Link between Mergers and Black Hole Growth? *ApJ*, 814(2):104, December 2015. doi: 10.1088/0004-637X/814/2/104.

Dale D. Kocevski, Masafusa Onoue, Kohei Inayoshi, Jonathan R. Trump, Pablo Arrabal Haro, Andrea Grazian, Mark Dickinson, Steven L. Finkelstein, Jeyhan S. Kartaltepe, Michaela Hirschmann, James Aird, Benne W. Holwerda, Seiji Fujimoto, Stéphanie Juneau, Ricardo O. Amorín, Bren E. Backhaus, Micaela B. Bagley, Guillermo Barro, Eric F. Bell, Laura Bisigello, Antonello Calabrò, Nikko J. Cleri, M. C. Cooper, Xuheng Ding, Norman A. Grogin, Luis C. Ho, Taylor A. Hutchison, Akio K. Inoue, Linhua Jiang, Brenda Jones, Anton M. Koekemoer, Wenxiu Li, Zhengrong Li, Elizabeth J. McGrath, Juan Molina, Casey Papovich, Pablo G. Pérez-González, Nor Pirzkal, Stephen M. Wilkins, Guang Yang, and L. Y. Aaron Yung. Hidden Little Monsters: Spectroscopic Identification of Low-mass, Broad-line AGNs at z $>$ 5 with CEERS. *ApJ*, 954(1):L4, September 2023. doi: 10.3847/2041-8213/ace5a0.

H. Koehn, A. Just, P. Berczik, and M. Tremmel. Dynamics of supermassive black hole triples in the ROMULUS25 cosmological simulation. *A&A*, 678:A11, October 2023. doi: 10.1051/0004-6361/202347093.

L. Koopmans, J. Pritchard, G. Mellema, J. Aguirre, K. Ahn, R. Barkana, I. van Bemmel, G. Bernardi, A. Bonaldi, F. Briggs, A. G. de Bruyn, T. C. Chang, E. Chapman, X. Chen, B. Ciardi, P. Dayal, A. Ferrara, A. Fialkov, F. Fiore, K. Ichiki, I. T. Illiev, S. Inoue, V. Jelic, M. Jones, J. Lazio, U. Maio, S. Majumdar, K. J. Mack, A. Mesinger, M. F. Morales, A. Parsons, U. L. Pen, M. Santos, R. Schneider, B. Semelin, R. S. de Souza, R. Subrahmanyan, T. Takeuchi, H. Vedantham, J. Wagg, R. Webster, S. Wyithe, K. K. Datta, and C. Trott. The Cosmic Dawn and Epoch of Reionisation with SKA. In *Advancing Astrophysics with the Square Kilometre Array (AASKA14)*, page 1, April 2015. doi: 10.22323/1.215.0001.

John Kormendy and Luis C. Ho. Coevolution (Or Not) of Supermassive Black Holes and Host Galaxies. , 51(1):511–653, August 2013. doi: 10.1146/annurev-astro-082708-101811.

John Kormendy and Douglas Richstone. Inward Bound—The Search For Supermassive Black Holes In Galactic Nuclei. , 33:581, January 1995. doi: 10.1146/annurev.aa.33.090195.003053.

Michael Koss, Richard Mushotzky, Ezequiel Treister, Sylvain Veilleux, Ranjan Vasudevan, and Margaret Trippe. Understanding Dual Active Galactic Nucleus Activation in the nearby Universe. *ApJ*, 746(2):L22, February 2012. doi: 10.1088/2041-8205/746/2/L22.

Michael J. Koss, Laura Blecha, Phillip Bernhard, Chao-Ling Hung, Jessica R. Lu, Benny Trakhtenbrot, Ezequiel Treister, Anna Weigel, Lia F. Sartori, Richard Mushotzky, Kevin Schawinski, Claudio Ricci, Sylvain Veilleux, and David B. Sanders. A population of luminous accreting black holes with hidden mergers. *Nature*, 563(7730):214–216, November 2018. doi: 10.1038/s41586-018-0652-7.

M. R. Krumholz and N. Y. Gnedin. A Comparison of Methods for Determining the Molecular Content of Model Galaxies. *ApJ*, 729:36, March 2011. doi: 10.1088/0004-637X/729/1/36.

Andrea Kulier, Jeremiah P. Ostriker, Priyamvada Natarajan, Claire N. Lackner, and Renyue Cen. Understanding Black Hole Mass Assembly via Accretion and Mergers at Late Times in Cosmological Simulations. *ApJ*, 799(2):178, February 2015. doi: 10.1088/0004-637X/799/2/178.

Cedric Lacey and Shaun Cole. Merger rates in hierarchical models of galaxy formation. *MNRAS*, 262(3): 627–649, June 1993. doi: 10.1093/mnras/262.3.627.

Dong Lai and Diego J. Muñoz. Circumbin@ARTICLE2003ApJ...591..499A, author = Abadi, Mario G. and Navarro, Julio F. and Steinmetz, Matthias and Eke, Vincent R., title = "Simulations of Galaxy Formation in a Λ Cold Dark Matter Universe. I. Dynamical and Photometric Properties of a Simulated Disk Galaxy", journal = ApJ, keywords = Cosmology: Theory, Cosmology: Dark Matter, Galaxies: Formation, Galaxies: Structure, Methods: Numerical, Astrophysics, year = 2003, month = jul, volume = 591, number = 2, pages = 499-514, doi = 10.1086/375512, archivePrefix = arXiv, eprint = astro-ph/0211331, primaryClass = astro-ph, adsurl = https://ui.adsabs.harvard.edu/abs/2003ApJ...591..499A, adsnote = Provided by the SAO/NASA Astrophysics Data System ary Accretion: From Binary Stars to Massive Binary Black Holes. , 61:517–560, August 2023. doi: 10.1146/annurev-astro-052622-022933.

G. Lanzuisi, F. Civano, S. Marchesi, A. Comastri, M. Brusa, R. Gilli, C. Vignali, G. Zamorani, M. Brightman, R. E. Griffiths, and A. M. Koekemoer. The Chandra COSMOS Legacy Survey: Compton thick AGN at high redshift. *MNRAS*, 480(2):2578–2592, October 2018. doi: 10.1093/mnras/sty2025.

B. D. Lehmer, A. R. Basu-Zych, S. Mineo, W. N. Brandt, R. T. Eufrasio, T. Fragos, A. E. Hornschemeier, B. Luo, Y. Q. Xue, F. E. Bauer, M. Gilfanov, P. Ranalli, D. P. Schneider, O. Shemmer, P. Tozzi, J. R. Trump, C. Vignali, J. X. Wang, M. Yukita, and A. Zezas. The Evolution of Normal Galaxy X-Ray Emission through Cosmic History: Constraints from the 6 MS Chandra Deep Field-South. *ApJ*, 825(1): 7, July 2016. doi: 10.3847/0004-637X/825/1/7.

Sean M. Lemons, Amy E. Reines, Richard M. Plotkin, Elena Gallo, and Jenny E. Greene. An X-Ray Selected Sample of Candidate Black Holes in Dwarf Galaxies. *ApJ*, 805(1):12, May 2015. doi: 10.1088/0004-637X/805/1/12.

Julien Lesgourgues. The Cosmic Linear Anisotropy Solving System (CLASS) I: Overview. *arXiv e-prints*, art. arXiv:1104.2932, April 2011. doi: 10.48550/arXiv.1104.2932.

Antony Lewis and Anthony Challinor. CAMB: Code for Anisotropies in the Microwave Background. Astrophysics Source Code Library, record ascl:1102.026, February 2011.

Shihong Liao, Dimitrios Irodotou, Peter H. Johansson, Thorsten Naab, Francesco Paolo Rizzuto, Jessica M. Hislop, Alexander Rawlings, and Ruby J. Wright. RABBITS – II. The crucial role of nuclear star formation in driving the coalescence of supermassive black hole binaries. *arXiv e-prints*, art. arXiv:2311.01499, November 2023a. doi: 10.48550/arXiv.2311.01499.

Shihong Liao, Dimitrios Irodotou, Peter H. Johansson, Thorsten Naab, Francesco Paolo Rizzuto, Jessica M. Hislop, Ruby J. Wright, and Alexander Rawlings. RABBITS – I. The impact of AGN feedback on coalescing supermassive black holes in disc and elliptical galaxy mergers. *arXiv e-prints*, art. arXiv:2311.01493, November 2023b. doi: 10.48550/arXiv.2311.01493.

A. P. Lightman and S. L. Shapiro. The distribution and consumption rate of stars around a massive, collapsed object. *ApJ*, 211:244–262, January 1977. doi: 10.1086/154925.

Xin Liu, Yue Shen, Michael A. Strauss, and Lei Hao. Active Galactic Nucleus Pairs from the Sloan Digital Sky Survey. I. The Frequency on ~5-100 kpc Scales. *ApJ*, 737(2):101, August 2011. doi: 10.1088/0004-637X/737/2/101.

Xin Liu, Yue Shen, and Michael A. Strauss. Active Galactic Nucleus Pairs from the Sloan Digital Sky Survey. II. Evidence for Tidally Enhanced Star Formation and Black Hole Accretion. *ApJ*, 745(1):94, January 2012. doi: 10.1088/0004-637X/745/1/94.

Jennifer M. Lotz, Patrik Jonsson, T. J. Cox, Darren Croton, Joel R. Primack, Rachel S. Somerville, and Kyle Stewart. The Major and Minor Galaxy Merger Rates at z $<$ 1.5. *ApJ*, 742(2):103, December 2011. doi: 10.1088/0004-637X/742/2/103.

Linhao Ma, Philip F. Hopkins, Xiangcheng Ma, Daniel Anglés-Alcázar, Claude-André Faucher-Giguère, and Luke Zoltan Kelley. Seeds don't sink: even massive black hole 'seeds' cannot migrate to galaxy centres efficiently. *MNRAS*, 508(2):1973–1985, December 2021. doi: 10.1093/mnras/stab2713.

John Magorrian, Scott Tremaine, Douglas Richstone, Ralf Bender, Gary Bower, Alan Dressler, S. M. Faber, Karl Gebhardt, Richard Green, Carl Grillmair, John Kormendy, and Tod Lauer. The Demography of Massive Dark Objects in Galaxy Centers. *AJ*, 115(6):2285–2305, June 1998. doi: 10.1086/300353.

Roberto Maiolino, Jan Scholtz, Joris Witstok, Stefano Carniani, Francesco D'Eugenio, Anna de Graaff, Hannah Uebler, Sandro Tacchella, Emma Curtis-Lake, Santiago Arribas, Andrew Bunker, Stéphane Charlot, Jacopo Chevallard, Mirko Curti, Tobias J. Looser, Michael V. Maseda, Tim Rawle, Bruno Rodriguez Del Pino, Chris J. Willott, Eiichi Egami, Daniel Eisenstein, Kevin Hainline, Brant Robertson, Christina C. Williams, Christopher N. A. Willmer, William M. Baker, Kristan Boyett, Christa DeCoursey, Andrew C. Fabian, Jakob M. Helton, Zhiyuan Ji, Gareth C. Jones, Nimisha Kumari, Nicolas Laporte, Erica Nelson, Michele Perna, Lester Sandles, Irene Shivaei, and Fengwu Sun. A small and vigorous black hole in the early Universe. *arXiv e-prints*, art. arXiv:2305.12492, May 2023. doi: 10.48550/arXiv.2305.12492.

Alberto Mangiagli, Matteo Bonetti, Alberto Sesana, and Monica Colpi. Merger Rate of Stellar Black Hole Binaries above the Pair-instability Mass Gap. *ApJ*, 883(1):L27, September 2019. doi: 10.3847/2041-8213/ab3f33.

Matias Mannerkoski, Peter H. Johansson, Pauli Pihajoki, Antti Rantala, and Thorsten Naab. Gravitational Waves from the Inspiral of Supermassive Black Holes in Galactic-scale Simulations. *ApJ*, 887(1):35, December 2019. doi: 10.3847/1538-4357/ab52f9.

Matias Mannerkoski, Peter H. Johansson, Antti Rantala, Thorsten Naab, Shihong Liao, and Alexander Rawlings. Signatures of the Many Supermassive Black Hole Mergers in a Cosmologically Forming Massive Early-Type Galaxy. *arXiv e-prints*, art. arXiv:2112.03576, December 2021.

F. Mannucci, E. Pancino, F. Belfiore, C. Cicone, A. Ciurlo, G. Cresci, E. Lusso, A. Marasco, A. Marconi, E. Nardini, E. Pinna, P. Severgnini, P. Saracco, G. Tozzi, and S. Yeh. Unveiling the population of dual and lensed active galactic nuclei at sub-arcsec separations. *Nature Astronomy*, 6:1185–1192, August 2022. doi: 10.1038/s41550-022-01761-5.

Madeline A. Marshall, Yueying Ni, Tiziana Di Matteo, J. Stuart B. Wyithe, Stephen Wilkins, Rupert A. C. Croft, and Jussi K. Kuusisto. The host galaxies of z = 7 quasars: predictions from the BLUETIDES simulation. *MNRAS*, 499(3):3819–3836, December 2020. doi: 10.1093/mnras/staa2982.

Madeline A. Marshall, J. Stuart B. Wyithe, Rogier A. Windhorst, Tiziana Di Matteo, Yueying Ni, Stephen Wilkins, Rupert A. C. Croft, and Mira Mechtley. Observing the host galaxies of high-redshift quasars with JWST: predictions from the BlueTides simulation. *arXiv e-prints*, art. arXiv:2101.01219, January 2021.

Jorryt Matthee, Rohan P. Naidu, Gabriel Brammer, John Chisholm, Anna-Christina Eilers, Andy Goulding, Jenny Greene, Daichi Kashino, Ivo Labbe, Simon J. Lilly, Ruari Mackenzie, Pascal A. Oesch, Andrea Weibel, Stijn Wuyts, Mengyuan Xiao, Rongmon Bordoloi, Rychard Bouwens, Pieter van Dokkum, Garth Illingworth, Ivan Kramarenko, Michael V. Maseda, Charlotte Mason, Romain A. Meyer, Erica J. Nelson, Naveen A. Reddy, Irene Shivaei, Robert A. Simcoe, and Minghao Yue. Little Red Dots: an abundant population of faint AGN at $z \sim 5$ revealed by the EIGER and FRESCO JWST surveys. *arXiv e-prints*, art. arXiv:2306.05448, June 2023. doi: 10.48550/arXiv.2306.05448.

R. C. McGurk, C. E. Max, D. J. Rosario, G. A. Shields, K. L. Smith, and S. A. Wright. Spatially Resolved Spectroscopy of SDSS J0952+2552: A Confirmed Dual Active Galactic Nucleus. *ApJ*, 738(1):L2, September 2011. doi: 10.1088/2041-8205/738/1/L2.

Matthew McQuinn, Steven R. Furlanetto, Lars Hernquist, Oliver Zahn, and Matias Zaldarriaga. The Kinetic Sunyaev-Zel'dovich Effect from Reionization. *ApJ*, 630(2):643–656, September 2005. doi: 10.1086/432049.

M. Mechtley, K. Jahnke, R. A. Windhorst, R. Andrae, M. Cisternas, S. H. Cohen, T. Hewlett, A. M. Koekemoer, M. Schramm, A. Schulze, J. D. Silverman, C. Villforth, A. van der Wel, and L. Wisotzki. Do the Most Massive Black Holes at z = 2 Grow via Major Mergers? *ApJ*, 830(2):156, October 2016. doi: 10.3847/0004-637X/830/2/156.

David Merritt. *Dynamics and Evolution of Galactic Nuclei*. 2013.

A. Mesinger, S. Furlanetto, and R. Cen. 21CMFAST: a fast, seminumerical simulation of the high-redshift 21-cm signal. *MNRAS*, 411:955–972, February 2011. doi: 10.1111/j.1365-2966.2010.17731.x.

Andrei Mesinger, Matthew McQuinn, and David N. Spergel. The kinetic Sunyaev-Zel'dovich signal from inhomogeneous reionization: a parameter space study. *MNRAS*, 422(2):1403–1417, May 2012. doi: 10.1111/j.1365-2966.2012.20713.x.

J. M. Miller. Relativistic X-Ray Lines from the Inner Accretion Disks Around Black Holes. , 45(1):441–479, September 2007. doi: 10.1146/annurev.astro.45.051806.110555.

Miloš Milosavljević and David Merritt. Formation of Galactic Nuclei. *ApJ*, 563(1):34–62, December 2001. doi: 10.1086/323830.

Chiara M. F. Mingarelli, T. Joseph W. Lazio, Alberto Sesana, Jenny E. Greene, Justin A. Ellis, Chung-Pei Ma, Steve Croft, Sarah Burke-Spolaor, and Stephen R. Taylor. The local nanohertz gravitational-wave landscape from supermassive black hole binaries. *Nature Astronomy*, 1:886–892, November 2017. doi: 10.1038/s41550-017-0299-6.

J. J. Monaghan. Smoothed particle hydrodynamics. , 30:543–574, January 1992. doi: 10.1146/annurev.aa.30.090192.002551.

C. J. Moore, R. H. Cole, and C. P. L. Berry. Gravitational-wave sensitivity curves. *Classical and Quantum Gravity*, 32(1):015014, January 2015. doi: 10.1088/0264-9381/32/1/015014.

Edward C. Moran, Karlen Shahinyan, Hannah R. Sugarman, Darik O. Vélez, and Michael Eracleous. Black Holes At the Centers of Nearby Dwarf Galaxies. *AJ*, 148(6):136, December 2014. doi: 10.1088/0004-6256/148/6/136.

Diptajyoti Mukherjee, Qirong Zhu, Hy Trac, and Carl L. Rodriguez. Fast Multipole Methods for N-body Simulations of Collisional Star Systems. *ApJ*, 916(1):9, July 2021. doi: 10.3847/1538-4357/ac03b2.

Diptajyoti Mukherjee, Qirong Zhu, Go Ogiya, Carl L. Rodriguez, and Hy Trac. Evolution of massive black hole binaries in collisionally relaxed nuclear star clusters - Impact of mass segregation. *MNRAS*, 518(4): 4801–4817, February 2023. doi: 10.1093/mnras/stac3390.

F. Müller-Sánchez, J. M. Comerford, R. Nevin, R. S. Barrows, M. C. Cooper, and J. E. Greene. The Origin of Double-peaked Narrow Lines in Active Galactic Nuclei. I. Very Large Array Detections of Dual AGNs and AGN Outflows. *ApJ*, 813(2):103, November 2015. doi: 10.1088/0004-637X/813/2/103.

Imran Nasim, Alessia Gualandris, Justin Read, Walter Dehnen, Maxime Delorme, and Fabio Antonini. Defeating stochasticity: coalescence time-scales of massive black holes in galaxy mergers. *MNRAS*, 497 (1):739–746, September 2020. doi: 10.1093/mnras/staa1896.

Priyamvada Natarajan, Fabio Pacucci, Andrea Ferrara, Bhaskar Agarwal, Angelo Ricarte, Erik Zackrisson, and Nico Cappelluti. Unveiling the First Black Holes With JWST:Multi-wavelength Spectral Predictions. *ApJ*, 838(2):117, April 2017. doi: 10.3847/1538-4357/aa6330.

Dieu D. Nguyen, Anil C. Seth, Nadine Neumayer, Satoru Iguchi, Michelle Cappellari, Jay Strader, Laura Chomiuk, Evangelia Tremou, Fabio Pacucci, Kouichiro Nakanishi, Arash Bahramian, Phuong M. Nguyen, Mark den Brok, Christopher C. Ahn, Karina T. Voggel, Nikolay Kacharov, Takafumi Tsukui, Cuc K. Ly, Antoine Dumont, and Renuka Pechetti. Improved Dynamical Constraints on the Masses of the Central Black Holes in Nearby Low-mass Early-type Galactic Nuclei and the First Black Hole Determination for NGC 205. *ApJ*, 872(1):104, February 2019. doi: 10.3847/1538-4357/aafe7a.

Yueying Ni, Tiziana Di Matteo, Yu Feng, Rupert A. C. Croft, and Ananth Tenneti. Gas outflows from the z = 7.54 quasar: predictions from the BLUETIDES simulation. *MNRAS*, 481(4):4877–4884, December 2018. doi: 10.1093/mnras/sty2616.

Yueying Ni, Tiziana Di Matteo, and Yu Feng. Not all peaks are created equal: the early growth of Supermassive Black Holes. *arXiv e-prints*, art. arXiv:2012.04714, December 2020.

Yueying Ni, Tiziana Di Matteo, Simeon Bird, Rupert Croft, Yu Feng, Nianyi Chen, Michael Tremmel, Colin DeGraf, and Yin Li. The ASTRID simulation: the evolution of Supermassive Black Holes. *arXiv e-prints*, art. arXiv:2110.14154, October 2021.

Yueying Ni, Tiziana Di Matteo, Simeon Bird, Rupert Croft, Yu Feng, Nianyi Chen, Michael Tremmel, Colin DeGraf, and Yin Li. The ASTRID simulation: the evolution of supermassive black holes. *MNRAS*, 513 (1):670–692, June 2022. doi: 10.1093/mnras/stac351.

Go Ogiya, Oliver Hahn, Chiara M. F. Mingarelli, and Marta Volonteri. Accelerated orbital decay of supermassive black hole binaries in merging nuclear star clusters. *MNRAS*, 493(3):3676–3689, April 2020. doi: 10.1093/mnras/staa444.

Takashi Okamoto, Carlos S. Frenk, Adrian Jenkins, and Tom Theuns. The properties of satellite galaxies in simulations of galaxy formation. *MNRAS*, 406(1):208–222, July 2010. doi: 10.1111/j.1365-2966.2010.16690.x.

Eve C. Ostriker. Dynamical Friction in a Gaseous Medium. *ApJ*, 513(1):252–258, March 1999. doi: 10.1086/306858.

J. P. Ostriker and E. T. Vishniac. Generation of microwave background fluctuations from nonlinear perturbations at the ERA of galaxy formation. *ApJ*, 306:L51–L54, July 1986. doi: 10.1086/184704.

Fabio Pacucci, Bao Nguyen, Stefano Carniani, Roberto Maiolino, and Xiaohui Fan. JWST CEERS and JADES Active Galaxies at z = 4-7 Violate the Local M -M $_\star$ Relation at $>3\sigma$: Implications for Low-mass Black Holes and Seeding Models. *ApJ*, 957(1):L3, November 2023. doi: 10.3847/2041-8213/ad0158.

L. Pagano, J. M. Delouis, S. Mottet, J. L. Puget, and L. Vibert. Reionization optical depth determination from Planck HFI data with ten percent accuracy. *A&A*, 635:A99, March 2020. doi: 10.1051/0004-6361/201936630.

K. Pardo, A. D. Goulding, J. E. Greene, R. S. Somerville, E. Gallo, R. C. Hickox, B. P. Miller, A. E. Reines, and J. D. Silverman. X-Ray Detected Active Galactic Nuclei in Dwarf Galaxies at $0 < z < 1$. *ApJ*, 831 (2):203, November 2016. doi: 10.3847/0004-637X/831/2/203.

Hyunbae Park, Paul R. Shapiro, Eiichiro Komatsu, Ilian T. Iliev, Kyungjin Ahn, and Garrelt Mellema. The Kinetic Sunyaev-Zel'dovich Effect as a Probe of the Physics of Cosmic Reionization: The Effect of Self-regulated Reionization. *ApJ*, 769(2):93, June 2013. doi: 10.1088/0004-637X/769/2/93.

KwangHo Park and Tamara Bogdanović. Gaseous Dynamical Friction in Presence of Black Hole Radiative Feedback. *ApJ*, 838(2):103, April 2017. doi: 10.3847/1538-4357/aa65ce.

Christian Partmann, Thorsten Naab, Antti Rantala, Anna Genina, Matias Mannerkoski, and Peter H. Johansson. The difficult path to coalescence: massive black hole dynamics in merging low mass dark matter haloes and galaxies. *arXiv e-prints*, art. arXiv:2310.08079, October 2023. doi: 10.48550/arXiv.2310.08079.

Sourabh Paul, Suvodip Mukherjee, and Tirthankar Roy Choudhury. Inevitable imprints of patchy reionization on the cosmic microwave background anisotropy. *MNRAS*, 500(1):232–246, January 2021. doi: 10.1093/mnras/staa3221.

Federico I. Pelupessy, Padeli P. Papadopoulos, and P. van der Werf. Incorporating the Molecular Gas Phase in Galaxy-sized Numerical Simulations: First Applications in Dwarf Galaxies. *ApJ*, 645(2):1024–1042, July 2006. doi: 10.1086/504366.

P. C. Peters. Gravitational Radiation and the Motion of Two Point Masses. *Physical Review*, 136(4B): 1224–1232, November 1964. doi: 10.1103/PhysRev.136.B1224.

P. C. Peters and J. Mathews. Gravitational Radiation from Point Masses in a Keplerian Orbit. *Physical Review*, 131(1):435–440, July 1963. doi: 10.1103/PhysRev.131.435.

Hugo Pfister, Marta Volonteri, Yohan Dubois, Massimo Dotti, and Monica Colpi. The erratic dynamical life of black hole seeds in high-redshift galaxies. *MNRAS*, 486(1):101–111, June 2019. doi: 10.1093/mnras/stz822.

Enrico Piconcelli, Cristian Vignali, Stefano Bianchi, Smita Mathur, Fabrizio Fiore, Matteo Guainazzi, Giorgio Lanzuisi, Roberto Maiolino, and Fabrizio Nicastro. Witnessing the Key Early Phase of Quasar Evolution: An Obscured Active Galactic Nucleus Pair in the Interacting Galaxy IRAS 20210+1121. *ApJ*, 722 (2):L147–L151, October 2010. doi: 10.1088/2041-8205/722/2/L147.

Annalisa Pillepich, Volker Springel, Dylan Nelson, Shy Genel, Jill Naiman, Rüdiger Pakmor, Lars Hernquist, Paul Torrey, Mark Vogelsberger, Rainer Weinberger, and Federico Marinacci. Simulating galaxy formation with the IllustrisTNG model. *MNRAS*, 473(3):4077–4106, January 2018. doi: 10.1093/mnras/stx2656.

Planck Collaboration, N. Aghanim, Y. Akrami, M. Ashdown, J. Aumont, C. Baccigalupi, M. Ballardini, A. J. Banday, R. B. Barreiro, and N. Bartolo. Planck 2018 results. VI. Cosmological parameters. *arXiv e-prints*, art. arXiv:1807.06209, Jul 2018.

Planck Collaboration, N. Aghanim, Y. Akrami, M. Ashdown, J. Aumont, C. Baccigalupi, M. Ballardini, A. J. Banday, R. B. Barreiro, N. Bartolo, S. Basak, R. Battye, K. Benabed, J. P. Bernard, M. Bersanelli, P. Bielewicz, J. J. Bock, J. R. Bond, J. Borrill, F. R. Bouchet, F. Boulanger, M. Bucher, C. Burigana, R. C. Butler, E. Calabrese, J. F. Cardoso, J. Carron, A. Challinor, H. C. Chiang, J. Chluba, L. P. L. Colombo, C. Combet, D. Contreras, B. P. Crill, F. Cuttaia, P. de Bernardis, G. de Zotti, J. Delabrouille, J. M. Delouis, E. Di Valentino, J. M. Diego, O. Doré, M. Douspis, A. Ducout, X. Dupac, S. Dusini, G. Efstathiou, F. Elsner, T. A. Enßlin, H. K. Eriksen, Y. Fantaye, M. Farhang, J. Fergusson, R. Fernandez-Cobos, F. Finelli, F. Forastieri, M. Frailis, A. A. Fraisse, E. Franceschi, A. Frolov, S. Galeotta, S. Galli, K. Ganga, R. T. Génova-Santos, M. Gerbino, T. Ghosh, J. González-Nuevo, K. M. Górski, S. Gratton, A. Gruppuso, J. E. Gudmundsson, J. Hamann, W. Handley, F. K. Hansen, D. Herranz, S. R. Hildebrandt, E. Hivon, Z. Huang, A. H. Jaffe, W. C. Jones, A. Karakci, E. Keihänen, R. Keskitalo, K. Kiiveri, J. Kim, T. S. Kisner, L. Knox, N. Krachmalnicoff, M. Kunz, H. Kurki-Suonio, G. Lagache, J. M. Lamarre, A. Lasenby, M. Lattanzi, C. R. Lawrence, M. Le Jeune, P. Lemos, J. Lesgourgues, F. Levrier, A. Lewis, M. Liguori, P. B. Lilje, M. Lilley, V. Lindholm, M. López-Caniego, P. M. Lubin, Y. Z. Ma, J. F. Macías-Pérez, G. Maggio, D. Maino, N. Mandolesi, A. Mangilli, A. Marcos-Caballero, M. Maris, P. G. Martin, M. Martinelli, E. Martínez-González, S. Matarrese, N. Mauri, J. D. McEwen, P. R. Meinhold, A. Melchiorri, A. Mennella, M. Migliaccio, M. Millea, S. Mitra, M. A. Miville-Deschênes, D. Molinari, L. Montier, G. Morgante, A. Moss, P. Natoli, H. U. Nørgaard-Nielsen, L. Pagano, D. Paoletti, B. Partridge, G. Patanchon, H. V. Peiris, F. Perrotta, V. Pettorino, F. Piacentini, L. Polastri, G. Polenta, J. L. Puget, J. P. Rachen, M. Reinecke, M. Remazeilles, A. Renzi, G. Rocha, C. Rosset, G. Roudier, J. A. Rubiño-Martín, B. Ruiz-Granados, L. Salvati, M. Sandri, M. Savelainen, D. Scott, E. P. S. Shellard, C. Sirignano, G. Sirri, L. D. Spencer, R. Sunyaev, A. S. Suur-Uski, J. A. Tauber, D. Tavagnacco, M. Tenti, L. Toffolatti, M. Tomasi, T. Trombetti, L. Valenziano, J. Valiviita, B. Van Tent, L. Vibert, P. Vielva, F. Villa, N. Vittorio, B. D. Wandelt, I. K. Wehus, M. White, S. D. M. White, A. Zacchei, and A. Zonca. Planck 2018 results. VI. Cosmological parameters. *A&A*, 641:A6, September 2020. doi: 10.1051/0004-6361/201833910.

Francisco Prada, Anatoly A. Klypin, Antonio J. Cuesta, Juan E. Betancort-Rijo, and Joel Primack. Halo concentrations in the standard Λ cold dark matter cosmology. *MNRAS*, 423(4):3018–3030, July 2012. doi: 10.1111/j.1365-2966.2012.21007.x.

Gerald D. Quinlan. The dynamical evolution of massive black hole binaries I. Hardening in a fixed stellar background. , 1(1):35–56, July 1996. doi: 10.1016/S1384-1076(96)00003-6.

Alireza Rahmati, Andreas H. Pawlik, Milan Raičević, and Joop Schaye. On the evolution of the H I column density distribution in cosmological simulations. *MNRAS*, 430(3):2427–2445, April 2013. doi: 10.1093/mnras/stt066.

Antti Rantala, Thorsten Naab, and Volker Springel. frost: a momentum-conserving CUDA implementation of a hierarchical fourth-order forward symplectic integrator. *MNRAS*, 502(4):5546–5562, April 2021. doi: 10.1093/mnras/stab057.

Alexander Rawlings, Matias Mannerkoski, Peter H. Johansson, and Thorsten Naab. Reviving stochasticity: uncertainty in SMBH binary eccentricity is unavoidable. *MNRAS*, 526(2):2688–2695, December 2023. doi: 10.1093/mnras/stad2891.

C. L. Reichardt, S. Patil, P. A. R. Ade, A. J. Anderson, J. E. Austermann, J. S. Avva, E. Baxter, J. A. Beall, A. N. Bender, B. A. Benson, F. Bianchini, L. E. Bleem, J. E. Carlstrom, C. L. Chang, P. Chaubal, H. C. Chiang, T. L. Chou, R. Citron, C. Corbett Moran, T. M. Crawford, A. T. Crites, T. de Haan, M. A. Dobbs, W. Everett, J. Gallicchio, E. M. George, A. Gilbert, N. Gupta, N. W. Halverson, N. Harrington, J. W. Henning, G. C. Hilton, G. P. Holder, W. L. Holzapfel, J. D. Hrubes, N. Huang, J. Hubmayr, K. D. Irwin, L. Knox, A. T. Lee, D. Li, A. Lowitz, D. Luong-Van, J. J. McMahon, J. Mehl, S. S. Meyer, M. Millea,

L. M. Mocanu, J. J. Mohr, J. Montgomery, A. Nadolski, T. Natoli, J. P. Nibarger, G. Noble, V. Novosad, Y. Omori, S. Padin, C. Pryke, J. E. Ruhl, B. R. Saliwanchik, J. T. Sayre, K. K. Schaffer, E. Shirokoff, C. Sievers, G. Smecher, H. G. Spieler, Z. Staniszewski, A. A. Stark, C. Tucker, K. Vanderlinde, T. Veach, J. D. Vieira, G. Wang, N. Whitehorn, R. Williamson, W. L. K. Wu, and V. Yefremenko. An Improved Measurement of the Secondary Cosmic Microwave Background Anisotropies from the SPT-SZ + SPTpol Surveys. *ApJ*, 908(2):199, February 2021. doi: 10.3847/1538-4357/abd407.

Amy E. Reines and Andrea Comastri. Observational Signatures of High-Redshift Quasars and Local Relics of Black Hole Seeds. , 33:e054, October 2016. doi: 10.1017/pasa.2016.46.

Amy E. Reines, Jenny E. Greene, and Marla Geha. Dwarf Galaxies with Optical Signatures of Active Massive Black Holes. *ApJ*, 775(2):116, October 2013. doi: 10.1088/0004-637X/775/2/116.

Amy E. Reines, James J. Condon, Jeremy Darling, and Jenny E. Greene. A New Sample of (Wandering) Massive Black Holes in Dwarf Galaxies from High-resolution Radio Observations. *ApJ*, 888(1):36, January 2020. doi: 10.3847/1538-4357/ab4999.

Christopher S. Reynolds. The spin of supermassive black holes. *Classical and Quantum Gravity*, 30(24): 244004, December 2013. doi: 10.1088/0264-9381/30/24/244004.

Angelo Ricarte and Priyamvada Natarajan. The observational signatures of supermassive black hole seeds. *MNRAS*, 481(3):3278–3292, December 2018. doi: 10.1093/mnras/sty2448.

Angelo Ricarte, Michael Tremmel, Priyamvada Natarajan, Charlotte Zimmer, and Thomas Quinn. Origins and demographics of wandering black holes. *MNRAS*, 503(4):6098–6111, June 2021. doi: 10.1093/mnras/stab866.

C. Ricci, F. E. Bauer, E. Treister, K. Schawinski, G. C. Privon, L. Blecha, P. Arevalo, L. Armus, F. Harrison, L. C. Ho, K. Iwasawa, D. B. Sanders, and D. Stern. Growing supermassive black holes in the late stages of galaxy mergers are heavily obscured. *MNRAS*, 468(2):1273–1299, June 2017. doi: 10.1093/mnras/stx173.

Vicente Rodriguez-Gomez, Shy Genel, Mark Vogelsberger, Debora Sijacki, Annalisa Pillepich, Laura V. Sales, Paul Torrey, Greg Snyder, Dylan Nelson, Volker Springel, Chung-Pei Ma, and Lars Hernquist. The merger rate of galaxies in the Illustris simulation: a comparison with observations and semi-empirical models. *MNRAS*, 449(1):49–64, May 2015. doi: 10.1093/mnras/stv264.

D. J. Rosario, R. C. McGurk, C. E. Max, G. A. Shields, K. L. Smith, and S. M. Ammons. Adaptive Optics Imaging of Quasi-stellar Objects with Double-peaked Narrow Lines: Are They Dual Active Galactic Nuclei? *ApJ*, 739(1):44, September 2011. doi: 10.1088/0004-637X/739/1/44.

Y. M. Rosas-Guevara, R. G. Bower, J. Schaye, M. Furlong, C. S. Frenk, C. M. Booth, R. A. Crain, C. Dalla Vecchia, M. Schaller, and T. Theuns. The impact of angular momentum on black hole accretion rates in simulations of galaxy formation. *MNRAS*, 454(1):1038–1057, November 2015. doi: 10.1093/mnras/stv2056.

Yetli M. Rosas-Guevara, Richard G. Bower, Stuart McAlpine, Silvia Bonoli, and Patricia B. Tissera. The abundances and properties of Dual AGN and their host galaxies in the EAGLE simulations. *MNRAS*, 483(2):2712–2720, February 2019. doi: 10.1093/mnras/sty3251.

Jaime Salcido, Richard G. Bower, Tom Theuns, Stuart McAlpine, Matthieu Schaller, Robert A. Crain, Joop Schaye, and John Regan. Music from the heavens - gravitational waves from supermassive black hole mergers in the EAGLE simulations. *MNRAS*, 463(1):870–885, November 2016. doi: 10.1093/mnras/stw2048.

Lia F. Sartori, Kevin Schawinski, Ezequiel Treister, Benny Trakhtenbrot, Michael Koss, Maryam Shirazi, and Kyuseok Oh. The search for active black holes in nearby low-mass galaxies using optical and mid-IR data. *MNRAS*, 454(4):3722–3742, December 2015. doi: 10.1093/mnras/stv2238.

S. Satyapal, N. J. Secrest, W. McAlpine, S. L. Ellison, J. Fischer, and J. L. Rosenberg. Discovery of a Population of Bulgeless Galaxies with Extremely Red Mid-IR Colors: Obscured AGN Activity in the Low-mass Regime? *ApJ*, 784(2):113, April 2014. doi: 10.1088/0004-637X/784/2/113.

Cecilia Scannapieco, Simon D. M. White, Volker Springel, and Patricia B. Tissera. The formation and survival of discs in a ΛCDM universe. *MNRAS*, 396(2):696–708, June 2009. doi: 10.1111/j.1365-2966.2009.14764.x.

Joop Schaye, Robert A. Crain, Richard G. Bower, Michelle Furlong, Matthieu Schaller, Tom Theuns, Claudio Dalla Vecchia, Carlos S. Frenk, I. G. McCarthy, John C. Helly, Adrian Jenkins, Y. M. Rosas-Guevara, Simon D. M. White, Maarten Baes, C. M. Booth, Peter Camps, Julio F. Navarro, Yan Qu, Alireza Rahmati, Till Sawala, Peter A. Thomas, and James Trayford. The EAGLE project: simulating the evolution and assembly of galaxies and their environments. *MNRAS*, 446(1):521–554, January 2015. doi: 10.1093/mnras/stu2058.

Alberto Sesana. Self Consistent Model for the Evolution of Eccentric Massive Black Hole Binaries in Stellar Environments: Implications for Gravitational Wave Observations. *ApJ*, 719(1):851–864, August 2010. doi: 10.1088/0004-637X/719/1/851.

Alberto Sesana and Fazeel Mahmood Khan. Scattering experiments meet N-body - I. A practical recipe for the evolution of massive black hole binaries in stellar environments. *MNRAS*, 454(1):L66–L70, November 2015. doi: 10.1093/mnrasl/slv131.

Alberto Sesana, Francesco Haardt, Piero Madau, and Marta Volonteri. Low-Frequency Gravitational Radiation from Coalescing Massive Black Hole Binaries in Hierarchical Cosmologies. *ApJ*, 611(2):623–632, August 2004. doi: 10.1086/422185.

Alberto Sesana, Francesco Haardt, Piero Madau, and Marta Volonteri. The Gravitational Wave Signal from Massive Black Hole Binaries and Its Contribution to the LISA Data Stream. *ApJ*, 623(1):23–30, April 2005. doi: 10.1086/428492.

Alberto Sesana, Francesco Haardt, and Piero Madau. Interaction of Massive Black Hole Binaries with Their Stellar Environment. II. Loss Cone Depletion and Binary Orbital Decay. *ApJ*, 660(1):546–555, May 2007a. doi: 10.1086/513016.

Alberto Sesana, Marta Volonteri, and Francesco Haardt. The imprint of massive black hole formation models on the LISA data stream. *MNRAS*, 377(4):1711–1716, June 2007b. doi: 10.1111/j.1365-2966.2007.11734.x.

N. I. Shakura and R. A. Sunyaev. Black holes in binary systems. Observational appearance. *A&A*, 24: 337–355, 1973.

Ray S. Sharma, Alyson M. Brooks, Rachel S. Somerville, Michael Tremmel, Jillian Bellovary, Anna C. Wright, and Thomas R. Quinn. Black Hole Growth and Feedback in Isolated ROMULUS25 Dwarf Galaxies. *ApJ*, 897(1):103, July 2020. doi: 10.3847/1538-4357/ab960e.

Laurie D. Shaw, Douglas H. Rudd, and Daisuke Nagai. Deconstructing the Kinetic SZ Power Spectrum. *ApJ*, 756(1):15, September 2012. doi: 10.1088/0004-637X/756/1/15.

Yue Shen, Xin Liu, Jenny E. Greene, and Michael A. Strauss. Type 2 Active Galactic Nuclei with Double-peaked [O III] Lines. II. Single AGNs with Complex Narrow-line Region Kinematics are More Common than Binary AGNs. *ApJ*, 735(1):48, July 2011. doi: 10.1088/0004-637X/735/1/48.

Yue Shen, Hsiang-Chih Hwang, Nadia Zakamska, and Xin Liu. Varstrometry for Off-nucleus and Dual Sub-Kpc AGN (VODKA): How Well Centered Are Low-z AGN? *ApJ*, 885(1):L4, November 2019. doi: 10.3847/2041-8213/ab4b54.

Yue Shen, Yu-Ching Chen, Hsiang-Chih Hwang, Xin Liu, Nadia Zakamska, Masamune Oguri, Jennifer I. Hsiu Li, Joseph Lazio, and Peter Breiding. A hidden population of high-redshift double quasars unveiled by astrometry. *Nature Astronomy*, 5:569–574, January 2021. doi: 10.1038/s41550-021-01323-1.

Yue. Shen et al. Statistics of galactic-scale quasar pairs at cosmic noon. 2022.

Debora Sijacki, Volker Springel, Tiziana Di Matteo, and Lars Hernquist. A unified model for AGN feedback in cosmological simulations of structure formation. *MNRAS*, 380(3):877–900, September 2007. doi: 10.1111/j.1365-2966.2007.12153.x.

Debora Sijacki, Mark Vogelsberger, Shy Genel, Volker Springel, Paul Torrey, Gregory F. Snyder, Dylan Nelson, and Lars Hernquist. The Illustris simulation: the evolving population of black holes across cosmic time. *MNRAS*, 452(1):575–596, September 2015. doi: 10.1093/mnras/stv1340.

J. D. Silverman, P. Kampczyk, K. Jahnke, R. Andrae, S. J. Lilly, M. Elvis, F. Civano, V. Mainieri, C. Vignali, G. Zamorani, P. Nair, O. Le Fèvre, L. de Ravel, S. Bardelli, A. Bongiorno, M. Bolzonella, A. Cappi, K. Caputi, C. M. Carollo, T. Contini, G. Coppa, O. Cucciati, S. de la Torre, P. Franzetti, B. Garilli, C. Halliday, G. Hasinger, A. Iovino, C. Knobel, A. M. Koekemoer, K. Kovač, F. Lamareille, J. F. Le Borgne, V. Le Brun, C. Maier, M. Mignoli, R. Pello, E. Pérez-Montero, E. Ricciardelli, Y. Peng, M. Scodeggio, M. Tanaka, L. Tasca, L. Tresse, D. Vergani, E. Zucca, M. Brusa, N. Cappelluti, A. Comastri, A. Finoguenov, H. Fu, R. Gilli, H. Hao, L. C. Ho, and M. Salvato. The Impact of Galaxy Interactions on Active Galactic Nucleus Activity in zCOSMOS. *ApJ*, 743(1):2, December 2011. doi: 10.1088/0004-637X/743/1/2.

John D. Silverman, Shenli Tang, Khee-Gan Lee, Tilman Hartwig, Andy Goulding, Michael A. Strauss, Malte Schramm, Xuheng Ding, Rogemar A. Riffel, Seiji Fujimoto, Chiaki Hikage, Masatoshi Imanishi, Kazushi Iwasawa, Knud Jahnke, Issha Kayo, Nobunari Kashikawa, Toshihiro Kawaguchi, Kotaro Kohno, Wentao Luo, Yoshiki Matsuoka, Yuichi Matsuda, Tohru Nagao, Masamune Oguri, Yoshiaki Ono, Masafusa Onoue, Masami Ouchi, Kazuhiro Shimasaku, Hyewon Suh, Nao Suzuki, Yoshiaki Taniguchi, Yoshiki Toba, Yoshihiro Ueda, and Naoki Yasuda. Dual Supermassive Black Holes at Close Separation Revealed by the Hyper Suprime-Cam Subaru Strategic Program. *ApJ*, 899(2):154, August 2020. doi: 10.3847/1538-4357/aba4a3.

Kendrick M. Smith and Simone Ferraro. Detecting patchy reionization in the cosmic microwave background. *Phys. Rev. Lett.*, 119:021301, Jul 2017. doi: 10.1103/PhysRevLett.119.021301. URL `https://link.aps.org/doi/10.1103/PhysRevLett.119.021301`.

A. Soltan. Masses of quasars. *MNRAS*, 200:115–122, July 1982. doi: 10.1093/mnras/200.1.115.

D. Spergel, N. Gehrels, C. Baltay, D. Bennett, J. Breckinridge, M. Donahue, A. Dressler, B. S. Gaudi, T. Greene, O. Guyon, C. Hirata, J. Kalirai, N. J. Kasdin, B. Macintosh, W. Moos, S. Perlmutter, M. Postman, B. Rauscher, J. Rhodes, Y. Wang, D. Weinberg, D. Benford, M. Hudson, W. S. Jeong, Y. Mellier, W. Traub, T. Yamada, P. Capak, J. Colbert, D. Masters, M. Penny, D. Savransky, D. Stern, N. Zimmerman, R. Barry, L. Bartusek, K. Carpenter, E. Cheng, D. Content, F. Dekens, R. Demers, K. Grady, C. Jackson, G. Kuan, J. Kruk, M. Melton, B. Nemati, B. Parvin, I. Poberezhskiy, C. Peddie, J. Ruffa, J. K. Wallace, A. Whipple, E. Wollack, and F. Zhao. Wide-Field InfrarRed Survey Telescope-Astrophysics Focused Telescope Assets WFIRST-AFTA 2015 Report. *arXiv e-prints*, art. arXiv:1503.03757, March 2015.

V. Springel and L. Hernquist. Cosmological smoothed particle hydrodynamics simulations: a hybrid multiphase model for star formation. *MNRAS*, 339:289–311, February 2003. doi: 10.1046/j.1365-8711.2003.06206.x.

V. Springel, T. Di Matteo, and L. Hernquist. Modelling feedback from stars and black holes in galaxy mergers. *MNRAS*, 361:776–794, August 2005a. doi: 10.1111/j.1365-2966.2005.09238.x.

Volker Springel. Smoothed Particle Hydrodynamics in Astrophysics. , 48:391–430, September 2010. doi: 10.1146/annurev-astro-081309-130914.

Volker Springel, Simon D. M. White, Giuseppe Tormen, and Guinevere Kauffmann. Populating a cluster of galaxies - I. Results at [formmu2]z=0. *MNRAS*, 328(3):726–750, December 2001. doi: 10.1046/j.1365-8711.2001.04912.x.

Volker Springel, Tiziana Di Matteo, and Lars Hernquist. Modelling feedback from stars and black holes in galaxy mergers. *MNRAS*, 361(3):776–794, August 2005b. doi: 10.1111/j.1365-2966.2005.09238.x.

Volker Springel, Rüdiger Pakmor, Oliver Zier, and Martin Reinecke. Simulating cosmic structure formation with the GADGET-4 code. *MNRAS*, 506(2):2871–2949, September 2021. doi: 10.1093/mnras/stab1855.

Lisa K. Steinborn, Klaus Dolag, Michaela Hirschmann, M. Almudena Prieto, and Rhea-Silvia Remus. A refined sub-grid model for black hole accretion and AGN feedback in large cosmological simulations. *MNRAS*, 448(2):1504–1525, April 2015. doi: 10.1093/mnras/stv072.

Lisa K. Steinborn, Klaus Dolag, Julia M. Comerford, Michaela Hirschmann, Rhea-Silvia Remus, and Adelheid F. Teklu. Origin and properties of dual and offset active galactic nuclei in a cosmological simulation at z=2. *MNRAS*, 458(1):1013–1028, May 2016. doi: 10.1093/mnras/stw316.

Aaron Stemo, Julia M. Comerford, R. Scott Barrows, Daniel Stern, Roberto J. Assef, Roger L. Griffith, and Aimee Schechter. A Catalog of 204 Offset and Dual Active Galactic Nuclei (AGNs): Increased AGN Activation in Major Mergers and Separations under 4 kpc. *ApJ*, 923(1):36, December 2021. doi: 10.3847/1538-4357/ac0bbf.

Kung-Yi Su, Philip F. Hopkins, Christopher C. Hayward, Xiangcheng Ma, Claude-André Faucher-Giguère, Dušan Kereš, Matthew E. Orr, T. K. Chan, and Victor H. Robles. The failure of stellar feedback, magnetic fields, conduction, and morphological quenching in maintaining red galaxies. *MNRAS*, 487(3):4393–4408, August 2019. doi: 10.1093/mnras/stz1494.

R. A. Sunyaev and Ia. B. Zeldovich. Microwave background radiation as a probe of the contemporary structure and history of the universe. , 18:537–560, January 1980. doi: 10.1146/annurev.aa.18.090180.002541.

Giuliano Taffoni, Lucio Mayer, Monica Colpi, and Fabio Governato. On the life and death of satellite haloes. *MNRAS*, 341(2):434–448, May 2003. doi: 10.1046/j.1365-8711.2003.06395.x.

Valentina Tamburello, Pedro R. Capelo, Lucio Mayer, Jillian M. Bellovary, and James W. Wadsley. Supermassive black hole pairs in clumpy galaxies at high redshift: delayed binary formation and concurrent mass growth. *MNRAS*, 464(3):2952–2962, January 2017. doi: 10.1093/mnras/stw2561.

Tomas Tamfal, Pedro R. Capelo, Stelios Kazantzidis, Lucio Mayer, Douglas Potter, Joachim Stadel, and Lawrence M. Widrow. Formation of LISA Black Hole Binaries in Merging Dwarf Galaxies: The Imprint of Dark Matter. *ApJ*, 864(1):L19, September 2018. doi: 10.3847/2041-8213/aada4b.

Takamitsu Tanaka and Zoltán Haiman. The Assembly of Supermassive Black Holes at High Redshifts. *ApJ*, 696(2):1798–1822, May 2009. doi: 10.1088/0004-637X/696/2/1798.

Hiroyuki Tashiro, Nabila Aghanim, Mathieu Langer, Marian Douspis, Saleem Zaroubi, and Vibor Jelić. Second order cross-correlation between kinetic Sunyaev-Zel'dovich effect and 21-cm fluctuations from the epoch of reionization. *MNRAS*, 414(4):3424–3433, July 2011. doi: 10.1111/j.1365-2966.2011.18644.x.

Ananth Tenneti, Tiziana Di Matteo, Rupert Croft, ThomasJae Garcia, and Yu Feng. The descendants of the first quasars in the BlueTides simulation. *MNRAS*, 474(1):597–603, February 2018. doi: 10.1093/mnras/stx2788.

Nicole Thomas, Romeel Davé, Daniel Anglés-Alcázar, and Matt Jarvis. Black hole - Galaxy correlations in SIMBA. *MNRAS*, 487(4):5764–5780, August 2019. doi: 10.1093/mnras/stz1703.

Christopher Tiede, Jonathan Zrake, Andrew MacFadyen, and Zoltan Haiman. Gas-driven Inspiral of Binaries in Thin Accretion Disks. *ApJ*, 900(1):43, September 2020. doi: 10.3847/1538-4357/aba432.

H. Trac. Parametrizing the Reionization History with the Redshift Midpoint, Duration, and Asymmetry. *ApJ*, 858:L11, May 2018. doi: 10.3847/2041-8213/aabff0.

H. Trac, R. Cen, and A. Loeb. Imprint of Inhomogeneous Hydrogen Reionization on the Temperature Distribution of the Intergalactic Medium. *ApJ*, 689:L81–L84, December 2008. doi: 10.1086/595678.

H. Trac, R. Cen, and P. Mansfield. SCORCH I: The Galaxy-Halo Connection in the First Billion Years. *ApJ*, 813:54, November 2015. doi: 10.1088/0004-637X/813/1/54.

Hy Trac, Paul Bode, and Jeremiah P. Ostriker. Templates for the Sunyaev-Zel'dovich Angular Power Spectrum. *ApJ*, 727(2):94, February 2011. doi: 10.1088/0004-637X/727/2/94.

Hy Trac, Nianyi Chen, Ian Holst, Marcelo A. Alvarez, and Renyue Cen. AMBER: A Semi-Numerical Abundance Matching Box for the Epoch of Reionization. *arXiv e-prints*, art. arXiv:2109.10375, September 2021.

Scott Tremaine, Karl Gebhardt, Ralf Bender, Gary Bower, Alan Dressler, S. M. Faber, Alexei V. Filippenko, Richard Green, Carl Grillmair, Luis C. Ho, John Kormendy, Tod R. Lauer, John Magorrian, Jason Pinkney, and Douglas Richstone. The Slope of the Black Hole Mass versus Velocity Dispersion Correlation. *ApJ*, 574(2):740–753, August 2002. doi: 10.1086/341002.

M. Tremmel, F. Governato, M. Volonteri, and T. R. Quinn. Off the beaten path: a new approach to realistically model the orbital decay of supermassive black holes in galaxy formation simulations. *MNRAS*, 451(2):1868–1874, August 2015. doi: 10.1093/mnras/stv1060.

M. Tremmel, M. Karcher, F. Governato, M. Volonteri, T. R. Quinn, A. Pontzen, L. Anderson, and J. Bellovary. The Romulus cosmological simulations: a physical approach to the formation, dynamics and accretion models of SMBHs. *MNRAS*, 470(1):1121–1139, September 2017. doi: 10.1093/mnras/stx1160.

M. Tremmel, F. Governato, M. Volonteri, T. R. Quinn, and A. Pontzen. Dancing to CHANGA: a self-consistent prediction for close SMBH pair formation time-scales following galaxy mergers. *MNRAS*, 475 (4):4967–4977, April 2018a. doi: 10.1093/mnras/sty139.

Michael Tremmel, Fabio Governato, Marta Volonteri, Andrew Pontzen, and Thomas R. Quinn. Wandering Supermassive Black Holes in Milky-Way-mass Halos. *ApJ*, 857(2):L22, April 2018b. doi: 10.3847/2041-8213/aabc0a.

Hannah Übler, Roberto Maiolino, Emma Curtis-Lake, Pablo G. Pérez-González, Mirko Curti, Michele Perna, Santiago Arribas, Stéphane Charlot, Madeline A. Marshall, Francesco D'Eugenio, Jan Scholtz, Andrew Bunker, Stefano Carniani, Pierre Ferruit, Peter Jakobsen, Hans-Walter Rix, Bruno Rodríguez Del Pino, Chris J. Willott, Torsten Boeker, Giovanni Cresci, Gareth C. Jones, Nimisha Kumari, and Tim Rawle. GA-NIFS: A massive black hole in a low-metallicity AGN at z $\sim$ 5.55 revealed by JWST/NIRSpec IFS. *A&A*, 677:A145, September 2023. doi: 10.1051/0004-6361/202346137.

Yoshihiro Ueda, Masayuki Akiyama, Günther Hasinger, Takamitsu Miyaji, and Michael G. Watson. Toward the Standard Population Synthesis Model of the X-Ray Background: Evolution of X-Ray Luminosity and Absorption Functions of Active Galactic Nuclei Including Compton-thick Populations. *ApJ*, 786(2):104, May 2014. doi: 10.1088/0004-637X/786/2/104.

R. van de Weygaert and E. Bertschinger. Peak and gravity constraints in Gaussian primordial density fields: An application of the Hoffman-Ribak method. *MNRAS*, 281:84, July 1996. doi: 10.1093/mnras/281.1.84.

S. Van Wassenhove, M. Volonteri, M. G. Walker, and J. R. Gair. Massive black holes lurking in Milky Way satellites. *MNRAS*, 408(2):1139–1146, October 2010. doi: 10.1111/j.1365-2966.2010.17189.x.

Sandor Van Wassenhove, Marta Volonteri, Lucio Mayer, Massimo Dotti, Jillian Bellovary, and Simone Callegari. Observability of Dual Active Galactic Nuclei in Merging Galaxies. *ApJ*, 748(1):L7, March 2012. doi: 10.1088/2041-8205/748/1/L7.

Eugene Vasiliev. AGAMA: action-based galaxy modelling architecture. *MNRAS*, 482(2):1525–1544, January 2019. doi: 10.1093/mnras/sty2672.

Eugene Vasiliev and David Merritt. The Loss-cone Problem in Axisymmetric Nuclei. *ApJ*, 774(1):87, September 2013. doi: 10.1088/0004-637X/774/1/87.

Eugene Vasiliev, Fabio Antonini, and David Merritt. The Final-parsec Problem in the Collisionless Limit. *ApJ*, 810(1):49, September 2015. doi: 10.1088/0004-637X/810/1/49.

Eugene Vasiliev, Vasily Belokurov, and N. Wyn Evans. Radialization of Satellite Orbits in Galaxy Mergers. *ApJ*, 926(2):203, February 2022. doi: 10.3847/1538-4357/ac4fbc.

Mark Vogelsberger, Shy Genel, Debora Sijacki, Paul Torrey, Volker Springel, and Lars Hernquist. A model for cosmological simulations of galaxy formation physics. *MNRAS*, 436(4):3031–3067, December 2013. doi: 10.1093/mnras/stt1789.

Mark Vogelsberger, Shy Genel, Volker Springel, Paul Torrey, Debora Sijacki, Dandan Xu, Greg Snyder, Dylan Nelson, and Lars Hernquist. Introducing the Illustris Project: simulating the coevolution of dark and visible matter in the Universe. *MNRAS*, 444(2):1518–1547, October 2014. doi: 10.1093/mnras/stu1536.

Mark Vogelsberger, Federico Marinacci, Paul Torrey, and Ewald Puchwein. Cosmological simulations of galaxy formation. *Nature Reviews Physics*, 2(1):42–66, January 2020. doi: 10.1038/s42254-019-0127-2.

M. Volonteri, Y. Dubois, C. Pichon, and J. Devriendt. The cosmic evolution of massive black holes in the Horizon-AGN simulation. *MNRAS*, 460(3):2979–2996, August 2016. doi: 10.1093/mnras/stw1123.

Marta Volonteri and Martin J. Rees. Rapid Growth of High-Redshift Black Holes. *ApJ*, 633(2):624–629, November 2005. doi: 10.1086/466521.

Marta Volonteri, Joseph Silk, and Guillaume Dubus. The Case for Supercritical Accretion onto Massive Black Holes at High Redshift. *ApJ*, 804(2):148, May 2015. doi: 10.1088/0004-637X/804/2/148.

Marta Volonteri, Hugo Pfister, Ricarda S. Beckmann, Yohan Dubois, Monica Colpi, Christopher J. Conselice, Massimo Dotti, Garreth Martin, Ryan Jackson, Katarina Kraljic, Christophe Pichon, Maxime Trebitsch, Sukyoung K. Yi, Julien Devriendt, and Sébastien Peirani. Black hole mergers from dwarf to massive galaxies with the NewHorizon and Horizon-AGN simulations. *MNRAS*, 498(2):2219–2238, August 2020. doi: 10.1093/mnras/staa2384.

Marta Volonteri, Hugo Pfister, Ricarda Beckmann, Massimo Dotti, Yohan Dubois, Warren Massonneau, Gibwa Musoke, and Michael Tremmel. Dual AGN in the Horizon-AGN simulation and their link to galaxy and massive black hole mergers, with an excursus on multiple AGN. *MNRAS*, 514(1):640–656, July 2022. doi: 10.1093/mnras/stac1217.

Feige Wang, Jinyi Yang, Xiaohui Fan, Joseph F. Hennawi, Aaron J. Barth, Eduardo Banados, Fuyan Bian, Konstantina Boutsia, Thomas Connor, Frederick B. Davies, Roberto Decarli, Anna-Christina Eilers, Emanuele Paolo Farina, Richard Green, Linhua Jiang, Jiang-Tao Li, Chiara Mazzucchelli, Riccardo Nanni, Jan-Torge Schindler, Bram Venemans, Fabian Walter, Xue-Bing Wu, and Minghao Yue. A Luminous Quasar at Redshift 7.642. *ApJ*, 907(1):L1, January 2021. doi: 10.3847/2041-8213/abd8c6.

Dacen Waters, Stephen M. Wilkins, Tiziana Di Matteo, Yu Feng, Rupert Croft, and Daisuke Nagai. Monsters in the dark: predictions for luminous galaxies in the early Universe from the BLUETIDES simulation. *MNRAS*, 461(1):L51–L55, September 2016. doi: 10.1093/mnrasl/slw100.

W Weibull. A statistical distribution function of wide applicability. *Journal of Applied Mechanics*, 18(3):293–297, 1951. URL `https://pdfs.semanticscholar.org/88c3/7770028e7ed61180a34d6a837a9a4db3b264.pdf`.

Rainer Weinberger, Volker Springel, Lars Hernquist, Annalisa Pillepich, Federico Marinacci, Rüdiger Pakmor, Dylan Nelson, Shy Genel, Mark Vogelsberger, Jill Naiman, and Paul Torrey. Simulating galaxy formation with black hole driven thermal and kinetic feedback. *MNRAS*, 465(3):3291–3308, March 2017. doi: 10.1093/mnras/stw2944.

Stephen M. Wilkins, Yu Feng, Tiziana Di Matteo, Rupert Croft, Christopher C. Lovell, and Dacen Waters. The properties of the first galaxies in the BlueTides simulation. *MNRAS*, 469(3):2517–2530, August 2017. doi: 10.1093/mnras/stx841.

Rogier A. Windhorst, Seth H. Cohen, Rolf A. Jansen, Chris Conselice, and Haojing Yan. How JWST can measure first light, reionization and galaxy assembly. , 50(1-3):113–120, March 2006. doi: 10.1016/j.newar.2005.11.018.

Tyrone E. Woods, Bhaskar Agarwal, Volker Bromm, Andrew Bunker, Ke-Jung Chen, Sunmyon Chon, Andrea Ferrara, Simon C. O. Glover, Lionel Haemmerlé, Zoltán Haiman, Tilman Hartwig, Alexander Heger, Shingo Hirano, Takashi Hosokawa, Kohei Inayoshi, Ralf S. Klessen, Chiaki Kobayashi, Filippos Koliopanos, Muhammad A. Latif, Yuexing Li, Lucio Mayer, Mar Mezcua, Priyamvada Natarajan, Fabio Pacucci, Martin J. Rees, John A. Regan, Yuya Sakurai, Stefania Salvadori, Raffaella Schneider, Marco Surace, Takamitsu L. Tanaka, Daniel J. Whalen, and Naoki Yoshida. Titans of the early Universe: The Prato statement on the origin of the first supermassive black holes. , 36:e027, August 2019. doi: 10.1017/pasa.2019.14.

Xue-Bing Wu, Feige Wang, Xiaohui Fan, Weimin Yi, Wenwen Zuo, Fuyan Bian, Linhua Jiang, Ian D. McGreer, Ran Wang, Jinyi Yang, Qian Yang, David Thompson, and Yuri Beletsky. An ultraluminous quasar with a twelve-billion-solar-mass black hole at redshift 6.30. *Nature*, 518(7540):512–515, February 2015. doi: 10.1038/nature14241.

J. Wurster and R. J. Thacker. A comparative study of AGN feedback algorithms. *MNRAS*, 431(3):2513–2534, May 2013. doi: 10.1093/mnras/stt346.

J. Stuart B. Wyithe and Abraham Loeb. Low-Frequency Gravitational Waves from Massive Black Hole Binaries: Predictions for LISA and Pulsar Timing Arrays. *ApJ*, 590(2):691–706, June 2003. doi: 10.1086/375187.

O. Zahn, A. Mesinger, M. McQuinn, H. Trac, R. Cen, and L. E. Hernquist. Comparison of reionization models: radiative transfer simulations and approximate, seminumeric models. *MNRAS*, 414:727–738, June 2011. doi: 10.1111/j.1365-2966.2011.18439.x.

O. Zahn, C. L. Reichardt, L. Shaw, A. Lidz, K. A. Aird, B. A. Benson, L. E. Bleem, J. E. Carlstrom, C. L. Chang, H. M. Cho, T. M. Crawford, A. T. Crites, T. de Haan, M. A. Dobbs, O. Doré, J. Dudley, E. M. George, N. W. Halverson, G. P. Holder, W. L. Holzapfel, S. Hoover, Z. Hou, J. D. Hrubes, M. Joy, R. Keisler, L. Knox, A. T. Lee, E. M. Leitch, M. Lueker, D. Luong-Van, J. J. McMahon, J. Mehl, S. S. Meyer, M. Millea, J. J. Mohr, T. E. Montroy, T. Natoli, S. Padin, T. Plagge, C. Pryke, J. E. Ruhl, K. K. Schaffer, E. Shirokoff, H. G. Spieler, Z. Staniszewski, A. A. Stark, K. Story, A. van Engelen, K. Vanderlinde, J. D. Vieira, and R. Williamson. Cosmic Microwave Background Constraints on the Duration and Timing of Reionization from the South Pole Telescope. *ApJ*, 756(1):65, Sep 2012. doi: 10.1088/0004-637X/756/1/65.

Oliver Zahn, Adam Lidz, Matthew McQuinn, Suvendra Dutta, Lars Hernquist, Matias Zaldarriaga, and Steven R. Furlanetto. Simulations and Analytic Calculations of Bubble Growth during Hydrogen Reionization. *ApJ*, 654(1):12–26, Jan 2007. doi: 10.1086/509597.

Ya. B. Zel'dovich. Gravitational instability: An approximate theory for large density perturbations. *A&A*, 5:84–89, March 1970.

Ya. B. Zeldovich and R. A. Sunyaev. The Interaction of Matter and Radiation in a Hot-Model Universe. *Ap&SS*, 4(3):301–316, July 1969. doi: 10.1007/BF00661821.

Pengjie Zhang, Ue-Li Pen, and Hy Trac. Precision era of the kinetic Sunyaev-Zel'dovich effect: simulations, analytical models and observations and the power to constrain reionization. *MNRAS*, 347(4):1224–1233, February 2004. doi: 10.1111/j.1365-2966.2004.07298.x.

Qirong Zhu. A momentum-conserving N-body scheme with individual time steps. , 85:101481, May 2021. doi: 10.1016/j.newast.2020.101481.